Advancing climate resilient agriculture in the U.S. Great Plains: Modeling climate dynamics and impacts on crop production

by

Zachary Todd Zambreski

B.S., Cornell University, 2014
M.S., Kansas State University, 2016

AN ABSTRACT OF A DISSERTATION

submitted in partial fulfillment of the requirements for the degree

DOCTOR OF PHILOSOPHY

Department of Agronomy
College of Agriculture

KANSAS STATE UNIVERSITY
Manhattan, Kansas

2020

Abstract

Climate variability has historically been a major driver of food production across the globe. Projections of climate demonstrate changes in the variability of temperature and precipitation, threatening the security of food production in areas such as the U.S Great Plains, one of the most agriculturally significant regions in the world. In this region over pumping of groundwater from the Ogallala Aquifer, which has been critical to sustain crop productivity in semiarid regions, has led to declines in the water table. Large-scale irrigated agriculture along with changes of land cover and land use may produce significant interactions with regional climate in the future. These critical issues motivated three objectives for this dissertation: 1) identify the historical behavior of drought, a major agricultural climate driver, 2) dynamically model the agricultural water management impacts on regional climate change, and 3) quantify changes in the resiliency of wheat production to environmental changes in the Great Plains.

In this dissertation, multiple long-term surface climate, regional satellite, and crop phenology and production datasets were integrated and investigated in simulations and analysis. Statistical and dynamic climate modeling were the main methodologies utilized in this study. Regional climate analysis indicated that winter and summer growing season temperatures and drought intensities have significantly increased in the U.S. Great Plains in recent decades. There were 9 −12 identified seasonal subregions of homogeneous drought variability, and several subregions demonstrated wetting trends since the early twentieth century. Summer and winter drought became more and less complex across space and time, respectively, indicating changes in resource management may be necessary to mitigate impacts in the future. Regional climate model simulations with new irrigation modules developed indicated that irrigation significantly

alters the ambient moisture and temperature profiles at the surface and the mid-levels of the atmosphere. Precipitation increased over irrigated grid cells that had a reduction in the number of acres under irrigation over the last thirty years. Choice of land surface model parameterizations and modeling scale was a significant source of uncertainty in several climate responses, suggesting that future research should carefully examine these options during initial experimental design. Statistical modeling of winter wheat yields demonstrated that at the regional level historical changes in climate since the early 1970s have negatively impacted yield trends while changes in phenology have partially offset some of the negative impacts from climate change. Furthermore, recently developed winter wheat varieties have higher sensitivities to both spring heat and cold stress. Newer varieties achieved their optimal yield response under higher precipitation regimes, indicating recent varieties were less resilient to weather-related impacts. Both changes in phenology and climate sensitivities helped explain the observed increase in yield variance in recent decades at the regional and variety levels. Overall, this dissertation explored diverse areas related to climate resiliency in agriculture, leading to new insights into relationships between major climate drivers and crop production while introducing new tools that provide pertinent information to a wide audience, including agronomists, breeders, and earth system modelers.

Advancing climate resilient agriculture in the U.S. Great Plains: modeling climate dynamics and impacts on crop production

by

Zachary Todd Zambreski

B.S., Cornell University, 2014
M.S., Kansas State University, 2016

A DISSERTATION

submitted in partial fulfillment of the requirements for the degree

DOCTOR OF PHILOSOPHY

Department of Agronomy
College of Agriculture

KANSAS STATE UNIVERSITY
Manhattan, Kansas

2020

Approved by:

Major Professor
Xiaomao Lin

Copyright

Abstract

Climate variability has historically been a major driver of food production across the globe. Projections of climate demonstrate changes in the variability of temperature and precipitation, threatening the security of food production in areas such as the U.S Great Plains, one of the most agriculturally significant regions in the world. In this region over pumping of groundwater from the Ogallala Aquifer, which has been critical to sustain crop productivity in semiarid regions, has led to declines in the water table. Large-scale irrigated agriculture along with changes of land cover and land use may produce significant interactions with regional climate in the future. These critical issues motivated three objectives for this dissertation: 1) identify the historical behavior of drought, a major agricultural climate driver, 2) dynamically model the agricultural water management impacts on regional climate change, and 3) quantify changes in the resiliency of wheat production to environmental changes in the Great Plains.

In this dissertation, multiple long-term surface climate, regional satellite, and crop phenology and production datasets were integrated and investigated in simulations and analysis. Statistical and dynamic climate modeling were the main methodologies utilized in this study. Regional climate analysis indicated that winter and summer growing season temperatures and drought intensities have significantly increased in the U.S. Great Plains in recent decades. There were 9 −12 identified seasonal subregions of homogeneous drought variability, and several subregions demonstrated wetting trends since the early twentieth century. Summer and winter drought became more and less complex across space and time, respectively, indicating changes in resource management may be necessary to mitigate impacts in the future. Regional climate model simulations with new irrigation modules developed indicated that irrigation significantly

alters the ambient moisture and temperature profiles at the surface and the mid-levels of the atmosphere. Precipitation increased over irrigated grid cells that had a reduction in the number of acres under irrigation over the last thirty years. Choice of land surface model parameterizations and modeling scale was a significant source of uncertainty in several climate responses, suggesting that future research should carefully examine these options during initial experimental design. Statistical modeling of winter wheat yields demonstrated that at the regional level historical changes in climate since the early 1970s have negatively impacted yield trends while changes in phenology have partially offset some of the negative impacts from climate change. Furthermore, recently developed winter wheat varieties have higher sensitivities to both spring heat and cold stress. Newer varieties achieved their optimal yield response under higher precipitation regimes, indicating recent varieties were less resilient to weather-related impacts. Both changes in phenology and climate sensitivities helped explain the observed increase in yield variance in recent decades at the regional and variety levels. Overall, this dissertation explored diverse areas related to climate resiliency in agriculture, leading to new insights into relationships between major climate drivers and crop production while introducing new tools that provide pertinent information to a wide audience, including agronomists, breeders, and earth system modelers.

Table of Contents

List of Figures

List of Tables

Acknowledgements

I like to first acknowledge my major adviser Xiaomao Lin, who has trained me over the last six years since the beginning of my Masters in 2014 through the end of my PhD in 2020. His knowledge, guidance, compassion, and empathy has molded me into a well-rounded researcher with a broad knowledge domain. He also graciously afforded me many additional opportunities such as a cooperative research exchange with China in 2017, which pushed me out of my comfort zone but increased my cultural awareness. I would also like to thank Mary Knapp, who was instrumental in providing specialized expertise on issues related to Kansas agriculture and climate and learning the fundamentals of many climate tools and bouncing off thoughts and ideas. My committee members Robert Aiken, Gerard Kluitenberg, and Shawn Hutchinson were also critical in sharpening skillsets related to research from class work selection to filling knowledge gaps and insights into the manuscript process. Robert Aiken in particular expanded my boundaries on many topics outside of climate and encouraged me to contemplate complex issues below the surface.

I am forever grateful for the love and support throughout my entire academic career of my mother and father April and John Zambreski. They have been enormous motivators throughout my time at Kansas State, visiting me frequently and encouraging me through my evanescent moments of imposter's syndrome and self-doubt. In addition, I would never have had the momentum to finish my PhD without my loving partner Trevyn Sell. He constantly teaches me new things, pushes my boundaries, and advocates for me no matter the situation. I am exceptionally fortunate to have met someone so amazing to be a major part of my life.

I like to also acknowledge the friendship and collaboration between members in my research group over the course of the last six years, including Seth Kutikoff, Yongjun Zhang, Ramesh Dhungel, Haidong Zhao, Shuang Sun, Tianyi Zhang, and Nenghan Wan. They taught me a great deal about the research process and offered advice on many subjects in addition to good conversation. I would also like to acknowledge Xuan Xu, Guillermo Balboa, and Ednaldo Borgato, who were PhD colleagues in the department who helped sharpened my knowledge in topics related to statistics, agronomy, and weed science. As a member of the Ogallala Water Collaborative Agricultural Project, I would like to thank project members for allowing me to be a part of an amazing group of students, faculty, and researchers. Many of the contacts, particularly the students and postdocs, helped strengthen my research credentials through collaboration efforts and assisted me in my own research by providing data or feedback. I would also like to thank Jane Lingenfelser who aided in the digitizing of the variety trial reports in the Kansas State Agronomy Library and researchers who provided any open-source model code.

Preface

Climate resilient agriculture is critical to sustain the stability of the food supply as the global population continues to increase simultaneously with anthropogenic and natural climate change. A production system is climate resilient if it can mitigate external stresses from sub-optimal environmental conditions while maintaining the overall integrity of the system. Climate change is predicted to have a wide range of negative impacts on crop growth and development that will limit crop productivity and ultimately food production. Therefore, climate resilient agriculture is becoming increasingly important with focus on improving management practices and genetics that can mitigate losses in crop productivity due to climate change.

Of the negative environmental factors faced by current crop systems, drought is widely accepted to be one of the most critical limitations to crop yields. Drought stress has been expected to limit the productivity of more than 50% of arable land in next 50 years especially for the U.S. Great Plains, a critically important agricultural region. Over the last century, the Great Plains has experienced highly variable drought conditions, contributing to large agricultural losses during several extreme drought and wet events. Understanding the climate dynamics that lead to drought stress on a spatio-temporal basis is important for both guiding climate adaption strategies and drought planning preparation, underlining the major motivation for chapter one in this dissertation.

Furthermore, drought stress can be mitigated using irrigation in order to meet crop water demands. Irrigation in agriculture is a dynamic and challenging subject for regional-scale modeling due to wide climate gradients, diverse crop types, and evolving management practices

in U.S. Great Plains. Agricultural practices can induce significant feedbacks on regional climate, which can affect crop productivity by altering the energy and water budgets. Recent satellite observations are instrumental for mapping irrigated cropland and land use, which provide powerful information for modifying a numerical weather prediction (NWP) system designed to serve both climate research and irrigation water forecasting needs. The WRF-irrigation model is such a NWP system for the simulation and prediction of the atmosphere. Declining groundwater levels across the Ogallala Aquifer region in the Great Plains have been a major catalyst for improving the representation of management practices into regional climate models in order to understand potential effects on changes in climate and consequently crop production, which was the motivation for the second chapter in this dissertation.

Finally, production systems need to be evaluated within the context of changes in genetics and management practices over time to assess how historical changes in climate have impacted crop productivity. However, it can be challenging to adequately quantify temporal changes in a crop production's resiliency to climate variability due to data limitations such as missing information on genetics or management. To overcome these limitations, we assembled long-term records of both genetics at the field-level and phenology progress at the state-level to quantify resiliency at multiple scales in Kansas for winter wheat, an important crop for food security. We developed a robust statistical modeling framework to examine the effectiveness of different climate adaptations, including changes in phenology and yield sensitivities at the variety level, to guide future strategies in breeding and agronomy programs.

Exploration of these research objectives in this dissertation will help guide agronomists, plant breeders, and modelers in understanding and improving critical components of climate resilient agriculture critical for global food security. Therefore, this dissertation was divided into four chapters with the following primary objectives:

1. Identify subregions of historical agricultural drought variability in the central U.S. (Chapter 1);

2. Model the atmospheric response to irrigation across the Ogallala Aquifer region (Chapter 2);

3. Quantify changes in the resiliency of winter wheat production systems in Kansas to climate change (Chapter 3);

4. Conclusions and agricultural implications (Chapter 4).

Chapter 1 - Identification of hydroclimate subregions for seasonal drought monitoring in the U.S. Great Plains

Zambreski, Z. T., X. Lin, R. M. Aiken, G. J. Kluitenberg, and R. A. Pielke Sr, 2018: Identification of hydroclimate subregions for seasonal drought monitoring in the U.S. Great Plains. *Journal of Hydrology*, **567,** 370-381, doi: https://doi.org/10.1016/j.jhydrol.2018.10.013.

Abstract

Identification of subregions that share similar historical drought variability provides useful information for drought monitoring, mitigation planning, and resource allocation. This study examined space-time historical drought variability for the Great Plains spanning from 1901 to 2015 by using rotated Empirical Orthogonal Functions (rEOFs). The Standardized Precipitation-Evapotranspiration Index (SPEI) on a three-month timescale was utilized to examine spatial and temporal changes in agricultural drought. We propose a new procedure for identifying the number of rEOFs to be selected for reconstructing subregions. Drought event intensities of moderate, severe, and extreme categories increased in recent years although the number of drought events decreased. Seasonal rEOFs demonstrated that 9 to 12 subregions were adequate to explain a significant proportion of the original variability in the Great Plains. The time series for each subregion was highly correlated to the original SPEI data and reflected the seasonal meteorological processes that drive drought variability. Several significant wetting trends were found, and there was statistical evidence that drought and wetting event severities had increased for a few subregions. Summer drought has become more variable across space and time, indicating that a more diverse set of resources and strategies might be needed to mitigate impacts of spatially-variable drought and wetting events in coming decades. Winter season drought has become less variable, indicating that perhaps resources could be consolidated when

dealing with impacts on a larger scale; however, less variability implies that drought and wetting events may occur across larger regions of the Great Plains during a given season.

Keywords: Drought; Empirical Orthogonal Functions; Climate; Agriculture; SPEI

1. Introduction

Regionalizing variability across space and time is a complex multi-scalar problem. The demand for regional assessments of historical climate variability is growing due to its value in decision-making processes such as the management of water resources and agricultural systems (Bonaccorso et al. 2003; Omondi et al. 2013). The Great Plains of the United States is a significant contributor to U.S. and global food production and relies on both optimal climatic conditions and crop management practices to sustain high production. Changes in regional climate due to human and natural variations and long-term change generate uncertainty in global food security (Easterling et al. 1993; Pielke et al. 2013). Daily, monthly, and annual perturbations in weather and climate across this agricultural region create significant impacts at local and regional scales. Drought, a condition of moisture deficit sufficient to have an adverse effect on vegetation, animals, and society, is a multi-faceted and complex climate-related phenomenon (Sönmez et al. 2005; Warwick 1975). The Great Plains has experienced highly variable drought conditions throughout the historical climate record (since the late 1800s). The most notable droughts include the multi-year droughts of the 1930s and 1950s and the more recent droughts in the late 1980s and 2011-2012 that resulted in billions of dollars in agricultural losses (Svoboda et al. 2002). Human activity such as the expansion of agriculture into marginal lands (Colaizzi et al. 2009) or groundwater depletion (Russo and Lall 2017) has been shown to modify the vulnerability of agricultural systems to drought impacts. Poor management practices during the Dust Bowl era of the 1930s led to high rates of soil erosion and decreasing land productivity that resulted in off-farm migration (McLeman et al. 2014). Changes in policy and management practices that resulted from lessons learned during the 1930s resulted in less severe agricultural impacts during the 1950s (Wiener et al. 2016). Rising temperatures would intensify

droughts due to increases in evaporation from the soil and transpiration from vegetation leading to more frequent withdrawals of underground water resources (IPCC 2013). Across the Great Plains, such a change would increase the number of climate-related challenges and might include 1) resolving increasing competition among land, water, and energy resources; 2) developing sustainable agricultural systems; 3) conserving diverse ecological systems; and 4) enhancing the resilience of communities to the impacts of extreme events, including more intense heat waves, cold snaps, drought, and flooding events (Shafer et al. 2014).

The Great Plains cover a wide range in latitude and elevation, spanning the continental land area between northern Mexico and the Prairie provinces of Canada and experiencing an elevation gain of more than a thousand meters from Texas to the base of the Rocky Mountains. Although its latitudinal extent exceeds its spread in longitude, the Great Plains has a gradient in annual precipitation of more than 1,200 mm in gulf coastal areas in the southeast to less than 400 mm at the eastern slopes of the Rocky Mountains (Pielke and Doesken 2008). The Köppen climate classification divides the Great Plains into four main categories: humid subtropical, hot-summer humid continental, warm-summer humid continental, and cold semi-arid (Köppen 2011). Differences in classifications are generally driven by latitude and elevation, corresponding with gradients in annual mean temperature and precipitation. The precipitation gradient results in two types of grasslands that dominate the Great Plains: short and tallgrass prairie in the west and east, respectively (Küchler 1964). These grasslands are vital ecosystems for farming, grazing, and biofuel production and are highly sensitive to rainfall variability (Knapp and Smith 2001; Shafer et al. 2014). Low precipitation during the growing season can trigger agricultural drought, which occurs when soil moisture availability falls below a level that

has an adverse effect on crop production (Panu and Sharma 2002). The economic importance of this region and the space-time variability of precipitation and temperature underscore the need for additional assessments of drought variability on timescales affecting these agricultural and socioeconomic systems, e.g., seasonal and monthly.

Several studies and methods have been used to examine historical drought variability of the Great Plains. Although records of climate observations began in the late 1800s, scientists have used tree rings to reconstruct the paleoclimatic record over the last several centuries, indicating that multi-decadal droughts as severe as major droughts of the twentieth century have occurred in the Great Plains in the last millennium (Sauchyn et al. 2003; Stockton and Meko 1983; Woodhouse and Overpeck 1998). Other methods have been utilized to examine the characteristics of drought during the instrumental record. Guttman (1998) used spectral analysis of several drought indices to classify weather stations across the United States according to their characteristics, and his results demonstrated incoherent regional patterns in the Great Plains. Other studies have used the trends directly calculated from the Standardized Precipitation Index (SPI) or the Palmer Drought Severity Index (PDSI) to show both wetting and drying has occurred across areas of the Great Plains (Logan et al. 2010; Yuan and Quiring 2014). In addition to drought indices, land surface modeling has been utilized to study the mechanisms that drive soil moisture deficits in the Great Plains, showing that antecedent moisture conditions can have an impact on drought severity during the summer growing season (Livneh and Hoerling 2016). Broader studies of drought trends over the contiguous United States show a decrease in the percentage of dry areas from the 1950s to 1990s and an increase in the percentage of dry areas since the 1990s (Dai 2011). These studies demonstrate that regional variations in drought

exist, and characterizing large areas such as the Great Plains as a single region can produce misleading drought metrics that are not representative of the unique subregions that may exist. Emerging techniques provide an opportunity to more accurately identify and characterize the spatio-temporal structures of regional historical drought variability.

Empirical Orthogonal Function (EOF) analysis, a multivariate statistical method first used for climatological applications in the 1950s (Lorenz 1956), has been utilized in diverse applications to analyze the spatial and temporal variability of geophysical datasets (Bjornsson and Venegas 1997). The EOF procedure constructs orthogonal linear combinations that explain the maximum amount of variance in both space and time. Through various rotations of these linear combinations, geographic regions of similar variability can be identified. Karl and Koscielny (1982) used EOF analysis to regionalize drought across the United States from long-term records of PDSI. Nine broad regions were identified, and spectral analysis revealed that regions in the interior U.S. experienced longer duration droughts. Other large- and small-scale studies of drought EOFs have been conducted across the globe in regions including China (Cai et al. 2015), Romania (Bojariu et al. 2012; Cheval et al. 2014), Portugal (Martins et al. 2012; Santos et al. 2010), the Iberian Peninsula (Vicente-Serrano 2006), Turkey (Tatli and Türkeş 2011), and Sicily (Bonaccorso et al. 2003). For example, Raziei et al. (2010) regionalized drought across Iran into four subregions based on the variability of the SPI at a time scale of 24 months. In these studies, applications of EOF analysis included but were not limited to 1) assessment of the similarities and differences amongst drought indices; 2) identification of strong and weak temporal signals in the drought time series; and 3) the separation of a region into sub-climate regimes. While many of these studies did not explore the drought metrics of these EOF

indices such as duration, severity, or intensity, analysis of these metrics would enhance our understanding of the space-time variability of these intrinsic drought characteristics. Identifying regions that share similar drought variability is important for drought monitoring, drought mitigation planning, and drought emergency management. Given that sub-climates can span administrative regions, interagency cooperation could help improve drought preparedness. These insights are crucial for drought management agencies that require detailed but concise information on changes in historical climate for their areas.

The objective of this study was to investigate the spatial and temporal variability structures of seasonal and full-record monthly drought and wetting episodes in the Great Plains from 1901 to 2015 by identification of subregions from EOF analysis. We proposed a new EOF selection rule to identify significant subregions of variability. The Standardized Precipitation-Evapotranspiration Index (SPEI), a recently developed multi-scalar drought index that includes the effects of temperature variability, was chosen for this analysis as it can identify an increase in drought severity due to higher water demand as a result of evapotranspiration (Vicente-Serrano et al. 2010).

2. Material and methods

2.1 Study area and data source

For this study, the domain extended between latitudes +32° and +48° and longitudes −93° and −106°, covering over 2,100,000 km^2 of the central United States (Fig. 1.1). Monthly precipitation, temperature (maximum and minimum), and potential evapotranspiration coverage (0.5° × 0.5° grid) were obtained from the Climatic Research Unit TS v. 3.24.01 (CRU) at the

University of East Anglia, UK (Harris et al. 2014) for years between 1901 and 2015. A total of 891 CRU grid points were used for the study. CRU was chosen for this analysis because its resolution allows for a reasonable number of grid points in the Great Plains to perform an EOF analysis. The inclusion of areas surrounding the Great Plains helps to avoid loss of variability and to isolate important drought features potentially hidden in a larger-scale analysis (Richman 1986).

2.2 Standardized Precipitation-Evapotranspiration Index

Potential evapotranspiration (PE) provided by CRU was estimated using a variant of the Penman-Monteith procedure, and the difference between precipitation and PE is calculated for each month. These differences are summed based on the time scale chosen. Following the procedure in Vicente-Serrano et al. (2010), these summed differences are fitted to a three-parameter log-logistic cumulative probability distribution function, and this procedure is performed separately for each month and grid point. These probabilities are standardized using the approximation found in Zelen and Severo (1964) to obtain the SPEI. This index ranges in value from approximately −3 to approximately +3, with negative values indicating drier than normal conditions and positive values indicating conditions wetter than normal. SPEI values less than −2.0 or greater than 2.0 are considered extreme. Time series of SPEI values were calculated using tools developed at Kansas State University. The index was calibrated using data from the period 1931-1990. A time scale of three months was used to represent short-term drought which is more closely related to agricultural drought (Vicente-Serrano et al. 2011). The earliest available 3-month SPEI was March 1901. The model fit between observed summed differences of precipitation and PE and the expected values from the fitted log-logistic distribution was evaluated for each month using the Kolmogorov-Smirnov test at each grid point. No test resulted

in rejection of the null hypothesis that the data come from the log-logistic distribution, indicating that the statistical assumptions behind the SPEI are valid for this region.

2.3 Drought metrics

Duration, severity, and intensity were used to characterize drought and wetting events in each time series of SPEI values. The duration of a drought event is the length of time (in months) that the drought index is consecutively at or below a given truncation threshold. Similarly, the duration of a wetting event is the length of time (in months) that the drought index is at or above a given threshold. The severity of each event is the cumulative sum of the index over the duration of the event. The intensity of a drought or wetting event is its severity divided by its duration and is considered the average index or 'rating' of that event. To robustly investigate the significance of drought trends, a modified Mann-Kendall test was employed (Mann 1945; Wilks 2011) to avoid inflated p-values due to the underestimation of the test statistic variance (Hamed and Ramachandra Rao 1998). Then, the Theil-Sen slope estimate was used to identify the magnitude of the trend (Theil 1950). The two-sample Kolmogorov-Smirnov test was implemented to test the hypothesis that the distributions of a metric calculated from drought or wetting events during different time periods come from the same continuous distribution (Massey 1951). Statistical significance was assessed at a level of 5% for these tests.

2.4 Empirical orthogonal function analysis

For this study, grid point location and SPEI values were the variables and observations, respectively, for the EOF analysis. The resulting orthogonal eigenvectors, also referred to as EOFs, point in the direction in which the data vectors exhibit the most variability. The principal

components (PCs), which represent how EOFs evolve through time, are obtained by projecting the EOFs onto the original SPEI data. EOFs often exhibit characteristics that hamper their utility to isolate individual patterns of variation, such as domain shape or size dependence (Richman 1986). Because weather in the Great Plains is generally dominated by large regional atmospheric processes, the orthogonality constraint on the eigenvectors can lead to problems with interpretation, especially for the second and subsequent PCs (Wilks 2011). Because of the limitations of EOF analysis in the Great Plains, a retained number of EOF loadings (each retained EOF scaled by the square root of its eigenvalue) were rotated using Varimax rotation (Kaiser 1958; Preisendorfer and Mobley 1988). Varimax rotation redistributes the variance among rotated EOFs (rEOFs) and PCs (rPCs) and attempts to simplify the rEOFs by pushing loading coefficients toward 0 or ±1. The loadings used for this rotation result in nonorthogonal rEOFs and rPCs (Wilks 2011) that are more regionally localized and highly correlated to the original SPEI data than the unrotated EOFs and PCs.

Several selection methods are available to determine the number of EOFs that capture most of the variability without significant loss of information. These methods can be divided into three classes: rules based on the size of the last retained eigenvalue (Hannachi et al. 2007), hypothesis-testing (Preisendorfer and Mobley 1988), and the structure of the retained principal components (Wilks 2011). One commonly used selection rule is North's Rule of Thumb (North et al. 1982) which uses the sampling error of each eigenvalue to determine non-degenerate EOFs. However, North's Rule of Thumb and other selection methods such as Kaiser's Rule or Rule N (Overland and Preisendorfer 1982) use the size or sampling properties of the eigenvalues and do not adequately fit the objective of this study because they do not use properties of the EOFs after

rotation. We argue that the primary utility of rEOFs in drought analysis is their ability to identify subregions of similar variability through time without the constraint of orthogonality and propose that a more useful criterion is the correlation of the rPCs with the original data. When subregions are identified with rPCs that are highly correlated to the original data, drought characteristics can be generalized across large land areas. As the number of EOFs rotated increases, the number of subregions identified increases, and correlation coefficients increase. At some rotation, there is no significant improvement in the correlation coefficients. Based on this observation, we propose a new rule to identify the rotation at which this occurs.

2.5 Selection rule for determining the number of rotated EOFs

The selection rule begins when a selected number of leading EOFs (N) are rotated (usually two). At each of the 891 grid points, the original standardized drought dataset is correlated with all N rPC time series, using the absolute value of the correlation coefficients. For each grid point, the rPC time series with the highest correlation is reported as i, which is designated as an integer between 1 and N. After all grid points have been matched with a single rPC, subregions can be identified by grouping together grid points with the same i, forming a subregion mask. Next, N+1 leading EOFs are independently rotated, and the same procedure is applied when N were rotated. The subregion mask created using N+1 leading rPCs is projected onto the grid of correlation coefficients that was calculated during the rotation of N EOFs. This projection creates two samples of paired correlation coefficients corresponding to the subregions in the current and previous rotation.

For each subregion j identified in the rotation of N+1 EOFs, the difference between the current and previous correlation coefficients from each rotation at each point in the subregion is calculated, and a sign test is performed to test the null hypothesis that the distribution of differences (D_j) has zero median against the alternative that the median is not equal to zero at a significance level of 1%. If the result of the sign test is statistically significant, H_j is recorded as,

$$H_j = \begin{cases} 1, \text{median}(D_j) > 0 \\ -1, \text{median}(D_j) < 0 \end{cases}$$

If the test is not significant, H_j is recorded as zero. When $\sum_{j=1}^{N+1} H_j > 0$ there was at least one subregion that had an improvement in the median correlation when an additional EOF was rotated. N is incremented by one, and the procedure is repeated until the first occurrence when the criteria $\sum_{j=1}^{N+1} H_j < 0$ is met, indicative that the inclusion of an additional rEOF weakened the overall relationship between subregion rPCs and the original SPEI data. The number of desirable rEOFs is given as N, and the procedure concludes. No statistically significant gains in information were made in the subregions identified using N+1 rEOFs, and the subregions have become relatively stable. It is important to note that there are cases when $\sum_{j=1}^{N+1} H_j = 0$ at a rotation followed by $\sum_{j=1}^{N+1} H_j > 0$ when additional rEOFs are included, which is the rational for using the criteria $\sum_{j=1}^{N+1} H_j < 0$. Also, if there were N rEOFs, there might be fewer subregions identified based on this correlation procedure.

After the final number of rEOFs to rotate has been decided, smooth boundaries between subregions can be drawn by interpolating the maximum correlations. Correlations should be presented with subregion boundaries to illustrate the strength of the relationship of these rPCs

with the original SPEI data. In some heterogeneous cases, non-continuous subregions can be identified due to similarities in drought dynamics separated at distance, and these cases should be carefully examined when constructing a subregion mask.

The numerical magnitude and sign of the standardized rPC of each subregion can be interpreted as a drought index that possesses statistical properties similar to the input dataset (i.e., the SPEI data). Thus, the same seasonal and full-record drought characteristics that were calculated for the SPEI can also be calculated for the rPC, allowing for drought and wetting event detection and statistical analysis across spatial scales larger than a single grid point. Full-record rPCs were used to calculate drought and wetting event durations, severities, and intensities for events occurring in two periods (1901-1957 and 1958-2015) to assess changes in the distributions of drought metrics. To assess whether seasonal drought variability has remained stationary over time, an rEOF analysis was conducted using a fixed number of rEOFs on a 50-year moving window (starting 1901-1950, 1902-1951, and continuing until 1966-2015). If the total variance explained by the rEOFs for each individual analysis stays approximately the same, then climatic features that influence drought across the Great Plains have remained relatively stable through time.

3. Results

3.1 Climate trends and drought statistics

CRU winter and summer growing season maximum temperature significantly increased between 1901 and 2015 across a majority of the northern and western High Plains (Fig. 1.2a(i), a(ii)). The strongest rates of warming (0.2 to 0.3 °C decade^{-1}) occurred across the foothills of the

Rocky Mountains in New Mexico, Colorado, and Wyoming in the summer (Fig. 1.2a(ii)) . Spatial distribution of trends during the summer and winter growing seasons were relatively similar, but across North Dakota and Minnesota, trends were larger during the winter than during the summer. During the summer season, there were also several notable areas in the eastern Great Plains that experienced significant decreases in maximum temperature. Minimum temperature during the winter increased at a faster rate than during the summer (Fig. 1.2b(i), b(ii)), and the proportion of grid points showing a statistically significant increasing trend was greater for minimum temperature than for maximum temperature (Fig. 1.2a, b). The largest differences between winter and summer minimum temperature trends occurred in eastern South Dakota, North Dakota, Minnesota, and New Mexico. There was also more significant warming in the southeast Plains over Arkansas during the summer than the winter. These warming trends during the summer in the southeast are in direct contrast to the cooling trends displayed by maximum temperatures.

Spatial distributions of growing season precipitation trends for both seasons were more variable and isolated (Fig. 1.2c(i), c(ii)). Of the grids with a statistically significant trend in precipitation, most exhibited a positive trend (Fig. 1.2c(i), c(ii)). Isolated areas east of the −100° meridian during the summer increased at the highest rates, and the rate of increase exceeded 2 mm decade^{-1} across northwest Louisiana (Fig. 1.2c(ii)). During the winter growing season, a small number of grids west of the −100° meridian had a modest decrease in precipitation (–0.2 to –0.5 mm decade^{-1} in Fig. 1.2c(i)).

When evaluated using a threshold of −0.5, the 3-month SPEI data revealed that there were on average 143 droughts per grid point (approximately 1.2 times per year in the Great Plains) with a standard deviation of 8.8 in the Great Plains between 1901 and 2015. When the period was divided into three time intervals of equal duration excluding 1901 (1902-1939, 1940-1977, and 1978-2015), the average number of drought events per grid point was approximately 48, 49, and 41, respectively. Notably the last 38 years had significantly fewer drought events than the previous two periods, which was offset by an increase in the number of wet events using a threshold of 0.5 (53 wet events for 1978-2015 vs. 48 for 1902-1939). Empirical cumulative frequency distributions (ECFD) of SPEI drought event intensities for these three time intervals are shown in Fig. 1.3a. The two-sample Kolmogorov-Smirnov test was statistically significant for all pairwise comparisons (p-values $< 10^{-5}$). These distributions demonstrate that of the drought events that occurred between 1978 and 2015, moderate, severe, and extreme drought events occurred at a higher frequency than in previous periods. While the number of drought events decreased in recent years, the intensity of those events increased. Divergence between time interval ECFDs is evident beginning at intensities of around −1.75, reaching maximum separation around the transition between severe and moderate drought categories.

All three time intervals had less than 10% of all droughts rated severe or extreme, and 35–40% of all drought events were rated as moderate. Notice that 0.18%, 0.09 %, and 0.50% of all drought events are categorized as extreme for the periods 1902-1939, 1940-1977, and 1978-2015, respectively (Fig. 1.3b). In context of the study area and the number of events per period, roughly 21% of grids experienced a drought event that rated on average as extreme between 1978 and 2015 while only 4% did between 1902 and 1939. Combining the information contained

across all grid points shows the overall status of the Great Plains; however, more relevant information can be acquired by analyzing the drought and wetting dynamics contained in subregions that contain distinctive information about drought variability.

3.2 Seasonal rEOFs

3.2.1 Spring and summer

Thirteen EOFs were selected for rotation using spring SPEI, resulting in 10 subregions of similar drought variability that explain about 85% of the total drought variability (Fig. 1.4a). Correlation coefficients of rPCs with the original SPEI data for grid points within subregions were generally greater than 0.75. These subregions span administrative units and political boundaries. For example, subregion 1, which covers most of central and western Kansas, also includes an extension of land in interior southern Colorado (east of subregion 7 in Colorado and northern New Mexico). It should be noted that the overall correlation in this area of Colorado comparatively lower, and it may be the result of high variability or it possessing characteristics more in common with areas west of the study domain. The area along subregional boundaries in western South Dakota demonstrate low correlation ($r < 0.75$), illustrating that the variability exhibited in these areas is not explained as well as other areas in the domain using this procedure.

The spring rPC time series demonstrate clear differences between subregion seasonal drought and wet spell onsets, durations, and severities (Fig. 1.4b). The time series also highlight periods when subregions experienced similar drought conditions (e.g., drought between 1960 and 1980). Based on severity and duration, subregion 9 centered on eastern Kansas and Missouri

experienced the longest period of sustained extreme spring drought during the 1960s. Spring droughts occurring during the 1960s and 1970s appear to have had somewhat larger areal coverage as evident by the red bands across most subregions in Figure 1.4b. The 2011-2012 springtime drought was the worst (rPC < –2) for subregion 4 in the Texas Panhandle. Overall, each time series shows its own unique drought characteristics with differences in onset, duration, and intensity of spring drought events.

Fourteen EOFs were selected for rotation using summer SPEI data, resulting in 9 subregions of similar drought variability that explain about 82% of the total drought variability (Fig. 1.4c). All subregions have at least one grid point with a correlation coefficient of 0.75 or greater, and the area in central Colorado (subregion 7) demonstrates a much stronger relationship with its rPC than subregion 7 in spring (Fig. 1.4a). The orientation of subregions is notably different in the summer than during the spring (Fig. 1.4a, c). There is a nearly vertical axis at about the −100° meridian that extends from the southern portion of the study domain into central Nebraska.

For most of the Great Plains, summer drought in the 1930s (Fig. 1.4d) was notably extreme and had much higher regional coverage than spring drought. The Dust Bowl era of the 1930s contained some of the driest and hottest growing seasons in modern U.S. history, which would have had significant negative impacts on crop production (Glotter and Elliott 2016). Subregions across Kansas and northward showed the most extreme decadal drought conditions during this time. Summer drought conditions between 2005-2015 were notably drier for subregions 1, 2, 5, and 7 extending across the High Plains.

3.2.2 Fall and winter

Fifteen EOFs were selected for rotation using fall SPEI data, resulting in 12 subregions of similar drought variability that explain about 85% of the total original drought variability (Fig. 1.5a). The orientation of subregions resembles the orientation for spring rEOFs (Fig. 1.4a) with boundaries angled towards the northeast. There are correlation coefficients greater than 0.75 within all subregions except subregion 9, which is located along the Minnesota and Iowa border. This area exhibits lower correlation during fall than spring or summer. Other areas exhibiting low correlation were in south central Nebraska and north central Kansas. The rPCs for each subregion demonstrate that the multi-decadal period starting in 1940 and ending during the early 1960s was notably dry (Fig. 1.5b), while 1970s fall conditions were overall wet with the most notable drought occurring in subregions 1 and 8 in the mid-1980s.

Eighteen EOFs were selected for rotation using winter SPEI data, resulting in 10 subregions of similar drought variability that explain about 88% of the total original drought variability (Fig. 1.5c). The subregions constructed in the southern plains are quite large compared to those for spring, summer, and fall. Notably there is one that spans across most of the portion of Texas within the study domain (subregion 1). This is significant because for the other seasons, the area of the domain that includes Texas is divided across the low rolling plains. Additionally, subregion 4 dominates most of Kansas, southeast Nebraska, and Iowa. These large subregions also demonstrate strong correlation, highlighting the broad and homogenous influence of synoptic features during the winter in the southern plains. Drought planners may be able to consolidate resources when assessing winter mitigation strategies. The area that demonstrates the most variability lies across Colorado and Minnesota. Upon examination of the

rPC time series, the period between 1960 and 1980 was notably the driest for most subregions (Fig. 1.5d). Subregion 6 across western South Dakota in the northern Great Plains experienced the longest duration of extreme decadal drought of any region during the late-1950s and early-1960s, followed closely by subregion 1 during the mid to late-1950s.

3.2.3 Seasonal trends

For springtime drought conditions, subregion 6 in north central Nebraska had a statistically significant trend of 0.06 rPC decade^{-1} (Fig. 1.6a). During the summer, subregion 8 across eastern Nebraska and Iowa had a statistically significant trend of 0.09 rPC decade^{-1} (Fig. 1.6b). Trends during the fall and winter showed the strongest statistical evidence among all seasons (Fig. 1.6c, d). Subregions 3 (centered on southern Colorado), 4 (centered on Minnesota), 7 (centered on eastern Texas), and 11 (centered on southeast South Dakota) demonstrated significant wetting trends of 0.06, 0.06, 0.08, and 0.09 rPC decade^{-1} during the fall, respectively (Fig. 1.6c). Winter subregions 5, 6, and 9 also demonstrated statistically significant wetting trends of 0.07, 0.06, and 0.16 rPC decade^{-1}, respectively, and all three are separated at distance across the domain and demonstrate no clear spatial pattern (Fig. 1.6d). As a whole, seasonal trend analysis showed that either some regions in the Great Plains have trended towards wetter conditions since 1901, or they do not have significant trend values. However, it is interesting to note that some areas across the Great Plains were characterized by temporal trends that were positive and negative in different seasons. For example, areas in northwest Nebraska demonstrated wetting and drying in winter (subregion 6) and spring (subregion 5), respectively. These results emphasize the importance of seasonal analysis which has major implications for the agricultural community who depend on timely rainfall during different growing seasons.

3.3 Full-record rEOFs

Fourteen EOFs were selected for rotation when using the full-record SPEI data resulting in 10 subregions of similar drought variability that explain about 87% of the total drought variability (Fig. 1.7a). All rPCs (excluding 9) for each subregion are highly correlated to the original SPEI data ($r > 0.85$). Spatially, the correlation matrix illustrated that the rPCs for most subregions in the Great Plains were significantly correlated ($0.05 < r \leq 0.7$) (Fig. 1.7b). The two pairs of subregions that have the strongest relationship are 2 and 7 and 5 and 8 ($0.6 < r \leq 0.7$). In contrast, subregions 4 and 7 across the southern Ogallala Aquifer and Minnesota, respectively, have non-significant correlations. The SPEI drought conditions of subregions 4 and 7 act independently. This demonstrates that summarizing the short-term drought variability of the Great Plains as a single region would be a mischaracterization of the complexities that exist in this region, particularly across the southern High Plains and northern Great Plains.

For each subregion's full-record rPC, distributions of drought events and corresponding metrics were calculated using thresholds of –0.5, –1.0, –1.5, and –2.0 for the periods before and after 1958. Likewise, distributions of wet events were calculated using thresholds of 0.5, 1.0, 1.5, and 2.0. The distributions for the thresholds of –0.5 and 0.5 and results of the two-sample Kolmogorov-Smirnov test are presented in Fig. 1.8. There is no statistical evidence for changes in drought metric distributions between these two periods at this threshold (Fig. 1.8a). In contrast, there is evidence of a distribution shift towards more severe (p-value: 0.04) and intense (p-value: 0.01) wet events between 1958 and 2015 across Minnesota in subregion 7 (Fig. 1.8b).

At thresholds less than −0.5 and greater than 0.5 (results not shown), only a few subregions had statistically significant changes in distributions for drought event metrics. Differences in drought event intensities between the two periods for subregion 2 at a threshold of −1.0 were statistically significant (p-value: 0.02). This is an indication that the intensity of moderate drought events increased during 1958-2015 across western North Dakota, South Dakota, and eastern Montana. At a threshold of −1.5, the intensities of drought events in subregion 8 were statistically significant, indicating an increase in drought event intensity during 1958-2015 (p-value: 0.04).

3.4 Temporal changes in drought variability

To examine temporal changes in drought variability, ten leading rEOFs were retained for this analysis based on the number of subregions identified previously, and a 50-year moving window starting from 1901 was used to calculate the total variance explained for each window. A decrease in the amount of variance explained by the same number of rEOFs is an indication that the space-time variability of drought increased because more rEOFs must be retained to explain the same proportion of variability. Figure 1.9 shows how the total variance explained by 10 rEOFs has changed over time by season. The variance explained by summer rEOFs changed significantly between the periods 1932-1981 and 1937-1986, decreasing from 82% to almost 80% within a period of several years. However, it steadily rebounded between 1940-1990 and 1966-2015. The variance explained by fall rEOFs steadily increased and decreased over the period, demonstrating little overall differences. One explanation for the increasing variability is the change in coverage of major drought and wetting events. Results from the seasonal rEOF time series showed that persistent and widespread droughts (e.g., in the 1930s and mid-to-late

1950s) affecting most subregions occurred less frequently in the latter half of the twentieth century. Subregions experienced more localized drought and wetting events of variable duration, severity, and intensity, increasing the space-time variability in EOF analysis. The sharp rebound starting around 1961-2010 during the summer was most likely due to the major drought event between 2011 and 2012, which had substantial coverage across most of the Great Plains. If historical trends continue, and seasonal drought becomes more variable, a more diverse set of resources and strategies may be required to deal with its impacts.

Overall, winter and spring showed an increase in variance explained by the rEOFs while the summer drought has become more complicated (i.e. more difficult to explain) in terms of variability (Fig. 1.9). Temporal variations of drought variability explained for the winter season were relatively smaller than those in other seasons, indicating that the effects of climatic structures that drive drought variability changed less rapidly year-to-year in winter. Thus, this suggests that spatially, the effects of drought and wetting events became more homogenous. Should this homogeneity continue among winter events across the Great Plains, there is the potential for resource managers to consolidate resources to mitigate impacts. However, when drought or wetting events do occur, their impacts could be more widespread.

4. Discussion

Our results showed that temperatures have significantly increased for a large portion of the Great Plains during the summer and winter growing seasons while trends in precipitation have significantly changed for only isolated areas of the Great Plains (Fig. 1.2). The seasonal rPC trends from EOF analysis demonstrated that only some subregions experienced statistically

significant changes in drought conditions, and the rPC trends more closely resembled the patterns displayed by the precipitation trends than the temperature trends. While much of the western Plains demonstrated statistically significant trends in temperature (Fig. 1.2a, b), only a few grid points in the western Great Plains had statistically significant precipitation trends (Fig. 1.2c). In the EOF analysis, the rPC trends of seasonal subregions in the western Great Plains were also not significant. Many areas in the eastern Great Plains that demonstrated positive trends in precipitation (Fig. 1.2c) also demonstrated significant wetting in the EOF analysis (Fig. 1.6). It is apparent that the warming that occurred in the western Great Plains did not significantly change the monthly differences between precipitation and PE that are inputted into the SPEI calculation, emphasizing that precipitation is most likely the dominant driver of SPEI variability in the Great Plains, which is similar to the results from previous work (Livneh and Hoerling 2016). Trend analysis also highlighted that some subregions covering similar areas demonstrated both drying and wetting trends depending on the season analyzed. Based on these results, we contend that analysis of the seasonal rPC trends instead of the full-record rPC trends has more practical implications for agriculture because full-record analysis can mask seasonal trends that are diametrically opposed, which would be misleading for crop producers. While previous drought EOF studies have focused more on the full drought record than the seasonal drought record, we argue that drought analysis should, where possible, be conducted seasonally to truly understand the complexity of drought dynamics.

An important caveat to acknowledge is that the trends calculated in this study may have been slightly different if another gridded dataset product was chosen for analysis. Because gridded datasets process station observations differently, it is important to consider the

uncertainties in trends that result from the methodology used in dataset construction (Wang et al. 2017). For example, CRU TS datasets are constructed using the Climate Anomaly Method (Peterson et al. 1998), which requires station data to meet a minimum number of observations for observed climatology. At each time step, available observation anomalies are gridded to 0.5° × 0.5° resolution using triangulated linear interpolation, which are converted to absolute values using the 1961-1990 climatology (Harris et al. 2014). Analysis of temperature trends over the period 1901-2015 (not shown) demonstrated relatively good spatial agreement among other higher resolution datasets such as the Parameter–Elevation Regressions on Independent Slopes Model (PRISM) (Di Luzio et al. 2008) and VOSE (Vose et al. 2014). Notably maximum temperature trends calculated from PRISM exhibited a higher coverage of grid points with significant decreases in temperature in the eastern areas of the Great Plains. PRISM does not adjust for changes in instrumentation (Wang et al. 2017), which may explain discrepancies among products. Precipitation trends among CRU, PRISM, VOSE, and Global Precipitation Climatology Centre (GPCC) exhibited much stronger agreement than minimum and maximum temperature.

There have been several proposed explanations for the observed wetting trends in the Great Plains and Midwest. Some studies suggest that widespread expansion of irrigation and cropland that occurred during the 1950s enhanced summer precipitation by increasing atmospheric moisture and moisture convergence (Alter et al. 2015; Alter et al. 2017). Other research suggests that the variability of the Great Plains low-level may have played a role in the alteration of precipitation patterns (Wang and Chen 2009). Rising temperatures resulting from an increase in global greenhouse concentrations have also been linked to an increase in atmospheric

water vapor across areas of the Great Plains, leading to an increase in the frequency of heavier rainfall events (Groisman et al. 2004; Villarini et al. 2012). While our study cannot directly explain the trends we observed, our results fit well within the current literature for this region. Although not explored in great detail, dividing the entire period of record into smaller moving windows, performing the EOF analysis, and examining changes in subregion patterns through time may provide insight into changes in synoptic structures that have dominated the Great Plains since instrumental records began.

Seasonal EOF analysis also demonstrated differences in the spatial patterns of the subregions. This is additional evidence for conducting seasonal EOF analysis because it provides insight into the different processes that dominate seasonal drought variability in the Great Plains. These processes were more apparent during the rotation of selected EOFs. Rotation of two leading EOFs demonstrated that the dominant seasonal subregions of drought variability in the Great Plains occur in the northern and southern plains. This division may be physically explained by the relative influence of sea surface temperatures in the Pacific Ocean for these two regions. Previous studies have found that drought variability in the southern Great Plains is more sensitive to changes in equatorial Pacific sea surface temperatures than drought variability exhibited in the northern Great Plains, which may respond greater to internal atmospheric variability (Hoerling et al. 2009). Warming and cooling of the sea surface temperatures in the Pacific Ocean can generate changes in the prevailing circulation patterns that transport moisture from this source region (Borchert 1950). Rotation of three EOFs divided the previously identified subregions into areas that resemble the synoptic structures that dominate weather. For example, during the summer in the southern plains, subregions are sharply divided at the −100°

meridian, representing the western boundary of the northward transport of gulf moisture by the low-level jet in the eastern Great Plains. For the winter season, subregions have boundaries that resemble synoptic fronts, which result from the cyclonic movement of air masses across the Great Plains. These physical modes of variability exhibited by the differences in seasonal synoptic structures provide a physical explanation of the subregion patterns in the EOF analysis.

Based on the total amount of drought variability in the Great Plains, the selection rule proposed in this study identified 9 to 12 subregions. Compared to the Karl and Koscielny (1982) study, the number of subregions identified in our analysis for the Great Plains was equal to or larger than the nine identified for the entire United States. However, the authors in that study chose the number of EOFs to retain for rotation based on the original resolution of the dataset, which included only 60 grid points across the entire U.S. In addition, none of the subregions had rPCs that were strongly correlated with drought data in the central Great Plains. Other studies in areas outside the U.S. used North's Rule to identify the number of EOFs to retain for rotation and then constructed subregions using cluster analysis or examination of the coefficients of the rEOFs (Cai et al. 2015; Raziei et al. 2010). We identified six to seven seasonal subregions using North's Rule in the Great Plains, which was less than the number identified using our selection rule. However, the correlation coefficients across subregions using North's Rule were lower, particularly in the areas identified in our analysis along subregion boundaries. Our rule could identify subregions across these areas that significantly improved correlation with the original data across most of the Great Plains. Analysis of the statistical properties of the rPCs in this study also demonstrated that the subregions had unique characteristics, such as different drought or wetting trends, providing strong evidence for their inclusion in drought monitoring. Because

the selection rule proposed in this study tests the differences in correlation coefficients within subregions in sequential rotations, we argue that they represent the best subregions of drought variability that can be obtained by EOF analysis. This was exhibited by the high correlation of the rPCs with the original SPEI data. Areas that consistently had lower correlations such as Colorado indicate that dimensional reduction of drought variability in this region was difficult to achieve, which may be expected given that this area represents a high degree of precipitation variability that results from the orographic lift of the Rocky Mountains that may not be represented adequately at the resolution of the CRU dataset. Because drought indices are usually standardized, the rPCs can be interpreted as a meaningful drought index, which has numerous advantages when the goal is to proceed beyond subregion identification. Highly correlated drought rPCs for identified subregions can be examined for detection of climate change signals, which has implications for drought management due to the information gain over a large area.

The design and properties of the selection rule in this study make the rule adaptable to different applications of drought monitoring or other dimension reductions of space-time geophysical data. We recognize that statistical tests other than the sign test could be utilized to determine improvements in the subregion correlation coefficients. Other tests that examine characteristics of a distribution other than the median might provide further insight into identifiable subregions, although the characteristics of those distributions would need to be examined to ensure that test assumptions are reasonably satisfied. Manual adjustments may also be desired if any subregions identified do not add useful information. Without implementation of the sign test, the upper-limit of the number of identified subregions using all 891 EOFs for rotation was approximately 18-20. The small, additional subregions extended across areas with

low correlation in the seasonal analysis. However, the correlation coefficients between those rPCs and the original SPEI data were still smaller than the coefficients for the main subregions and explains why they were excluded in this analysis using our selection rule. The selection rule is also relatively robust to changes in the size of the domain. Increasing the domain size can change regional features along the domain boundary, and reconstructing the regional patterns produced using the smaller domain generally requires a larger number of rEOFs because additional variability is introduced. These properties make it suitable for applications in other areas of the world at larger and smaller spatial scales to identify subregions of variability of a geophysical variable through time. Because of the properties demonstrated by this selection rule and its ability to identify subregions that have physical basis in the synoptic structures that drive drought variability, we argue that future drought management strategies and planning would be more advantageous in terms of these subregions.

5. Summary and conclusions

There has been an increase in growing season maximum and minimum temperatures across many areas of the Great Plains between 1901 and 2015. The greatest increases in growing season precipitation have been isolated to areas primarily east of the −100° meridian. Three-month SPEI drought event intensities increased in magnitude during the period 1978-2015 across the Great Plains although the number of events was lower compared to previous periods. Higher intensity droughts, while less frequent, will have negative impacts on agriculture as short-term and large water deficits occur in critical stages of crop growth. In contrast, the number of total wet events has risen in recent years, indicating an increased risk of excess moisture that may have major impacts on agriculture in the future.

Rotated EOF analysis using our selection rule identifies the main subregions of variability in the Great Plains and can be used to integrate drought monitoring information and inform drought management decisions at a local scale, especially when there are not sufficient in-situ climate stations. Our method produces subregions that are consistent with synoptic features and can be easily interpreted by drought management agencies. It has been shown that the number and spatial extent of subregions changes by season, reflecting the meteorological processes that dominate drought variability. Seasonal trends showed significant wetting for several subregions, and there is statistical evidence that the distributions of drought and wetting events for a few subregions have changed between 1901-1957 and 1958-2015.

Changes in weather patterns both naturally and from the diverse set of human forcings (Council 2005; Pielke et al. 2007) have the potential to alter the dominant features that affect drought variability in the Great Plains. The water resource community is considering the need to include changes in weather patterns from what occurred in the past to inform future management practices (Hossain et al. 2015). Analysis showed that drought variability was not stationary over the historical period. There is evidence of increased space-time drought variability since 1980 or later during the summer and decreased variability during the winter. Decision makers should interpret these changes in variability as an increase or decrease in the spatial drought complexities. If drought and wetting events become more variable across space and time, greater interregional cooperation will be desirable to accommodate for the wide-range of potential impacts. Decision makers in the Great Plains that have an understanding of these trends in

variability will be able to adjust long-term resource management strategies that may help mitigate the economic and agricultural impacts throughout the twenty-first century.

References

Alter, R. E., Y. Fan, B. R. Lintner, and C. P. Weaver, 2015: Observational Evidence that Great Plains Irrigation Has Enhanced Summer Precipitation Intensity and Totals in the Midwestern United States. *Journal of Hydrometeorology*, **16,** 1717-1735, doi: 10.1175/JHM-D-14-0115.1.

Alter, R. E., H. C. Douglas, J. M. Winter, and E. A. B. Eltahir, 2017: Twentieth Century Regional Climate Change During the Summer in the Central United States Attributed to Agricultural Intensification. *Geophysical Research Letters*, **45,** 1586-1594, doi: 10.1002/2017GL075604.

Bjornsson, H., and S. A. Venegas, 1997: A Manual for EOF and SVD Analyses of Climatic Data. Report No 97-1, McGill University, 52 pp.

Bojariu, R., L. F. Velea, R. D. Cica, A. E. Dobrinescu, M. Birsan, and A. Dumitrescu, 2012: Mechanisms of Drought Persistence in Romania in the Climate Change Perspective. *Annals of the University of Craiova-Biology, Horticulture, Food Produce Processing, Technology, Environmental Engineering*, **17**, Issue: XVII.

Bonaccorso, B., I. Bordi, A. Cancelliere, G. Rossi, and A. Sutera, 2003: Spatial Variability of Drought: An Analysis of the SPI in Sicily. *Water Resources Management*, **17,** 273-296, doi: 10.1023/a:1024716530289.

Borchert, J. R., 1950: The Climate of the Central North American Grassland. *Annals of the Association of American Geographers*, **40,** 1-39, doi: 10.2307/2561016.

Cai, W., Y. Zhang, Q. Chen, and Y. Yao, 2015: Spatial Patterns and Temporal Variability of Drought in Beijing-Tianjin-Hebei Metropolitan Areas in China. *Advances in Meteorology*, **2015,** 1-14, doi: 10.1155/2015/289471.

Cheval, S., A. Busuioc, A. Dumitrescu, and M. V. Birsan, 2014: Spatiotemporal variability of meteorological drought in Romania using the standardized precipitation index (SPI). *Climate Research*, **60,** 235-248, doi: 10.3354/cr01245.

Colaizzi, P. D., P. H. Gowda, T. H. Marek, and D. O. Porter, 2009: Irrigation in the Texas High Plains: a brief history and potential reductions in demand. *Irrigation and Drainage*, **58,** 257-274, doi: 10.1002/ird.418.

Council, N. R., 2005: *Radiative Forcing of Climate Change: Expanding the Concept and Addressing Uncertainties.* The National Academies Press, 222 pp.

Dai, A., 2011: Characteristics and trends in various forms of the Palmer Drought Severity Index during 1900–2008. *Journal of Geophysical Research*, **116**, doi: 10.1029/2010jd015541.

Di Luzio, M., G. L. Johnson, C. Daly, J. K. Eischeid, and J. G. Arnold, 2008: Constructing Retrospective Gridded Daily Precipitation and Temperature Datasets for the Conterminous United States. *Journal of Applied Meteorology and Climatology*, **47,** 475-497, doi: 10.1175/2007JAMC1356.1.

Easterling, W. E., P. R. Crosson, N. J. Rosenberg, M. S. McKenney, L. A. Katz, and K. M. Lemon, 1993: Paper 2. agricultural impacts of and responses to climate change in the Missouri-Iowa-Nebraska-Kansas (MINK) region. *Climatic Change*, **24,** 23-61, doi: 10.1007/bf01091476.

Glotter, M., and J. Elliott, 2016: Simulating US agriculture in a modern Dust Bowl drought. *Nature Plants*, **3,** 16193, doi: 10.1038/nplants.2016.193.

Groisman, P. Y., R. W. Knight, T. R. Karl, D. R. Easterling, B. Sun, and J. H. Lawrimore, 2004: Contemporary Changes of the Hydrological Cycle over the Contiguous United States:

Trends Derived from In Situ Observations. *Journal of Hydrometeorology*, **5,** 64-85, doi: 10.1175/1525-7541(2004)005<0064:CCOTHC>2.0.CO;2.

Guttman, N. B., 1998: Comparing the Palmer Drought Index and the Standardized Precipitation Index. *Journal of the American Water Resources Association*, **34,** 113-121, doi: 10.1111/j.1752-1688.1998.tb05964.x.

Hamed, K. H., and A. Ramachandra Rao, 1998: A modified Mann-Kendall trend test for autocorrelated data. *Journal of Hydrology*, **204,** 182-196, doi: http://dx.doi.org/10.1016/S0022-1694(97)00125-X.

Hannachi, A., I. T. Jolliffe, and D. B. Stephenson, 2007: Empirical orthogonal functions and related techniques in atmospheric science: A review. *International Journal of Climatology*, **27,** 1119-1152, doi: 10.1002/joc.1499.

Harris, I., P. D. Jones, T. J. Osborn, and D. H. Lister, 2014: Updated high-resolution grids of monthly climatic observations - the CRU TS3.10 Dataset. *International Journal of Climatology*, **34,** 623-642, doi: 10.1002/joc.3711.

Hoerling, M., X.-W. Quan, and J. Eischeid, 2009: Distinct causes for two principal U.S. droughts of the 20th century. *Geophysical Research Letters*, **36**, doi: 10.1029/2009GL039860.

Hossain, F., J. Arnold, E. Beighley, C. Brown, S. Burian, and Coauthors, 2015: Local-To-Regional Landscape Drivers of Extreme Weather and Climate: Implications for Water Infrastructure Resilience. *Journal of Hydrologic Engineering*, **20,** 02515002, doi: 10.1061/(asce)he.1943-5584.0001210.

IPCC, 2013: Summary for Policymakers. *Climate Change 2013: The Physical Science Basis. Contribution of Working Group I to the Fifth Assessment Report of the Intergovernmental Panel on Climate Change.* Cambridge University Press, 1-30 pp.

Kaiser, H. F., 1958: The varimax criterion for analytic rotation in factor analysis. *Psychometrika*, **23,** 187-200, doi: 10.1007/bf02289233.

Karl, T. R., and A. J. Koscielny, 1982: Drought in the United States: 1895–1981. *Journal of Climatology*, **2,** 313-329, doi: 10.1002/joc.3370020402.

Knapp, A. K., and M. D. Smith, 2001: Variation Among Biomes in Temporal Dynamics of Aboveground Primary Production. *Science*, **291,** 481-484, doi: 10.1126/science.291.5503.481.

Köppen, W., 2011: The thermal zones of the Earth according to the duration of hot, moderate and cold periods and to the impact of heat on the organic world. *Meteorologische Zeitschrift*, **20,** 351-360, doi: 10.1127/0941-2948/2011/105.

Küchler, A. W., 1964: *Potential Natural Vegetation of the Conterminous United States: Map.* American Geographical Society.

Livneh, B., and M. P. Hoerling, 2016: The Physics of Drought in the U.S. Central Great Plains. *Journal of Climate*, **29,** 6783-6804, doi: 10.1175/JCLI-D-15-0697.1.

Logan, K. E., N. A. Brunsell, A. R. Jones, and J. J. Feddema, 2010: Assessing spatiotemporal variability of drought in the U.S. central plains. *Journal of Arid Environments*, **74,** 247-255, doi: http://dx.doi.org/10.1016/j.jaridenv.2009.08.008.

Lorenz, E. N., 1956: *Empirical Orthogonal Functions and Statistical Weather Prediction.* Massachusetts Institute of Technology, Department of Meteorology.

Mann, H. B., 1945: Nonparametric Tests Against Trend. *Econometrica*, **13,** 245-259, doi: 10.2307/1907187.

Martins, D. S., T. Raziei, A. A. Paulo, and L. S. Pereira, 2012: Spatial and temporal variability of precipitation and drought in Portugal. *Natural Hazards and Earth System Science*, **12,** 1493-1501, doi: 10.5194/nhess-12-1493-2012.

Massey, F. J., 1951: The Kolmogorov-Smirnov Test for Goodness of Fit. *Journal of the American Statistical Association*, **46,** 68-78, doi: 10.1080/01621459.1951.10500769.

McLeman, R. A., J. Dupre, L. Berrang Ford, J. Ford, K. Gajewski, and G. Marchildon, 2014: What we learned from the Dust Bowl: lessons in science, policy, and adaptation. *Population and Environment*, **35,** 417-440, doi: 10.1007/s11111-013-0190-z.

North, G. R., T. L. Bell, R. F. Cahalan, and F. J. Moeng, 1982: Sampling Errors in the Estimation of Empirical Orthogonal Functions. *Monthly Weather Review*, **110,** 699-706, doi: 10.1175/1520-0493(1982)110<0699:seiteo>2.0.co;2.

Omondi, P., L. A. Ogallo, R. Anyah, J. M. Muthama, and J. Ininda, 2013: Linkages between global sea surface temperatures and decadal rainfall variability over Eastern Africa region. *International Journal of Climatology*, **33,** 2082-2104, doi: 10.1002/joc.3578.

Overland, J. E., and R. W. Preisendorfer, 1982: A Significance Test for Principal Components Applied to a Cyclone Climatology. *Monthly Weather Review*, **110,** 1-4, doi: 10.1175/1520-0493(1982)110<0001:astfpc>2.0.co;2.

Panu, U. S., and T. C. Sharma, 2002: Challenges in drought research: some perspectives and future directions. *Hydrological Sciences Journal*, **47,** S19-S30, doi: 10.1080/02626660209493019.

Peterson, T. C., T. R. Karl, P. F. Jamason, R. Knight, and D. R. Easterling, 1998: First difference method: Maximizing station density for the calculation of long-term global temperature

change. *Journal of Geophysical Research: Atmospheres*, **103,** 25967-25974, doi: 10.1029/98JD01168.

Pielke, R., and N. Doesken, 2008: Climate of the short grass steppe in the United States. *Ecology of the Shortgrass Steppe: A Long-Term Perspective*, W. K. Lauenroth, and I. C. Burke, Eds., Oxford University Press.

Pielke, R. A., J. O. Adegoke, T. N. Chase, C. H. Marshall, T. Matsui, and D. Niyogi, 2007: A new paradigm for assessing the role of agriculture in the climate system and in climate change. *Agricultural and Forest Meteorology*, **142,** 234-254, doi: https://doi.org/10.1016/j.agrformet.2006.06.012.

Pielke, R. A., D. Niyogi, J. Adegoke, G. Kallos, T. R. Seastedt, and F. Hossain, 2013: *Climate vulnerability: understanding and addressing threats to essential resources.* Elsevier/Academic Press.

Preisendorfer, R. W., and C. D. Mobley, 1988: *Principal component analysis in meteorology and oceanography.* Elsevier.

Raziei, T., I. Bordi, L. S. Pereira, and A. Sutera, 2010: Space-time variability of hydrological drought and wetness in Iran using NCEP/NCAR and GPCC datasets. *Hydrology and Earth System Sciences*, **14,** 1919-1930, doi: 10.5194/hess-14-1919-2010.

Richman, M. B., 1986: Rotation of principal components. *Journal of Climatology*, **6,** 293-335, doi: 10.1002/joc.3370060305.

Russo, T. A., and U. Lall, 2017: Depletion and response of deep groundwater to climate-induced pumping variability. *Nature Geoscience*, **10,** 105-108, doi: 10.1038/ngeo2883.

Santos, J. F., I. Pulido-Calvo, and M. M. Portela, 2010: Spatial and temporal variability of droughts in Portugal. *Water Resources Research*, **46**, doi: 10.1029/2009WR008071.

Sauchyn, D. J., J. Stroich, and A. Beriault, 2003: A paleoclimatic context for the drought of 1999–2001 in the northern Great Plains of North America. *The Geographical Journal*, **169,** 158-167, doi: 10.1111/1475-4959.05003.

Shafer, M., D. Ojima, J. M. Antle, D. Kluck, R. A. McPherson, and Coauthors, 2014: Ch19: Great Plains. *Climate Change Impacts in the United States: The Third National Climate Assessment*, J. M. Melillo, T. C. Richmond, and G. W. Yohe, Eds., U.S. Global Change Research Program, 441-461, doi: 10.7930/J0D798BC.

Sönmez, F. K., A. L. I. Ü. Kömüscü, A. Erkan, and E. Turgu, 2005: An Analysis of Spatial and Temporal Dimension of Drought Vulnerability in Turkey Using the Standardized Precipitation Index. *Natural Hazards*, **35,** 243-264, doi: 10.1007/s11069-004-5704-7.

Stockton, C. W., and D. M. Meko, 1983: Drought Recurrence in the Great Plains as Reconstructedfrom Long-Term Tree-Ring Records. *Journal of Climate and Applied Meteorology*, **22,** 17-29, doi: 10.1175/1520-0450(1983)022<0017:DRITGP>2.0.CO;2.

Svoboda, M., D. LeComte, M. Hayes, R. Heim, K. Gleason, and Coauthors, 2002: The Drought Monitor. *Bulletin of the American Meteorological Society*, **83,** 1181-1190, doi: 10.1175/1520-0477(2002)083<1181:TDM>2.3.CO;2.

Tatli, H., and M. Türkeş, 2011: Empirical Orthogonal Function analysis of the palmer drought indices. *Agricultural and Forest Meteorology*, **151,** 981-991, doi: 10.1016/j.agrformet.2011.03.004.

Theil, H., 1950: A rank-invariant method of linear and polynomial regression analysis, 1, 2, and 3. *Ned. Akad. Wetensch Proc.*, **53,** 386-392.

Vicente-Serrano, S. M., 2006: Differences in Spatial Patterns of Drought on Different Time Scales: An Analysis of the Iberian Peninsula. *Water Resources Management*, **20,** 37-60, doi: 10.1007/s11269-006-2974-8.

Vicente-Serrano, S. M., S. Beguería, and J. I. López-Moreno, 2010: A Multiscalar Drought Index Sensitive to Global Warming: The Standardized Precipitation Evapotranspiration Index. *Journal of Climate*, **23,** 1696-1718, doi: 10.1175/2009jcli2909.1.

——, 2011: Comment on "Characteristics and trends in various forms of the Palmer Drought Severity Index (PDSI) during 1900–2008" by Aiguo Dai. *Journal of Geophysical Research*, **116**, doi: 10.1029/2011jd016410.

Villarini, G., J. A. Smith, and G. A. Vecchi, 2012: Changing Frequency of Heavy Rainfall over the Central United States. *Journal of Climate*, **26,** 351-357, doi: 10.1175/JCLI-D-12-00043.1.

Vose, R. S., S. Applequist, M. Squires, I. Durre, M. J. Menne, and Coauthors, 2014: Improved Historical Temperature and Precipitation Time Series for U.S. Climate Divisions. *Journal of Applied Meteorology and Climatology*, **53,** 1232-1251, doi: 10.1175/JAMC-D-13-0248.1.

Wang, K. J., A. P. Williams, and D. P. Lettenmaier, 2017: How much have California winters warmed over the last century? *Geophysical Research Letters*, **44,** 8893-8900, doi: 10.1002/2017GL075002.

Wang, S.-Y., and T.-C. Chen, 2009: The Late-Spring Maximum of Rainfall over the U.S. Central Plains and the Role of the Low-Level Jet. *Journal of Climate*, **22,** 4696-4709, doi: 10.1175/2009JCLI2719.1.

Warwick, R. A., 1975: Drought hazard in the United States: A research assessment: Boulder, Colorado. I. o. B. S. University of Colorado, Ed.

Wiener, J. D., R. S. Pulwarty, and D. Ware, 2016: Bite without bark: How the socioeconomic context of the 1950s U.S. drought minimized responses to a multiyear extreme climate event. *Weather and Climate Extremes*, **11,** 80-94, doi: https://doi.org/10.1016/j.wace.2015.11.007.

Wilks, D. S., 2011: *Statistical Methods in the Atmospheric Sciences.* International Geophysics Series. 3rd ed. Academic Press, 676 pp.

Woodhouse, C. A., and J. T. Overpeck, 1998: 2000 Years of Drought Variability in the Central United States. *Bulletin of the American Meteorological Society*, **79,** 2693-2714, doi: 10.1175/1520-0477(1998)079<2693:yodvit>2.0.co;2.

Yuan, S., and S. M. Quiring, 2014: Drought in the U.S. Great Plains (1980–2012): A sensitivity study using different methods for estimating potential evapotranspiration in the Palmer Drought Severity Index. *Journal of Geophysical Research: Atmospheres*, **119,** 10,996-911,010, doi: 10.1002/2014JD021970.

Zelen, M., and N. Severo, 1964: Probability Functions. *Handbook of Mathematical Functions: With Formulas, Graphs, and Mathematical Tables*, M. Abramowitz, and I. A. Stegun, Eds., 925-995.

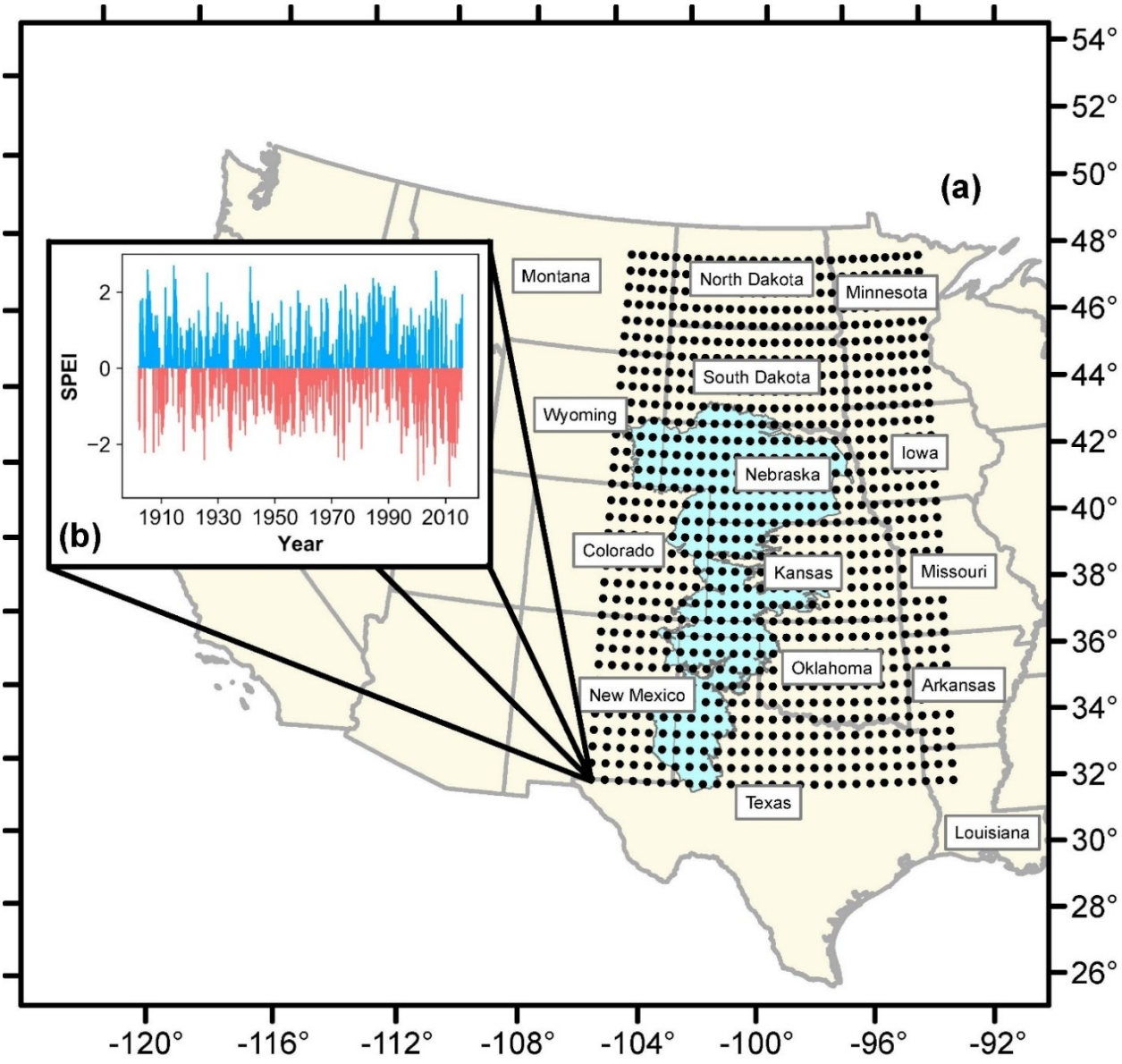

Figure 1.1 (a) Study area of the U.S. Great Plains region and the Ogallala Aquifer (light blue) with black dots that illustrate selected grid points (0.5°×0.5°), and (b) Standardized Precipitation-Evapotranspiration Index (SPEI) for one grid point in the domain with dry (red) and wet (blue) events.

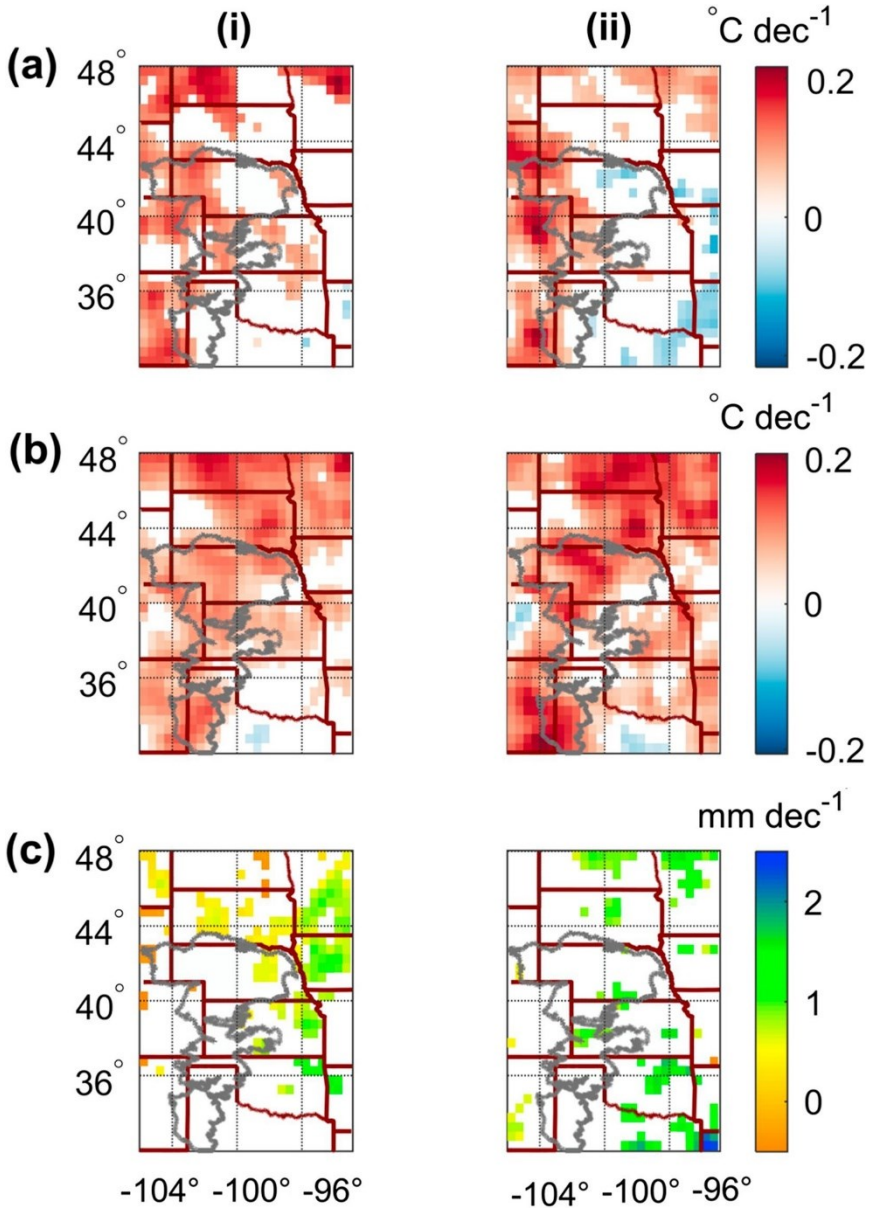

Figure 1.2 Growing season trends for (a) maximum temperature, (b) minimum temperature, and (c) precipitation between 1901 and 2015 for (i) Nov. – Apr. (winter) and (ii) May – Oct. (summer). Only grids with statistically significant trends using the modified Mann-Kendall test (α=0.05) are shaded. Grids with non-significant trends are unshaded (i.e., white).

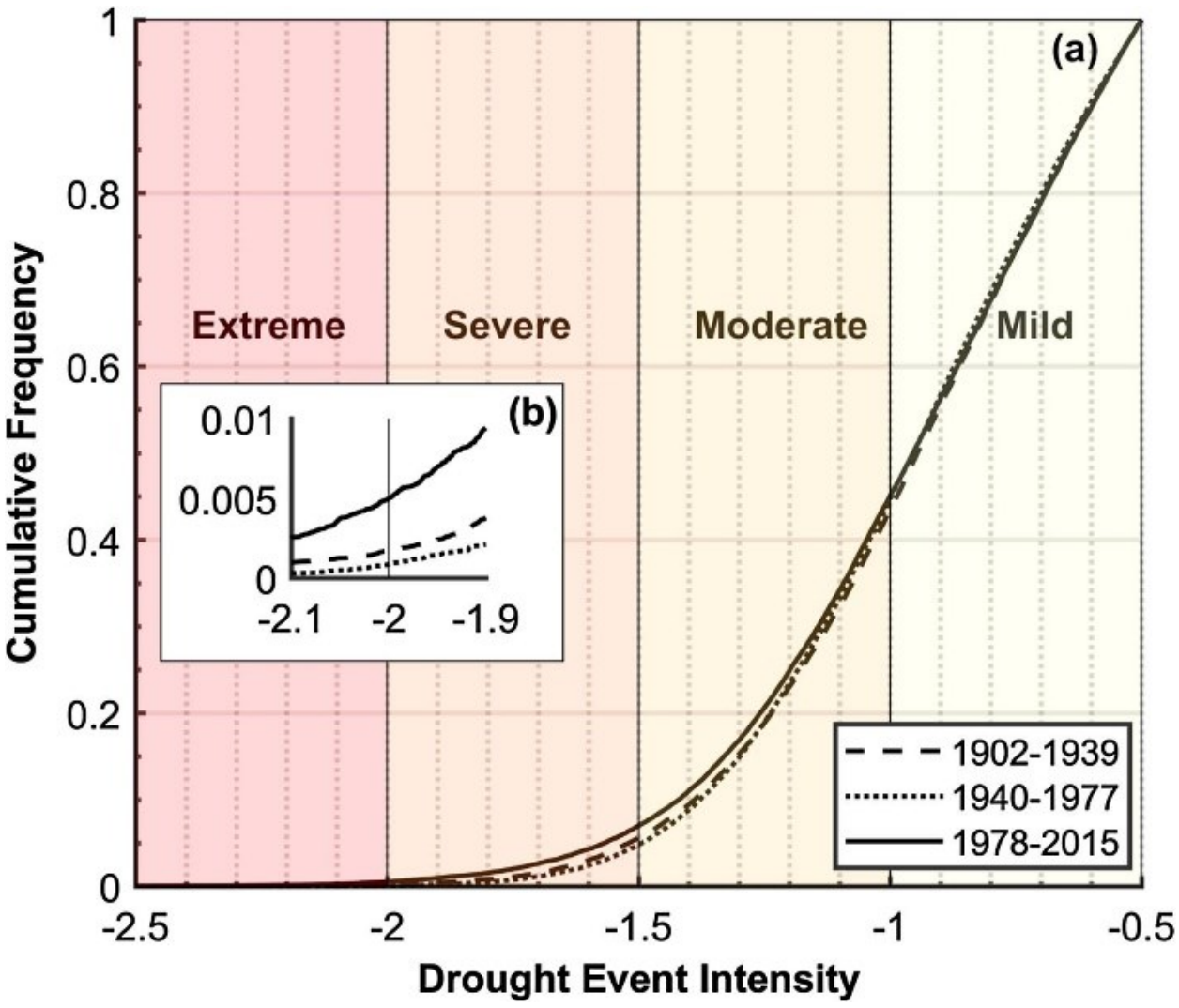

Figure 1.3 (a) Empirical cumulative frequency distributions for Standardized Precipitation-Evapotranspiration Index drought event intensities across the entire study area for three periods: 1902–1939, 1940–1977, and 1978–2015. Drought events were grouped based on the month each drought event terminated. (b) Cumulative frequency distribution magnified near the extreme drought boundary.

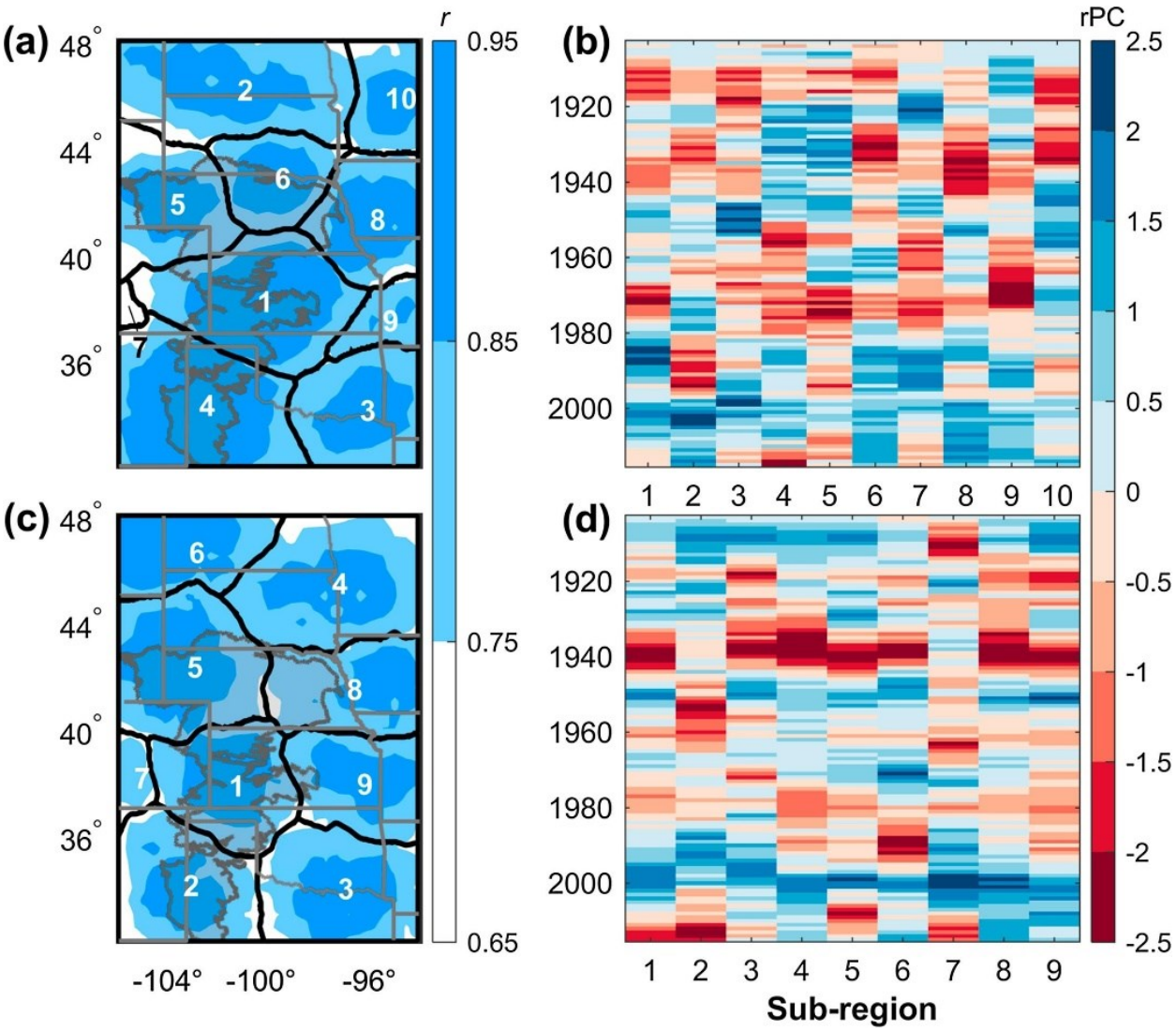

Figure 1.4 Subregions identified in the U.S. Great Plains for (a) spring and (c) summer drought variability and the standardized rotated principal component (rPC) time series for subregions in (b) spring and (d) summer. Each subregion in (a) and (c) has a number that corresponds to its rPC time series in (b) and (d), respectively. Subregion and state boundaries are black and gray, respectively, and the Ogallala Aquifer is shaded gray. The left color bar represents the correlation coefficients for each subregion's rPC time series on the right and the original drought dataset at individual grid points. The right color bar represents the magnitude and sign of each rPC time series from 1901 to 2015. Negative and positive rPC values indicate dry and wet

conditions, respectively. Time series of rPC are 10-year running average filtered (used as a smoother to remove interannual variability and retain decadal variations).

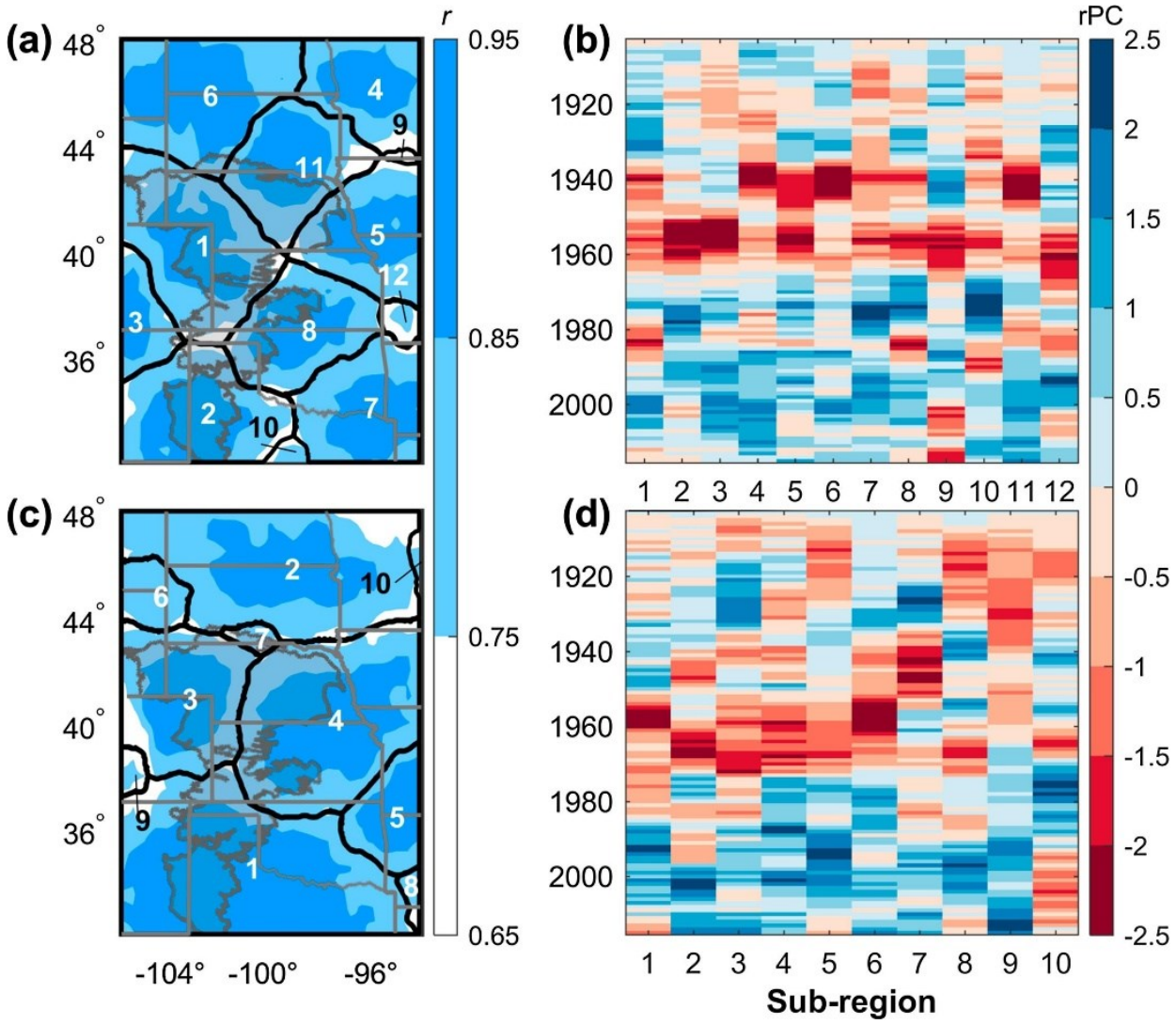

Figure 1.5 Same as Fig. 1.4 but for (top) fall and (bottom) winter.

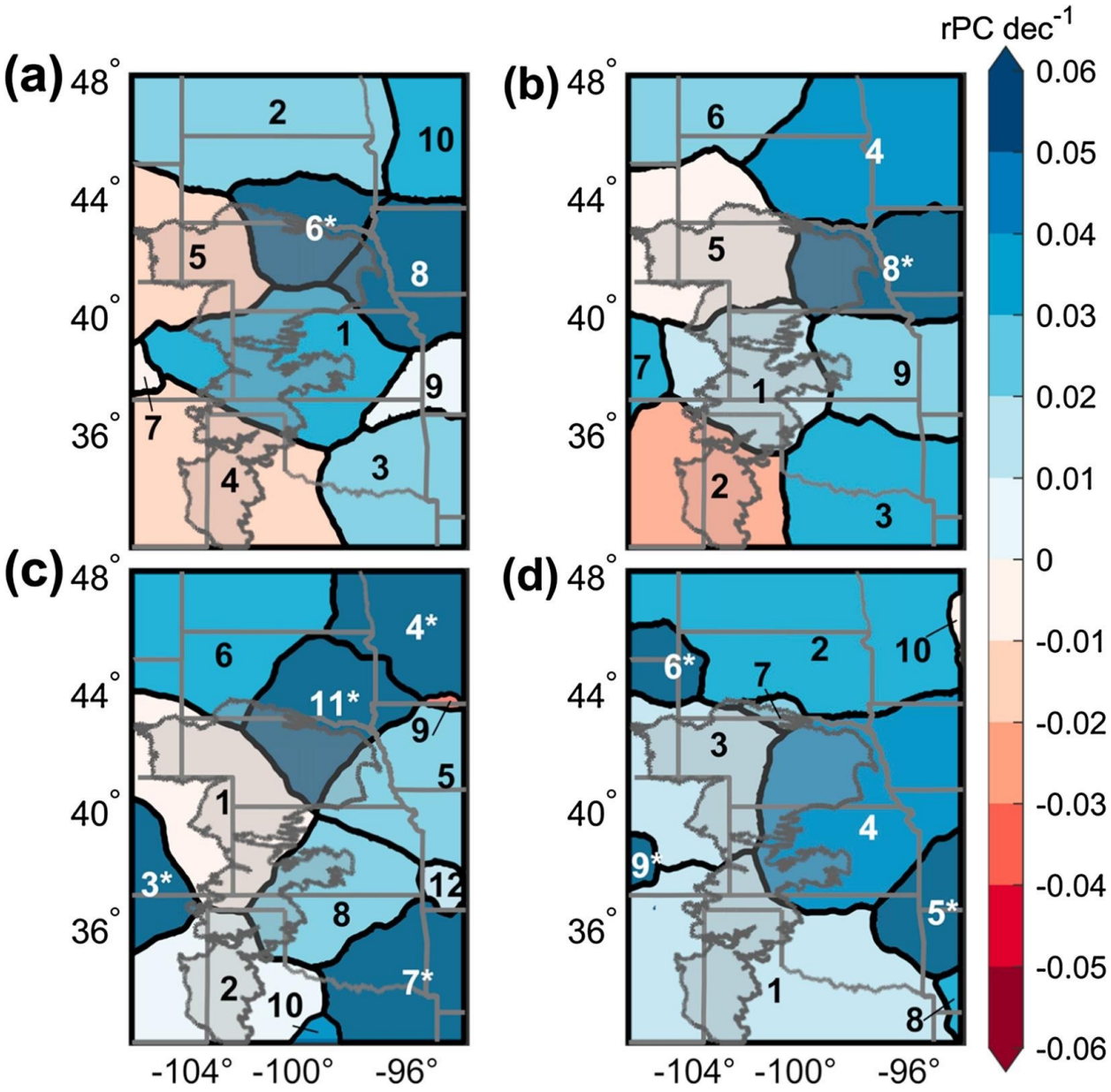

Figure 1.6 Theil-Sen slope estimates for the rPCs associated with the subregions in Figs. 1.4 and 1.5 for (a) spring, (b) summer, (c) fall, and (d) winter. Subregions with a * indicate statistical significance (α=0.05) determined using the modified Mann-Kendall test.

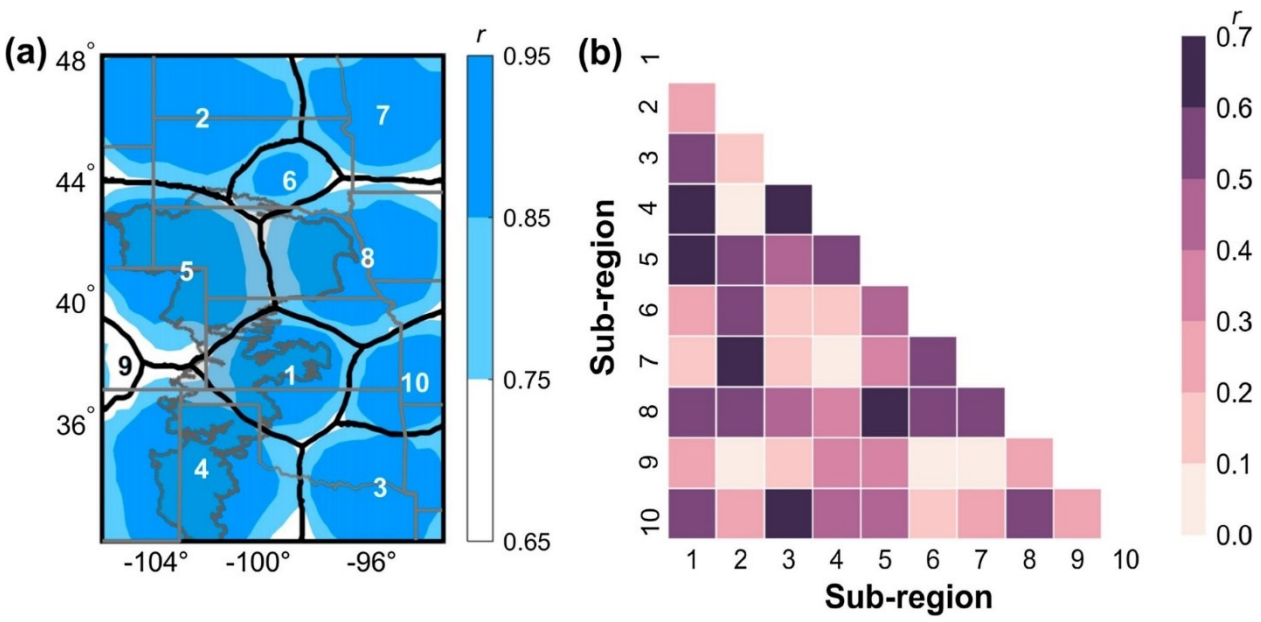

Figure 1.7 (a) Subregions identified for full-record Standardized Precipitation-Evapotranspiration Index (SPEI) and (b) the correlation coefficients between subregion rPC time series.

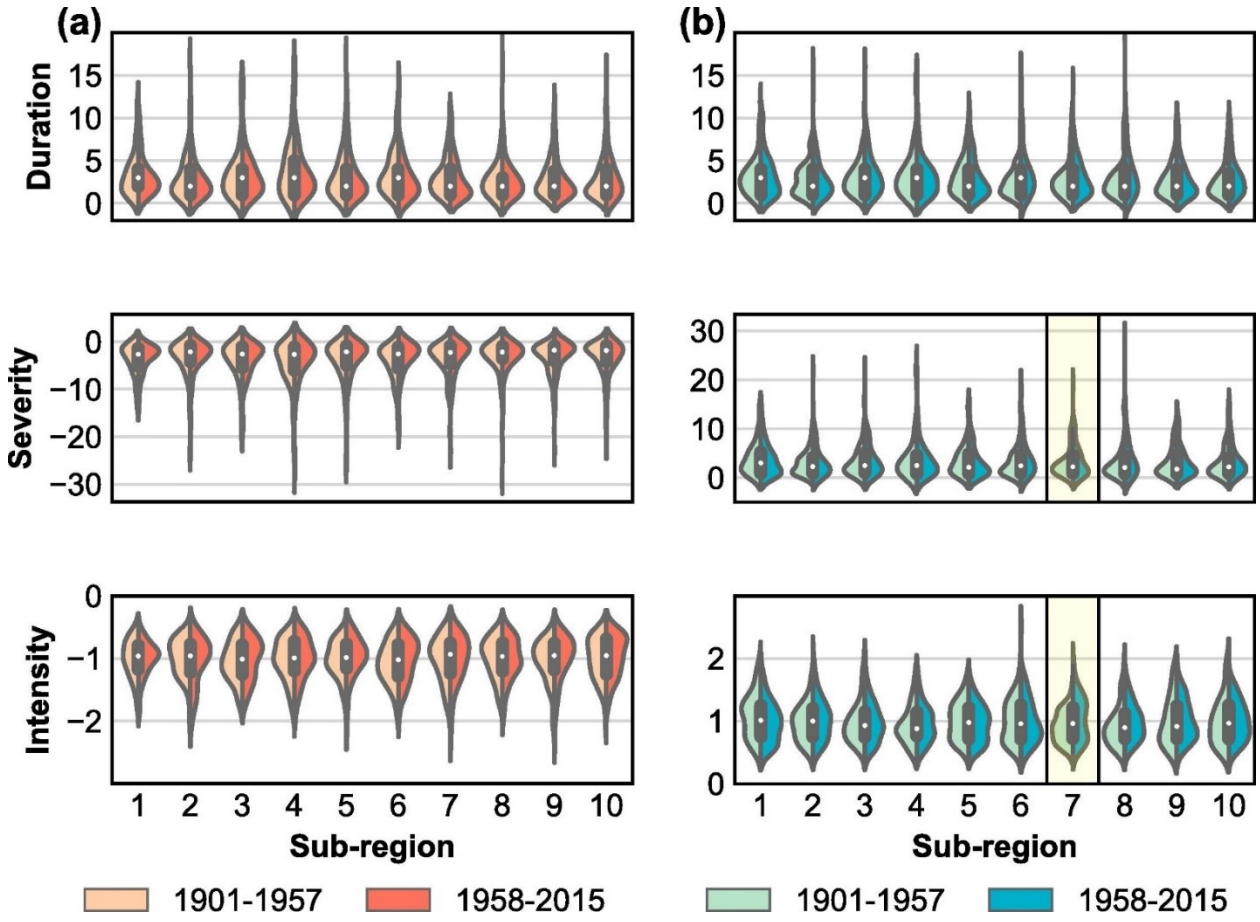

Figure 1.8 Violin plots of (a) drought and (b) wet event durations (months), severities, and intensities for subregions shown in Fig. 1.7 using thresholds of (a) −0.5 and (b) 0.5. For each subregion, the distributions for each drought event metric are split into the periods 1901–1957 and 1958–2015. The white circle for each violin is the joint median for both periods. Distributions that significantly changed (α=0.05) between periods are highlighted in yellow.

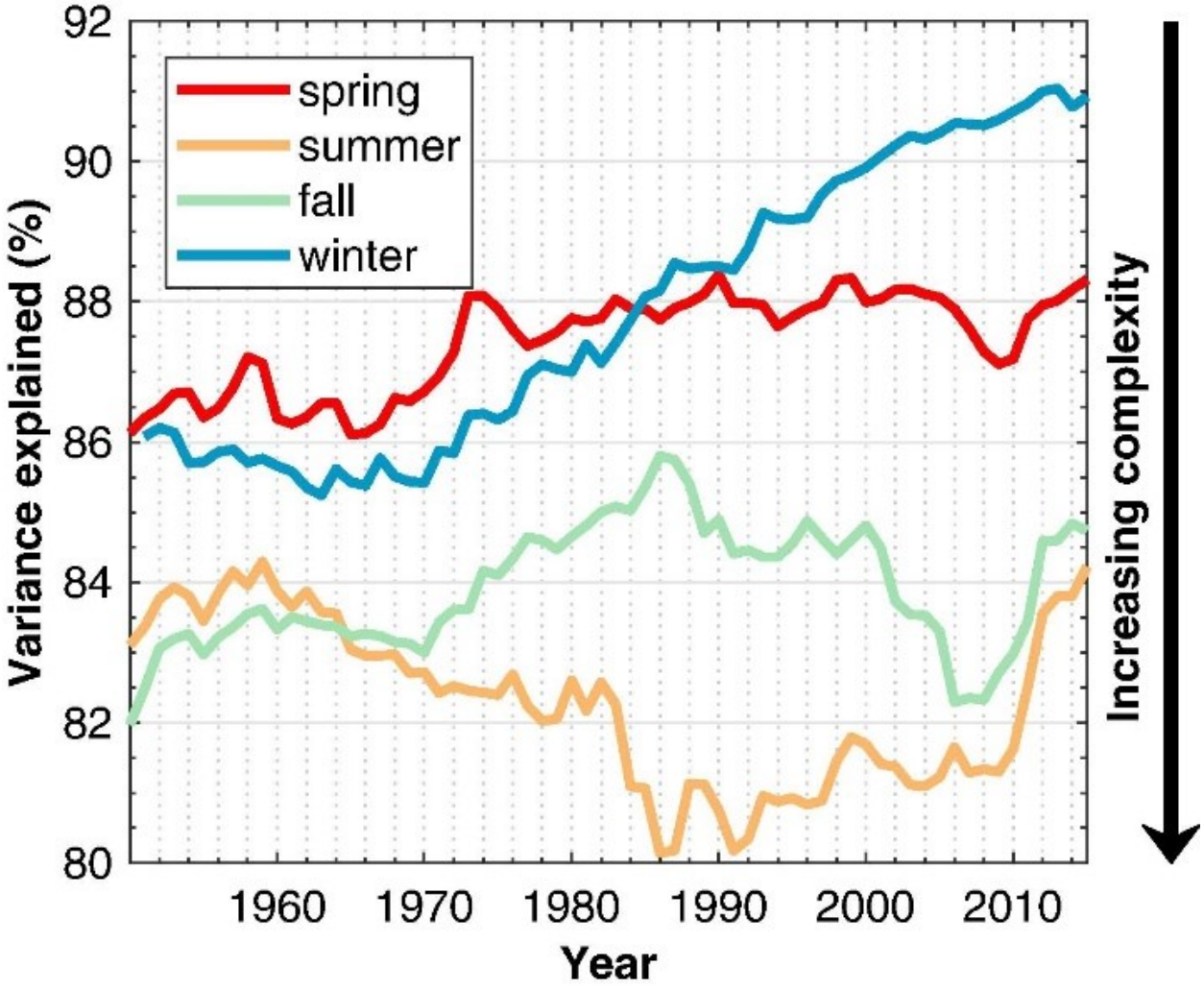

Figure 1.9 The seasonal variances explained by 10 EOFs using a 50-year moving window for the U.S. Great Plains from 1901 to 2015. The x-axis labels (year) indicate the end year of each moving window in the EOF analysis (e.g., 1960 corresponds to 1911–1960). Lower variance explained corresponds to a higher complexity in the spatial-temporal drought features during that period, whereas higher variance corresponds to lower complexity.

Chapter 2 - Simulating the atmospheric response to irrigation over the Ogallala Aquifer Region

Abstract

The Ogallala Aquifer Region (OAR) in the U.S. High Plains has been the main source of freshwater used for irrigation since its introduction in the early to mid-twentieth century. The historical decline in the saturated thickness of the aquifer, which is expected to continue in the future, has been the impetus of water conservation efforts. Anthropogenic land-use forcings such as irrigation can significantly influence regional climate. The objective of this study was to integrate an irrigation module into the Weather Research and Forecasting (WRF) Model to compare the atmospheric response using different irrigation scenarios and land surface model (LSM) parameterizations. Four years were chosen for simulation: 1980, 1993, 2012, and 2015 to sample both drought and pluvial years. Two LSMs with multiple parameterizations including predictive and static vegetation were evaluated. Our results showed that total irrigation and the surface atmospheric response were reasonably simulated across the OAR compared to observations. Differences in the magnitude of climate responses were found across land surface models. Irrigation reduced the average OAR air temperature between 0.1 and 0.5°C, increased the near-surface relative humidity between 1-5% over and downwind of the OAR, and suppressed vertical motion over densely irrigated cropland, resulting in less moisture transport into the mid-levels of the atmosphere. Precipitation increased over grid cells that demonstrated a decrease in irrigated cropland between 1984 and 2017. Changes in agricultural water management in the future will likely drive the atmospheric response with our results demonstrating differential impacts both locally and downwind under different irrigation

scenarios.

Keywords: WRF; irrigation; Ogallala; Noah; climate change

1. Introduction

Anthropogenic land-use forcings can significantly influence regional changes in climate. Conversion of land from grassland to agriculture across the U.S. High Plains and Midwest rapidly occurred over the last century (Schilling et al. 2008; Zhang and Schilling 2006), driven by increased demand for food and biofuel, improvements in technology and pest management, and climate and water resources. Over a five-year period from 2006 to 2011, there was a net decline in grassland of approximately 530,000 hectares across the western corn belt, largely resulting from an increase in the utilization of marginal lands for corn and soybeans (Wright and Wimberly 2013). Such agricultural intensifications in water-limited regions of the U.S. High Plains necessitated the creation and expansion of irrigation, an intensive land-use practice that increases yields and minimizes the influence of climatic variations on crop productivity (Lobell et al. 2009; Walker 1989). The practice of irrigated agriculture in the U.S. increased in the second half of the twentieth century as advances in technology lead to increased accessibility to farmers (Mahmood et al. 2006; T. Musick et al. 1990). Irrigation is a significant anthropogenic climatic forcing that modifies regional water and energy budgets during the growing season (Hansen et al. 2005; Pielke et al. 1998). Thus, irrigated regions are climatically sensitive to changes in management practices that conserve water including a reduction in the number of irrigated acres, the amount of irrigation, or the conversion of irrigated to dryland cropping systems (Deines et al. 2019a).

One area where management practices are coming under scrutiny is across the Ogallala Aquifer Region (OAR) in the U.S. High Plains (Haacker et al. 2019b; Smidt et al. 2016). This aquifer is the main source of freshwater for irrigation across eight states in the High Plains, but

declining water table levels during the last sixty-years across the aquifer have necessitated the implementation of new water management practices that will help prolong the life of the aquifer and the agricultural economy that exists in a semiarid landscape where evapotranspiration exceeds precipitation (Haacker et al. 2016). However, despite these water table declines, the number of estimated irrigated acres in northwest Kansas and southern Nebraska increased between 1999 and 2016 according to Landsat satellite images (Deines et al. 2017). In fact, irrigated cropland using groundwater increased by more than double the national rate (8.7%) with the largest regional change occurring across northeast Nebraska (Brown and Pervez 2014). In 2015, there were almost 19 million acres of irrigated cropland across counties within the OAR estimated by the USGS (Dieter et al. 2018). Because of its size and spatial variations in saturated thickness, the OAR is a notable example of an area that will face complex water resource management issues in the present and near-future with changes driven by economics and climate (Haacker et al. 2016; Haacker et al. 2019a). These groundwater issues require multi-faceted solutions in irrigation management that are integrated with national and global food security demands. Climate model projections across the U.S. High Plains region suggest that this region may become more arid over time (Seager et al. 2018), which may further exacerbate already complex water resource issues. Region-wide changes in water use in this region may have significant, unintended consequences on regional climate patterns over and downwind of the aquifer during the course of the twenty-first century (Lu and Kueppers 2015).

As a first order land use forcing on climate (Hansen et al. 2005), irrigation modifies the environment by changing the land surface albedo, vegetation coverage, and soil moisture content that results in a significant feedback system on local and regional climate, which in some cases,

may have a greater radiative forcing than increases in greenhouse gases in some areas of the world (Chen et al. 2018; Pielke et al. 1998; Pielke et al. 2002). At the regional scale, irrigation may have influenced the geographic patterns of historical temperature trends. Average maximum temperature trends during the summer growing season across the central U.S. since 1901 demonstrate the greatest warming across the High Plains while many areas east of the High Plains have not observed a significant change or even decreased, suggesting a combination of agriculture and irrigation may have played a role in suppressing warming downwind of the aquifer (Zambreski et al. 2018). Similarly, analysis of observed trends in equivalent temperature at weather stations over irrigated cropland in Kansas and Nebraska revealed decreasing trends between 1990−2014, further emphasizing the role that irrigation can play in the modification of local or regional trends (Zhang et al. 2019). At the field scale, it has been shown that temperature differences between irrigated and non-irrigated crops is on average approximately 1 °C with the extent of cooling varying between crop types (Chen et al. 2018). For example, the cooling effect over irrigated maize was stronger and lasted significantly longer than irrigated soybean potentially as a result of higher plant height and leaf area index for maize. Overall, these observational studies that have detected regional trends or analyzed field-scale differences have been the motivation of a growing body of regional climate model attribution studies.

Dynamic modeling has been the main tool used to attribute the effects of irrigation and agriculture to changes in regional climate. Irrigation has been incorporated into land surface models, which are run either coupled with a regional climate model to simulate atmospheric feedback mechanisms or offline as its own stand-alone model. Some studies have used a sub-surface approach by keeping designated soil layers at saturation (Harding and Snyder 2012a),

field capacity (Huber et al. 2014), or applying water when a soil moisture threshold is triggered (Lawston et al. 2015). Other studies have used sprinkler irrigation, which applies water at or above the canopy level (Harding et al. 2015; Lu and Kueppers 2015; Ozdogan et al. 2010; Pei et al. 2016). At the surface, irrigation enhances the local latent heat flux and decreases sensible heat flux, causing a decrease in near-surface temperature (Adegoke et al. 2003; Baidya Roy et al. 2003; Mahmood et al. 2006). When coupled to the atmosphere, models suggest that cooler surface temperatures induce local subsidence and low-level anticyclonic circulation, which can suppress precipitation (Im et al. 2014). In the Great Plains, this low-level subsidence may even help weaken and enhance the low level jet in certain areas, changing the frequency and intensity of convection downwind (Huber et al. 2014). Higher in the atmosphere, irrigation during the drought of 2012 may have enhanced the upper-level ridge over the central Great Plains and deepened the trough over the Midwest (Pei et al. 2016). This feedback system helped reduce and enhance precipitation over and downwind of the central High Plains, respectively. On a long-term basis, the increase in downwind precipitation and cloud-cover from agricultural intensification may have suppressed the rate of warming in the Midwest compared to other areas of the U.S. during the twentieth century (Alter et al. 2017). Intercomparison studies have even shown differential responses in precipitation, wind speed, and surface fluxes between wet and dry growing seasons and between dynamic and static vegetation parameterizations (Harding and Snyder 2012a; Harding et al. 2015). The method of irrigation application incorporated into the model (e.g. sub-surface, flood, or sprinkler) may also have differential and significant impacts on the atmosphere (Lawston et al. 2015). Furthermore, there has been work emerging addressing how reduced irrigation over the OAR might influence climate extremes in the future. One study found that reductions in irrigated area and irrigation amount over the southern High Plains

resulted in longer, more frequent, and severe heat waves over the period 2002 − 2011 (Lu and Kueppers 2015). The authors also found that the response in the frequency of heat waves was dependent on the initial concentration of irrigated cropland. Additional modeling research using the latest guidance on historical and projected land use change may provide new insights into the regional effects of irrigation on climate for the future.

The objectives of this study were to develop an irrigation mechanism into a regional climate model and compare the atmospheric response to irrigation under different irrigation scenarios and land surface model parameterizations across the central U.S. We selected two irrigated land use datasets and validated simulated irrigation amounts and responses using available observations. Finally, we compared the regional climate responses from the land surface model parameterizations and discuss potential impacts on agriculture at the regional-scale as a result of irrigation changes that may occur in the future.

2. Material and methods

2.1 Study area and model configuration

The Weather Research and Forecasting (WRF) model version 4.0 with the ARW core was chosen for regional climate modeling simulations in our study. The initial and lateral boundary conditions for WRF were from the North American Regional Reanalysis (NARR) dataset, which has a three-hour temporal resolution and a spatial resolution of approximately 32 km at the lowest latitude (Mesinger et al. 2006; NCEP 2005). We created a 136 × 185 grid with a 10-km resolution bounded by the area 30°N − 48°N and 108°W − 90°, which includes most of the central United States and covers areas of Texas, Oklahoma, Kansas, Nebraska, Colorado, Missouri, Iowa, and Arkansas (Fig. 2.1a). This area sufficiently bounds the OAR and includes

regions downwind (north and east) that would be expected to be climatically influenced by irrigation. To facilitate data analysis, we divided the OAR into northern, central, and southern subdomains and included one downwind region over the upper U.S. corn belt in order to regionally summarize the effects of irrigation over areas of the domain in which effects may differ (Qi 2009). The five grid cells adjacent to the domain boundary (e.g. specified and relaxation zones) were excluded in all summary statistics to remove potential spurious lateral boundary effects (Miguez-Macho et al. 2005; Seth and Giorgi 1998).

The physics parameterization options that were constant across all simulations include the following: the single-moment 3-class simple ice scheme for microphysics, the Kain-Fritsch scheme for cumulus parameterization, the Revised MM5 Monin-Obukhov scheme for the surface layer physics, the Yonsei University scheme for the planetary boundary layer physics, and the Rapid Radiative Transfer Model and the Dudhia schemes for longwave and shortwave physics, respectively. Thirty atmospheric layers were used during each simulation. Four years were chosen for simulation: 1980, 1993, 2012, and 2015. The years 1980 and 2012 (1993 and 2015) were classified as major drought (pluvial) years based on observed precipitation anomalies. Simulations began March 1 and were run through October 1 for each summer growing season, saving output every three hours. Starting simulations during the early spring allows the model adequate time to initialize antecedent pre-irrigation moisture that may impact climatic conditions during the summer. The model physics were solved at a 60 second time step, and the adaptive time step was employed to allow the model to iterate at time steps up to 180 seconds. The period between March 1 and May 31 was considered spin-up and discarded before analysis. The results

of our study focus from June 01 00Z – Aug 31 18Z (abbreviated as summer hereafter) as this period represents when irrigation demand is highest across the domain.

2.2 Land surface model configurations

2.2.1 Noah with mosaic option

The widely-used unified Noah land surface model within the WRF framework allows subgrid variability of land surface characteristics to be parametrized through a mosaic or tiling approach, hereafter referred to as Noah: Mosaic (Li et al. 2013) (Table 2.1). Without the mosaic option, Noah simulations assume each grid cell is composed of only the dominant land use category, which can be a problem for simulations with coarse resolutions. Because only approximately three percent of grid cells in our study domain have a dominant land use designated as irrigated cropland or pasture, we increased the number of grid cells that receive irrigation by creating a subroutine within Noah-Mosaic that applies irrigation to the fraction of each grid cell containing irrigated cropland or pasture. For each run, the five categories with the largest land use fractions were simulated. At the spatial resolution used in this study, five categories were deemed more than sufficient as the land use fraction for the fifth category for over 98% of grid cells was zero, suggesting a larger number of categories would be an inefficient use of computational resources. The surface fluxes and state variables over each of the five dominant land use categories were calculated at each grid cell, and a weighted average was calculated to yield the overall grid cell average. One critical disadvantage of the overall Noah framework is that it does not simulate vegetation development in response to either climatic conditions or irrigation, thereby causing potential biases in the partitioning of sensible and latent heat fluxes at the land surface. For example, without vegetation development, evapotranspiration

can only increase due to a decrease in plant moisture stress and direct evaporation from the soil surface, not from enhanced vegetation growth (Harding and Snyder 2012a), which may result in underestimations of latent heat flux as the growing season progresses.

2.2.2 Noah with multiple parameterizations (Noah-MP)

The Noah land surface model with multiparameterization options (Noah-MP) was developed to improve the original Noah land surface model by including more sophisticated physics schemes and allowing multiple options for significant land-atmosphere feedback processes (Niu et al. 2011). In particular, Noah-MP can calculate horizontal and vertical vegetation density using predictive photosynthesis and dynamic vegetation models. In this study, root, stem, and leaf development was calculated both dynamically (Noah-MP: LAI_P) and interpolated from monthly values prescribed based on the land use category following a fixed annual cycle (Noah-MP: LAI_T). In addition, an additional simulation in which vegetation was held static at the initial conditions (Noah-MP: LAI_S) was performed as a reference to the results from the Noah-MP simulations in which vegetation changes over the growing season. Noah-MP: LAI_S was similar to Noah: Mosaic in that both LSM configurations do not simulate vegetation changes. Utilizing the dynamic vegetation parameterization should produce more realistic simulations of flux partitioning at the surface during the summer growing season due to the inherent feedback between seasonal crop development and irrigation. In addition, enhanced vegetation growth should deplete available soil moisture more rapidly and increase the frequency of irrigation applications. These different configurations allow for more critical and comphrensive insights in simulations studies relying heavily on land surface model performance.

2.3 Irrigation methodology

Simulations that include (exclude) irrigation are designated as irrigated (non-irrigated). Non-irrigated scenarios still include land use that is categorized as irrigated cropland; however, the mechanism that applies irrigation is turned off. Irrigation mechanisms were incorporated into both Noah and Noah-MP land surface models to compare their effects on regional climate when an irrigation component is included. In order for irrigation to be applied at a particular grid cell, it must have an irrigated cropland or pasture land use fraction greater than zero for the Noah: Mosaic configuration or the dominant land use category must be irrigated cropland or pasture for Noah-MP configurations (Table 2.1). It is important to emphasize that in the Noah-MP framework only one land use category is assigned to each grid cell, and grid cells assigned as dominantly irrigated cropland or pasture receive the irrigation application across the entire grid cell. Three percent of grid cells have a dominant land use category as irrigated cropland or pasture, and they are predominately over the OAR, which largely rely on groundwater for irrigation. In contrast, the percentage of grid cells that have land use fraction greater than 0.1 for irrigated cropland or pasture is 12%. Therefore, the number of grid cells that receive irrigation using the Noah-MP configurations is less than Noah: Mosaic although the applications are applied to one-hundred percent of the grid cell and only the fraction of the grid cell in Noah: Mosaic (Fig. A.1).

Irrigation could only be applied after May 15 to prevent erroneous irrigation during the spin-up period before typical planting dates or during the early part of the growing season when farmers are less likely to irrigate because crop water demand is low (Huber et al. 2014). The approach integrates methods derived from several studies using a trigger based on the percentage

of plant available water in the soil (Ozdogan et al. 2010; Pei et al. 2016). Each morning at the first time step after 6 AM local time, the weighted average soil moisture availability (*MA*) for the 0 – 10 cm, an upper soil layer subscripted as 1, and 10 – 40 cm, a root zone layer subscripted as 2 in Eq. (1), is evaluated as:

$$MA = 0.25 \times [(\theta_v - \theta_{wp})/(\theta_{fc} - \theta_{wp})]_1 + 0.75 \times [(\theta_v - \theta_{wp})/(\theta_{fc} - \theta_{wp})]_2 \quad (1)$$

where θ_v is the current volumetric soil moisture content, θ_{wp} is the soil moisture content at the wilting point, and θ_{fc} is the soil moisture content at field capacity. When *MA* falls below 0.5, the depth of water required to bring the soil to field capacity is applied in the form of non-convective precipitation at a constant rate of 20 mm hr^{-1} starting from 6 AM until the application is complete, typically ranging from 2– 4 hours. This represents a sprinkler irrigation approach, which is the most widely used technology in the region as of 2015 (Dieter et al. 2018).

2.4 Data sources

2.4.1 Observations of water and climate

Annual county estimates of irrigation withdrawals in 2010 and 2015 from the United States Geological Survey (USGS) were used for model verification of irrigation applications in WRF (Dieter et al. 2018; Maupin et al. 2014). Counties with any portion contained within the OAR boundary were used in the aggregation process. These aggregated USGS observations of total annual irrigation were compared directly with the total amount of irrigation applied from WRF model grid cells contained within the OAR boundary. Irrigated cropland or pasture land

use fraction was used to convert model irrigation depth to billion gallons and divided by the time extent of the simulation to derive daily rates of irrigation applications.

Ameriflux data from two sites in eastern Nebraska during 2012 was used to evaluate WRF model performance (Fig. 2.1a). US-Ne2 and US-Ne3 are two long-term irrigated and non-irrigated sites, respectively, within 1.6 km of one another (Chen et al. 2018) that provide hourly measurements of meteorological and flux data since 2001 (Suyker 2001--a, 2001--b). US-Ne3 and US-Ne2 are both maize-soybean rotations, and during the 2012 summer growing season, both sites were planted with soybean (Fig. 2.1). Hourly differences of temperature and latent heat flux between US-Ne2 and US-Ne3 were compared with hourly differences between the irrigated and non-irrigated WRF simulations for the nearest dominantly irrigated grid cell to the coordinates from US-Ne2. Differences were compared using histograms or kernel-density estimation with a Gaussian kernel. This comparison was performed to assess whether our irrigation methodology produces a similar atmospheric response at the surface to observations.

Summer average temperature and accumulated precipitation from WRF were compared with daily gridded meteorological data from METDATA (Abatzoglou 2013) for each simulated year to assess the overall model bias. METDATA has a spatial resolution of approximately 4 km that makes it an acceptable dataset for resolving small-scale features in meteorological data that may be masked in a coarser resolution observational dataset. For direct comparison with results from WRF simulations, METDATA was aggregated to the same resolution as each WRF simulation using bilinear interpolation.

2.4.2 Land use and land cover

The twenty-four category USGS-Global Land Cover Characterization (GLCC) raster dataset for North America was used as the base land use dataset (Loveland et al. 2000). The resolution of this dataset is approximately 1 km. Because the classification scheme relied on satellite imagery from 1992 and 1993, it underestimated the number of irrigated acres over many areas of the OAR based on more recent land use products. The nature of this study requires the most robust estimates of irrigated land use and land cover in order to examine the effects of irrigation on the climate in the central U.S. Therefore, in this study, we modified the base GLCC dataset using two recent irrigated land use datasets described as follows.

First, the default GLCC dataset was updated using the 1-km Moderate Resolution Imaging Spectroradiometer Irrigated Agriculture dataset for the U.S (MIrAD-US) in 2012 (Brown and Pervez 2014). Grid cells in the original GLCC dataset were changed to either irrigated or non-irrigated cropland or pasture across the U.S. based on the information in the MIrAD-US dataset. This procedure drastically increased the number of irrigated pixels in regions of the central and northern OAR. In this study, two land use scenarios (irrigated and non-irrigated) were simulated using the updated MIrAD-US GLCC dataset.

Second, newly-released annual irrigation maps (AIMs) over the OAR were used to update the USGS-GLCC dataset to realistically represent water management in WRF over time (Deines et al. 2019b). These AIMs have a 30 m resolution and represent the longest record of irrigation for any region of the world, covering the period from 1984 to 2017. They are binary rasters that classify pixels as either irrigated or non-irrigated using a random forest classifier

trained with satellite imagery, environmental variables, and ground truth datasets. The integration of these AIMs into WRF is briefly described. All AIMs were resampled to 1 km using the majority algorithm in order to match the resolution of the USGS-GLCC dataset. Next, all irrigated cropland in the USGS-GLCC dataset contained within the buffer region of the AIMs were converted to dryland cropland. In the final step, pixels in the GLCC dataset that overlapped with resampled pixels classified as irrigated cropland in the AIMs were updated, creating a total of 34 new land use rasters from 1984 to 2017. For this study, irrigated land use data from 1984 and 2017 were incorporated into WRF as two distinct land use datasets for simulations. Because of major differences in irrigated acreage between 1984 and 2017, early estimates of irrigation can be used as a proxy for examining how regional climate may change if the number of irrigated acres were to decrease for high-risk areas of the OAR. In this study, two irrigated simulations were conducted using the updated GLCC dataset with AIMs based on data from 1984 and 2017. The difference between irrigated land use fraction between 2017 and 1984 at each grid cell in WRF is shown in figure 2.1.

2.5 Analysis and tools

Sixty-four WRF **s**imulations were conducted on a Dell PowerEdge T640 at Kansas State University using 2 Intel Xeon (R) Silver processors with 21 cores (4 years × 4 experiments × 4 land use scenarios). WRF-python software was used in several phases of data generation and analysis (Ladwig 2017), including the derivations of convective available potential energy, convective inhibition, cloud fraction, and geopotential height from raw WRF output. Toolboxes in ArcGIS 10.6.1 were used to process all land use and land cover data before integration into the WRF Preprocessing System.

The two-sample t-test was used to evaluate differences in surface output from the Ameriflux and WRF configurations. The non-parametric sign test was used to evaluate whether differences for different regions were significant between irrigated and non-irrigated model simulations. Statistical significance was assessed at a level of 5% for all hypothesis tests in this study. In addition, the spatial efficiency metric (SPAEF) was used to evaluate geospatial differences in output from irrigated and non-irrigated simulations. SPAEF calculates the correlation, coefficient of variation, and the percentage of histogram intersection between two geospatial rasters to measure the degree of similarity (Demirel et al. 2018; Koch et al. 2018). The maximum value of the SPAEF is 1 and indicates that two rasters are exactly the same. The larger the SPAEF deviates from 1, the more dissimilar the rasters are with respect to one another.

3. Results

3.1 Irrigation verification

Figures 2.2a and 2.2b demonstrate the spatial variability in total amount of irrigation applied at each grid cell for 2012 for two land surface model configurations: Noah: Mosaic and Noah-MP: LAI_P, respectively. Units are in billion gallons (bgal) for comparison with statistics from the USGS. Because the Noah: Mosaic model configuration applies irrigation at the sub-grid level and only for the fraction of the grid cell containing irrigated cropland, the total amount of irrigation applied at each grid cell was much less than the Noah-MP land surface model. However, the total number of grid cells that received any amount of irrigation in Noah-Mosaic was greater than the Noah-MP configurations. The greatest regional difference in irrigation applications between Figs 2.2a and 2.2b occurred over eastern Nebraska, which has a high

concentration of irrigated cropland. Inclusion of the dynamic vegetation (Noah-MP: LAI_P) in this densely irrigated agricultural region increased plant-water consumption, resulting in a significant increase in the frequency of irrigation compared to Noah-Mosaic. The total irrigation applications for Noah: Mosaic and Noah-MP: LAI_P grid cells within the OAR boundary were 7,200 and 12,000 bgals, respectively. For Noah-MP: LAI_T and Noah-MP: LAI_S, which are not shown, the total irrigation applications for the OAR were 9,200 and 6,300 bgals, respectively, clearly demonstrating that the inclusion of dynamic vegetation in the land surface model results in a larger amount of irrigation applied. This is further illustrated in the time series of total amount of daily irrigation applied between June and August 2012 (Fig. 2.2c). All four land surface model configurations demonstrated peak irrigation demand during July and August, which is typically the warmest period of the summer growing season and also when peak crop-water demand is the highest for corn, soybean, and cotton. Not only were the irrigation amounts for Noah-MP: LAI_P and LAI_T much larger than Noah-Mosaic and Noah-MP: LAI_S but also the durations of the peak irrigation periods were longer. Besides for a steep decline in irrigation around day 190, Noah-MP: LAI_P and LAI_T stayed between approximately 100−150 bgal day^{-1} from day of year (DOY) 180 to DOY 220 while land surface models with static vegetation gradually increased and peaked around DOY 210 before declining thereafter. The average amount of daily irrigation applied for the entire 7-month simulation were 34.8, 56.2, 43.0, and 29.5 bgal day^{-1} for Noah: Mosaic, Noah-MP: LAI_P, Noah-MP: LAI_T, and Noah-MP: LAI_S, respectively.

The USGS reported estimated observed total irrigation withdrawals in 2010 and 2015 for counties within the OAR were 17.3 and 17.1 bgal day^{-1}, respectively. As a direct comparison, the

average simulated irrigation applied during 2015 (not shown) within the OAR was 13 and 23 bgal day^{-1} for Noah: Mosaic and Noah-MP: LAI_P configurations, respectively, for the entire simulation duration. This result indicates relatively good agreement between observed and simulated irrigation during growing seasons with above normal precipitation but does highlight some variability between land surface model configurations. As discussed previously, simulated irrigation in the OAR during the drought year of 2012 significantly increased for all land surface model configurations compared to 2015. Although a direct comparison to observations cannot be made for 2012 given that USGS surveys are conducted every five years, the larger modeled irrigation application makes intuitive sense and provides confidence in our methodology. In addition, larger applications should accentuate the atmospheric response to irrigation.

3.2 Ameriflux comparison

The distributions of differences in hourly two-meter temperature (T2M) between irrigated (US-Ne2) and non-irrigated (US-Ne3) Ameriflux sites and the irrigated and non-irrigated WRF simulations during the summer of 2012 are presented in Figure 2.3a. Monthly averaged temperature differences for summer 2012 between the irrigated and non-irrigated Ameriflux sites and WRF simulations are in Figure 2.3b. The mean difference in temperature for the Ameriflux sites was −0.28 °C and for the four WRF simulations were −0.12 (Noah: Mosaic), −1.88 (Noah-MP: LAI_P), −0.78 (Noah-MP: LAI_T), and 0.01 °C (Noah-MP: LAI_S). The effect of irrigation based on observations and modeled responses WRF was a moderate decrease in temperature, excluding the Noah-MP: LAI_S configuration, which overall exhibited minimal temperature response. The temperature decrease was notably overestimated for the two Noah-MP configurations with vegetation prediction, which was not surprising based on the modeling

scale of 10 km and the entire grid cell received the irrigation application. For the adjacent grid cell that was not dominantly irrigated, the response was less extreme for Noah-MP: LAI_P (−0.4 °C). Visual inspection of the distributions reveals more similar characteristics between Ameriflux and Noah: Mosaic and Noah-MP: LAI_S. On a monthly basis, WRF was able to capture the within season temporal cycle although the magnitude of differences differed from Ameriflux (Fig. 2.3b). Two-sample t-tests between the hourly T2M differences from Ameriflux sample and each model WRF configuration in 2012 revealed statistically significant differences between the means of observations and each model simulation. This suggests that no configuration was able to statistically outperform the other configurations for simulation of summer T2M in 2012.

In figures 2.3c and 2.3d, differences in latent heat fluxes are presented similarly as Figs. 2.3a and 2.3b. The mean difference in latent heat fluxes (LH) for the Ameriflux sites was 34.3 W m^{-2} and for the four WRF simulations were 5.53 (Noah: Mosaic), 78.06 (Noah-MP: LAI_P), 47.07 (Noah-MP: LAI_T), and 8.24 W m^{-2} (Noah-MP: LAI_S). The two configurations without a vegetation response significantly underestimate the LH response while the other two overestimate the response. Similar to T2M, two-sample t-tests of differences with the Ameriflux data produced all statistically significant results. In the Ameriflux data, the distribution is notably skewed to the right, and the two configurations with vegetation responses were better able to capture large departures greater than 50 W m^{-2}. In the context of historical Ameriflux data, June 2012 was an unusual month (Fig. A.2). In a typical central U.S. summer, the difference in latent heat flux typically increases throughout the summer and peaks in July and early August due to differences in crop phenology. In 2012 for soybean, differences peaked in June and declined

thereafter. Below normal precipitation in June 2012 resulted in abnormally large differences in latent heat fluxes between Ameriflux sites. Precipitation in late June resulted in a decline in latent heat differences towards more typical values the rest of the summer. In the 2015 simulation, results for T2M were more similar between WRF and Ameriflux (Fig. A.3).

Based on these surface-based observations, we cannot state conclusively that one configuration outperforms another configuration at the surface as each has its own benefits and drawbacks. For example, while the configurations without dynamic vegetation have better absolute T2M performance in 2012, they are not able to simulate the large differences in latent heat flux that were observed. A more conservative irrigation methodology within Noah-MP may help constrain temperatures when vegetation is dynamically simulated. More observed site-based measurements of irrigated and non-irrigated data across the OAR would help assess model performance, particularly in more densely irrigated regions as the Ameriflux site lies outside of the OAR boundary. While perfect agreement between the model configurations and observations was not expected, the results support a local near-surface atmospheric response due to irrigation with the "true" model response most likely occurring somewhere in between the results from our model parameterizations. This key result should be used to contextualize the results presented in the following sections.

3.3 Irrigation effects at the surface

The simulation results from the summer of 2012 are mainly discussed in the following sections due to the severity and extent of the drought. Results from 1980, 1993, and 2015 are provided in Appendix A and referenced when relevant. During the summer of 2012, an

abnormally strong, persistent ridge centered over the central U.S. caused temperatures to soar, resulting in average mean temperature anomalies 3 − 4.0 °C above the 1981−2010 normal across Nebraska, eastern Kansas, Missouri, and Iowa. The majority of the central U.S. received below normal precipitation with the largest departures from normal across central and northeast Nebraska, eastern Kansas, and Iowa. The average simulated accumulated summer precipitation over the OAR across all non-irrigated WRF land surface model configurations was 119 mm, which was an overestimation of observed precipitation in METDATA (101 mm). For irrigated simulations, average precipitation increased to 120 mm or 1 mm greater than the non-irrigated simulations. Because the duration of the simulation was approximately seven months, perfect agreement with observations was not expected.

Differences in four surface climate variables between the irrigated and non-irrigated WRF simulations using the MIrAD modified land use dataset are presented in Figure 2.4. Differences in T2M for all four land surface model configurations averaged across all grid cells in the OAR are less than zero, confirming the result found locally in section 3.2 on the regional-scale (Figs. 2.4a−2.4d). The largest difference in magnitude was −0.45 °C for Noah-MP: LAI_P, and the smallest in magnitude was both Noah: Mosaic and Noah-MP: LAI_S at −0.10 °C. Not surprisingly, the northern OAR had the largest in magnitude average difference for all land surface models, excluding Noah-MP: LAI_S, which had a stronger response across the southern OAR than central or northern OAR. The grid cell with the smallest difference was −2.6 °C in the northern OAR for Noah-MP: LAI_P. Sign tests of the average differences between the irrigated and non-irrigated WRF simulations across the entire OAR and each region were statistically significant ($p < 0.001$). Similar results over the irrigated regions in the OAR were found for

1980, 1993, and 2015, but the responses in the pluvial years were not as strong given that the amount of irrigation applied in each of those two years was less (Figs. A.5−A.8).

Downwind of the OAR over the upper Midwest corn belt, mean summer T2M decreased between 0.04 and 0.13 °C for three of the four configurations with the strongest response for Noah-MP: LAI_P. In Noah-MP: LAI_S, the irrigated simulation demonstrated an increase of 0.07 °C. The domain average difference for all four land surface models was −0.09 °C. Temperature increases for areas outside of the OAR do not exceed 0.25 °C. The spatial efficiency metric (SPAEF) for summer T2M demonstrates the most spatial dissimilarity between irrigated and non-irrigated simulations for Noah-MP: LAI_P (Fig. 2.5) with the central OAR demonstrating the most dissimilarity (SPAEF = 0.72).

Differences in two-meter specific humidity (Q2M; g kg^{-1}) generally mirrored the same spatial structure as T2M (Figs. 2.4e−2.4h). All land surface models configurations demonstrated an increase in Q2M over the OAR and the entire domain, increasing the net mass of the air column near the surface. The increase in soil moisture and latent heat flux at the surface decreased sensible heat flux and T2M and increased relative humidity. The largest and smallest mean differences between the irrigated and non-irrigated simulations across the OAR were 0.37 and 0.10 g kg^{-1} for Noah-MP: LAI_P and Noah-MP: LAI_S, respectively. The response for Noah-MP: LAI_P was driven by an increase in the transpiration rate, which added additional water vapor to the air column. For the Noah-MP configurations, the differences soil and canopy evaporation rates remained the same across configurations. Downwind of the OAR, Q2M increased between 0.06 and 0.11 g kg^{-1} for the same three configurations that demonstrated a

decrease in T2M, suggesting that moisture transport downwind was closely related to the decrease in temperature previously found. The SPAEF for Q2M was on the same order of magnitude if not higher than T2M, emphasizing more spatial similarities between irrigated and non-irrigated simulations.

Of the four variables presented in Figure 2.4, differences in accumulated precipitation (mm) demonstrated the highest spatial variability at the local and regional scales both within and between land surface models (Figs. 2.4i−2.4l), emphasizing model sensitivity of land surface processes that influence precipitation. Analyzed on a daily basis, irrigation caused precipitation to vary in timing, location, and intensity across the region; however, regional averages demonstrated that spatially coupled positive and negative differences tended to cancel each other out. Simulations using Noah: Mosaic and Noah-MP: LAI_P had mean average precipitation differences across the OAR of 2.35 and 4.43 mm, respectively, while Noah-MP: LAI_T and Noah-MP: LAI_S had average differences of −2.90 mm and −1.28 mm, demonstrating opposing responses depending on the choice of land surface model parameterization. However, there are some common spatial similarities between the land surface models. Analyzed by region, all WRF simulations consistently resulted in decreases in precipitation over the central OAR with the largest difference of −12.91 mm for Noah-MP: LAI_P followed by Noah-MP: LAI_T at −8.77 mm. In fact, this region experienced the strongest and most consistent response across the OAR, supporting the notion that the effect was not due to internal variability. Furthermore, an interesting feature common among land surface models in the precipitation patterns is the reduction immediately east of the southern OAR. The effect was most accentuated in the configurations using Noah-MP. Downwind over the corn belt, precipitation increased between 2

and 7 mm for three of the four configurations. In addition, the number of hourly periods with a rainfall intensity over 50 mm increased under irrigation for many locations east of the OAR. Overall, the average difference in accumulated precipitation across the entire domain for all land surface model configurations was slightly positive, indicating that on average surface irrigation increased precipitation.

Spatial differences in vapor pressure deficit (VPD in hPa) at two meters notably follow the spatial structure of precipitation differences outside of the OAR. In the areas with no irrigation, an increase in precipitation generally increases the moisture content and thus vapor pressure of the air, thereby increasing the difference between the saturation and actual vapor pressure. When the mean temperature also decreased, there was a decrease in e_{sat} with the overall effect being to further increase VPD. In non-water-limited cropping systems, an increase in VPD does not typically induce crop stress if the amount of soil water is able to meet crop-water demand. Over the OAR, for the simulations with static vegetation, the effect of irrigation was to decrease VPD uniformly over most of the region (Figs. 2.4m and 2.4p). In fact, the average VPD response for the OAR in Noah: Mosaic and Noah: MP_LAI_S were both −0.11 hPa. Directly over the irrigated regions in the north and southern OAR for Noah-MP: LAI_P and Noah-MP: LAI_T, VPD distinctly increased as a result of the dynamic vegetation response (Figs. 2.4n and 2.4o). However, in the semiarid locations over the OAR (e.g. western Kansas and Nebraska), the net effect of irrigation was a decrease in VPD. Thus, the overall net response across the OAR for Noah-MP: LAI_P and Noah-MP: LAI_T was also a decrease in VPD (−0.06 and −0.08 hPa, respectively) but smaller in magnitude compared to simulations with static vegetation as a result of the increase in VPD directly over dense areas of irrigated cropland. East of the OAR in Texas,

Oklahoma, and Kansas, VPD increased up to 0.4 hPa in simulations with vegetation responses (Figs. 2.4n and 2.4o). Downwind over the corn belt, VPD decreased on average between −0.10 and −0.13 hPa in all four configurations. Across the entire WRF domain, the mean VPD response was slightly negative for Noah: Mosaic and Noah: MP_LAI_S and positive for Noah-MP: LAI_P and Noah-MP: LAI_T, illustrating the importance of different land surface parameterizations when evaluating the atmospheric response for pertinent agricultural variables.

3.4 Irrigation effects above the surface

The most unstable convective available potential energy (MCAPE), a measure of the atmospheric instability or the energy for strong thunderstorm updrafts, increased on average across the OAR for all land surface model configurations except Noah-MP: LAI_T (Figs. 2.6a – 2.6d). The mean difference in MCAPE over the OAR ranged from 27.6 and −0.84 J kg^{-1} in Noah-MP: LAI_P and Noah-MP: LAI_T, respectively. The increase in MCAPE was higher in the simulations with dynamic vegetation with maximum grid cell differences of 80 and 120 J kg^{-1} in Noah-MP: LAI_T and Noah-MP: LAI_P directly over the irrigated regions in the northern OAR and downwind in South Dakota. The response was most pronounced in Noah-MP: LAI_P. Three of the four configurations demonstrated a decrease in MCAPE downwind (4 − 7 J kg^{-1}) over the corn belt.

Mean convective inhibition (CIN) decreased by −2.8 and −0.2 J kg^{-1} over the OAR in Noah: Mosaic and Noah-MP: LAI_S, respectively, and increased by 2.1 and 1.4 J kg^{-1} in Noah-MP: LAI_P and Noah-MP: LAI_T, respectively. In the Noah-MP configurations, CIN generally increased directly over the heavily irrigated regions in the OAR across all of the land surface

model configurations (Figs. 2.6e – 2.6h). An increase in CIN enhances the negative buoyancy of rising air parcels, indicating that additional energy is required for air parcels to rise to the level of free convection to develop deep convection. In contrast to MCAPE, which generally increased directly over and downwind of heavily irrigated regions, CIN decreased downwind on average between 1.5 and 5.5 J kg^{-1}, making the environmental profile more conducive to thunderstorm development under favorable synoptic conditions.

Cloud fraction, the percentage of a grid cell covered by clouds between 2 and 6 km above the surface, decreased over most areas of the OAR (Figs. 2.6i – 2.6l). However, the magnitudes of the differences are small because the response was only observed for select hourly periods in the simulation. Among all land surface models, the average difference across the OAR was −0.002 % with all land surface models reporting average differences less than zero. Regionally, the decrease in cloud fraction was up to 0.053% over the heavily irrigated area in the southern OAR for Noah-MP: LAI_P. Across the northern OAR for the same land surface model, the largest decrease was only up to 0.020%. This regional response was consistent across configurations. While Noah-MP: LAI_P and Noah-MP: LAI_T had the largest decreases in cloud fraction, the simulations also showed some areas downwind increasing in cloud fraction. In Noah-MP: LAI_P, there was a 0.032% increase over eastern South Dakota. In addition, the mean downwind response over the corn belt was positive for three of the four configurations (excluding Noah-MP: LAI_T).

Surface cooling as a result of the net increase in moisture from irrigation had the effect of increasing the geopotential height at 850 hPa consistently across all land surface model

configurations (Figs. 2.6m−2.6p). Because the molecular weight of water vapor is lighter than diatomic nitrogen and oxygen, the addition of near-surface moisture decreased the air density of the air column near the surface, causing an increase the geopotential heights above this "moisture bubble". The effect of this increase was to reduce vertical motion and turbulent mixing in the boundary layer as the average planetary boundary heights decreased between 50 and 200 m over the irrigated regions in the OAR. This was supported by the decrease in cloud fraction in the mid-levels of the atmosphere, indicating a decrease in vertical motion that prevents air from rising, cooling, and reaching saturation. Among all land surface model configurations, the average change in geopotential height at 850 hPa was 0.44 m. The largest single grid cell increase was 2.9 m in Noah: Mosaic, which occurred in the southern OAR. In all land surface models except Noah-MP: LAI_S, the coverage of the height rise is generally over and northeast of the OAR. In Noah-MP: LAI_S, there is a noticeable regionalization of the height rise over the central and southern OAR. This spatial response in Noah-MP: LAI_S was consistent among all simulated years, suggesting that the static vegetation in the irrigated region in southeast Nebraska played a role in this regionalization.

Vertical cross-sections of the change in mean summer relative humidity (RH) across three densely irrigated regions in northern, central, and southern OAR are shown in figure 2.7. The responses over irrigated cropland were similar across configurations although the magnitudes differ. In general, RH increased from the surface up to approximately 4 km over and near the irrigated regions for all surface models with the effect most pronounced in Noah-MP: LAI_P over the northern OAR (greater than 4% in the first 300 meters in Fig. 2.7d). The increase in RH was carried downwind through Iowa and Minnesota although the magnitude decreases

with distance from Nebraska, indicating transport of moisture out of the OAR. Across all three cross-sections, there is a coupled decrease in relative humidity of 3 − 4% in the mid-level atmosphere between 4 and 6 km above the surface. This suggests that surface moisture is not able to penetrate as deep into the atmosphere under irrigation, resulting in less intense convection. This was supported by decreases in vertical velocity up to 2 − 3 cm s^{-1} over irrigated regions in the southern and northern OAR (Fig. A.18). The response was largest over the northern and southern OAR where irrigated cropland density is greatest with Noah: Mosaic showing a similar but less intense response. Noah-MP: LAI_S is the only configuration that does not exhibit this coupling structure over the northern OAR (Fig. 2.7j).

3.5 Effects of changes in amount and distribution of irrigation on surface climate

Figure 2.8 demonstrates the difference in summer accumulated precipitation and mean T2M for the two different land use type simulations described in the material and methods. Figs 2.8a – 2.8b are for precipitation and T2M differences between irrigated and non-irrigated simulations as a function of irrigated land use fraction (LUF) for only grid cells in the OAR. The difference in precipitation is positive or near zero from irrigated LUF 0.1 to 1.0 for Noah: Mosaic and Noah-MP: LAI_P (Fig. 2.8a). In contrast, as irrigated land use fraction increases for Noah-MP: LAI_T and Noah-MP: LAI_S, average total precipitation decreases up to −0.035 mm with the largest decreases between 0.4 and 0.8 LUF. For T2M, all land surface model configurations demonstrated decreases in T2M with increasing LUF (Fig. 2.8b). The largest rate of change occurs between 0.5 and 0.6 irrigated LUF in the Noah-MP configurations. As the irrigated LUF increased from 0.5 to 0.6, there was a − 0.69 °C decrease in temperature for Noah-

MP: LAI_P. In Noah: Mosaic, the response was linear with an approximate decrease of − 0.02 °C for every 0.1 increase in irrigated cropland fraction.

Figs. 2.8c – 2.8d demonstrate the change in precipitation and T2M between the irrigated simulations using irrigated cropland land use from 1984 and 2017. At each grid cell, the difference in irrigated LUF was calculated between 2017 and 1984. For example, when the change in irrigated LUF is less than 0, this indicates a decrease in irrigated cropland from 1984 and 2017. Generally, all land surface model configurations demonstrated an increase in precipitation for those grid cells that decreased in irrigated LUF (Fig. 2.8c). As the change in LUF increased above 0, three of the four land surface model configurations exhibited a decrease in precipitation with the largest decreases occurring for configurations with dynamic vegetation. Noah−MP: LAI_S was the only configuration that showed a slight increase in precipitation with increasing irrigated LUF. Change in temperature demonstrated a similar response to the irrigated and non-irrigated simulations (Figs. 2.8b and 2.8d). For grid cells that demonstrated a decrease in irrigated LUF, the response was near zero to slightly positive. Because the frequency of grid cells that had decreased in irrigated LUF was less than 1%, it is likely that grid cells were still influenced by the effects of other irrigated grid cells as well as the increase in precipitation, which can moderate temperatures for many days after the precipitation occurs.

4. Discussion

4.1 Implications on agriculture and climate

Our results showed that the inclusion of irrigation clearly has a significant atmospheric response in regional climate modeling. Based on recent geologic estimates of saturated thickness

and rates of water table decline across the OAR, the use of irrigation across arable cropland in the northern OAR may hold steady or increase from current estimates while irrigation in the central and southern OAR may decrease (Haacker et al. 2016). Thus, using the results as guidance, we can surmise with high certainty that a reduction in the amount of irrigation applied at the surface will increase local temperatures. Decreases in local surface temperatures were driven by an increase in soil evaporation and transpiration from simulations that include a vegetation response, which resulted in an increase in latent heat flux and evaporative cooling at the surface. At the extreme, one simulation that included a dynamic vegetation parameterization showed a local mean decrease of 2.6 °C in the densely irrigated region of Nebraska during the 2012 drought. While the overall temperature may decrease due to the suppression of daytime temperatures, an increase in surface humidity keeps temperatures warmer at night because moist air retains more heat than dry air. Because we applied irrigation in the early morning, the effect was more notable in some of the downwind areas that do not directly receive irrigation applications. High nighttime temperatures can interfere with the respiration processes of summer row crops and decrease yield (Fahad et al. 2016; Jagadish et al. 2007). In areas with declining groundwater, reduced irrigation in the future may increase the vulnerability of dryland cropping systems to heat waves and drought during critical growth stages (Fahad et al. 2017; Gowda et al. 2018; Zhang and Lin 2016). Furthermore, higher VPD in soybean and maize production systems has been shown to have negative impact on yields in the corn belt due to the increase in water stress and reduction in plant growth (Lobell et al. 2014). Densely irrigated regions in the northern and southern OAR had the largest local T2M, Q2M, and VPD responses compared to the central OAR, which has a heterogeneous mix of dryland and irrigated cropping systems and grassland (USDA-NASS 2019). Thus, these regions will with high probability see the largest

climatic response in the future compared to other regions of the OAR, subtly affecting the environmental conditions for summer production systems in the northern and southern OAR including maize, soybean, and cotton.

Our simulation results also demonstrated other latent climate responses. For example, a decrease in sprinkler irrigation may lead to slight increases in cloud fraction in the mid-levels of the atmosphere across areas in the central and southern OAR. An increase in cloud fraction reduces the amount of photosynthetically active radiation (PAR) that reaches the crop canopy, particularly over the southern OAR in which the response was the strongest across land surface model configurations. This decrease could affect grain filling under current climatic conditions but potentially help minimize the increase in T2M that is expected to occur with high probability as a result of reduced irrigation and an increase in global greenhouse gas concentrations (Hayhoe et al. 2018; IPCC 2013). In contrast, in the northern OAR, an increase in sprinkler irrigation may further decrease cloud fraction as a result of local increase in subsidence, thereby increasing the PAR reaching the crop canopy. This would be beneficial in irrigated maize and soybean during the grain filling stage. Historically, solar brightening has been shown to account for a large proportion of the increase in maize yields over the Midwest with our results suggesting that irrigation may be a contributing factor to the increase in solar radiation at the surface (Tollenaar et al. 2017). Furthermore, an increase in MCAPE across a majority of the domain indicates more available energy for convective development and precipitation. However, the increase in storm intensity may enhance the risk of severe weather such as hail or high winds, which causes significant crop damage at the field scale such as lodging. In configurations that also demonstrated an increase in CIN over the irrigated regions, additional energy from forcing

mechanisms such as surface heating, mechanical lifting, or upper-level divergence has to be present in order for air parcels to reach the level of free convection. This increase in CIN helps suppress convective development and oppose the increase in MCAPE. However, CIN consistently decreased downwind, which in combination with the increase in MCAPE, helps increase the frequency and intensity of precipitation and enhance the risk of severe weather over the corn belt.

4.2 Land surface model and study intercomparison

The parameterizations within the physics options are a critical source of uncertainty in regional climate modeling. In our study, choice of land surface model and parameterization had a significant impact on some but not of all the analyzed climate variables. When compared to observations, no model configuration had superior performance over another. The spatial distributions of the climate responses near and above the surface downwind of the OAR were more heterogeneous than the climate responses observed directly over the irrigated cropland although spatial averaging helped to separate the signal from the noise. The inclusion of dynamic vegetation in the land surface model increased crop water demand and consequentially the amount of applied irrigation. The increase in irrigation and leaf area index increased transpiration rates and thus the near-surface water vapor content, changing the thermodynamic structure of the lower atmosphere more significantly than the parameterizations without dynamic vegetation. For example, MCAPE was higher over and downwind of the OAR due to the increase in surface moisture, which lowers the lifted condensation level and increases positive buoyancy for a rising air parcel (Yin et al. 2015). Above the surface, we found that response was more coherent across configurations, indicating the influence of differences in the land surface models with increasing

distance from the surface. For example, an increase in geopotential height at 850 hPa was spatially consistent among all configurations in this study in addition to changes in mid-level cloud fraction. Despite some of the grid cell scale uncertainties resulting from different land surface model parameterizations, identifiable patterns were found at the regional scale as a result of irrigation.

To complement the intercomparison of land surface models conducted in our study, we also compared our results with previous studies to comment on potential model sensitivities with respect to alternative irrigation or model parameterizations and domain specifications. In our study, the increase in geopotential height at 850 hPa for Noah: Mosaic in our study was similar to results from Pei et al. (2016), which used the same land surface model configuration but a coarser resolution (30 km) over the entire continental United States. However, the change in geopotential heights at 500 hPa was dissimilar as their results demonstrated an increase of 4 m over the southwest Great Plains, indicating an intensified mid-level ridge. We demonstrated that geopotential heights at 500 hPa decreased between 0.5 – 1 m over the northern OAR and to the northeast with responses close to zero elsewhere (Fig. A.4). Irrigation in our study had the strongest response on the synoptic flow closer to the surface. In addition, the authors showed spatially uniform responses in precipitation across the Great Plains while our results demonstrated changes in precipitation to be highly heterogeneous. This suggests that model resolution and domain specification plays an important role in the simulation response to surface irrigation. Future work could evaluate the magnitude of this uncertainty using multiple domain specifications.

At the surface, our results for surface variables such as T2M and Q2M were comparable with Harding and Snyder (2012b) and Huber et al. (2014) and demonstrated similar spatial heterogeneity in precipitation. Huber et al. (2014) also showed that irrigation increased geopotential heights at 850 hPa across the OAR. Higher in the atmosphere, the geopotential height response was weak. A key similarity between our study and these two studies was a similar model resolution even though the irrigation methodologies were different, again emphasizing the importance of domain specification in the WRF experimental design. Furthermore, our model sensitivity results to dynamic and static vegetation parameterizations were similar to Harding et al. (2015). Despite using the Community Land Model (CLM), which uses subgrid variability, the changes in average T2M and Q2 response over irrigated cropland were within range of our results. They also observed that dynamic vegetation increased the response of variables such as CAPE and CIN. Overall, our analysis of results from this study and previous studies suggests that specification of the domain (e.g. boundaries and resolution) or parameterizations within the individual land surface model may be more important than the individual land surface models themselves (e.g. Noah vs. CLM).

4.3 Scale of irrigation

Given that the implementation of irrigation into the WRF model is a critical component in this study, a discussion of the suitability and limitations of modeling scale is warranted. At the field-scale, irrigation occurs on the order of 1 km; however, in most modeling studies, the resolution at which irrigation is applied is much coarser due to computational limitations and the limitations of model performance at high resolution simulations in climate research applications. In this study, the 10 km resolution may be sufficient in densely irrigated regions in the southern

and northern OAR but may be inadequate in areas with a mix of non-irrigated and irrigated agriculture such as the central OAR. Land surface models coupled in the WRF framework such as Noah that include a mosaic option attempt to better represent the surface energy balance for coarser model resolutions by calculating surface fluxes for each land use type within a grid cell. Therefore, irrigation can be applied only to the fraction of the grid cell containing irrigated cropland. In contrast, Noah-MP currently only simulates the surface energy balance for the dominant land use type, and consequently, irrigation was applied to an entire grid cell if the dominant land use designation was irrigated cropland. Interestingly, the two land surface models and all parameterizations in this study simulated relatively similar amount of irrigation in each of the four years. Including sub-grid variability within the Noah-MP framework may improve model simulations and also moderate the climate responses for coarse resolutions. The spatial distribution of total irrigation amounts, a key difference between Noah: Mosaic and Noah-MP configurations, plays a role in the location, intensity, and duration of the surface temperature, humidity, and other climate variable responses.

In addition, the initialization, timing, and duration of each irrigation application in this study was idealized. In this study, a single check was performed each morning at 6 AM to determination whether an irrigation application was required to minimize losses from evaporation. In practice, producers may irrigate at any time during the day and for a duration over 24 hours. The specific timing of each application may be responsible for subtle changes in the spatial distribution and intensity of precipitation given a set of synoptic conditions. For example, water that has not infiltrated into the soil immediately after an irrigation event can be mixed into the boundary layer and transported downwind in the presence of a significant forcing

mechanism, changing the thermodynamic structure of the downwind boundary layer that may alter precipitation intensity. Future work could explore the sensitivity of the spatial distributions of climate responses as a result of irrigation methodology or timing in order to explain some of the noise seen in certain model outputs in this study.

5. Summary and conclusions

Groundwater levels across many areas in the OAR are projected to drastically decline over the next several decades (Haacker et al. 2016), which may have consequences on regional climate as a result of changes in irrigation practices. As producers are forced to conserve water resources either by their own sense of stewardship, policy initiatives, or eventual depletion of groundwater, they will turn to practices that limit the amount of irrigation applied or switch to non-irrigated or less water-intensive crops, resulting in alterations to the water and energy balance. Irrigation plays a significant role in modifying the land and above surface climate features such as temperature and humidity and alters surface energy partitioning primarily between sensible and latent heat fluxes. Both observations and model results from AmeriFlux and WRF support these conclusions although there is remaining uncertainty to the extent and intensity of the effects. The net effect across all land surface model configurations was to increase specific humidity and decrease temperature over the OAR and downwind over the upper Midwest corn belt. Locally within the OAR, the largest temperature and specific humidity responses by absolute magnitude occurred over the northern and southern OAR due to the high density of irrigated cropland. In contrast, the central OAR consistently demonstrated a decrease in precipitation across land surface models. Vapor pressure deficit increased over the irrigated cropland if vegetation development was simulated and allowed to increase in response to the

addition of irrigation. Mid-level cloud fraction over the OAR decreased consistently across land surface models with the largest response in the southern OAR. Vertical cross-sections of relative humidity across the most densely irrigated areas revealed increases up to 4 and 5% isolated below 3 km directly coupled with decreases in relative humidity between 3 and 7 km due to a decrease in vertical motion over the irrigated regions. The change in irrigated cropland land use fraction between 1984 and 2017 demonstrated similar results to the irrigated and non-irrigated simulations. Therefore, these modeling results suggest that the influence of irrigation on climate in the central U.S. is notable. Thus, a change in the amount of applied sprinkler irrigation water across the OAR will have consequences on important ag-climate variables including temperature, precipitation, solar radiation, and vapor pressure deficit.

Furthermore, the choice of land surface model parameterization plays an important role in quantifying the strength of the atmospheric response to irrigation. For example, the inclusion of dynamic vegetation changed the sign of vapor pressure deficit and MCAPE in regions of the OAR with significant agricultural production. In other cases, the parameterization increased the magnitude of the response directly over and downwind of the OAR. Given the sharp seasonal cycle in crop vegetation that occurs in this region during the growing season, dynamic vegetation components should be included to account for enhanced transpiration that results from crop development in both irrigated and dryland cropping systems. Additional sensitivity analysis with different land surface and other WRF physics parameterizations as well as model domain coverage and resolution would be beneficial for increased understanding of the role of irrigation on climate in the central United States.

References

Abatzoglou, J. T., 2013: Development of gridded surface meteorological data for ecological applications and modelling. *International Journal of Climatology*, **33,** 121-131, doi: 10.1002/joc.3413.

Adegoke, J. O., R. A. P. Sr., J. Eastman, R. Mahmood, and K. G. Hubbard, 2003: Impact of Irrigation on Midsummer Surface Fluxes and Temperature under Dry Synoptic Conditions: A Regional Atmospheric Model Study of the U.S. High Plains. *Monthly Weather Review*, **131,** 556-564, doi: 10.1175/1520-0493(2003)131<0556:ioioms>2.0.co;2.

Alter, R. E., H. C. Douglas, J. M. Winter, and E. A. B. Eltahir, 2017: Twentieth Century Regional Climate Change During the Summer in the Central United States Attributed to Agricultural Intensification. *Geophysical Research Letters*, **45,** 1586-1594, doi: 10.1002/2017GL075604.

Baidya Roy, S., G. C. Hurtt, C. P. Weaver, and S. W. Pacala, 2003: Impact of historical land cover change on the July climate of the United States. *Journal of Geophysical Research: Atmospheres*, **108,** n/a-n/a, doi: 10.1029/2003jd003565.

Brown, J. F., and M. S. Pervez, 2014: Merging remote sensing data and national agricultural statistics to model change in irrigated agriculture. *Agricultural Systems*, **127,** 28-40, doi: https://doi.org/10.1016/j.agsy.2014.01.004.

Chen, F., X. Xu, M. Barlage, R. Rasmussen, S. Shen, S. Miao, and G. Zhou, 2018: Memory of irrigation effects on hydroclimate and its modeling challenge. *Environmental Research Letters*, **13,** 064009, doi: 10.1088/1748-9326/aab9df.

Deines, J. M., A. D. Kendall, and D. W. Hyndman, 2017: Annual Irrigation Dynamics in the US Northern High Plains Derived from Landsat Satellite Data. *Geophysical Research Letters*, **44,** 9350-9360, doi: https://doi.org/10.1002/2017GL074071.

Deines, J. M., A. D. Kendall, J. J. Butler, and D. W. Hyndman, 2019a: Quantifying irrigation adaptation strategies in response to stakeholder-driven groundwater management in the US High Plains Aquifer. *Environmental Research Letters*, **14,** 044014, doi: 10.1088/1748-9326/aafe39.

Deines, J. M., A. D. Kendall, M. A. Crowley, J. Rapp, J. A. Cardille, and D. W. Hyndman, 2019b: Mapping three decades of annual irrigation across the US High Plains Aquifer using Landsat and Google Earth Engine. *Remote Sensing of Environment*, **233,** 111400, doi: https://doi.org/10.1016/j.rse.2019.111400.

Demirel, M. C., J. Mai, G. Mendiguren, J. Koch, L. Samaniego, and S. Stisen, 2018: Combining satellite data and appropriate objective functions for improved spatial pattern performance of a distributed hydrologic model. *Hydrol. Earth Syst. Sci.*, **22,** 1299-1315, doi: 10.5194/hess-22-1299-2018.

Dieter, C. A., M. A. Maupin, R. R. Caldwell, M. A. Harris, T. I. Ivahnenko, and Coauthors, 2018: Estimated use of water in the United States in 2015. *Circular.* Report 1441, 76 pp.

Fahad, S., S. Hussain, S. Saud, S. Hassan, M. Tanveer, and Coauthors, 2016: A combined application of biochar and phosphorus alleviates heat-induced adversities on physiological, agronomical and quality attributes of rice. *Plant physiology and biochemistry : PPB*, **103,** 191-198, doi.

Fahad, S., A. A. Bajwa, U. Nazir, S. A. Anjum, A. Farooq, and Coauthors, 2017: Crop Production under Drought and Heat Stress: Plant Responses and Management Options. *Frontiers in Plant Science*, **8**, doi: 10.3389/fpls.2017.01147.

Gowda, P., J. L. Steiner;, C. Olson, M. Boggess, T. Farrigan, and M. A. Grusa, 2018: Agriculture and Rural Communities. *Impacts, Risks, and Adaptation in the United States:Fourth National Climate Assessment.* 391-437 pp.

Haacker, E. M., A. D. Kendall, and D. W. Hyndman, 2016: Water Level Declines in the High Plains Aquifer: Predevelopment to Resource Senescence. *Ground Water*, **54,** 231-242, doi: 10.1111/gwat.12350.

Haacker, E. M. K., K. A. Cotterman, S. J. Smidt, A. D. Kendall, and D. W. Hyndman, 2019a: Effects of management areas, drought, and commodity prices on groundwater decline patterns across the High Plains Aquifer. *Agricultural Water Management*, **218,** 259-273, doi: 10.1016/j.agwat.2019.04.002.

Haacker, E. M. K., V. Sharda, A. M. Cano, R. A. Hrozencik, A. Núñez, and Coauthors, 2019b: Transition Pathways to Sustainable Agricultural Water Management: A Review of Integrated Modeling Approaches. *JAWRA Journal of the American Water Resources Association*, **55,** 6-23, doi: 10.1111/1752-1688.12722.

Hansen, J., M. Sato, R. Ruedy, L. Nazarenko, A. Lacis, and Coauthors, 2005: Efficacy of climate forcings. *Journal of Geophysical Research: Atmospheres*, **110**, doi: 10.1029/2005jd005776.

Harding, K. J., and P. K. Snyder, 2012a: Modeling the Atmospheric Response to Irrigation in the Great Plains. Part I: General Impacts on Precipitation and the Energy Budget. *Journal of Hydrometeorology*, **13,** 1667-1686, doi: 10.1175/JHM-D-11-098.1.

——, 2012b: Modeling the Atmospheric Response to Irrigation in the Great Plains. Part II: The Precipitation of Irrigated Water and Changes in Precipitation Recycling. *Journal of Hydrometeorology*, **13,** 1687-1703, doi: 10.1175/jhm-d-11-099.1.

Harding, K. J., T. E. Twine, and Y. Lu, 2015: Effects of Dynamic Crop Growth on the Simulated Precipitation Response to Irrigation. *Earth Interactions*, **19,** 1-31, doi: 10.1175/ei-d-15-0030.1.

Hayhoe, K., D.J. Wuebbles, D.R. Easterling, D.W. Fahey, S. Doherty, and Coauthors, 2018: Our Changing Climate. *Impacts, Risks, and Adaptation in the United States: Fourth National Climate Assessment.* U.S. Global Change Research Program, 72-144 pp.

Huber, D. B., D. B. Mechem, and N. A. Brunsell, 2014: The Effects of Great Plains Irrigation on the Surface Energy Balance, Regional Circulation, and Precipitation. *Climate*, **2,** 103-128, doi.

Im, E.-S., M. P. Marcella, and E. A. B. Eltahir, 2014: Impact of Potential Large-Scale Irrigation on the West African Monsoon and Its Dependence on Location of Irrigated Area. *Journal of Climate*, **27,** 994-1009, doi: 10.1175/jcli-d-13-00290.1.

IPCC, 2013: Summary for Policymakers. *Climate Change 2013: The Physical Science Basis. Contribution of Working Group I to the Fifth Assessment Report of the Intergovernmental Panel on Climate Change.* Cambridge University Press, 1-30 pp.

Jagadish, S., P. Craufurd, and T. Wheeler, 2007: High temperature stress and spikelet fertility in rice (Oryza sativa L.). *Journal of Experimental Botany*, **58,** 1627-1635, doi: 10.1093/jxb/erm003.

Koch, J., M. C. Demirel, and S. Stisen, 2018: The SPAtial EFficiency metric (SPAEF): multiple-component evaluation of spatial patterns for optimization of hydrological models. *Geosci. Model Dev.*, **11,** 1873-1886, doi: 10.5194/gmd-11-1873-2018.

Ladwig, W., 2017. wrf-python (Version 1.3.2) [Software].

Lawston, P. M., J. A. Santanello, B. F. Zaitchik, and M. Rodell, 2015: Impact of Irrigation Methods on Land Surface Model Spinup and Initialization of WRF Forecasts. *Journal of Hydrometeorology*, **16,** 1135-1154, doi: 10.1175/JHM-D-14-0203.1.

Li, D., E. Bou-Zeid, M. Barlage, F. Chen, and J. A. Smith, 2013: Development and evaluation of a mosaic approach in the WRF-Noah framework. *Journal of Geophysical Research: Atmospheres*, **118,** 11,918-911,935, doi: 10.1002/2013jd020657.

Lobell, D. B., K. G. Cassman, and C. B. Field, 2009: Crop Yield Gaps: Their Importance, Magnitudes, and Causes. *Annual Review of Environment and Resources*, **34,** 179-204, doi: 10.1146/annurev.environ.041008.093740.

Lobell, D. B., M. J. Roberts, W. Schlenker, N. Braun, B. B. Little, R. M. Rejesus, and G. L. Hammer, 2014: Greater Sensitivity to Drought Accompanies Maize Yield Increase in the U.S. Midwest. *Science*, **344,** 516, doi: 10.1126/science.1251423.

Loveland, T. R., B. C. Reed, J. F. Brown, D. O. Ohlen, Z. Zhu, L. Yang, and J. W. Merchant, 2000: Development of a global land cover characteristics database and IGBP DISCover from 1 km AVHRR data. *International Journal of Remote Sensing*, **21,** 1303-1330, doi: 10.1080/014311600210191.

Lu, Y., and L. Kueppers, 2015: Increased heat waves with loss of irrigation in the United States. *Environmental Research Letters*, **10,** 064010, doi: 10.1088/1748-9326/10/6/064010.

Mahmood, R., S. Foster, T. Keeling, K. Hubbard, C. Carlson, and R. Leeper, 2006: Impacts of irrigation on 20th century temperature in the northern Great Plains. *Global and Planetary Change*, **54,** 1-18, doi: 10.1016/j.gloplacha.2005.10.004.

Maupin, M. A., J. F. Kenny, S. S. Hutson, J. K. Lovelace, N. L. Barber, and K. S. Linsey, 2014: Estimated use of water in the United States in 2010. *Circular.* Report 1405, 64 pp.

Mesinger, F., G. DiMego, E. Kalnay, K. Mitchell, P. C. Shafran, and Coauthors, 2006: North American Regional Reanalysis. *Bulletin of the American Meteorological Society*, **87,** 343-360, doi: 10.1175/BAMS-87-3-343.

Miguez-Macho, G., G. L. Stenchikov, and A. Robock, 2005: Regional Climate Simulations over North America: Interaction of Local Processes with Improved Large-Scale Flow. *Journal of Climate*, **18,** 1227-1246, doi: 10.1175/jcli3369.1.

NCEP, 2005. NCEP North American Regional Reanalysis (NARR). Research Data Archive at the National Center for Atmospheric Research, Computational and Information Systems Laboratory. Available online at http://rda.ucar.edu/datasets/ds608.0/.

Niu, G.-Y., Z.-L. Yang, K. E. Mitchell, F. Chen, M. B. Ek, and Coauthors, 2011: The community Noah land surface model with multiparameterization options (Noah-MP): 1. Model description and evaluation with local-scale measurements. *Journal of Geophysical Research: Atmospheres*, **116**, doi: 10.1029/2010jd015139.

Ozdogan, M., M. Rodell, H. K. Beaudoing, and D. L. Toll, 2010: Simulating the Effects of Irrigation over the United States in a Land Surface Model Based on Satellite-Derived Agricultural Data. *Journal of Hydrometeorology*, **11,** 171-184, doi: 10.1175/2009jhm1116.1.

Pei, L., N. Moore, S. Zhong, A. D. Kendall, Z. Gao, and D. W. Hyndman, 2016: Effects of Irrigation on Summer Precipitation over the United States. *Journal of Climate*, **29,** 3541-3558, doi: 10.1175/jcli-d-15-0337.1.

Pielke, R. A., R. Avissar, M. Raupach, A. J. Dolman, X. Zeng, and A. S. Denning, 1998: Interactions between the atmosphere and terrestrial ecosystems: influence on weather and climate. *Global change biology*, **4,** 461-475, doi.

Pielke, R. A., G. Marland, R. A. Betts, T. N. Chase, J. L. Eastman, and Coauthors, 2002: The influence of land-use change and landscape dynamics on the climate system: relevance to climate-change policy beyond the radiative effect of greenhouse gases. *Philosophical Transactions of the Royal Society of London. Series A: Mathematical, Physical and Engineering Sciences*, **360,** 1705, doi.

Qi, S. L., 2009. Digital map of aquifer boundary for the High Plains aquifer in parts of Colorado, Kansas, Nebraska, New Mexico, Oklahoma, South Dakota, Texas, and Wyoming. U.S. Geological Survey. Available online at https://water.usgs.gov/lookup/getspatial?ds543.

Schilling, K. E., M. K. Jha, Y.-K. Zhang, P. W. Gassman, and C. F. Wolter, 2008: Impact of land use and land cover change on the water balance of a large agricultural watershed: Historical effects and future directions. *Water Resources Research*, **44**, doi: 10.1029/2007wr006644.

Seager, R., J. Feldman, N. Lis, M. Ting, A. P. Williams, and Coauthors, 2018: Whither the 100th Meridian? The Once and Future Physical and Human Geography of America's Arid–Humid Divide. Part II: The Meridian Moves East. *Earth Interactions*, **22,** 1-24, doi: 10.1175/ei-d-17-0012.1.

Seth, A., and F. Giorgi, 1998: The Effects of Domain Choice on Summer Precipitation Simulation and Sensitivity in a Regional Climate Model. *Journal of Climate*, **11,** 2698-2712, doi: 10.1175/1520-0442(1998)011<2698:teodco>2.0.co;2.

Smidt, S. J., E. M. K. Haacker, A. D. Kendall, J. M. Deines, L. Pei, and Coauthors, 2016: Complex water management in modern agriculture: Trends in the water-energy-food nexus over the High Plains Aquifer. *Science of the Total Environment*, **566,** 988-1001, doi: https://doi.org/10.1016/j.scitotenv.2016.05.127.

Suyker, A., 2001--a. AmeriFlux US-Ne3 Mead - rainfed maize-soybean rotation site.

——, 2001--b. AmeriFlux US-Ne2 Mead - irrigated maize-soybean rotation site.

T. Musick, J., F. B. Pringle, W. L. Harman, and B. A. Stewart, 1990: Long-Term Irrigation Trends – Texas High Plains. *Applied Engineering in Agriculture*, **6,** 717-724, doi: https://doi.org/10.13031/2013.26454.

Tollenaar, M., J. Fridgen, P. Tyagi, P. W. Stackhouse Jr, and S. Kumudini, 2017: The contribution of solar brightening to the US maize yield trend. *Nature Climate Change*, **7,** 275-278, doi: 10.1038/nclimate3234.

USDA-NASS, 2019, cited 2019: USDA National Agricultural Statistics Service Cropland Data Layer. Available online at https://nassgeodata.gmu.edu/CropScape/.

Walker, W. R., 1989: *Guidelines for designing and evaluating surface irrigation systems.*

Wright, C. K., and M. C. Wimberly, 2013: Recent land use change in the Western Corn Belt threatens grasslands and wetlands. *Proceedings of the National Academy of Sciences*, **110,** 4134, doi.

Yin, J., J. D. Albertson, J. R. Rigby, and A. Porporato, 2015: Land and atmospheric controls on initiation and intensity of moist convection: CAPE dynamics and LCL crossings. *Water Resources Research*, **51,** 8476-8493, doi: 10.1002/2015wr017286.

Zambreski, Z. T., X. Lin, R. M. Aiken, G. J. Kluitenberg, and R. A. Pielke Sr, 2018: Identification of hydroclimate subregions for seasonal drought monitoring in the U.S. Great Plains. *Journal of Hydrology*, **567,** 370-381, doi: https://doi.org/10.1016/j.jhydrol.2018.10.013.

Zhang, T., and X. Lin, 2016: Assessing future drought impacts on yields based on historical irrigation reaction to drought for four major crops in Kansas. *Sci Total Environ*, **550,** 851-860, doi: 10.1016/j.scitotenv.2016.01.181.

Zhang, T., R. Mahmood, X. Lin, and R. A. Pielke, 2019: Irrigation impacts on minimum and maximum surface moist enthalpy in the Central Great Plains of the USA. *Weather and Climate Extremes***,** 100197, doi: https://doi.org/10.1016/j.wace.2019.100197.

Zhang, Y. K., and K. E. Schilling, 2006: Increasing streamflow and baseflow in Mississippi River since the 1940s: Effect of land use change. *Journal of Hydrology*, **324,** 412-422, doi: 10.1016/j.jhydrol.2005.09.033.

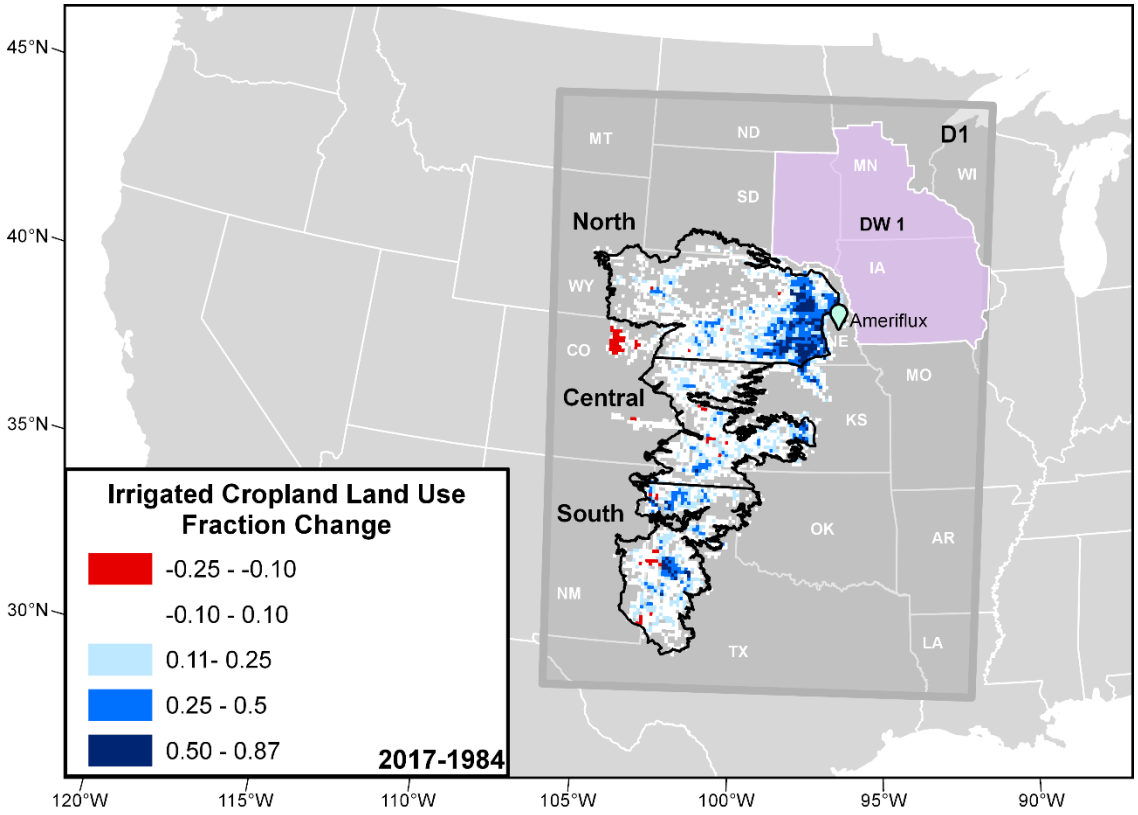

Figure 2.1 The domain (D1) used in the Weather Research and Forecasting (WRF) model v4.0. The Ogallala Aquifer Region (OAR) in the center of the domain (black outline) was divided into three regions: north, central, and south. Colors within the OAR correspond to the change in irrigated cropland land use fraction in WRF simulations between 2017 and 1984 using the High Plains Aquifer annual irrigation maps. The green pin in eastern NE indicates the approximate location of two Ameriflux sites used for model validation. There is one downwind region (DW1) over the upper U.S corn belt used for summary analysis.

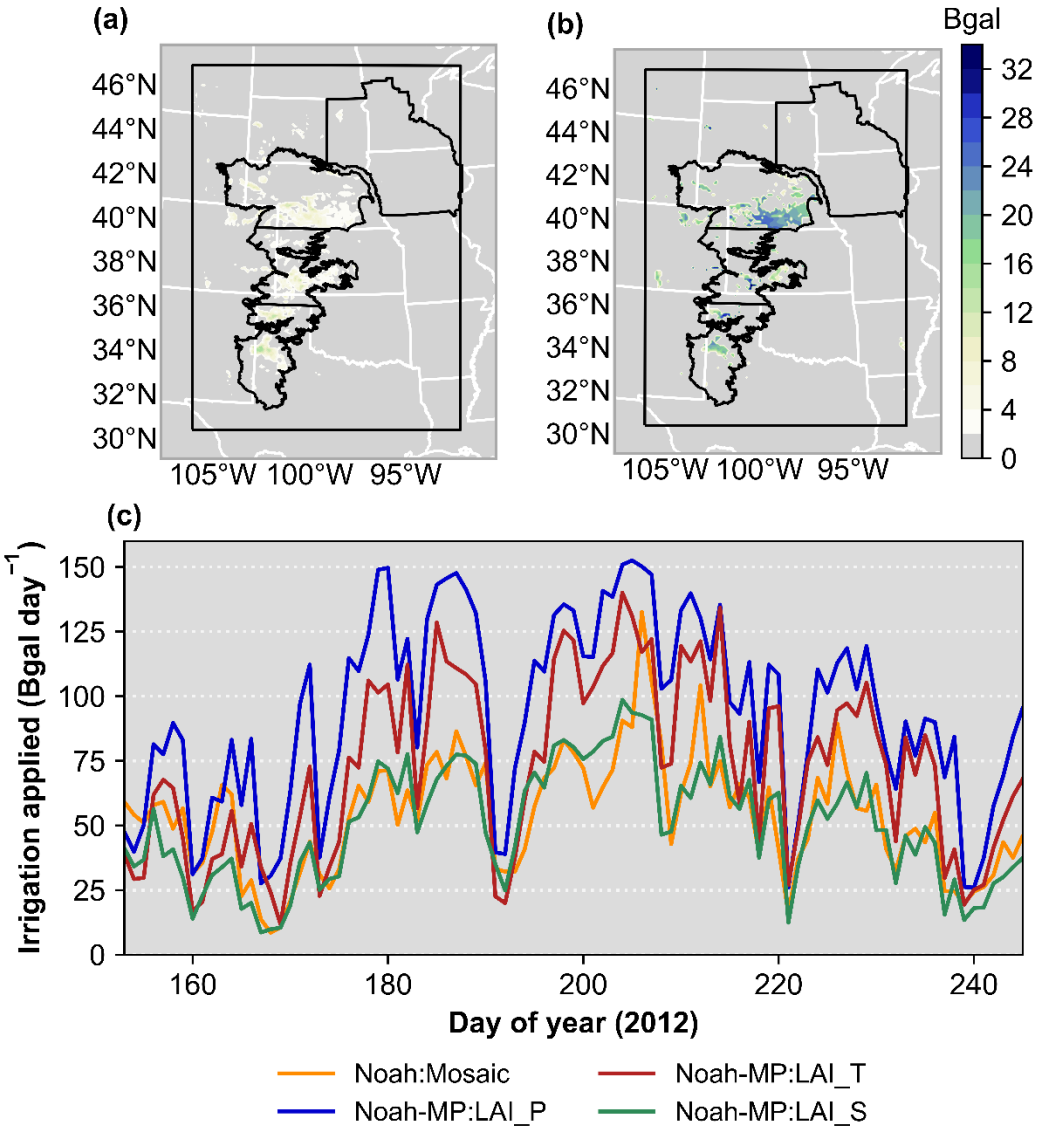
(a)
(b)
Bgal
32
28
24
20
16
12
8
4
0
46°N
44°N
42°N
40°N
38°N
36°N
34°N
32°N
30°N
105°W 100°W 95°W
(c)
Irrigation applied (Bgal day^{-1})
150
125
100
75
50
25
0
160
180
200
220
240
Day of year (2012)
Noah:Mosaic
Noah-MP:LAI_P
Noah-MP:LAI_T
Noah-MP:LAI_S

Figure 2.2 (a) Total amount of irrigation applied in billion gallons (Bgal) from May to Oct during 2012 in WRF using Noah: Mosaic and (b) Noah-MP:LAI_P land surface model configurations. (c) Time series of total daily irrigation applied across the domain from June 1 to Aug 31 for all land surface model configurations used in WRF. Irrigated land use was estimated from MIrAD for 2012. Legend abbreviations: Noah-MP: LAI_P, leaf area index (LAI) dynamically predicted; Noah-MP: LAI_T, LAI interpolated from table; Noah-MP: LAI_S, LAI held constant.

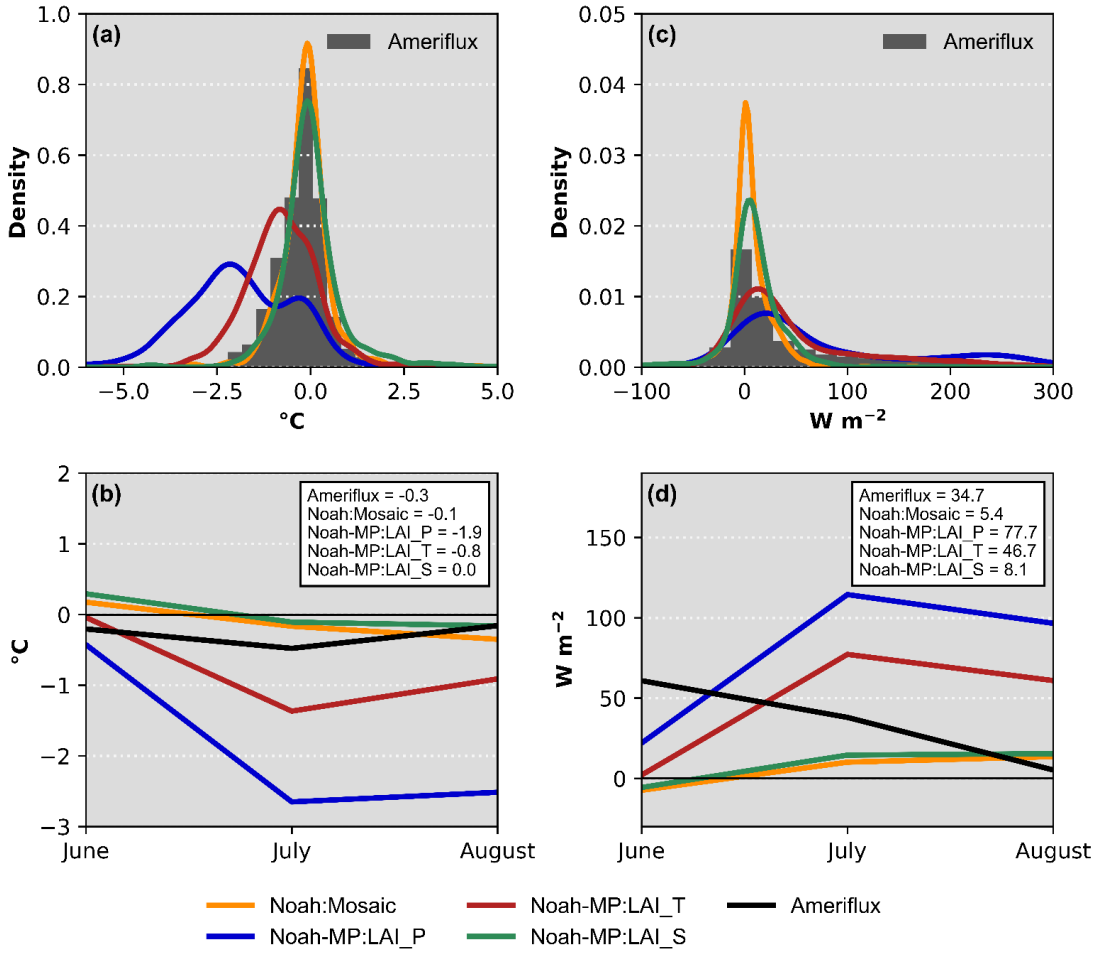

Figure 2.3 (a) Distributions of observed differences in hourly two-meter temperature between irrigated (US-Ne3) and non-irrigated (US-Ne2) Ameriflux sites and modeled irrigated and non-irrigated WRF simulations for the nearest irrigated grid point for all land surface model configurations during the summer of 2012. (b) Monthly averaged temperature differences between irrigated and non-

irrigated Ameriflux sites and WRF simulations in 2012. (c−d) As in (a−b) but for latent heat flux. The nearest irrigated grid point was centered at −96.72°, 41.34°. Legend abbreviations: Noah-MP: LAI_P, leaf area index (LAI) dynamically predicted; Noah-MP: LAI_T, LAI interpolated from table; Noah-MP: LAI_S, LAI held constant.

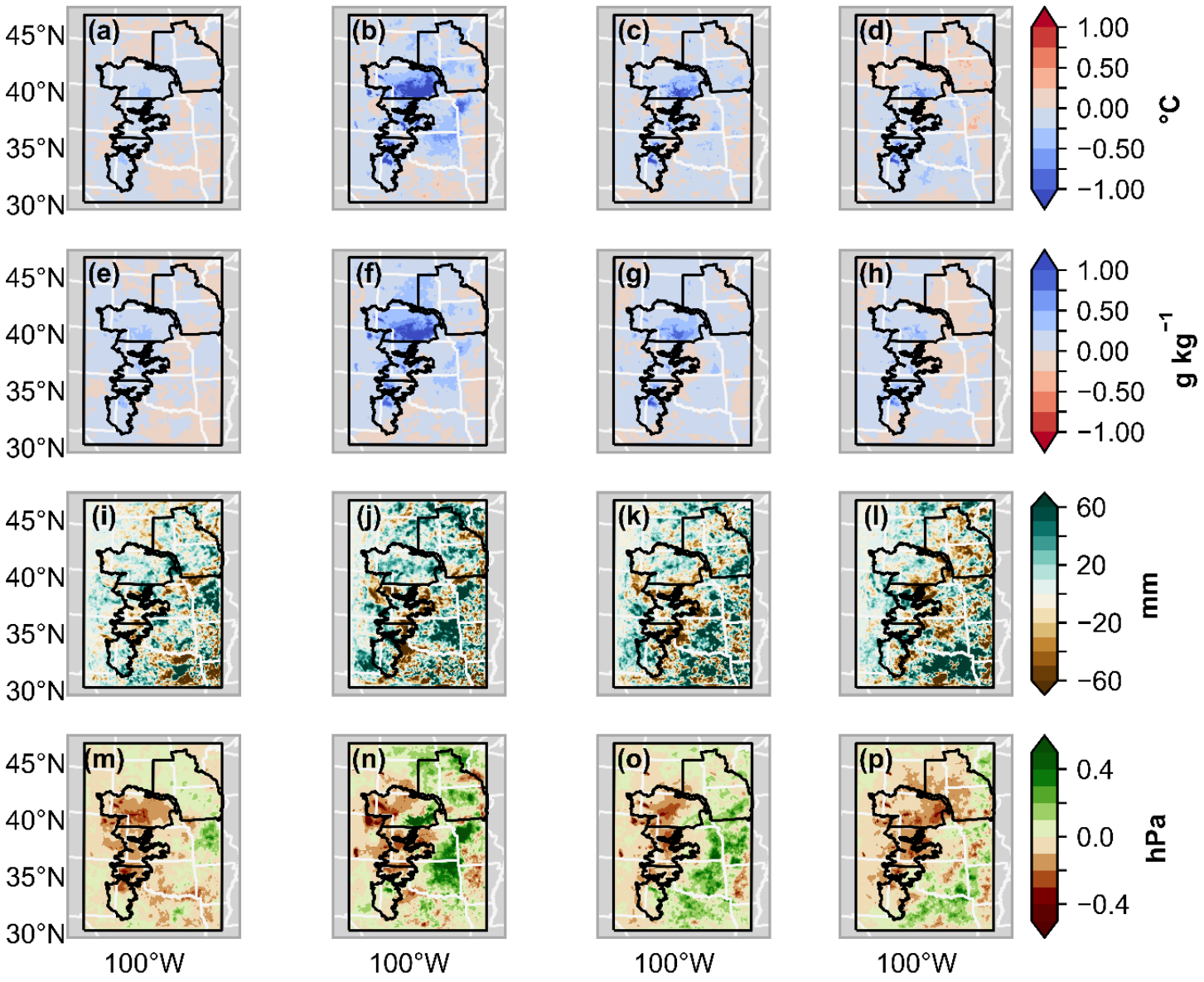
(a)
(b)
(c)
(d)
(e)
(f)
(g)
(h)
(i)
(j)
(k)
(l)
(m)
(n)
(o)
(p)
45°N
40°N
35°N
30°N
100°W
1.00
0.50
0.00
−0.50
−1.00
°C
g kg−1
60
20
−20
−60
mm
0.4
0.0
−0.4
hPa

Figure 2.4 (a−d) Difference in mean two-meter temperature (°C) between the irrigated and non-irrigated WRF simulations during the summer of 2012 for the following four land surface model configurations in order: Noah: Mosaic, Noah-MP: LAI_P, Noah-MP: LAI_T, and Noah-MP: LAI_S. (e−h) As in (a−d) but for two-meter specific humidity (g kg^{-1}). (i−l) As in (a−d) but for accumulated precipitation (mm). (m−p) As in (a−d) but for vapor pressure deficit (hPa). Abbreviations: Noah-MP: LAI_P, leaf area index (LAI) dynamically predicted; Noah-MP: LAI_T, LAI interpolated from table; Noah-MP: LAI_S, LAI held constant.

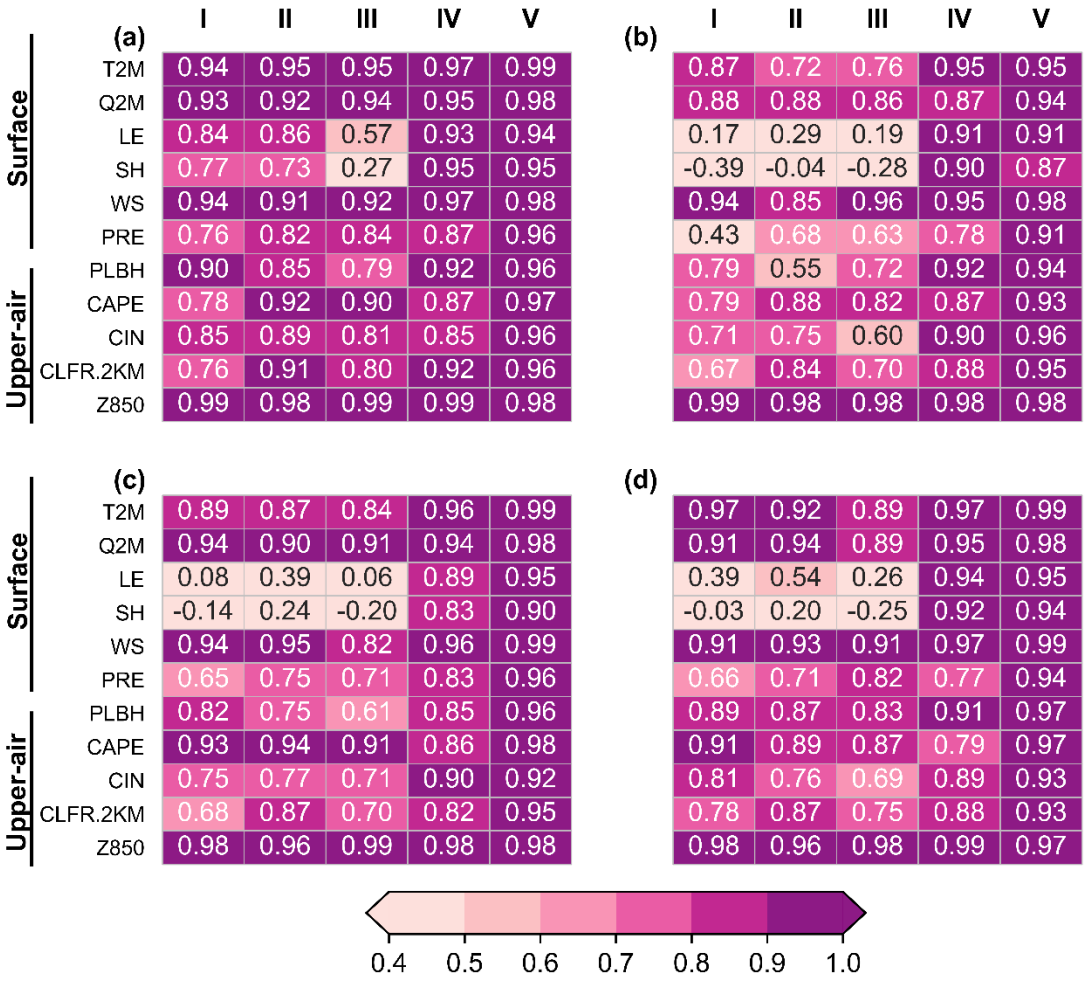

Figure 2.5 (a) Spatial efficiency metric for the irrigated and non-irrigated WRF simulations during 2012 for summer-averaged surface and upper-air variables across the northern (I), central (II), southern (III) Ogallala Aquifer Region, downwind region (IV) and the entire domain (V) for the Noah: Mosaic land surface model WRF configuration. Lower values indicate greater spatial dissimilarity. (b) As in (a) but for the Noah-MP: LAI_P. (c) As in (a) but for Noah-MP: LAI_T. (d) As in (a) but for Noah-MP: LAI_S. Abbreviations: Noah-MP:LAI_P, leaf area index (LAI) dynamically predicted; Noah-MP:LAI_T, LAI interpolated from table; Noah-MP: LAI_S, LAI held constant; T2M, two-meter temperature; Q2M, two-meter specific humidity; LE, latent heat

flux; SH, sensible heat flux; WS, wind speed; PRE, precipitation; PLBH, planetary boundary height; CAPE, convective available potential energy; CIN, convective inhibition; CLFR.2KM, cloud fraction at 2 km above the surface; Z850, geopotential height at 850 hPa.

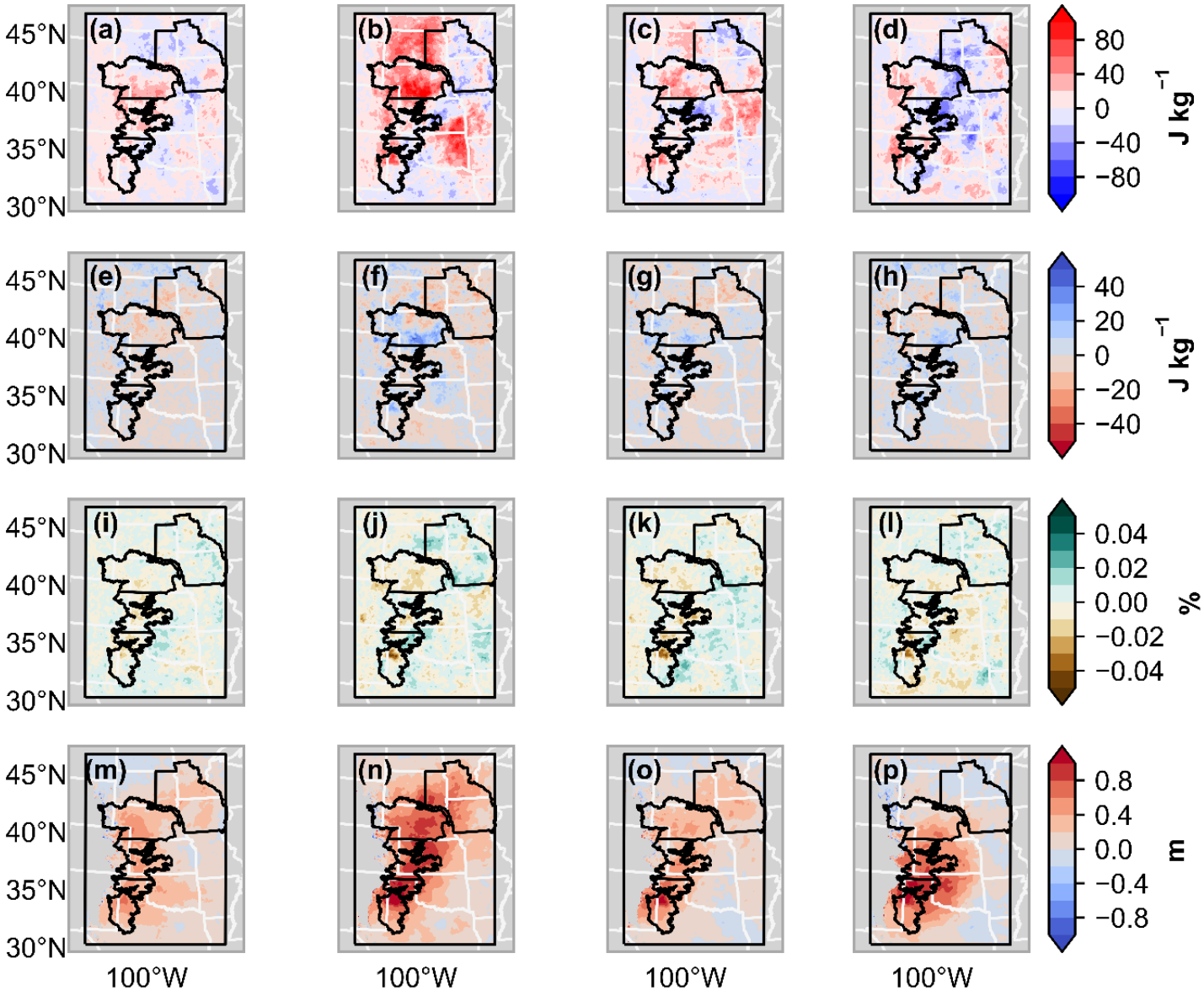
(a)
(b)
(c)
(d)
(e)
(f)
(g)
(h)
(i)
(j)
(k)
(l)
(m)
(n)
(o)
(p)
45°N
40°N
35°N
30°N
100°W
80
40
0
−40
−80
J kg−1
40
20
0
−20
−40
J kg−1
0.04
0.02
0.00
−0.02
−0.04
%
0.8
0.4
0.0
−0.4
−0.8
m

Figure 2.6 (a−d) Difference in mean convective available potential energy (J kg $^{-1}$) between the irrigated and non-irrigated simulations during the summer of 2012 for the following four land surface model configurations in order: Noah: Mosaic, Noah-MP: LAI_P, Noah-MP: LAI_T, and Noah-MP: LAI_S. (e−h) As in (a−d) but for convective inhibition (J kg $^{-1}$). (i−l) As in (a−d) but for cloud fraction at 2 km above the surface (%). (m−p) As in (a−d) but for geopotential height at 850 hPa (m). Abbreviations: Noah-MP: LAI_P, leaf area index (LAI) dynamically predicted; Noah-MP: LAI_T, LAI interpolated from table; Noah-MP: LAI_S, LAI held constant.

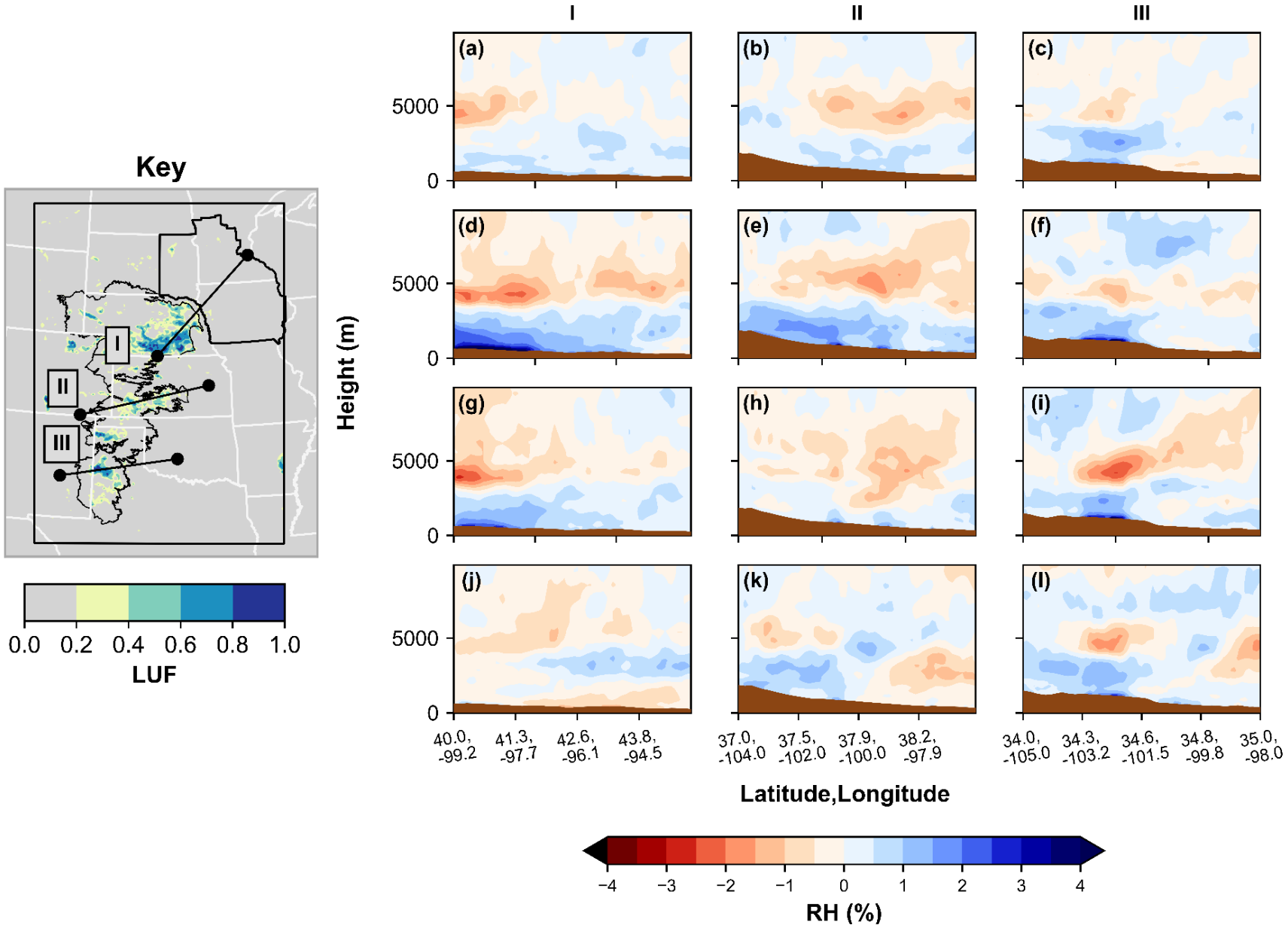
Key
I
II
III
0.0 0.2 0.4 0.6 0.8 1.0
LUF
Height (m)
I
II
III
(a)
(b)
(c)
(d)
(e)
(f)
(g)
(h)
(i)
(j)
(k)
(l)
5000
0
40.0, -99.2
41.3, -97.7
42.6, -96.1
43.8, -94.5
37.0, -104.0
37.5, -102.0
37.9, -100.0
38.2, -97.9
34.0, -105.0
34.3, -103.2
34.6, -101.5
34.8, -99.8
35.0, -98.0
Latitude,Longitude
−4 −3 −2 −1 0 1 2 3 4
RH (%)

Figure 2.7 Vertical cross sections of the difference in relative humidity (RH, %) (right panels) between irrigated and non-irrigated WRF simulations spanning three densely irrigated areas (left panel) of the Ogallala Aquifer Region (OAR) for the following land surface model configurations: Noah: Mosaic (a−c), Noah-MP: LAI_P (d−f), Noah-MP: LAI_T (g−i), and Noah-MP: LAI_S (j−l). The locations of each vertical cross section for the northern (I), central (II), and southern (III) OAR and the irrigated land use fraction (LUF) are provided in the key. Abbreviations: Noah-MP: LAI_P, leaf area index (LAI) dynamically predicted; Noah-MP: LAI_T, LAI interpolated from table; Noah-MP: LAI_S, LAI held constant.

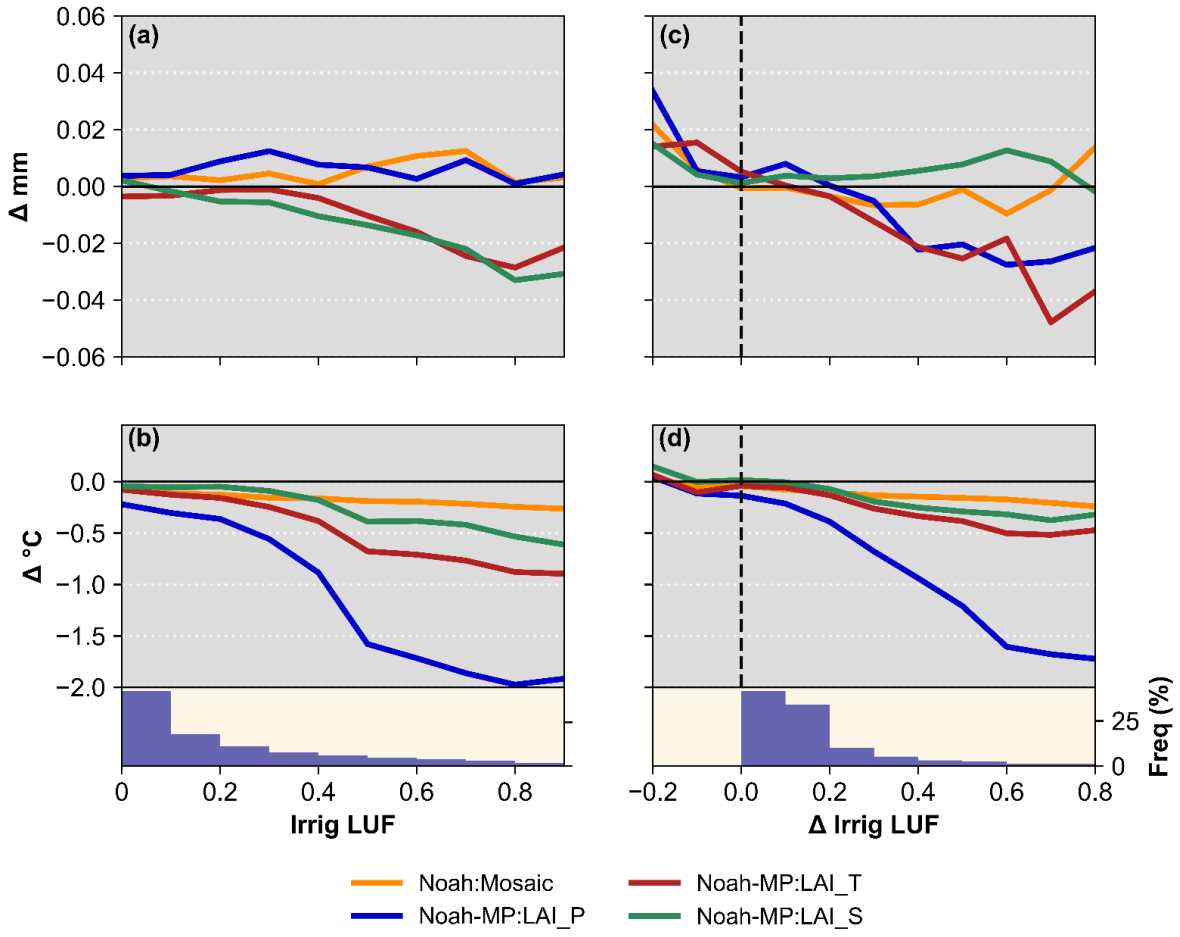

Figure 2.8 (a–b) Difference between irrigated and non-irrigated WRF simulations across the Ogallala Aquifer Region (OAR) for the summer of 2012 for (a) accumulated precipitation and (b) mean temperature, averaged by irrigated land use fraction. Irrigated land use fraction (LUF) is binned in intervals of 0.1. (c–d) Difference between simulations using change irrigated LUF for the OAR in 2017 and 1984 (e.g. 2017 minus 1984) for (c) accumulated precipitation and (d) mean temperature. The frequency (%) in each LUF bin is provided at the bottom of (b) and (d).

Table 2.1 Description of the four land surface model configurations used in this study.

Configuration	Land surface model	Flux simulation	Vegetation scheme	Irrigation (IRR)
Noah: Mosaic	Unified Noah	Mosaic of the 5 largest LU categories	Input LAI (static)	Fraction of grid cell designated as IRR cropland
Noah-MP: LAI_P	Noah-MP	Only for the dominant LU category	Predicted LAI (dynamic)	Entire grid cell designated as IRR cropland (dominant)
Noah-MP: LAI_T	Noah-MP	Same as Noah-MP: LAI_P	Fixed annual LAI cycle (table)	Same as Noah-MP: LAI_P
Noah-MP: LAI_S	Noah-MP	Same as Noah-MP: LAI_P	Input LAI (static)	Same as Noah-MP: LAI_P

Chapter 3 - Modeling the impacts of changes in agronomic practices on climate mitigation in winter wheat production systems in Kansas

Abstract

Improving the resiliency of agriculture to climate change involves innovations in genetics and management practices that help maintain the integrity of the food supply. As an important food security crop, winter wheat experienced abiotic and biotic stresses during its crop season in Kansas over the past several decades. In this study we examined the impacts of climate change, phenological timing, and genetics on Kansas winter wheat yield characteristics from 1973 to 2019 at the county and field-scale using multiple statistical modeling approaches. Results demonstrated that historical trends in killing degree days (KDD), growing degree days (GDD), freezing degree days (FDD), and precipitation have negatively contributed to yield trends across most of the state. However, these negative contributions from climate change have been partially offset by phenology trends of earlier jointing and heading dates. Phenology trends showed the greatest beneficial impact on yield trends in eastern Kansas. In addition, changes in phenology timing may be partially responsible for the increase in yield variance over time. For the varieties tested across the state, there has been an increase toward higher sensitivities of wheat yields to KDDs and FDDs for recently released varieties. In addition, optimal jointing to heading precipitation increased by 18 mm decade^{-1}, suggesting recent varieties have their greatest yield response under higher precipitation regimes. The results of this study indicate that the current trajectory of climate trends may negatively affect yields in the future under current sensitivity levels, emphasizing the need for additional efforts in climate mitigation strategies in both breeding and agronomic programs.

Keywords: winter; wheat; adaptation; mitigation; climate change

1. Introduction

Climate change poses a monumental risk to agricultural production at the regional and global scales during the twenty-first century (Mbow et al. 2019). Agricultural systems have a high vulnerability to climate change due to the direct exposure of field-scale cropping systems to weather events over the course of the growing season. These events can affect productivity steadily over time or abruptly in a single day, ultimately decreasing food availability in local to global markets depending on scale of the event. Global food security, which includes the four pillars of availability, access, utilization, and stability (FAO 2001), will be detrimentally impacted by climate change as a result of an increase in temperatures and weather extremes with the global population expecting to reach 10 billion by 2050 (UNPD 2011). Changes in food availability contribute significantly to changes in the other three pillars, and thus, adaptive and remediation practices in response to climate change will have to be implemented preemptively in order to stabilize or reduce challenges related to global food security. Crop production systems that are resilient to environmental variations are able to sustain their economic, ecological, and social benefits in response to climate change, and they will be crucial in the future for feeding the world population (Challinor et al. 2014; Reddy 2015).

One of the most important crops for meeting future food security goals is wheat, a staple cereal crop that provides 20% of the calories consumed globally (Lobell and Gourdji 2012). Improvements in genetics and management practices over the last century have increased wheat yields, which have helped close the gap between the supply and demand of food (Tadesse et al. 2017). Modern wheat varieties have larger harvest indices (e.g., shorter stems), greater number of kernels per head, better nitrogen use efficiency, allocate more biomass to kernels, and longer

duration of grain filling (Brancourt-Hulmel et al. 2003; Maeoka et al. 2020). In the United States, winter wheat is the most planted variety of wheat, grown in the central and southern Great Plains, lower Midwest, and the Pacific Northwest with Kansas leading production at 1.3 billion bushels in 2019 (USDA 2017). Across most winter wheat production systems, challenges include both abiotic and biotic stressors such as drought and disease (Acevedo et al. 2002; Boyer 1982), availability of fertilizer and pesticide inputs (Tadesse et al. 2017), and yield stagnation (Grassini et al. 2013), which all may be exacerbated by climate change and increasing global population.

Abiotic stressors have been the major drivers of interannual changes in crop productivity across the United States (Jones and Qualset 1984). For winter wheat, the five largest causes of losses for Kansas producers between 1989 and 2018 were drought (1.73 billion), freeze (0.55 billion), hail (0.49 billion), excess precipitation (0.25 billion), and cold winter (0.20 billion) (RMA 2020). Water supply extremes are significant drivers of wheat yield loss as water is critical for proper maintenance of physiological processes related to enzyme activity and photosynthesis (Gupta et al. 2020). In water-limited cropping systems, prolonged precipitation deficits decrease plant available soil moisture, leading to drought stress that triggers the crop to reduce water loss and minimize crop damage. Drought can exhibit differential impacts on production systems depending on genetics, management, and phenological stage. Crop-water demand for winter wheat is lowest during dormancy and has a small peak near emergence and a larger peak near heading and anthesis (Yonts et al. 2009). Over the entire growing season, winter wheat generally requires a cumulative water use between 400 and 600 mm to achieve high productivity (Tang et al. 2018; Yonts et al. 2009). These amounts are close to the annual amounts of precipitation in central and western Kansas, highlighting the enhanced vulnerability

of this region to drought stress for wheat compared to eastern Kansas. On the other hand, excess precipitation may saturate the soil profile, reducing the oxygen content in soil pores and preventing adequate aeration in the root zone. It can also delay or prevent management practices in the field due to mechanical and soil limitations. Prolonged wet weather and high humidity conditions can lead to favorable conditions for biotic stresses such as an increase in pests or diseases or lodging, which negatively impacts yield (Kristensen et al. 2010; McMullen et al. 2012). Over the twentieth century, drought and heavy precipitation events have increased in frequency and intensity in many areas of the U.S., emphasizing the urgency of ag-climate mitigation efforts (Easterling et al. 2017). Improvements in drought tolerance in wheat have focused on gene manipulation, increase in water use efficiency, osmotic adjustments, changes in leaf area, and improvements in management practices such as increasing field residue, which helps retain moisture within the soil profile by reducing soil evaporation and increasing infiltration (Nezhadahmadi et al. 2013).

Temperature is another important environmental variable impacting wheat production. Crop development is strongly determined by air temperature or thermal time, often tracked through the measure of growing degree days (GDDs) (McMaster and Wilhelm 1997). GDDs generally have an optimal crop-specific temperature range with additional GDDs accelerating crop development. However, at lower and upper temperature extremes, cold and heat stress can negatively impact yields during critical crop physiological stages if thresholds are exceeded, which can vary over the wheat's developmental cycle. From planting until dormancy, wheat can withstand lower and upper thresholds of approximately 4 °C and 33 °C, respectively (Porter and Gawith 1999). Wheat that has adequately hardened can withstand temperatures below −20°C

during its dormancy period (Acevedo et al. 2002). In reality, cold injury depends on many factors including the duration of the cold snap, crop genetics, management practices (e.g., till or no-till), and the environment such as presence of snow cover, soil chemistry, or biotic stresses (Fowler and Gusta 1979). After dormancy, the cold stress threshold gradually increases, peaking near 0 °C at anthesis. At this stage, winter wheat is extremely susceptible to freeze damage and exposure to sub-freezing temperatures may be lethal as a result of sterile florets or anthers and embryo death (Frederiks et al. 2008; Marcellos and Single 1984). For heat stress, temperatures above 27 − 31 °C before and around anthesis may induce pollen sterility and reduce grain yield (Acevedo et al. 2002; Wheeler et al. 2009). During grain filling, extreme heat can reduce leaf chlorophyll and lead to premature death of kernel heads (Stone and Nicolas 1995; Wardlaw and Wrigley 1994). Environmental variables that capture the effects of crop-specific heat thresholds have been referred to extreme degree days (Lobell et al. 2013) or killing degree days (KDDs) (Butler et al. 2018) and cold thresholds as freeze degree days (Tack et al. 2015). Furthermore, sustained above normal GDDs during the late winter and early spring may release wheat from dormancy earlier than normal, leaving it susceptible to late season freeze damage, which occurred across large areas of the U.S. in 2007 (Lianhong et al. 2008). This phenomenon is known as a false spring and may increase in frequency as a result of climate change (Kral-O'Brien et al. 2019; Labe et al. 2017). Over the last century, maximum and minimum temperatures have significantly increased during the winter growing season in the Great Plains by up 0.2 °C dec^{-1}, warming at a faster rate than summer growing season temperatures in areas in the central and northern Great Plains (Zambreski et al. 2018). Cold extremes have become less severe over the last century with the northern Great Plains experience the greatest change in the coldest day of year (Vose et al. 2017). Based on climate projections that shown an increase in the

frequency of temperature extremes with a high confidence (Hayhoe et al. 2018; IPCC 2013), negative yield responses resulting from climate change may become more frequent for present-day varieties, warranting additional research in improving management practices that mitigate the effects of climate change and developing freeze and heat resistant varieties (Balla et al. 2019; Kulkarni et al. 2017).

Statistical modeling has frequently been utilized to evaluate the relationships between crop productivity and environmental stresses at the regional and field scales (Butler et al. 2018; Ortiz-Bobea et al. 2019; Tack et al. 2015; Tack et al. 2017; Tollenaar et al. 2017). While researchers may develop their own statistical frameworks and methodologies, the main objective is similar: quantification of yield sensitivities to inter-seasonal environmental variations that can be used to guide climate change adaptation strategies. The relationship between yield variations and environmental sensitivities can vary by regions, crop species, and even varieties, highlighting the importance of crop-specific and regional-scale analysis. Considerable efforts have been given to maize and wheat in the U.S as a result of their economic significance and recognized sensitivities to environmental stresses. Some of the key findings from selected studies are briefly described below.

One study demonstrated that maize in the U.S corn belt has benefitted from an increase in the number of GDDs during its pre-flowering developmental stages and a decrease in the number of KDDs during grain-filling (Butler et al. 2018). Another study suggested that solar brightening contributed significantly to the increase in maize yields since the early 1980s, identifying several factors such as policy changes and a decrease in cloud cover that may have

contributed to the increase in solar brightening (Tollenaar et al. 2017). For winter wheat, one U.S. study found changes in intraseasonal sensitivities to soil moisture and temperature (Ortiz-Bobea et al. 2019), and another found that irrigation was ineffective in reducing sensitivities to drought and extreme heat in the Great Plains (Zhang et al. 2015). At the field scale, GDDs and FDDs with varying seasonal temperature thresholds demonstrated strong ability for prediction of Kansas winter wheat variety trial yields (Tack et al. 2015). The authors also found that genotypic heat resistance has decreased in newer varieties, suggesting that newer varieties may be more susceptible to yield loss in a warmer climate. As new climate challenges emerge and improved varieties are developed, additional statistical analysis with the most current data is pertinent to assess whether newer production systems are more resilient to weather variations than older production systems. In addition, it would be beneficial to have a deeper understanding of the impact of historical climate change and phenology timing on yield trends. Therefore, the objectives in this study were to 1) determine winter wheat yield sensitivities to environmental indicators across phenological stages, 2) quantify the contributions of climate change and phenological timing to winter wheat yields at the county level in Kansas since the 1970s, and 3) estimate changes in wheat variety sensitives to environmental indicators that are major contributors to yield loss in Kansas. This study to our knowledge uses one of the longest records of winter wheat yield at the field-scale in the United States.

2. Materials and methods

2.1 Study area and wheat phenology

The study area includes twelve trial sites and ninety-one counties in Kansas, USA that had sufficient long-term data records. There are nine crop reporting districts in the state, and in this study, counties and trial sites were divided into east, central, and west regions (Fig. 3.1a). In

Kansas, winter wheat planting begins in late September and October, typically emerging 1 – 2 weeks after planting (Kansas Cooperative Extension Service 1997). The gradually lowering of temperatures increases winter hardiness, and little development occurs during the wheat vernalization process for approximately three − eight weeks during the winter. As temperatures warm during the spring and the photoperiod increases, winter wheat emerges from dormancy, and the stem elongates during jointing as the head progresses up the stem. Within days after the main head appears from the flag leaf (heading), anthesis and pollination occur with the number of pollinated flowers determining final kernel number. Afterwards, grain filling of the kernels occurs until physiological maturity, followed by ripening, dry-down, and harvest in June and July. Fundamental understanding of winter wheat phenology is critical for development of the covariates used in the statistical model (section 2.3).

2.2 Data Sources

2.2.1 Winter wheat trials: sites and varieties

Winter wheat variety trials have been recorded since 1954 across Kansas as a result of a cooperative effort between researchers and producers for the systematic evaluation of yield performance under the wide variety of environmental conditions. Data obtained from field trials are based on small test plots with multiple replicates for each variety, and management practices at each location are generally uniform and represent best management practices at the time of the trial. Annual spreadsheets were digitized from 1973 to 2019 into a single database including planting and harvest dates at each location for consistency with USDA-NASS. Each observation contained information on yield, site-location, variety planted, and irrigated or non-irrigated wheat crops. Brand information was also reported in variety trials since the 1980s. Agronomic

data from twelve, non-irrigated sites that reported yields in at least ten years were used in this study (Fig. 3.1a and Table B.1). The sites in eastern Kansas are Powhattan (PW), Manhattan (MA), Ottawa (OT), Parsons (PA), and Belleville (BE). The sites in central Kansas are Hays (HA), Hesston (HE), and Caldwell (CD). The sites in western Kansas are Colby (CO), Tribune (TR), and Garden City (GC). There were several years and locations in which wheat was planted at a site but later abandoned for multiple reasons including but not limited to damage from freezing temperatures, hail, lodging, or a combination of these events. Extreme weather conditions during the growing season can result in complete crop failure or high stand variability, contaminating the trial results and leading to plot abandonment. Based on information provided in the site descriptions, abandonments were subjectively categorized by location and year in Table B.2. Varieties that appeared in less than three years were removed, and the final number of varieties used in this study was 325.

2.2.2 Winter wheat county-level: USDA-NASS

Winter wheat yield information at the county-level was available from 1973 to 2019 for Kansas from the National Agricultural Statistics Service within the United States Department of Agriculture (USDA 2017). Yield was defined as the total production per harvested acre in metric tons per hectare (tons ha^{-1}). Estimates of yield are based on survey information collected by agents from multiple producers in each county. Starting in the 1982 growing season, the USDA began consistently reporting state-level management and phenology progress data for planting, emergence, jointing, heading, and harvest at a weekly frequency. Phenology progress is estimated as the percentage of the state's crop that has reached a phenological stage and is non-decreasing. Because the period of record for state-level winter wheat phenology data provided by

USDA-NASS is highly variable between states, our study had to exclude counties outside of Kansas such as Oklahoma and Texas that would normally be considered as part of the U.S. winter wheat belt. Phenology data was interpolated to daily values to be used in the weighting of environmental covariates (section 2.3).

Counties that did not have at least 25 years of observations or had ten percent of acres under irrigation in the 2012 census were removed from the analysis. Counties with insufficient observations may not satisfactorily sample the interannual climate variability expected for the region, and irrigation may confound the yield sensitivity results by reducing drought or heat sensitivities. In 2018, of the 7.7 million acres of winter wheat planted, only 9.5% were irrigated (USDA 2017). Because of the declining saturated thickness of the aquifer in many areas of western Kansas and the relatively low returns of wheat in global markets, the exclusion of these counties may be an appropriate reflection of management decisions in the future (Fenichel et al. 2016; Haacker et al. 2019). These locations fall within counties in the semi-arid region of southwest Kansas over the Ogallala Aquifer. Based on these criteria, there were 14 counties excluded in this analysis. There were 4080 county-year observations since 1973.

2.2.3 Weather data

For analysis using variety trial data, daily maximum and minimum temperature and precipitation from the nearest Global Historical Climatology Network (GHCN) stations were used to calculate environmental covariates (Menne et al. 2012) (Table B.1). If the number of days with missing weather data during the growing season exceeded 10 %, the corresponding yield-observation for that year was removed from the analysis. In county-scale USDA-NASS

statistical modeling, daily maximum, minimum, and accumulated precipitation were retrieved from 172 GHCN stations in Kansas and the surrounding five states. Each daily variable was interpolated from available stations to each county centroid using Delaunay Triangulation (Voglis and Lagaris 2004). Hourly temperatures were calculated from daily estimates of maximum and minimum temperature following the procedure in Ye et al. (2017), which was shown to have good performance for sites in Kansas.

2.3 Crop-related environmental covariates

Environmental covariates based on weather conditions were derived for four phenological stages: planting to emergence (PT−EM), emergence to jointing (EM−JT), jointing to heading (JT−HD), and heading to harvest (HD−HA). Phenology progress was converted to the fraction of state's crop within each stage by subtracting progress data in successive stages. These daily fractions or weights were multiplied by each covariate with the assumption that weights are applied similarly at each location and day. Because temperature sensitivities and water demand may change over the growing season as a result of phenology, we argue that this approach is more cogent over traditional monthly or seasonal aggregation approaches. Three temperature-based degree-day covariates were computed from hourly temperatures: growing degree days (GDD_{tip}), killing degree days (KDD_{tip}), and freeze degree days (FDD_{tip}) for each year *t*, location *i*, and phenological stage *p* as:

$$GDD_{tip} = \frac{1}{24}\sum_{d=1}^{n} w_{pd} \sum_{h=1}^{24} DD_h \qquad DD_h = \begin{cases} T_h - T_{base} & \text{if } T_{base} < T_h < T_{opt} \\ T_{opt} - T_{base} & \text{if } T_h \geq T_{opt} \\ 0 & \text{if } T_h \leq T_{base} \end{cases} \tag{1}$$

$$\mathrm{KDD}_{tip} = \frac{1}{24}\sum_{d=1}^{n} w_{pd} \sum_{h=1}^{24} \mathrm{DD}_h \qquad \mathrm{DD}_h = \begin{cases} \mathrm{T}_h - \mathrm{T}_{high} & \text{if } \mathrm{T}_h \geq \mathrm{T}_{high} \\ 0 & \text{if } \mathrm{T}_h < \mathrm{T}_{high} \end{cases} \tag{2}$$

$$\mathrm{FDD}_{tip} = \frac{1}{24}\sum_{d=1}^{n} w_{pd} \sum_{h=1}^{24} \mathrm{DD}_h \qquad \mathrm{DD}_h = \begin{cases} \left|\mathrm{T}_h - \mathrm{T}_{freeze}\right| & \text{if } \mathrm{T}_h < \mathrm{T}_{freeze} \\ 0 & \text{if } \mathrm{T}_h \geq \mathrm{T}_{freeze} \end{cases} \tag{3}$$

where DD_h represents degree days for hour h with different specifications for each covariate in Eqs. 1−3, w_{pd} is the weight for phenological stage p at day d, n is the number of days in the year from August 1 to July 31, T_h is the hourly temperature, and T_{base}, T_{opt}, T_{high}, and T_{freeze}, are fixed parameters that bound the upper and lower thresholds for crop development or stress over the growing season (Butler et al. 2018; Lobell et al. 2013; Tack et al. 2015). We evaluated the model performance of multiple thresholds across growth stages for T_{base}, T_{opt}, T_{high}, and T_{freeze}, for USDA-NASS yields but found minimal improvements even though experimental research has shown these stress thresholds evolve over wheat's developmental cycle. In this study T_{base}, T_{opt}, T_{high}, and T_{freeze} were constant at 0, 21, 27, and 0 °C, respectively (Acevedo et al. 2002; McMaster and Wilhelm 1997).

2.4 Statistical modeling

Design matrices for both variety trials and USDA-NASS data were constructed and modeled independently. The two fixed effects statistical models for predicting county (Eq. 4) and trial (Eq. 5) wheat yields were as follows:

$$\sqrt{Y_{it}} = \alpha_i + \beta_1 y_t + f\left(env_{it}; \boldsymbol{\beta}_{\boldsymbol{env}}\right) + \varepsilon_{it} \tag{4}$$

$$\sqrt{Y_{ijt}} = \alpha_i + \alpha_j + \beta_1 y_t + f\left(env_{it}; \boldsymbol{\beta}_{\boldsymbol{env}}\right) + \varepsilon_{ijt} \tag{5}$$

where in Eq. 4 the response Y_{it} is the yield for county i in year t, α_i represents a fixed factor from county, β_1 is the coefficient for the background yield trend over time, y_t is the yield year, $f(env_{it};\boldsymbol{\beta}_{env})$ is a function of environmental covariates with a vector of fixed effect coefficients $\boldsymbol{\beta}_{env}$, and ε_{it} is the random error for each yield observation, which follows a normal distribution with mean 0 and variance σ^2. In Eq. 5, Y_{ijt} is the yield for trial location i and variety j in year t, α_i represents a fixed factor from trial location, α_j represents a fixed factor from wheat variety, and $\beta_1, y_t, f(env_{it};\boldsymbol{\beta}_{env})$, and ε_{ijt} have similar interpretations to the variables in Eq. 4. We found that using the square root of yield instead of the logarithm as the response variable resulted in improved model performance and residual behavior at the extremes, which is important for constructing a statistically robust model. Furthermore, it is important to take into account the underlying data structure when dealing with repeated observations within individual years. Because yield observations are correlated within years, the error terms in Eqs. 4 and 5 are not independently distributed. This dependence structure may overstate the significance of the fixed effects parameters if not taken into account. Thus, we specified the model in Eq. 4 with robust covariance with year as the cluster to account for this correlation structure (Barrios et al. 2012). For Eq. 5, year and variety were used as clusters. This specification does not change coefficient estimates of the fixed effect parameters in linear regression but increases their standard errors. Statistical significance was assessed at a level of 5% for all hypothesis tests in this study.

For the function of environmental covariates, we adapted an approach used by Butler et al. (2018):

$$f(env_{it};\boldsymbol{\beta}_{env}) = \sum_{p=1}^{4} \left[\beta_{2,p}GDD_{tip} + \beta_{3,p}KDD_{tip} + \beta_{4,p}FDD_{tip} + \beta_{5,p}PRC_{tip} + \beta_{6,p}PRC^2{}_{tip}\right] \quad (6)$$

where p represents one of the four phenological stages during year t at county (Eq. 4) or trial location (Eq.5) i, and $\boldsymbol{\beta}_{env}$ is the vector of fixed effects slopes for each environmental covariate. The squared precipitation term (PRC^2) is included to model the non-linear effects of precipitation (PRC). Thus, there are a total of 20 environmental covariates (4 phenological stages × 5 environmental variables) in the full model. The estimates in $\boldsymbol{\beta}_{env}$ can be used to quantify their impacts or sensitives with yield. Large and small values of $f(env_{it};\boldsymbol{\beta}_{env})$ indicate years with favorable and unfavorable climatic conditions for yield response, respectively.

To extend the record of phenology observations before 1982, we fit two-parameter logistic growth models to the daily progress data for each stage and year (1982 −2019) assuming the range of progress values varies between 0 and 1. The parameters for the curve midpoint (e.g., day of year) and growth rate were optimized with the Trust Region Reflective algorithm based on minimizing the residuals (Voglis and Lagaris 2004). Then the relationship between each parameter and moving-window averages of county temperature and accumulated precipitation weighted by annual planting area was modeled using an Elastic Net with ten-fold cross-validation (Zou and Hastie 2005). Multiple windows of varying lengths were evaluated for each parameter and stage given minimal prior knowledge of the temporal relationship was known beforehand. Performance metrics are provided in Table B.3. Trained models were used to make out-of-sample parameter predictions between 1973 to 1981. For the training dataset, statistical model performance was not altered using modeled daily phenology instead of the observed values, indicating the relationship was well fitted by a logistic growth model.

2.5 Evidence of climate mitigation

Yield trends were partitioned into contributions from only climate change and changes in phenology timing at the county level (Butler et al. 2018). To quantify the contribution of yield trends due to only climate change, the fixed effects coefficients $\boldsymbol{\beta}_{\boldsymbol{env}}$ from Eq. 4 were multiplied by the county-level time trends for each environmental covariate using the Thiel-Sen slope, which is robust to outliers, with variable weather conditions each year but phenology weights fixed at daily average values for 1973- 2019. Thus, if an environmental covariate has a negative relationship with yield and the trend over time is positive, this indicates climate change has negatively impacted wheat yields for that covariate. Similarly, contributions to yield trends due to only phenology timing were evaluated by multiplying the coefficients in Eq. 4 by trends calculated from a design matrix with each environmental covariate fixed at its county-level climatological daily values for all years with phenology weights varying each year. Changes in phenology timing that demonstrate a positive yield trend contribution provide evidence that changes have helped mitigate climate impacts at the regional-scale. The combined effects due to both climate change and phenology timing were the summation of both contributions. The overall background trend due to other factors was estimated as the fixed effect coefficient β_1 in Eq. 4. The background trend reflects long-term adaptations producers make to management practices and variety selections based on the prevailing state of knowledge for the region each year.

At the variety level, we adapted a procedure similar to Tack et al. (2015) to quantify temporal trends in variety environmental sensitivities to yield response. A fixed effects model

such as Eqs. 5 assumes that the yield responses to weather are the same across years and varieties. However, breeding programs are developing new varieties with greater yield potential with the goal of increasing tolerance, resistance, or avoidance to heat, cold, and drought stresses. Similarly, disease resistant varieties should demonstrate lower sensitivity under favorable environmental conditions for disease (e.g. wet and humid). It is now common practice for varieties to be rated in their ability to resist these stresses based on trials or under controlled conditions. Based on selected identified significant drivers of yield loss from the fixed effects model in Eq. 5, we fit a linear mixed effects model with random effects (RE) on significant environmental covariates and fixed effects (FE) on all covariates following the form:

$$\sqrt{Y_{rit}} = \left[\alpha_i + \beta_1 y_t + \mathrm{f}(\mathrm{env}_{it}; \boldsymbol{\beta}_{\boldsymbol{env}})\right]_{\mathrm{FE}} + \left[\gamma_{0r} + \gamma_{1r} Z_{rit} + \varepsilon_{rit}\right]_{\mathrm{RE}} \quad (7)$$

where the cluster group is variety release year r, γ_{0r} is a random intercept for each release year, γ_{1r} is a random slope for each release year, Z_{ir} is the environmental covariate selected for random effects, and other terms are as written in Eq. 5. The RE predictors γ_{0r} and γ_1 follow a bivariate normal distribution with mean vector zero and variance-covariance matrix ψ. The random effects parameters ψ and σ^2 were estimated by restricted maximum likelihood using an expected-maximization algorithm with the *statsmodels* library in Python (Lindstrom and Bates 1988; Seabold and Perktold 2010), and γ_{0r} and γ_{1r} are defined as the best linear unbiased predictors. Thus, trends over time in the predictors γ_{1r} can be used to evaluate whether newer varieties are more resilient to environmental variations than older varieties. Release year was defined as the year a variety was first tested in the trial data. Grouping by release year instead of individual varieties resulted in more consistent parameter convergence as a result of larger group sizes. Release years were from 1973 to 2017 to satisfy the three-year replication requirement.

3. Results

3.1 Historical wheat overview

The median yield across all site/county years was 3.1 and 2.3 ton ha^{-1} for variety trials and USDA-NASS, respectively (Fig. 3.1b and Fig. B.1b). This yield potential gap embodies the differences of small-scale variety plots under best management practices and the realities of large-scale on-farm practices and conditions that farmers face each year. The site with the highest and lowest median yields were Belleville (north central) and Caldwell (south central), respectively. From the USDA-NASS data, Brown (northeast) and Elk (southeast) counties had the highest and lowest average yields, respectively. Across all stations, a notable trend in yield by latitude is evident in the boxplots of site yields. Northern site-locations across all regions in Kansas had significantly higher yields than sites in the southern portion of the state, which is significant given that the highest number of planted hectares occurred in south central Kansas. This yield differential closely follows the annual north-south temperature gradient, suggesting the importance of temperature on management and crop development and yields. USDA county yields grouped by agricultural division demonstrate similar behavior. For USDA-NASS yields, the median yield trend was 0.19 ton ha^{-1} $decade^{-1}$ ($p < 0.05$) (Fig. 3.1c). The counties with the largest yield trends were located in east central and northeast Kansas (Fig. 3.1a). An increase in the variance of yields over time is visually evident. The coefficient of variation for early (1973-1995) and recent (1996-2019) periods were 0.23 and 0.26, respectively. For the combined trial yields across sites, the median yield in Kansas has increased by an average of 0.18 ton ha^{-1} $decade^{-1}$ ($p < 0.05$) representing an average gain of 0.85 ton ha^{-1} across the period (Fig. B.1c).

The cause of trial abandonment with the highest frequency was damage from freezing temperatures either during the winter or spring (Table B.2). Based on anecdotal evidence, freeze damage increased the vulnerability to other stressors such as lodging, which ultimately prevented final harvest. Trial locations in western Kansas had the highest frequency of abandonment, followed by sites in eastern Kansas. In eastern Kansas, wet conditions prevented planting and harvest, particularly in recent years. Drought was generally not a reason for complete plot abandonment, excluding Garden City in southwest Kansas, which was abandoned four times between 2011 and 2015. Abandonments need to be taken into account when interpreting results as their impact may be under represented in the model coefficients since yields are missing observations for each occurrence.

3.2 Winter-season climate change

Thirty-day moving county-average GDDs, KDDs, and FDDs weighted by annual planted area across the winter wheat growing season are shown in figure 3.2a. Daily averages are calculated for early (1973 – 1995) and recent (1996 – 2019) periods to illustrate climatic and phenological differences that have occurred over time. To frame the degree-day covariates in phenological context, state-average winter wheat developmental phases for four growth stages are provided in the bottom panel: planting to emergence (PM-EM), emergence to jointing (EM-JT), jointing to heading (JT-HD), and heading to harvest (HD-HA) (Fig. 3.2c). For GDDs, there is an increase of 1 to 3 GDDs is notable during EM-JT in January (Fig. 3.2a). KDDs decreased in September and October after emergence during planting and emergence but increased at peak jointing through early heading and harvest. There is clear evidence of a false spring signal in FDDs, decreasing on average between January and mid-February by 0.5 to 1 FDDs, indicative of

a trend towards warmer winters. During March as winter wheat emerges from dormancy, there is a clear increase in the number of FDDs during the recent period. Thirty-day accumulated precipitation decreased between 10 and 20 mm during EM-JT and JT-HD and (EM-JT and JT-HD) (Fig. 3.2b). However, precipitation increased between 10 and 20 mm during wheat planting and harvest, which may delay or prevent field work in regions such as eastern Kansas which has a negative association with precipitation.

Trends in phenology are notable over the last forty-seven years (Fig. 3.2c). There is a shift in the peak of the planting to emergence distribution towards later in the growing season. However, the actual duration of this stage is lower by two days compared to the earlier period as there is less area under the curve driven by later planting with little change in the distribution of the emergence to jointing (EM-JT) curve between September to middle of October. The EM-JT period has notably decreased from 188 days to 183 days in recent years from slower emergence starting in middle of October in the fall and shift towards earlier dormancy breaking in the spring. The springtime shift is largely driven by producers utilizing early maturing varieties in order to minimize exposure to spring and early summer heat stress and maximize grain filling. The average duration of the JT-HD stage increased from 21 to 22 days. In addition, the lower peak of the distribution of the HD-HA stage for the recent period indicates the duration of grain filling is longer, which contributes to yield gain under favorable environmental conditions. As a whole, the duration of the entire growing season decreased from 271 to 265 days.

3.3 Model performance

The USDA-NASS model (Eq. 4) was able to explain 56% of the total variation in yield, and the root mean square error (RMSE) was 0.14 $\sqrt{\text{ton ha}^{-1}}$, indicating strong model performance at the regional scale (Table 3.1). To ensure the statistical validity of our linear regression results, we examined several model diagnostics for any violations of statistical assumptions. Plots of residuals and fitted values do not demonstrate obvious patterns, and the Q-Q plots of the residuals showed no significant departures from normality (Fig. B.3). Furthermore, the spatial distribution of mean RMSE across all years grouped by county reveals no obvious bias (Fig. B.4a), and performance is significantly better than a baseline model with only county and year fixed effects. Some counties in southeast and western Kansas have slightly lower performance than other counties in the state, suggesting there may be underlying factors not accounted for in the current model. Leave-one-year-out cross validation demonstrated a similar spatial distribution of RMSE for out-of-sample predictions with a small shift toward larger values, indicating the model has minimal overfitting and better performance over a baseline model (Fig. B.4c). The variety trial model was able to explain only 38 % of the total yield variation, indicating a weaker relationship between the current specification of environmental covariates and yield (Table 3.1). Management practices, large variety differences in sensitivities, and field trial abandonments are likely contributing factors to the lower performance compared to the USDA-NASS model. Between the USDA-NASS and variety trial models, the magnitude and sign of the coefficients on each environmental covariate are overall similar with larger standard errors for the variety trial yields (Fig. 3.3a, b).

3.4 Largest drivers of yield loss

At the county level, freezing temperatures during the heading to harvest stage are the largest driver of temperature-based yield loss in Kansas by a significant margin (Fig. 3.3a, $p < 0.001$). For every one FDD during this stage, there is a yield reduction of $0.07 \sqrt{\text{ton ha}^{-1}}$. This period near anthesis is highly sensitive to below freezing temperatures and causes significant damage to the head, reducing dry matter accumulation and even causing crop senescence (Acevedo et al. 2002). Even though the frequency of these events is low given they typically occur in late April and early May, their impact on yield is substantial. The second significant contributor to yield loss is JT-HD KDD ($p < 0.05$), which supports experimental evidence that exposure to heat stress during stem elongation and near anthesis can detrimentally impact processes critical to reproduction. Furthermore, GDDs during PT-EM and EM-JT are statistically significant ($p < 0.05$) and are negatively associated with yield, indicating higher contributions to yields when seasonal temperatures are cooler than normal during the fall and winter, which helps vernalization requirements (Wheeler et al. 2009). For the temperature-based environmental coefficients on variety trials, standard errors were much larger, resulting in no statistically significant coefficients (Fig. 3.3b).

For the USDA-NASS model, the total growing season precipitation that maximized the yield response was 490 mm (Fig. 3.3c), which climatologically occurs in central Kansas. This suggests that precipitation in an average year negatively impacts yield for counties in eastern and southeast Kansas, which receive on average between 600 – 800 mm of precipitation. The sub-humid region of eastern Kansas on average faces more disease pressure under conditions of high humidity and above-normal precipitation than central and western Kansas. In addition, optimal

precipitation varied significantly by growth stage, and there was clear evidence of non-linear behavior, particularly during PT-EM and JT-HD. At planting more than 40 mm negatively impacts yield loss, capturing the effects that excess precipitation can pose challenges for field work or result in uneven stand emergence. Because the duration of EM-JT at the state-level is longer than other stages, the optimal precipitation amount is just over 370 mm. After dormancy, optimal JT-HD precipitation is 83 mm and more than 180 mm decreases model yields. There is a small negative relationship between precipitation and yield response from HD-HA, indicating that less precipitation is generally more beneficial to yields from dry down and harvest. The coefficients on precipitation for EM-JT and JT-HD were statistically significant ($p < 0.001$).

3.5 Climate change has negatively impacted yield

Historical climate trends for KDDs and precipitation aggregated across growth stages have generally negatively impacted yields across most counties (Fig. 3.4). For example, the increase in KDD for counties in southwest and western Kansas have suppressed yield trends between −0.025 and −0.05 $\sqrt{\text{ton ha}^{-1}}$ decade^{-1}, which is the region of Kansas that experiences the highest frequency of KDDs on average (Fig. B4). However, historical trends in FDDs have been slightly favorable for counties in areas of central and southern Kansas, driven primarily by a decrease in FDDs during EM−JT. Trends in precipitation are notably worse for counties in western and south central Kansas due to drier EM-JT and wetter HD-HA (Fig. B.6). The combined climate effects demonstrate that climate trends negatively impact yield between −0.02 and −0.05 $\sqrt{\text{ton ha}^{-1}}$ decade^{-1} with only a few counties in eastern Kansas having neutral climate trends. Counties were climate change is the most detrimental to yield trends are in north central, northwest, west central, and southwest Kansas. These values are close in magnitude to the

background trend (0.06 $\sqrt{\text{ton ha}^{-1}}$ decade^{-1}), indicating that historical climate trends are likely contributing to the observed decreasing rate in yield gains, particularly in western Kansas. This result is noteworthy given the considerable efforts that have been made in breeding programs over the last century. If the current historical climate trends continue in the future, breeders and producers may focus their efforts on varieties and practices that minimize the sensitivities to these climate responses.

3.6 Phenology trends improve GDD exposure but increase vulnerability to late season freeze in northwest Kansas

The effect of phenology timing on GDDs has been beneficial across the entire state, contributing about 0.01 and 0.03 $\sqrt{\text{ton ha}^{-1}}$ decade^{-1} (Fig. 3.4). However, changes in phenology timing on KDD exposure have not significantly contributed to yield trends as a whole. Analyzed by individual phenological stage, only during JT-HD does phenology timing help reduce exposure to KDDs (Fig. B.9). Thus, timing as an avoidance mechanism at the regional-level may not be an ideal approach to mitigate yield loss from KDDs. Tolerance as a mechanism for adaptation may be more appropriate based on the increase in KDDs over time, particularly in southwest Kansas, which counteracts the benefits of shifting to earlier maturing varieties. Furthermore, the earlier shift has increased exposure to yield loss from freezing temperatures for counties in western and northern Kansas, contributing about −0.01 to −0.02 $\sqrt{\text{ton ha}^{-1}}$ decade^{-1} to yield trends. Studies have shown that the use of early maturing varieties increases the freeze risk for wheat in the southern Plains (Lollato et al. 2020). Because freezing temperatures near anthesis are a significant driver of yield loss, breeding programs that are not taking into account this yield sensitivity may be underestimating this risk given the false spring signal in the

historical environmental data. Agronomists may focus on management strategies that help minimize yield loss to sub-freezing temperatures beginning in March and lasting through May. The combined effects across timing and climate have been most beneficial in east central and northeast Kansas, which has historically planted fewer hectares than central and western Kansas. Breeding and management efforts in southeast Kansas should focus on minimizing the negative impact of precipitation trends on yield while efforts in southwest Kansas should focus on GDDs and KDDs as changes in phenology timing have not made a significant contribution to yield improvements.

3.7 Yield variance increases with phenology trends

When weather and phenology vary each year, the most favorable growing seasons based on weather conditions were 1973 in western Kansas and 1998 in central and eastern Kansas (Fig. 3.5a). These two years had relatively low FDDs, GDDs, and KDDs, and timely precipitation from emergence to heading (Figs. B.10 – B.13). For years with the most unfavorable weather conditions, there was more spatial variability in the growing seasons with the lowest yield response (Fig. 3.5b). For example, 1989, a severely dry growing season, was the worst for counties in central Kansas while counties in south central and southeast Kansas varied among 2006, 2014, 2018, or 2019, which occurred in the last 13 years. Fixing phenology weights at average values slightly altered the spatial distributions with more counties in southeast Kansas indicating that 2019 produced the most unfavorable weather conditions (Fig. 3.5c, d). Subtracting the yield response between varying weather and phenology and fixed phenology in the most favorable years demonstrated that yields improved in all counties due to changes in phenology timing (Fig. 3.5e, f). The largest gains were in central, east central, and southeast

Kansas (Fig. 3.5e). However, the yield response in the most unfavorable growing seasons decreased across counties with two significantly worse regions: counties in eastern Kansas and far northwest Kansas. These results suggest as a state phenology timing trends have contributed to an increase in yield variance as yields during the most favorable years increased, and the yields in the most unfavorable years decreased. Ideally, changes in phenological timing would increase the mean of the yield distribution without changing or increasing the variance. This result in combination with the negative impacts from climate change helps explain the observed increase in yield variance and presents new challenges given the increased susceptibility to yield loss when weather conditions are not ideal.

3.8 Newer varieties have larger spring water demands and higher sensitivities to KDD and FDDs

Focusing on the main environmental drivers of yield variability during JT-HD (e.g. spring), we hypothesized that environmental sensitivities that demonstrated a negative relationship with yield have remained constant or decreased in magnitude for recent variety release years. However, we found that yield sensitives to KDDs have increased in recently released varieties, indicating less heat resistance after breaking dormancy and before anthesis, which is consistent with findings from Tack et al. (2015) (Fig. 3.6a). These results also explain the high standard errors in fixed effects model coefficients as varieties grouped by year vary widely in their sensitivity at the field-scale. For example, varieties released before 2000 demonstrated limited or no effect in western and central Kansas. The negative impact on yield of KDD has been increasing since approximately 2005 at an increasing rate. A similar pattern was found for JT-HD FDDs with an increasing sensitivity in recently released varieties for all regions

combined (Fig. 3.6b). Notably, varieties grown in eastern Kansas demonstrated a variable, non-linear response and larger sensitivities to yield loss from FDDs than the other regions. These results indicate temperature sensitivities for varieties in Kansas have become more sensitive to heat and cold stress after breaking dormancy with variations across different regions. Larger sensitivities in magnitude also indicate the potential for higher variance in yields.

For drought stress, we focus on optimal JT-HD precipitation given it was statistically significant in the fixed effects model. The relationship between optimal yield response and variety release year in Kansas suggests increased water demand for newer varieties, particularly in central Kansas (Fig. 3.6c). Across all regions, water demand has increased by about 18 mm decade^{-1}, indicating that newer varieties on average have an optimal yield response under higher precipitation regimes during the spring. However, optimal precipitation requirements for varieties tested in western Kansas have stayed relatively constant at approximately 67 mm, indicating little change in water demand for peak yield response. While varieties in eastern Kansas demonstrated an optimal precipitation of 0 mm for earlier release years, which is evidence of the negative association with precipitation in this sub-humid environment due to underlying factors such as disease, there is a trend towards optimal precipitation greater than 0 mm in recent years. Given that eastern Kansas is generally not a water-limited environment, this suggests additional resiliency as variety tolerance from disease or other factors has improved under higher precipitation regimes.

4. Summary and conclusions

Winter wheat yields in Kansas have increased since the early 1970s with the largest yield trends observed in central and eastern Kansas (up to 0.4 ton ha^{-1} $decade^{-1}$), but there has been an increase in yield variance over time. There is evidence of a decrease in FDDs during the winter and an increase in early spring after wheat begins jointing, indicating the frequency of false springs increased in recent years. Historical changes in climate during the winter growing season are not temporally uniform, emphasizing the importance of applying time-specific management decisions for different periods of the growing season. Furthermore, the duration of planting to emergence and emergence to jointing has decreased while jointing to heading and heading to harvest have increased. Jointing and heading have begun earlier in recent years as a result of shift towards earlier maturing varieties. The combination of changes in climate and phenology timing have altered the temporal distribution of exposure to heat, cold, and drought stresses.

We developed a statistical framework based on critical stages of wheat phenology for identification of the significant weather-based drivers of yield loss or gain for both regional and field scales. At the regional-scale, the largest temperature-based drivers of yield loss were freeze degree days from heading to harvest and killing degree days from jointing to heading. Optimal accumulated precipitation amounts across the growing season was approximately 490 mm with emergence to heading the most critical for yield gain or loss. The association between environmental drivers and yield was not as strong for variety trials compared to USDA-NASS county level yields. Based on the identified relationships between weather and wheat yields, historical climate trends have severely impacted yield trends across the state with the most negative trends for counties in western Kansas. Changes in phenology timing have improved

yield trends from GDDs across the state but increased the risk of FDDs for counties in western and northwest Kansas. Surprisingly, in comparison to FDDs and GDDs, phenology timing has only marginally helped improved yields by minimizing exposure to KDDs. Across all environmental covariates, phenology timing has helped increased yields the most in south central and eastern Kansas, indicating that phenology timing as a form of climate mitigation has helped offset some of the impacts of climate change. However, we also used the framework to demonstrate that changes in phenology timing have contributed to an increase in yield variance, leaving yields vulnerable to greater yield loss in unfavorable climatic growing seasons. Mixed effects modeling at the variety level demonstrated increasing sensitivity to KDDs and FDDs during JT-HD and increase in water demand for optimal yield response in newer varieties.

Some potential drawbacks of using progress data on a state-wide level are the regional differences in phenology that occur during the growing season. Planting dates occur earlier in northwest Kansas than southeast Kansas, and in the spring, varieties in northern Kansas usually reach phenological stages at later dates than southern Kansas due to the seasonal temperature gradient, which may, for example, over emphasize yield loss from freezing temperatures if progress is slower than what the USDA-NASS reports. Future research that could disaggregate progress data by agricultural district or incorporate deterministic modeling may improve model performance and reduce the variability of parameter estimates. In addition, this study did not consider changes in federal or state policy that may have contributed to changes in agronomic practices over time that influenced either the trends or variance in wheat yields.

We highlight in this chapter some of the drawbacks associated with wheat breaking dormancy earlier in the spring. Earlier heading dates increase the potential of yield loss from FDDs in northwest Kansas, which may outweigh the yield benefits of more favorable GDDs for this region. Historical climate trends towards lower frequencies of FDDs only marginally cancel out the effects of phenology timing in northwest and west central Kansas. Breeders should be aware that spring FDDs will not likely disappear for the foreseeable future, even under climate change. Warmer winters may further increase the frequency of false springs, increasing the risk of yield loss if varieties cannot adapt. The increasing trend in spring KDDs outweighs the beneficial impact of moving to earlier jointing and heading dates, suggesting that tolerance or resistance may be a better mechanism for heat resistance than avoidance. However, recently released varieties have demonstrated a larger negative yield response to KDDs and FDDs in the spring, suggesting that newer varieties may be less resilient to springtime temperature extremes. The need to find balance between improving the resiliency of wheat to abiotic stress such as heat and drought and maintaining high yields will be challenging and critical for breeding and agronomy programs in the future under climate change.

References

Acevedo, E., P. Silva, and H. Silva, 2002: *Wheat growth and physiology.* Bread Wheat, Improvement and Production. Vol. 30.

Balla, K., I. Karsai, P. Bónis, T. Kiss, Z. Berki, and Coauthors, 2019: Heat stress responses in a large set of winter wheat cultivars (Triticum aestivum L.) depend on the timing and duration of stress. *PLOS ONE*, **14,** e0222639, doi: 10.1371/journal.pone.0222639.

Barrios, T., R. Diamond, G. W. Imbens, and M. Kolesár, 2012: Clustering, Spatial Correlations, and Randomization Inference. *Journal of the American Statistical Association*, **107,** 578-591, doi: 10.3386/w15760.

Boyer, J. S., 1982: Plant productivity and environment. *Science*, **218,** 443-448, doi: 10.1126/science.218.4571.443.

Brancourt-Hulmel, M., G. Doussinault, C. Lecomte, P. Bérard, B. Le Buanec, and M. Trottet, 2003: Genetic Improvement of Agronomic Traits of Winter Wheat Cultivars Released in France from 1946 to 1992. *Crop Science*, **43,** 37-45, doi: 10.2135/cropsci2003.3700.

Butler, E. E., N. D. Mueller, and P. Huybers, 2018: Peculiarly pleasant weather for US maize. *Proceedings of the National Academy of Sciences*, **115,** 11935, doi: 10.1073/pnas.1808035115.

Challinor, A. J., J. Watson, D. B. Lobell, S. M. Howden, D. R. Smith, and N. Chhetri, 2014: A meta-analysis of crop yield under climate change and adaptation. *Nature Climate Change*, **4,** 287-291, doi: 10.1038/nclimate2153.

Easterling, D. R., K.E. Kunkel, J.R. Arnold, T. Knutson, A.N. LeGrande, and Coauthors, 2017: Precipitation change in the United States. *Climate Science Special Report: Fourth*

National Climate Assessment, Volume I U.S. Global Change Research Program, 207-230 pp.

FAO, 2001: Undernourishment around the world. *Food Insecurity in the World 2001* Food and Agriculture Organization of the United Nations, 8-11 pp.

Fenichel, E. P., J. K. Abbott, J. Bayham, W. Boone, E. M. K. Haacker, and L. Pfeiffer, 2016: Measuring the value of groundwater and other forms of natural capital. *Proceedings of the National Academy of Sciences*, **113,** 2382-2387, doi: https://doi.org/10.1073/pnas.1513779113.

Fowler, D., and L. Gusta, 1979: Selection for Winterhardiness in Wheat. I. Identification of Genotypic Variability 1. *Crop Science*, **19,** 769-772, doi: 10.2135/cropsci1979.0011183X001900060005x.

Frederiks, T., J. Christopher, and A. Borrell, 2008: Low temperature adaption of wheat post head-emergence in northern Australia. *Proceedings of the 11th International Wheat Genetics Symposium*.

Grassini, P., K. M. Eskridge, and K. G. Cassman, 2013: Distinguishing between yield advances and yield plateaus in historical crop production trends. *Nature Communications*, **4,** 2918, doi: 10.1038/ncomms3918.

Gupta, A., A. Rico-Medina, and A. I. Caño-Delgado, 2020: The physiology of plant responses to drought. *Science*, **368,** 266, doi: 10.1126/science.aaz7614.

Haacker, E. M. K., K. A. Cotterman, S. J. Smidt, A. D. Kendall, and D. W. Hyndman, 2019: Effects of management areas, drought, and commodity prices on groundwater decline patterns across the High Plains Aquifer. *Agricultural Water Management*, **218,** 259-273, doi: 10.1016/j.agwat.2019.04.002.

Hayhoe, K., D.J. Wuebbles, D.R. Easterling, D.W. Fahey, S. Doherty, and Coauthors, 2018: Our Changing Climate. *Impacts, Risks, and Adaptation in the United States: Fourth National Climate Assessment.* U.S. Global Change Research Program, 72-144 pp.

IPCC, 2013: Summary for Policymakers. *Climate Change 2013: The Physical Science Basis. Contribution of Working Group I to the Fifth Assessment Report of the Intergovernmental Panel on Climate Change.* Cambridge University Press, 1-30 pp.

Jones, R. A., and C. O. Qualset, 1984: Breeding crops for environmental stress tolerance. *Applications of genetic engineering to crop improvement*, Springer, 305-340.

Kansas Cooperative Extension Service, 1997: Wheat production handbook. Available online at https://bookstore.ksre.ksu.edu/Item.aspx?catId=299&pubId=128.

Kral-O'Brien, K. C., P. L. O'Brien, and J. P. Harmon, 2019: Need for False Spring Research in the Northern Great Plains, USA. *Agricultural & Environmental Letters*, **4,** 190025, doi: 10.2134/ael2019.07.0025.

Kristensen, K., K. Schelde, and J. E. Olesen, 2010: Winter wheat yield response to climate variability in Denmark. *The Journal of Agricultural Science*, **149,** 33-47, doi: 10.1017/S0021859610000675.

Kulkarni, M., R. Soolanayakanahally, S. Ogawa, Y. Uga, M. G. Selvaraj, and S. Kagale, 2017: Drought Response in Wheat: Key Genes and Regulatory Mechanisms Controlling Root System Architecture and Transpiration Efficiency. *Front Chem*, **5,** 106-106, doi: 10.3389/fchem.2017.00106.

Labe, Z., T. Ault, and R. Zurita-Milla, 2017: Identifying anomalously early spring onsets in the CESM large ensemble project. *Climate Dynamics*, **48,** 3949-3966, doi: 10.1007/s00382-016-3313-2.

Lianhong, G., J. H. Paul, W. M. Post, P. K. Dale, Y. Bai, and Coauthors, 2008: The 2007 Eastern US Spring Freeze: Increased Cold Damage in a Warming World. *BioScience*, **58,** 253-262, doi: 10.1641/B580311.

Lindstrom, M. J., and D. M. Bates, 1988: Newton-Raphson and EM Algorithms for Linear Mixed-Effects Models for Repeated-Measures Data. *Journal of the American Statistical Association*, **83,** 1014-1022, doi: 10.2307/2290128.

Lobell, D. B., and S. M. Gourdji, 2012: The Influence of Climate Change on Global Crop Productivity. *Plant Physiology*, **160,** 1686, doi: 10.1104/pp.112.208298.

Lobell, D. B., G. L. Hammer, G. McLean, C. Messina, M. J. Roberts, and W. Schlenker, 2013: The critical role of extreme heat for maize production in the United States. *Nature Climate Change*, **3,** 497-501, doi: 10.1038/nclimate1832.

Lollato, R. P., G. P. Bavia, V. Perin, M. Knapp, E. A. Santos, A. Patrignani, and E. D. DeWolf, 2020: Climate-risk assessment for winter wheat using long-term weather data. *Agronomy Journal*, **112,** 2132-2151, doi: 10.1002/agj2.20168.

Maeoka, R. E., V. O. Sadras, I. A. Ciampitti, D. R. Diaz, A. K. Fritz, and R. P. Lollato, 2020: Changes in the Phenotype of Winter Wheat Varieties Released Between 1920 and 2016 in Response to In-Furrow Fertilizer: Biomass Allocation, Yield, and Grain Protein Concentration. *Frontiers in Plant Science*, **10**, doi: 10.3389/fpls.2019.01786.

Marcellos, H., and W. Single, 1984: Frost injury in wheat ears after ear emergence. *Functional Plant Biology*, **11,** 7-15, doi: 10.1071/PP9840007.

Mbow, C., C. Rosenzweig, L.G. Barioni, T.G. Benton, M. Herrero, and Coauthors, 2019: Food Security. *Climate Change and Land: an IPCC special report on climate change,*

desertification, land degradation, sustainable land management, food security, and greenhouse gas fluxes in terrestrial ecosystems. 437-550 pp.

McMaster, G. S., and W. W. Wilhelm, 1997: Growing degree-days: one equation, two interpretations. *Agricultural and Forest Meteorology*, **87,** 291-300, doi: https://doi.org/10.1016/S0168-1923(97)00027-0.

McMullen, M., G. Bergstrom, E. De Wolf, R. Dill-Macky, D. Hershman, G. Shaner, and D. Van Sanford, 2012: A Unified Effort to Fight an Enemy of Wheat and Barley: Fusarium Head Blight. *Plant Disease*, **96,** 1712-1728, doi: 10.1094/PDIS-03-12-0291-FE.

Menne, M. J., I. Durre, R. S. Vose, B. E. Gleason, and T. G. Houston, 2012: An Overview of the Global Historical Climatology Network-Daily Database. *Journal of Atmospheric and Oceanic Technology*, **29,** 897-910, doi: 10.1175/JTECH-D-11-00103.1.

Nezhadahmadi, A., Z. H. Prodhan, and G. Faruq, 2013: Drought Tolerance in Wheat. *The Scientific World Journal*, **2013,** 610721, doi: 10.1155/2013/610721.

Ortiz-Bobea, A., H. Wang, C. M. Carrillo, and T. R. Ault, 2019: Unpacking the climatic drivers of US agricultural yields. *Environmental Research Letters*, **14,** 064003, doi: 10.1088/1748-9326/ab1e75.

Porter, J. R., and M. Gawith, 1999: Temperatures and the growth and development of wheat: a review. *European Journal of Agronomy*, **10,** 23-36, doi: https://doi.org/10.1016/S1161-0301(98)00047-1.

Reddy, P. P., 2015: Introduction. *Climate Resilient Agriculture for Ensuring Food Security*, P. P. Reddy, Ed., Springer India, 1-15.

RMA, 2020. AgRisk Viewer. USDA Southwest Climate Hub. Available online at https://swclimatehub.info/rma/rma-data-viewer.html. Accessed March 10, 2020.

Seabold, S., and J. Perktold, 2010: Statsmodels: Econometric and statistical modeling with python. *Proceedings of the 9th Python in Science Conference*, Austin, TX, 61.

Stone, P., and M. Nicolas, 1995: A survey of the effects of high temperature during grain filling on yield and quality of 75 wheat cultivars. *Australian journal of agricultural research*, **46,** 475-492, doi: 10.1071/AR9950475.

Tack, J., A. Barkley, and L. L. Nalley, 2015: Effect of warming temperatures on US wheat yields. *Proc Natl Acad Sci U S A*, **112,** 6931-6936, doi: 10.1073/pnas.1415181112.

Tack, J., J. Lingenfelser, and S. V. K. Jagadish, 2017: Disaggregating sorghum yield reductions under warming scenarios exposes narrow genetic diversity in US breeding programs. *Proceedings of the National Academy of Sciences*, **114,** 9296, doi: 10.1073/pnas.1706383114.

Tadesse, W., H. Halila, M. Jamal, S. El hanafi, S. Assefa, T. Oweis, and M. Baum, 2017: Role of Sustainable Wheat Production to Ensure Food Security in the CWANA region. *Journal of Experimental Biology and Agricultural Sciences*, **5,** 15-32, doi: 10.18006/2017.5(Spl-1-SAFSAW).S15.S32.

Tang, X., N. Song, Z. Chen, J. Wang, and J. He, 2018: Estimating the potential yield and ETc of winter wheat across Huang-Huai-Hai Plain in the future with the modified DSSAT model. *Scientific Reports*, **8,** 15370, doi: 10.1038/s41598-018-32980-4.

Tollenaar, M., J. Fridgen, P. Tyagi, P. W. Stackhouse Jr, and S. Kumudini, 2017: The contribution of solar brightening to the US maize yield trend. *Nature Climate Change*, **7,** 275-278, doi: 10.1038/nclimate3234.

UNPD, 2011: World population prospects: the 2010 revision. United Nations Population Division New York, NY.

USDA, 2017. NASS - Quick Stats. USDA National Agricultural Statistics Service. Available online at https://quickstats.nass.usda.gov/. Accessed January 10, 2020.

Voglis, C., and I. Lagaris, 2004: A rectangular trust region dogleg approach for unconstrained and bound constrained nonlinear optimization. *WSEAS International Conference on Applied Mathematics*, 7.

Vose, R. S., D.R. Easterling, K.E. Kunkel, A.N. LeGrande, and M. F. Wehner, 2017: Temperature Changes in the United States. *Climate Science Special Report: Fourth National Climate Assessment, Volume I* U.S. Global Change Research Program, 185-206 pp.

Wardlaw, I., and C. Wrigley, 1994: Heat tolerance in temperate cereals: an overview. *Functional Plant Biology*, **21,** 695-703, doi: 10.1071/pp9940695.

Wheeler, T. R., G. R. Batts, R. H. Ellis, P. Hadley, and J. I. L. Morison, 2009: Growth and yield of winter wheat (Triticum aestivum) crops in response to CO2 and temperature. *The Journal of Agricultural Science*, **127,** 37-48, doi: 10.1017/S0021859600077352.

Ye, Q., X. Lin, E. Adee, D. Min, Y. Assefa Mulisa, D. O'Brien, and I. A. Ciampitti, 2017: Evaluation of climatic variables as yield-limiting factors for maize in Kansas. *International Journal of Climatology*, **37,** 464-475, doi: 10.1002/joc.5015.

Yonts, C. D., D. J. Lyon, J. A. Smith, R. M. Harveson, G. W. Hergert, G. L. Hein, and D. K. Santra, 2009: Producing Irrigated Winter Wheat.

Zambreski, Z. T., X. Lin, R. M. Aiken, G. J. Kluitenberg, and R. A. Pielke Sr, 2018: Identification of hydroclimate subregions for seasonal drought monitoring in the U.S. Great Plains. *Journal of Hydrology*, **567,** 370-381, doi: https://doi.org/10.1016/j.jhydrol.2018.10.013.

Zhang, T., X. Lin, and G. F. Sassenrath, 2015: Current irrigation practices in the central United States reduce drought and extreme heat impacts for maize and soybean, but not for wheat. *Sci Total Environ*, **508,** 331-342, doi: 10.1016/j.scitotenv.2014.12.004.

Zou, H., and T. Hastie, 2005: Regularization and variable selection via the elastic net. *Journal of the Royal Statistical Society: Series B (Statistical Methodology)*, **67,** 301-320, doi: 10.1111/j.1467-9868.2005.00503.x.

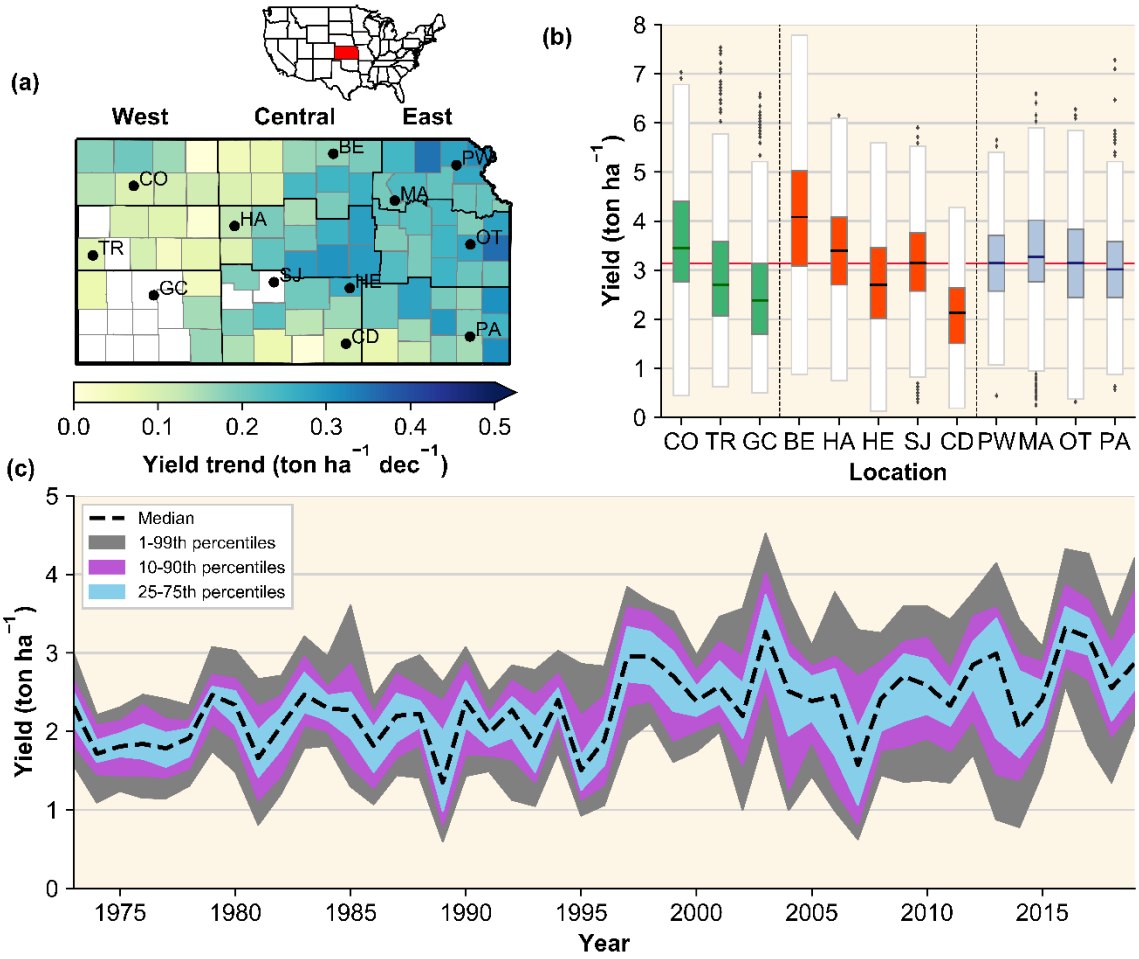

Figure 3.1 (a) Locations of 12 dryland winter wheat variety trials and 91 counties in Kansas, U.S. included in this study. White counties are not included in this study due to irrigation. Observed USDA-NASS county-level yield trends (ton ha $^{-1}$ dec $^{-1}$) between 1973 and 2019 are shaded. (b) Box plots of yield by variety trial location. (c) Time series of combined county USDA-NASS yield statistics between 1973 and 2019.

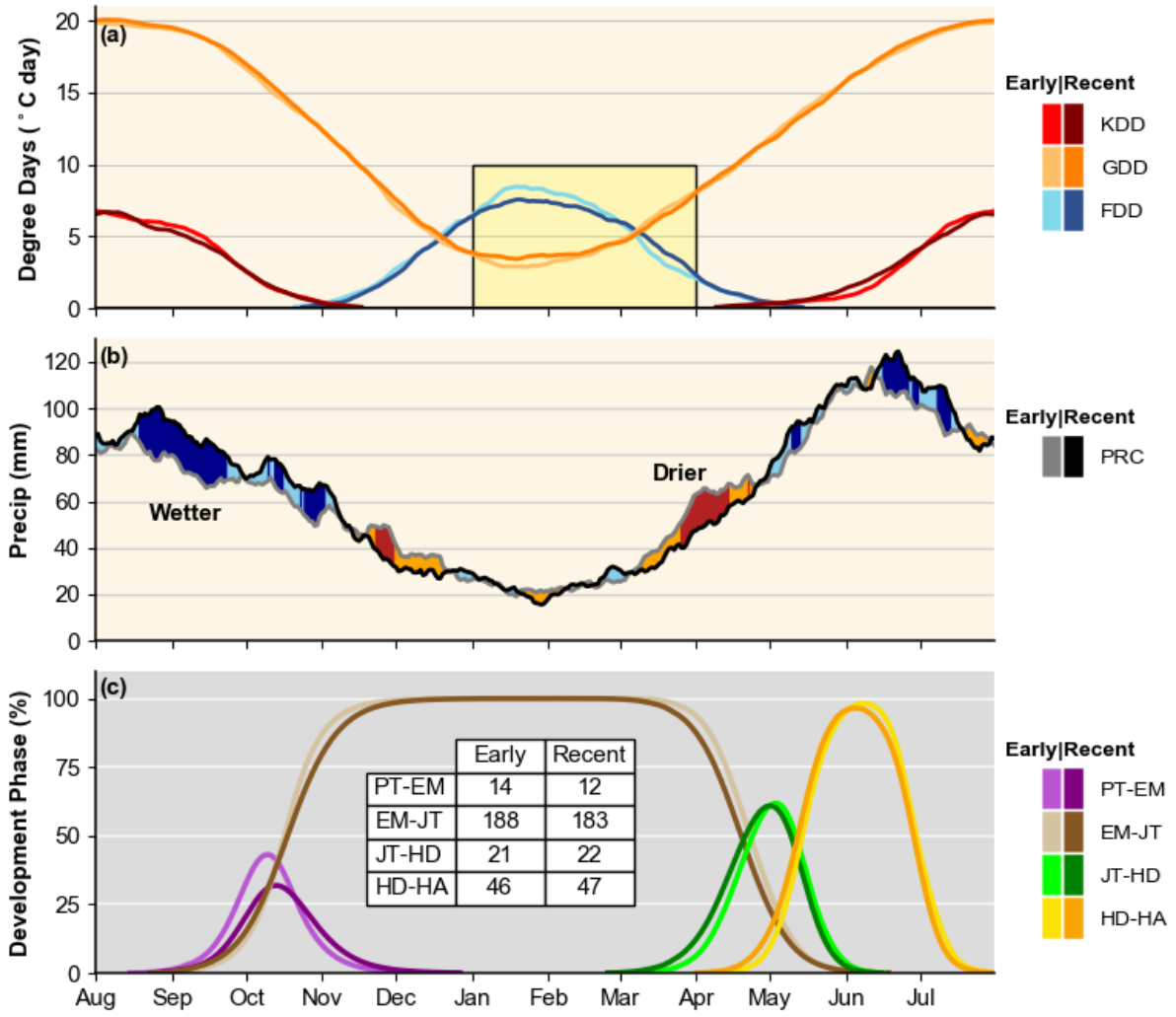

Figure 3.2 (a) 30-day moving county average killing degree days (KDD), growing degree days (GDD), and freeze degree days (FDD) for early (1973−1995) and recent (1996−2019) periods. The yellow box outlines evidence for false spring. (b) Same as (a) but for 30-day moving sum of precipitation (PRC). Darker colors indicate differences larger than 10 mm. (c) State-wide average winter wheat development phases (%) from planting to emergence (PT-EM), emergence to jointing (EM-JT), jointing to heading(JT-HD), and heading to harvest (HD-HA) for early and recent periods. Table of the average duration in days for each developmental phase is provided.

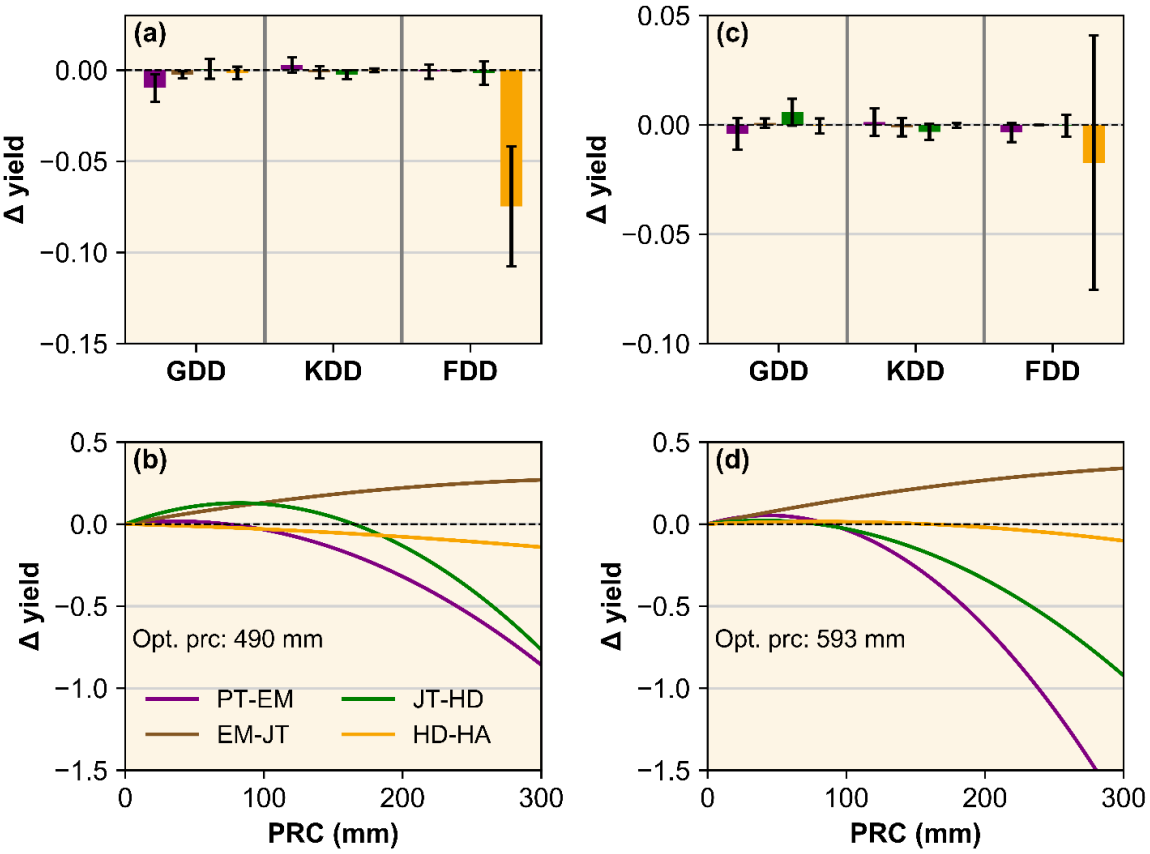

Figure 3.3 (a) Change in yield (Δ yield in ton ha^{-1} after square root transformation**)** due to a unit increase in growing degree days (GDD*10), killing degree days (KDD), and freezing degree days (FDD) by growth stage for the USDA-NASS model. For each environmental covariate, the color of each bar corresponds to one of four phenological stages: planting to emergence (PT-EM), emergence to jointing (EM-JT), jointing to heading (JT-HD), and heading to harvest (HD-HA). The 95% confidence intervals for each coefficient are shown by standard error bars, which were clustered by year. (b) The change in yield with as a function of precipitation (PRC) by growth stage. Optimum total growing season precipitation is shown. (c−d) Same as (a) and (b) but for winter wheat variety trials. Standard errors were clustered by year and variety.

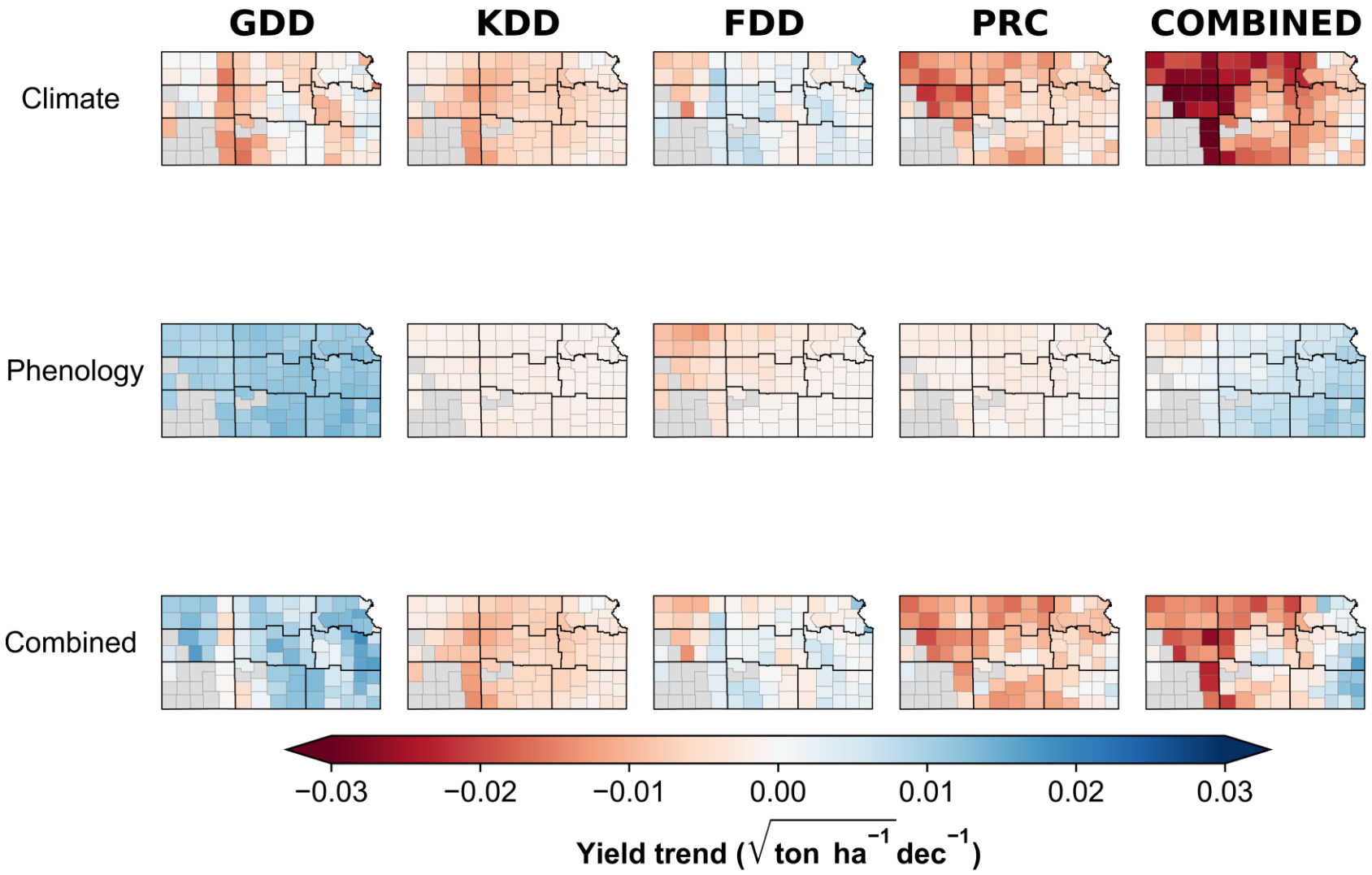
GDD
KDD
FDD
PRC
COMBINED
Climate
Phenology
Combined
−0.03
−0.02
−0.01
0.00
0.01
0.02
0.03
Yield trend (√ton ha−1 dec−1)

Figure 3.4 Contributions to winter wheat yield trends from 1973 to 2019 due to changes in climate, phenology, and the combination of both climate and phenology. The effects from growing degree days (GDD), killing degree days (KDD), freezing degree days (FDD), and precipitation (PRC) are aggregated across all four phenological stages. PRC includes both PRC and PRC^2. Yield was transformed using a square root transformation.

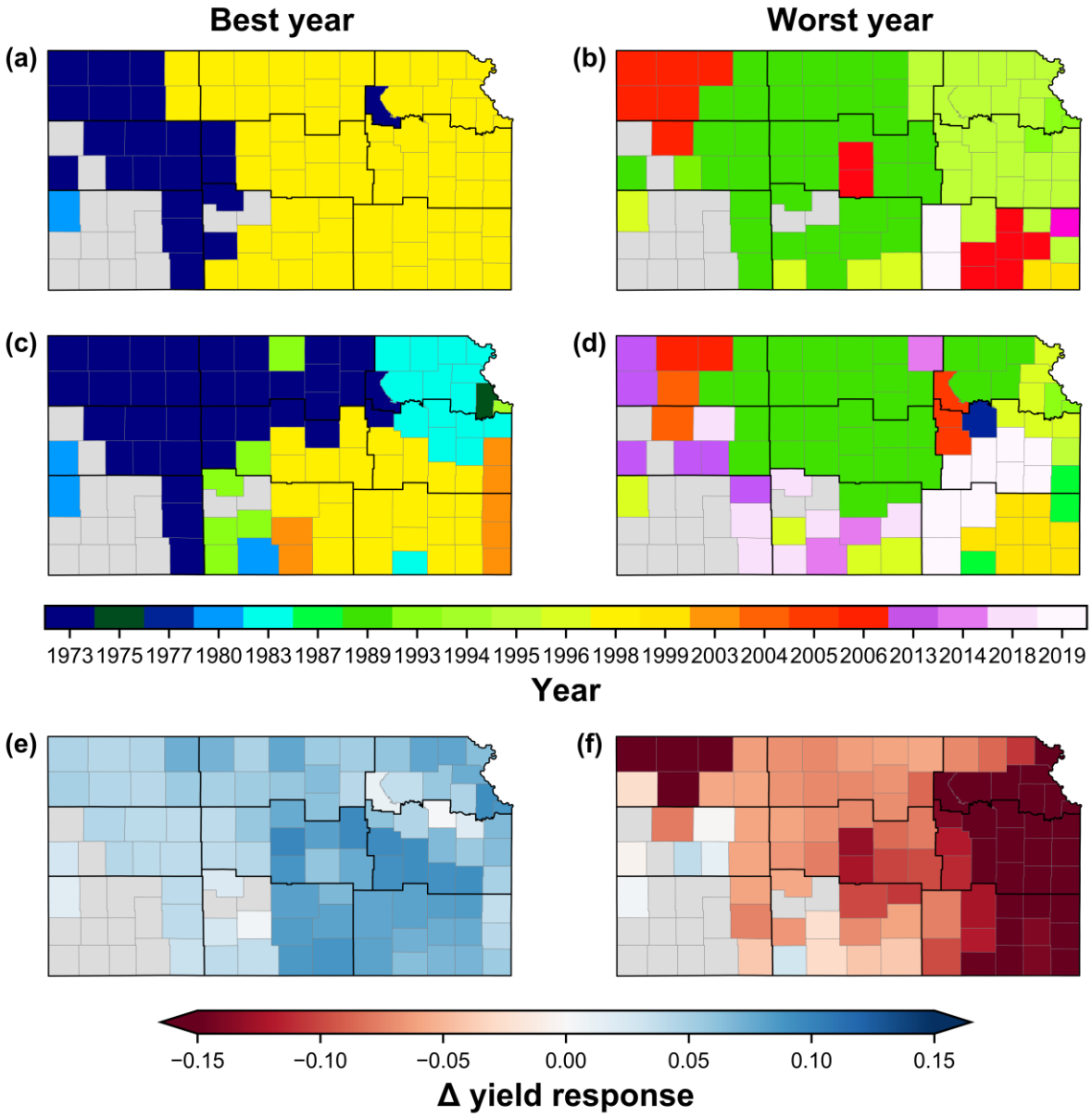
Best year
Worst year
(a)
(b)
(c)
(d)
1973 1975 1977 1980 1983 1987 1989 1993 1994 1995 1996 1998 1999 2003 2004 2005 2006 2013 2014 2018 2019
Year
(e)
(f)
−0.15 −0.10 −0.05 0.00 0.05 0.10 0.15
Δ yield response

Figure 3.5 (a) Years with the most favorable weather conditions for model yield response. Weather and phenology vary each year. (b) Same as (a) but years with the most unfavorable weather conditions. (c−d) Same as (a) and (b) but with phenology weights fixed at average 1973-2019 values. (e) The change in yield response during the most favorable years (e.g. (a) minus (c)). (f) Same as (e) but for the most unfavorable years.

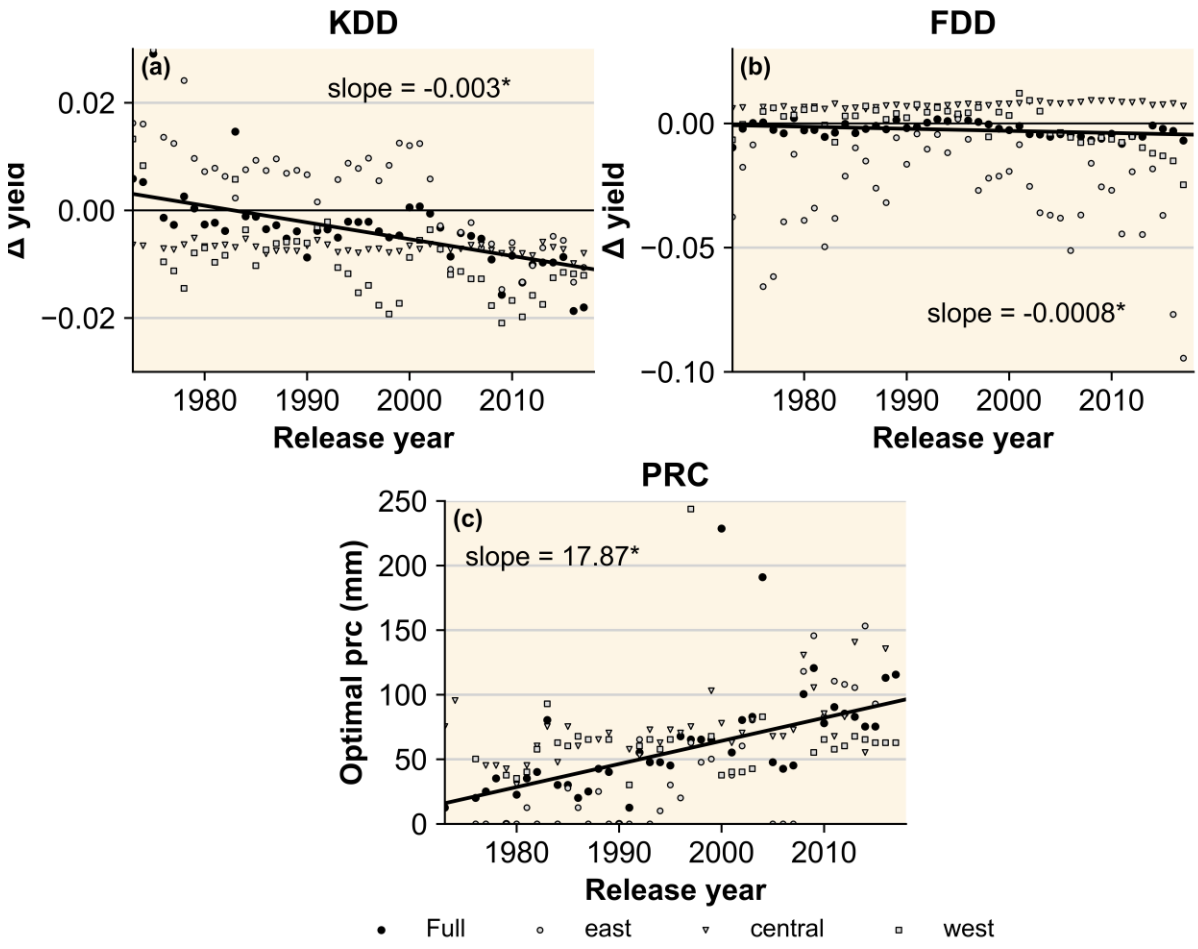

Figure 3.6 (a) Yield sensitivity to jointing to heading killing degree days (JT-HD KDD) as a function of variety release year. Smaller values in magnitude indicate lower sensitivity to a degree day of exposure. Sensitivities were defined as the random effects best linear unbiased predictors from a linear mixed effects model (LMEM) with release year as the cluster. LMEMs were fit for all trial locations together (full) and by individual regions (east, central, and west). Trend lines for the random effects for the LMEM results from the full model were estimated using Theil Sen slope, and the units of slope are per decade. * indicates statistical significance at the five percent level. (b) Same as (a) but for JT-HD freeze degree days (FDD). (c) Same as (a) but for optimal JT-HD precipitation (PRC).

Table 3.1 Model performance statistics for yield data from USDA-NASS (Eq. 4) and winter wheat variety trials (Eq. 5) with various model specifications. Statistics include the coefficient of determination (R^2) and root mean square error (RMSE).

Source	Model specification	R^2	RMSE
USDA-NASS	County and year fixed effects	0.10	0.19
	Climate fixed effects + intercept	0.39	0.17
	Full model	0.56	0.14
Variety trials	Fixed effects from variety	0.14	0.30
	Location, variety, and year fixed effects	0.28	0.28
	Climate fixed effects + intercept	0.16	0.30
	Full model	0.38	0.26

Chapter 4 - Conclusions and agricultural implications

Chapter 1

Growing season temperatures have increased over the last century for many regions of the Great Plains with a stronger signal during the winter. However, during the summer, several regions were identified that demonstrated a decrease in temperature. While the number of drought events was lower from 1978 to 2015 compared to the early and mid-twentieth century, drought intensities were significantly higher, having potential impacts on crop productivity due to the rapid onset and intensification of drought events. Quantification of the historical behavior of drought variability revealed insights into the number of homogenous subregions within the Great Plains and areas that have more complex variability. The identified subregions provide information about the synoptic processes that govern their shape and size across space and time and have advantages over political boundaries due to their physical basis in climate. Analysis at the seasonal scale was critical as subregions and their temporal characteristics for similar areas were heterogeneous. Our study allowed statistics such as trend identification and drought metrics to be summarized across large areas without losing significant information. Despite the identified warming trends, many subregions demonstrated seasonal wetting trends, which is important to account for in climate change adaptation planning in agriculture. For future research, the introduced techniques could be used to analyze historical and projected global climate model output (GCM) to examine whether GCMs produce historical subregions patterns similar to those observed in addition to potential projected changes in drought variability. For agronomists, seasonal subregions can be helpful for selecting and optimizing field trial locations if the study emphasis is on drought variability. The selection rule introduced provides a framework that may motivate other researchers to extend the current method or develop alternative methods into

detecting subregion stability.

Chapter 2

The areas identified in the eastern Great Plains with summer cooling trends in chapter 1 suggested that irrigation as a tool for agricultural water management in the semiarid Ogallala Aquifer Region may be influencing regional climate trends. Our regional climate model simulations revealed that irrigation can reduce the ambient surface temperature between 0.5 – 1.0 °C, which is on the order of magnitude of the observed cooling trend in the historical record. This suggests that both agriculture and water management may play a role in suppressing the long-term anthropogenic summer warming trend that is evident across most regions of the world. Across at-risk areas in the central and southern OAR, future reductions in irrigation due to improvements in technology or changes in applied water may result in climatic effects that influence producers such as increasing local maximum temperatures at peak heating and decreasing local and downwind transport of moisture, which may reduce cloud cover and increase the amount of radiation reaching the canopy. Because vertical velocities are reduced over irrigated cropland, precipitation rates may increase under favorable synoptic conditions.

Previous studies have typically only used a single set of parameterizations to quantify the effects of irrigation on climate, but we have shown that changes in the parameterizations in the land surface model altered some of the results and thus the implications on agriculture. This information is critical for researchers and earth system modelers when designing future experiments. Furthermore, our study was one of the first to integrate the latest irrigated land use datasets into WRF, providing insights into the behavior of the WRF model under different

historical irrigation scenarios. Future research could explore the influence of modeling scale on the atmospheric response as some of our simulations suggests that higher resolution runs may change the response above the surface. In addition, researchers could use the same framework to model the effects of irrigation under a warmer climate using output from GCMs for initial and lateral boundary conditions. The latest version of the Noah-MP land surface model allows users the option to run simulations with crop vegetation classified as either maize or soybean. Including cotton and wheat as crop options, and then running similar simulations will provide additional insights over generic crop vegetation schemes.

Chapter 3

Our final chapter introduced techniques in statistical modeling that demonstrated concrete evidence linking the negative impacts of climate change on yield trends in non-irrigated winter wheat production systems in Kansas. We demonstrated historical evidence of a false spring signal in Kansas. This false spring may have detrimental impacts for winter wheat production in the future under current phenology trends. Breeding programs that have focused on improvements in phenology timing as a form of climate adaptation have been overall successful in taking advantage of exposure time to environmental variable such as growing degree days. However, because freezing temperatures near heading are detrimental to yields, management practices should focus on minimizing damage from late spring freezes, as historical trends indicate an increase in the frequency of false springs. At the variety level, our results indicated that newer varieties have a larger yield response under higher spring precipitation in central and eastern Kansas, which was a novel finding. In chapter 1 we identified that many subregions in the Great Plains have demonstrated statistically significant wetting trends, suggesting that if

trends continue, these yield responses under optimal precipitation may be sustainable in the future. In addition, this was the first study to our knowledge linking the observed increase in wheat yield variance to phenology changes and climate sensitivities at the county and field trial scales. This information to our knowledge has not been previously reported in the literature for winter wheat.

Future modeling work in winter wheat or other field crops could disaggregate the phenology progress data for use at the regional or county level to improve overall model performance as the application of state-level data uniformly across counties is a limitation in this study. While the model developed in this study showed minimal geographic biases, there were years in which the model underperformed, most likely due to potential environmental interactions that might be confounded by state-level progress data. Furthermore, as the data extent and quality from mesonets continues to improve, these alternative sources for climate data could improve statistical modeling efforts at the field trial scale due to site proximity and measurement frequency (e.g. hourly, 5-minute). Including covariates such as hours of exposure to freezing or killing degree days may lead to additional insights as understanding exposure duration has increasingly become more critical for assessing crop yield impacts during different phenological stages. Overall, continued efforts into the understanding of major environmental drivers affecting wheat and agricultural production in general will help meet the global food demand in the future under climate change.

Appendix A - Supplemental Information for Chapter Two

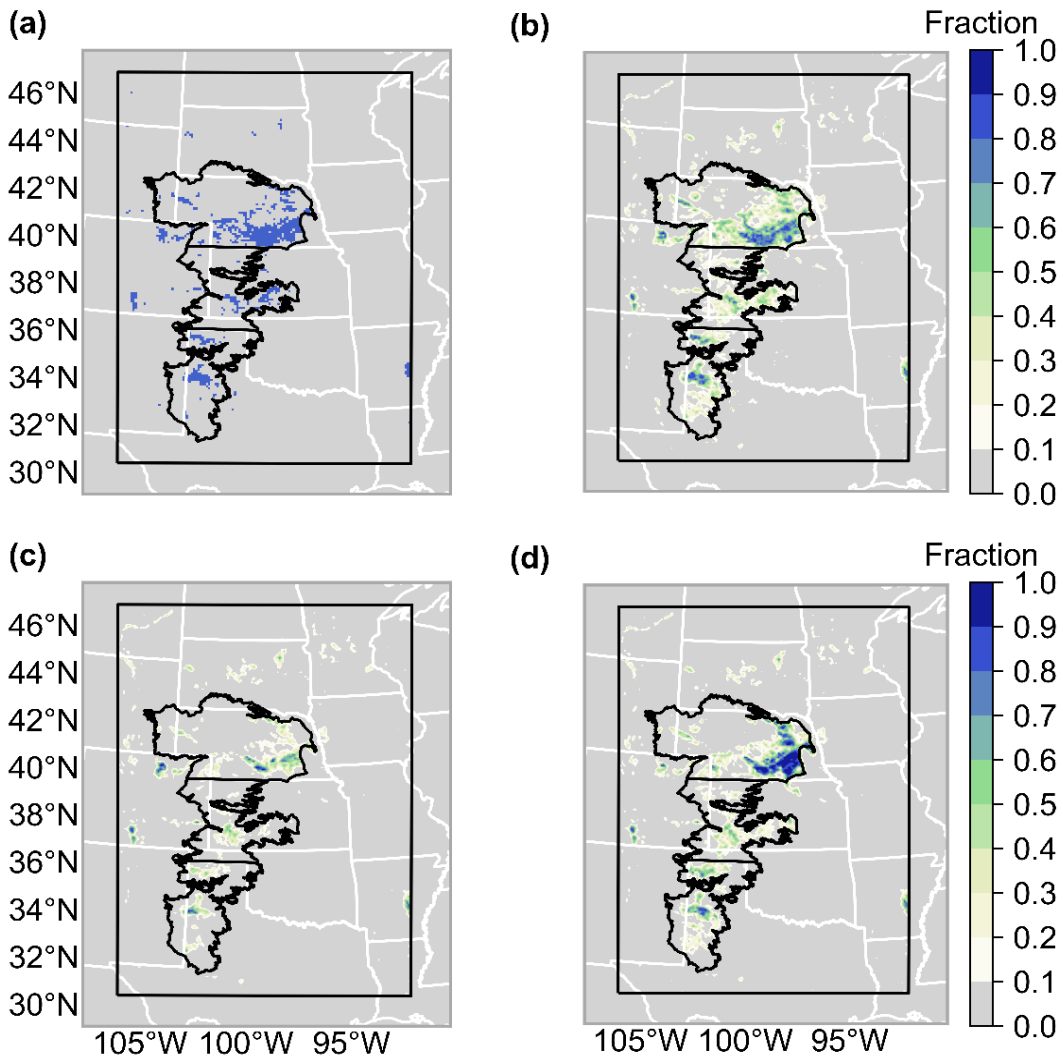

Figure A.1 (a) Grid cells (blue) in the domain that have a dominant land use category of irrigated cropland or pasture based on the MiRAD-2012 dataset. (b) The fraction of each grid cell that is irrigated cropland or pasture based on the MiRAD-2012 dataset. (c) Same as (b) but for the Deines annual irrigation map from 1984. (d) Same as (b) but for the Deines annual irrigation map from 2017.

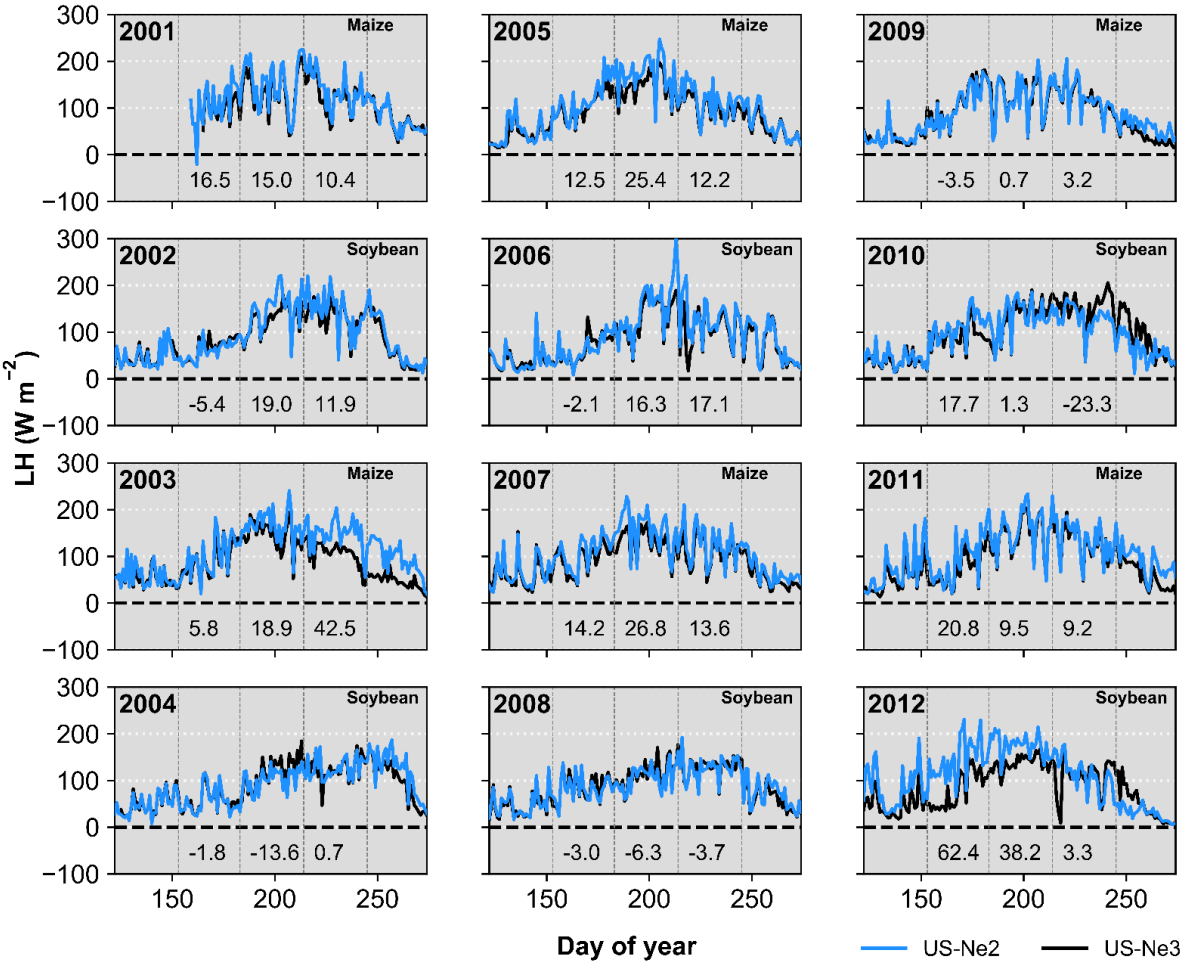

Figure A.2 Daily average latent heat flux (LH) for Ameriflux sites US-Ne2 (blue; irrigated) and US-Ne3 (black; non-irrigated) between 2001 and 2012 from May to September. Vertical lines divide summer into June, July, and August. Average differences between US-Ne2 and US-Ne3 are provided for June, July, and August at the bottom of each subplot.

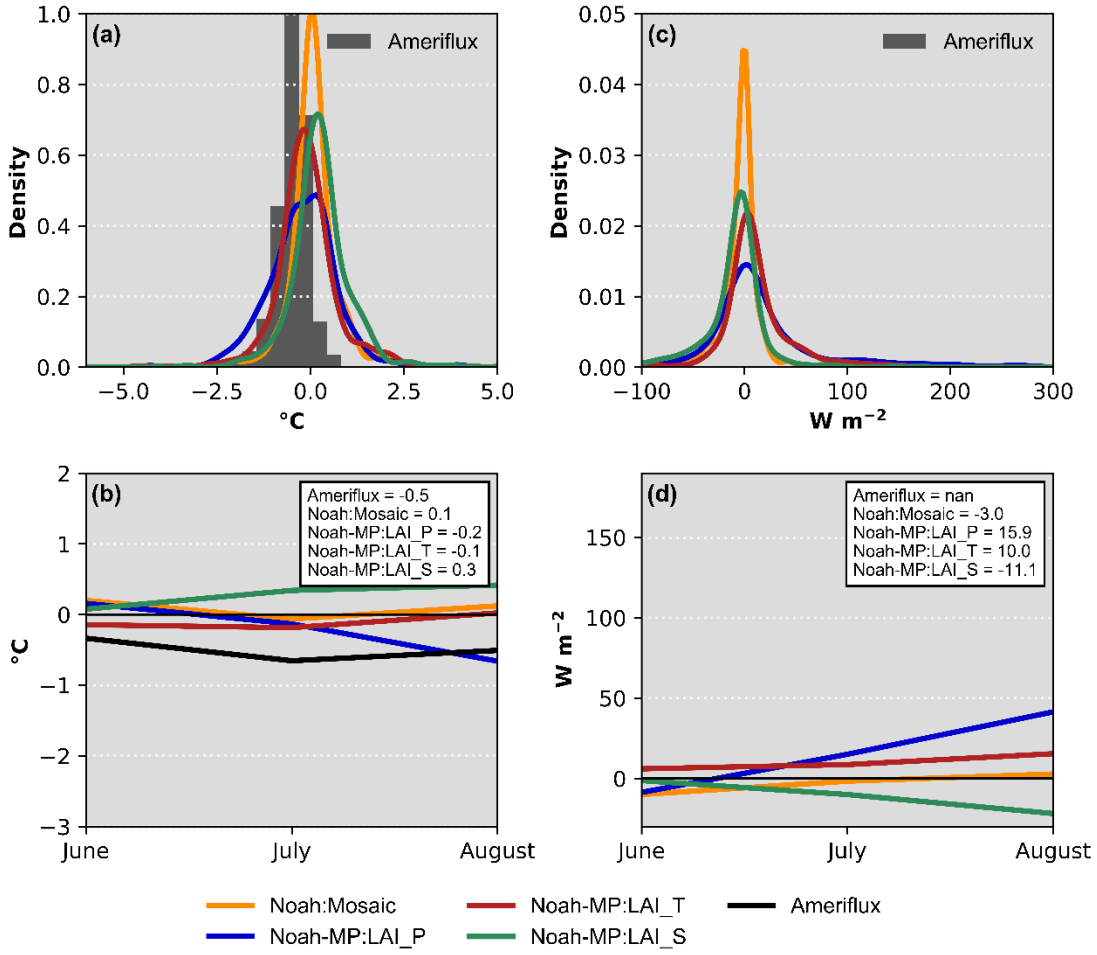

Figure A.3 Same as figure 2.3 but for 2015 (pluvial). There is no reliable latent heat flux data from Ameriflux site US-Ne3 during this year.

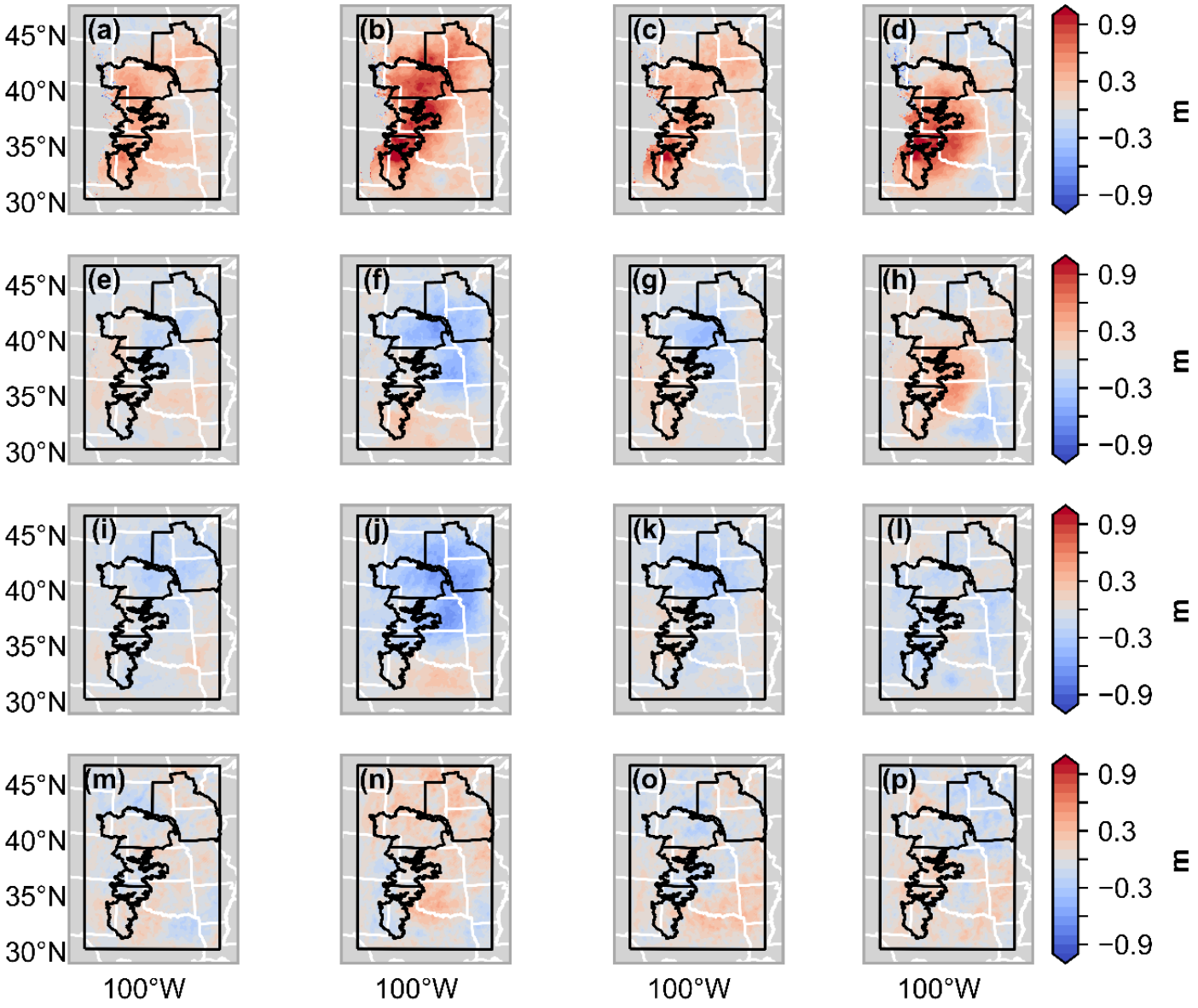
(a)
(b)
(c)
(d)
(e)
(f)
(g)
(h)
(i)
(j)
(k)
(l)
(m)
(n)
(o)
(p)
45°N
40°N
35°N
30°N
100°W
0.9
0.3
−0.3
−0.9
m

Figure A.4 (a−d) Difference in mean geopotential height at 850 hPa (m) between the irrigated and non-irrigated simulations during the summer of 2012 for the following four land surface model configurations in order: Noah: Mosaic, Noah-MP: LAI_P, Noah-MP: LAI_T, and Noah-MP: LAI_S. (e−h) As in (a−d) but for geopotential height at 700 hPa (m). (i−l) As in (a−d) but for geopotential height at 500 hPa (m). (m−p) As in (a−d) but for geopotential height at 200 hPa (m). Abbreviations: Noah-MP: LAI_P, leaf area index (LAI) dynamically predicted; Noah-MP: LAI_T, LAI interpolated from table; Noah-MP: LAI_S, LAI held constant.

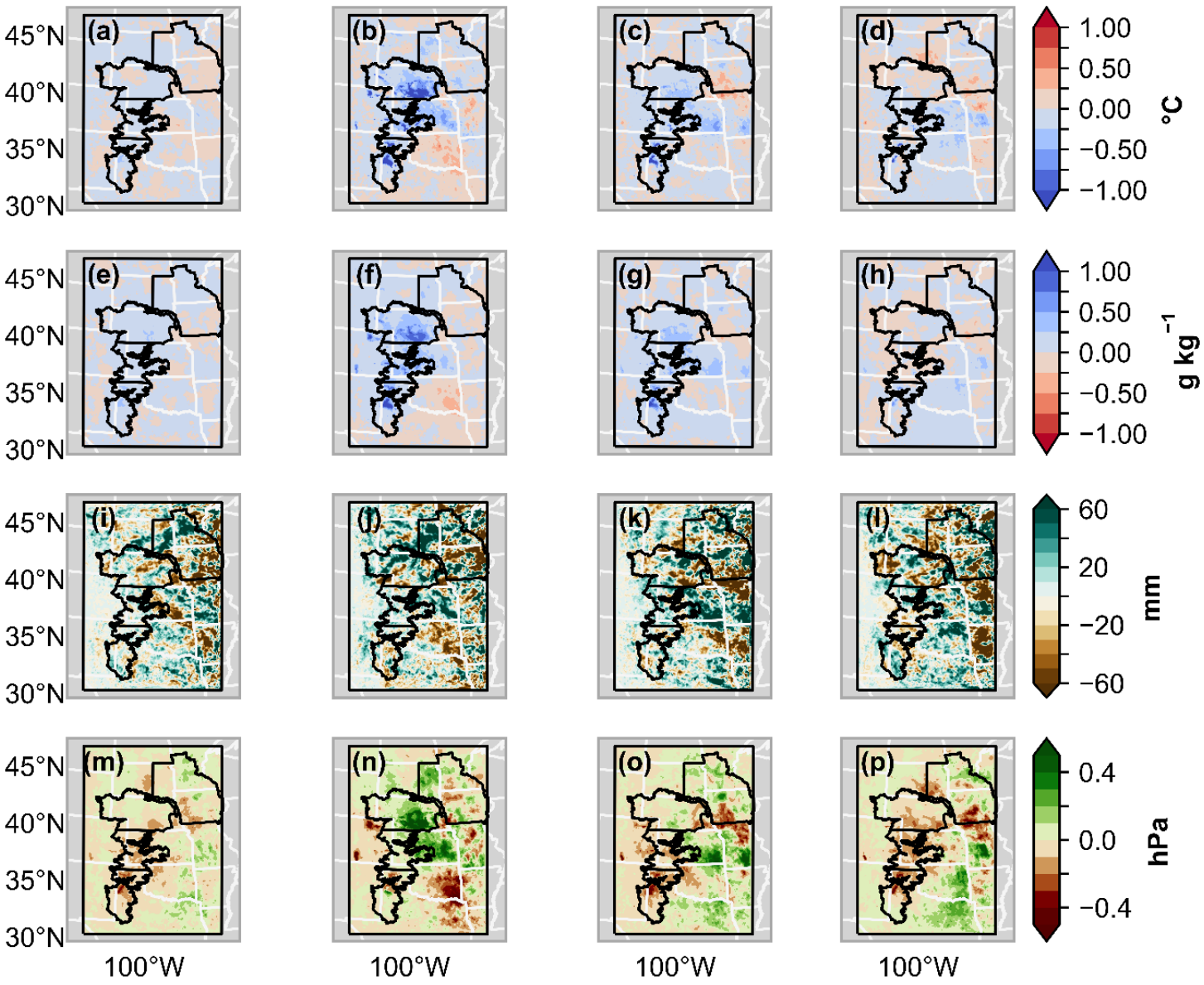
(a)
(b)
(c)
(d)
(e)
(f)
(g)
(h)
(i)
(j)
(k)
(l)
(m)
(n)
(o)
(p)
45°N
40°N
35°N
30°N
100°W
1.00
0.50
0.00
−0.50
−1.00
°C
g kg−1
60
20
−20
−60
mm
0.4
0.0
−0.4
hPa

Figure A.5 Same as figure 2.4 but for 1980 (drought).

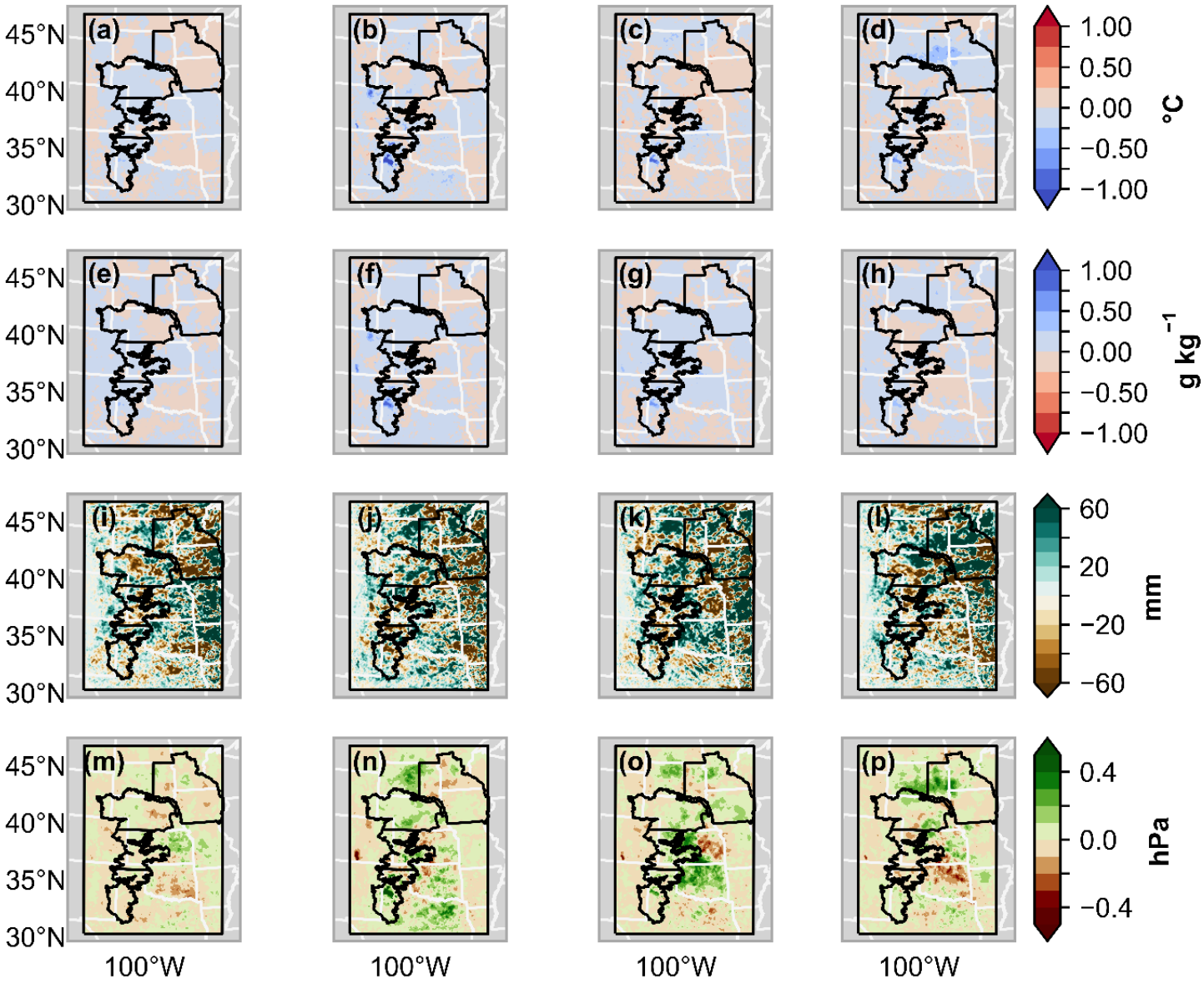
(a)
(b)
(c)
(d)
(e)
(f)
(g)
(h)
(i)
(j)
(k)
(l)
(m)
(n)
(o)
(p)
45°N
40°N
35°N
30°N
100°W
1.00
0.50
0.00
−0.50
−1.00
°C
g kg−1
60
20
−20
−60
mm
0.4
0.0
−0.4
hPa

Figure A.6 Same as figure 2.4 but for 1993 (pluvial).

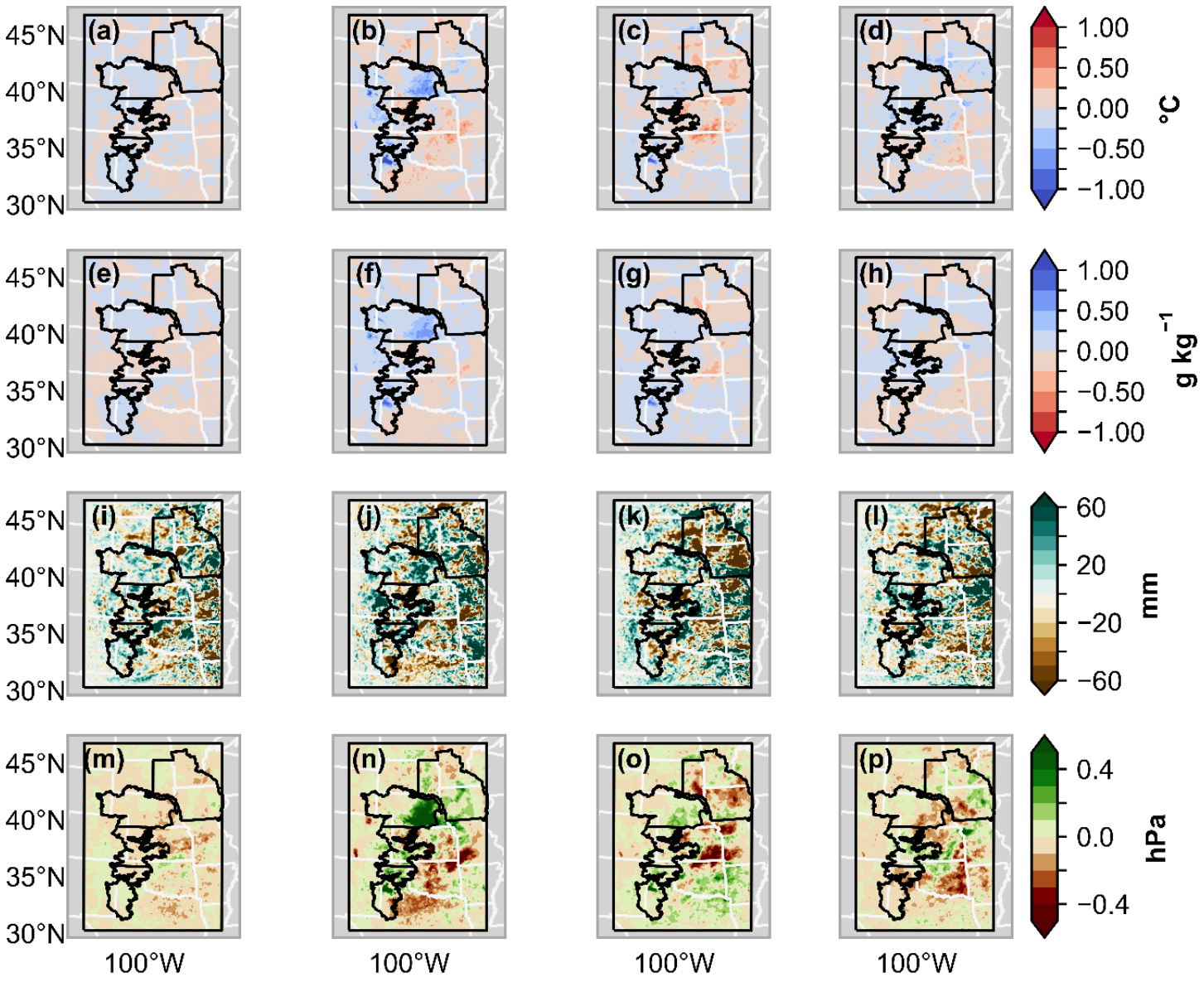
45°N
40°N
35°N
30°N
100°W
(a)
(b)
(c)
(d)
(e)
(f)
(g)
(h)
(i)
(j)
(k)
(l)
(m)
(n)
(o)
(p)
1.00
0.50
0.00
−0.50
−1.00
°C
g kg−1
60
20
−20
−60
mm
0.4
0.0
−0.4
hPa

Figure A.7 Same as figure 2.4 but for 2015 (pluvial).

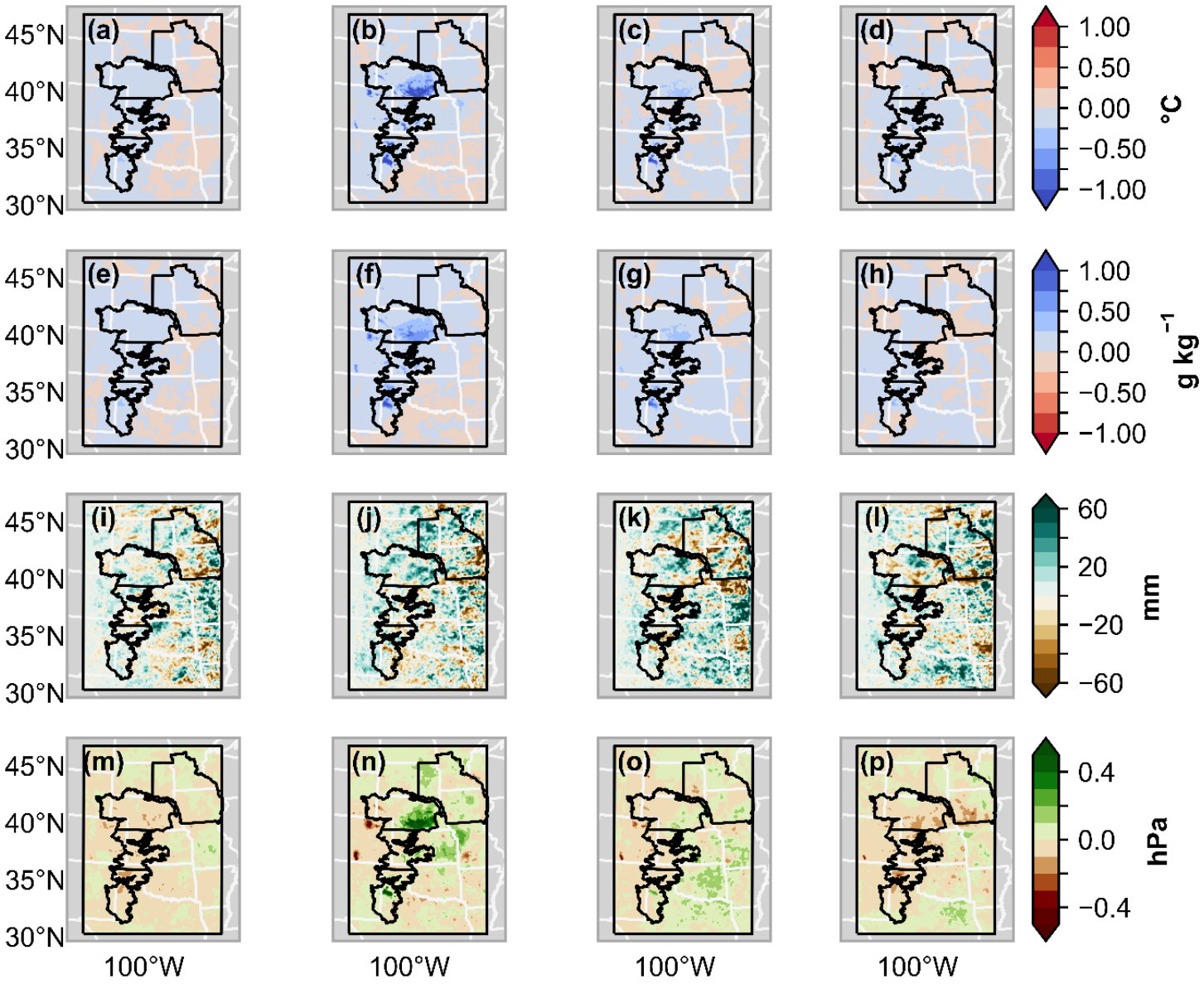
(a)
(b)
(c)
(d)
(e)
(f)
(g)
(h)
(i)
(j)
(k)
(l)
(m)
(n)
(o)
(p)
45°N
40°N
35°N
30°N
100°W
1.00
0.50
0.00
−0.50
−1.00
°C
g kg−1
60
20
−20
−60
mm
0.4
0.0
−0.4
hPa

Figure A.8 Same as figure 2.4 but for the average of 1980, 1993, 2012, and 2015.

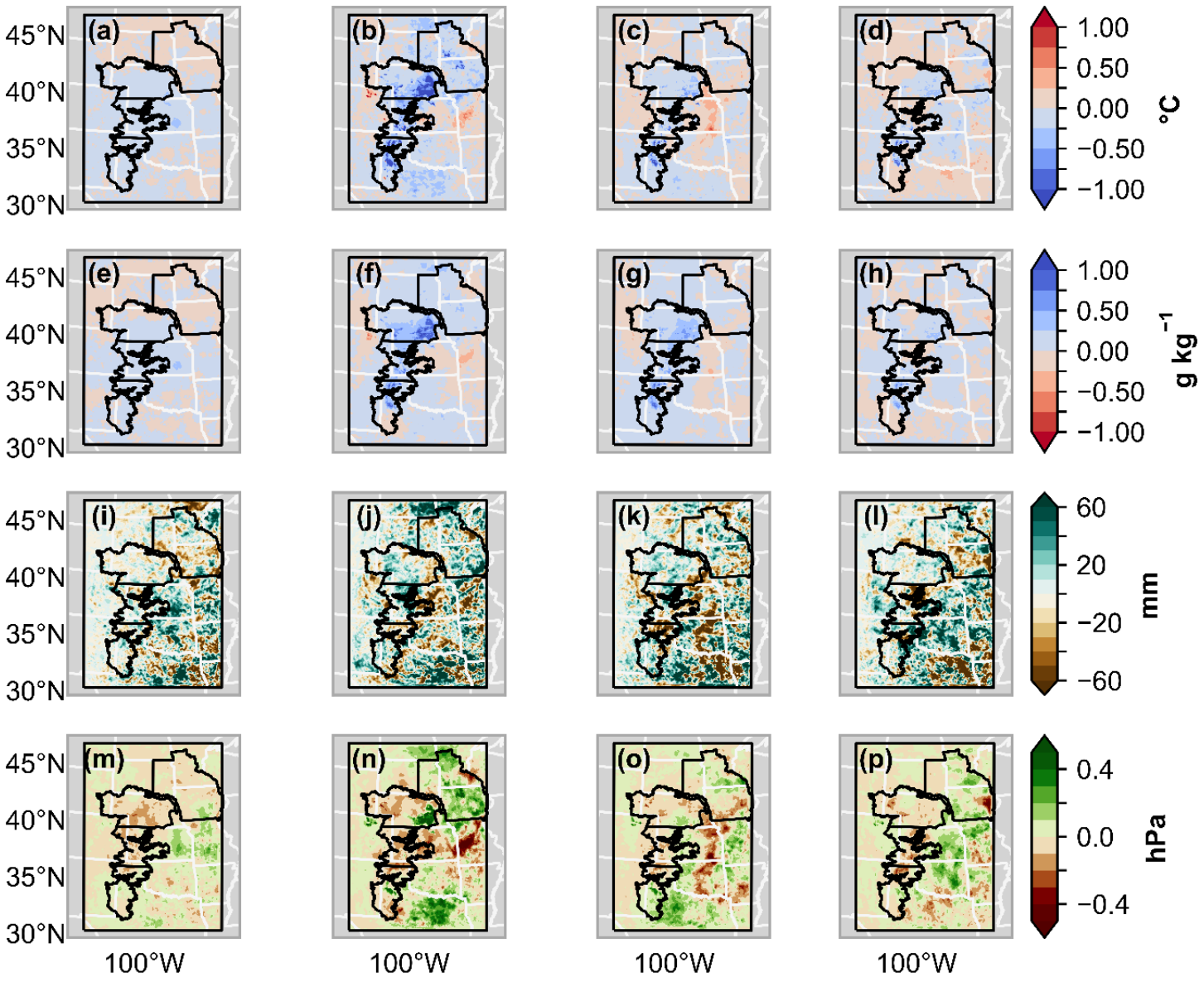
(a)
(b)
(c)
(d)
(e)
(f)
(g)
(h)
(i)
(j)
(k)
(l)
(m)
(n)
(o)
(p)
45°N
40°N
35°N
30°N
100°W
1.00
0.50
0.00
−0.50
−1.00
°C
g kg−1
60
20
−20
−60
mm
0.4
0.0
−0.4
hPa

Figure A.9 Similar to figure 2.4 using climate forcing data from NARR in 2012 (drought), but differences were calculated using simulations that incorporated irrigated land use data from 2017 and 1984 (e.g. 2017 minus 1984). Both simulations were irrigated.

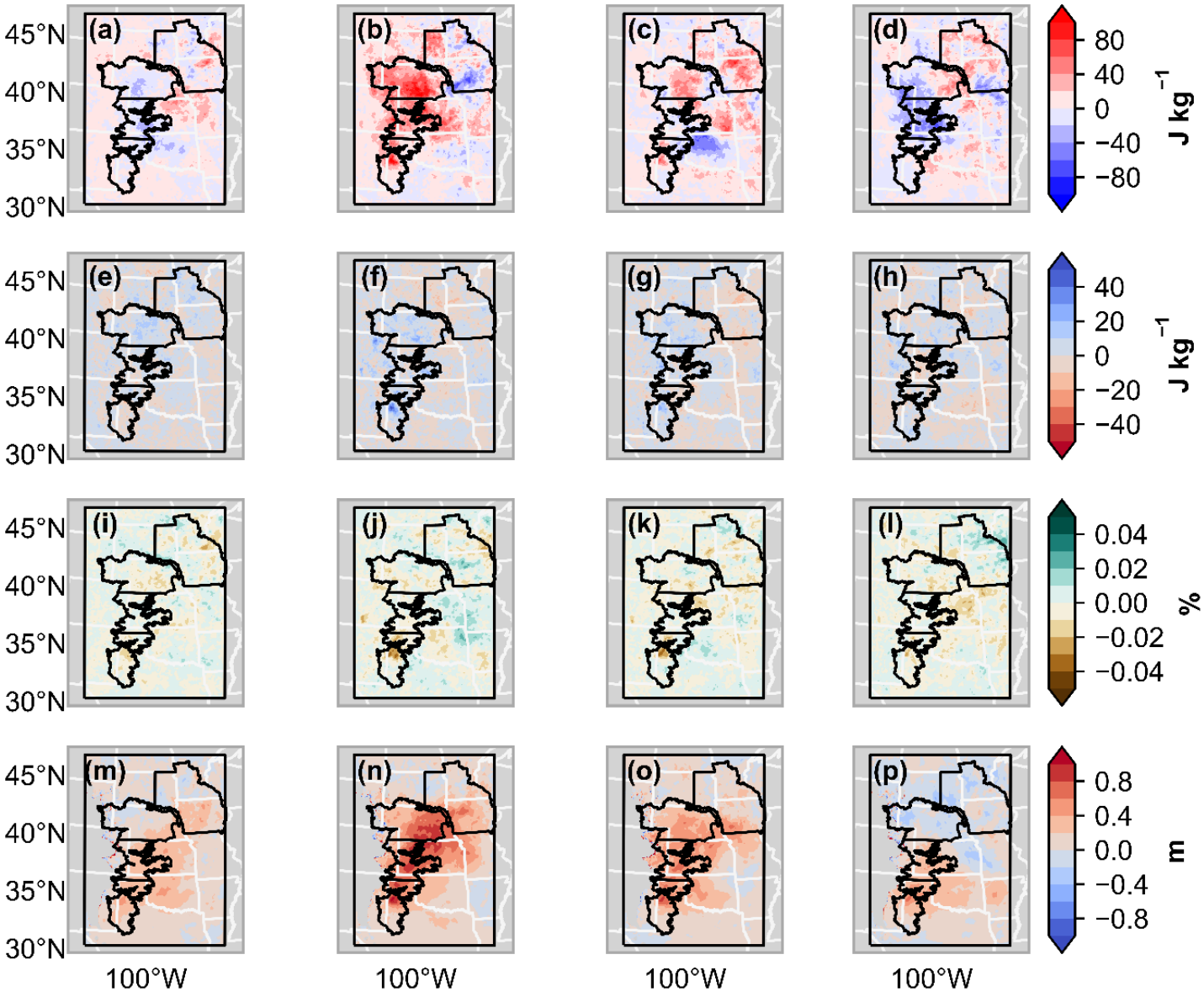
(a)
(b)
(c)
(d)
(e)
(f)
(g)
(h)
(i)
(j)
(k)
(l)
(m)
(n)
(o)
(p)
45°N
40°N
35°N
30°N
100°W
80
40
0
−40
−80
J kg−1
40
20
0
−20
−40
J kg−1
0.04
0.02
0.00
−0.02
−0.04
%
0.8
0.4
0.0
−0.4
−0.8
m

Figure A.10 Same as figure 2.6 but for 1980 (drought).

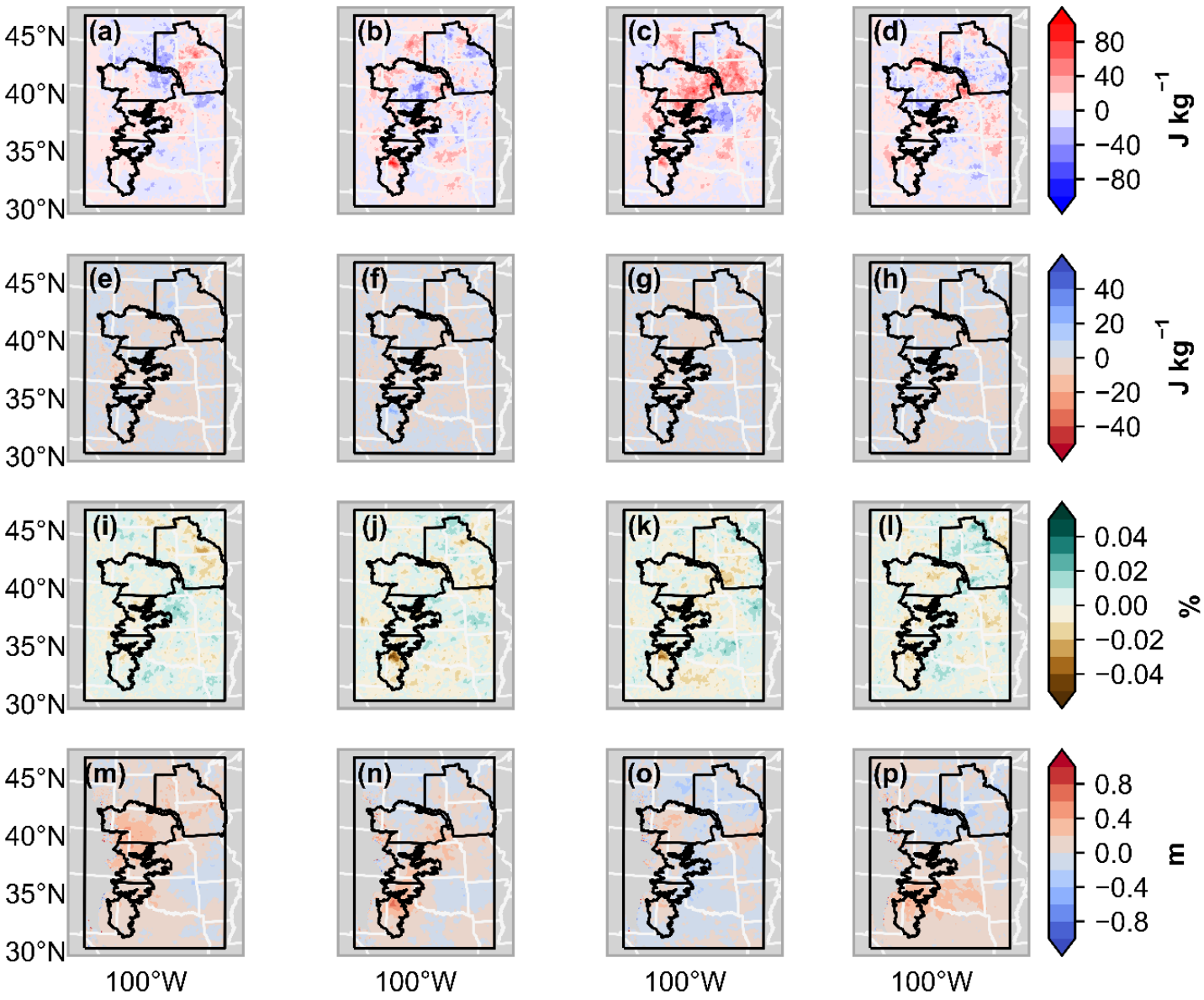
(a)
(b)
(c)
(d)
(e)
(f)
(g)
(h)
(i)
(j)
(k)
(l)
(m)
(n)
(o)
(p)
45°N
40°N
35°N
30°N
100°W
80
40
0
−40
−80
J kg−1
40
20
0
−20
−40
J kg−1
0.04
0.02
0.00
−0.02
−0.04
%
0.8
0.4
0.0
−0.4
−0.8
m

Figure A.11 Same as figure 2.6 but for 1993 (pluvial).

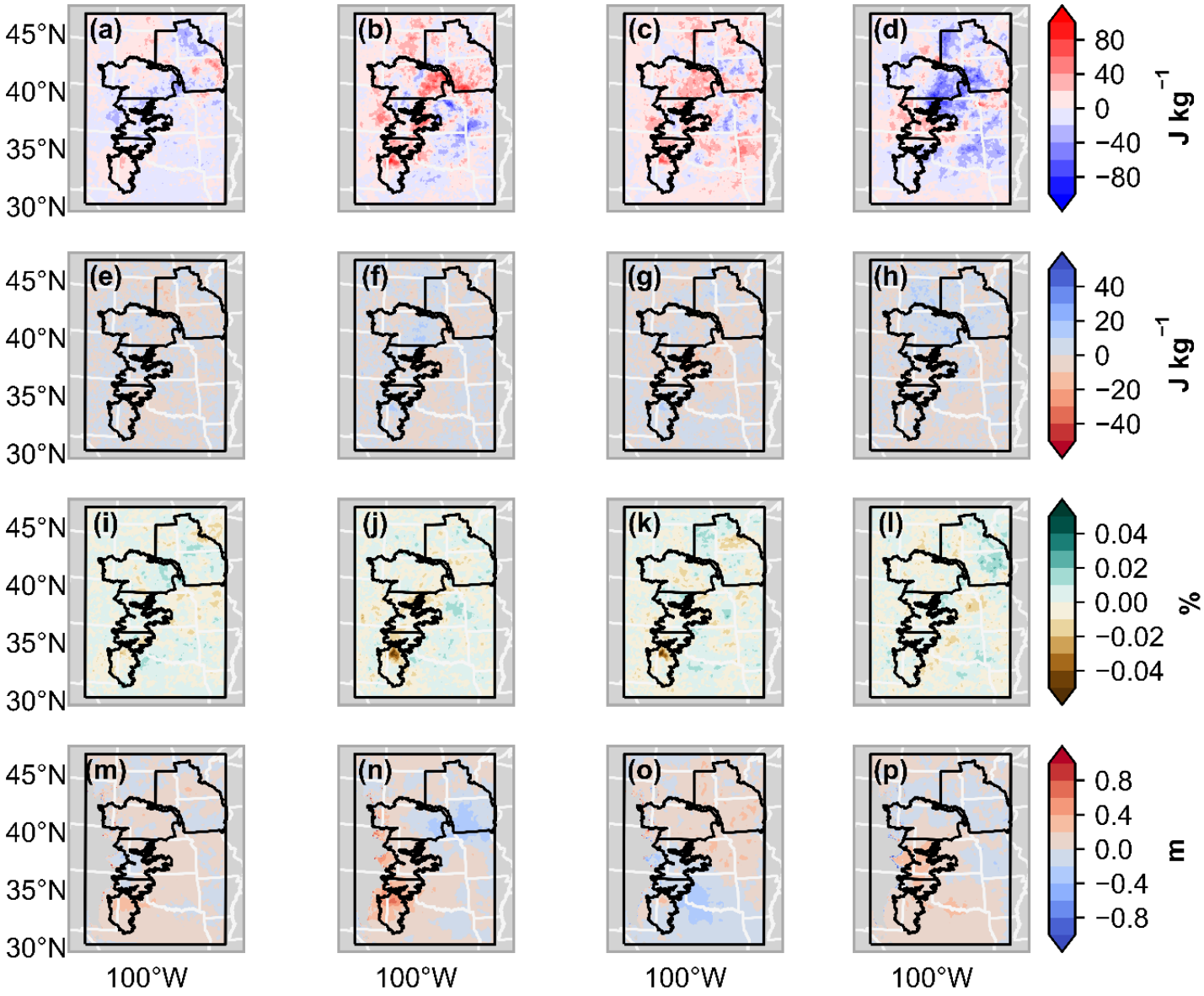
45°N
40°N
35°N
30°N
(a)
(b)
(c)
(d)
80
40
0
−40
−80
J kg−1
(e)
(f)
(g)
(h)
40
20
0
−20
−40
J kg−1
(i)
(j)
(k)
(l)
0.04
0.02
0.00
−0.02
−0.04
%
(m)
(n)
(o)
(p)
0.8
0.4
0.0
−0.4
−0.8
m
100°W

Figure A.12 Same as figure 2.6 but for 2015 (pluvial).

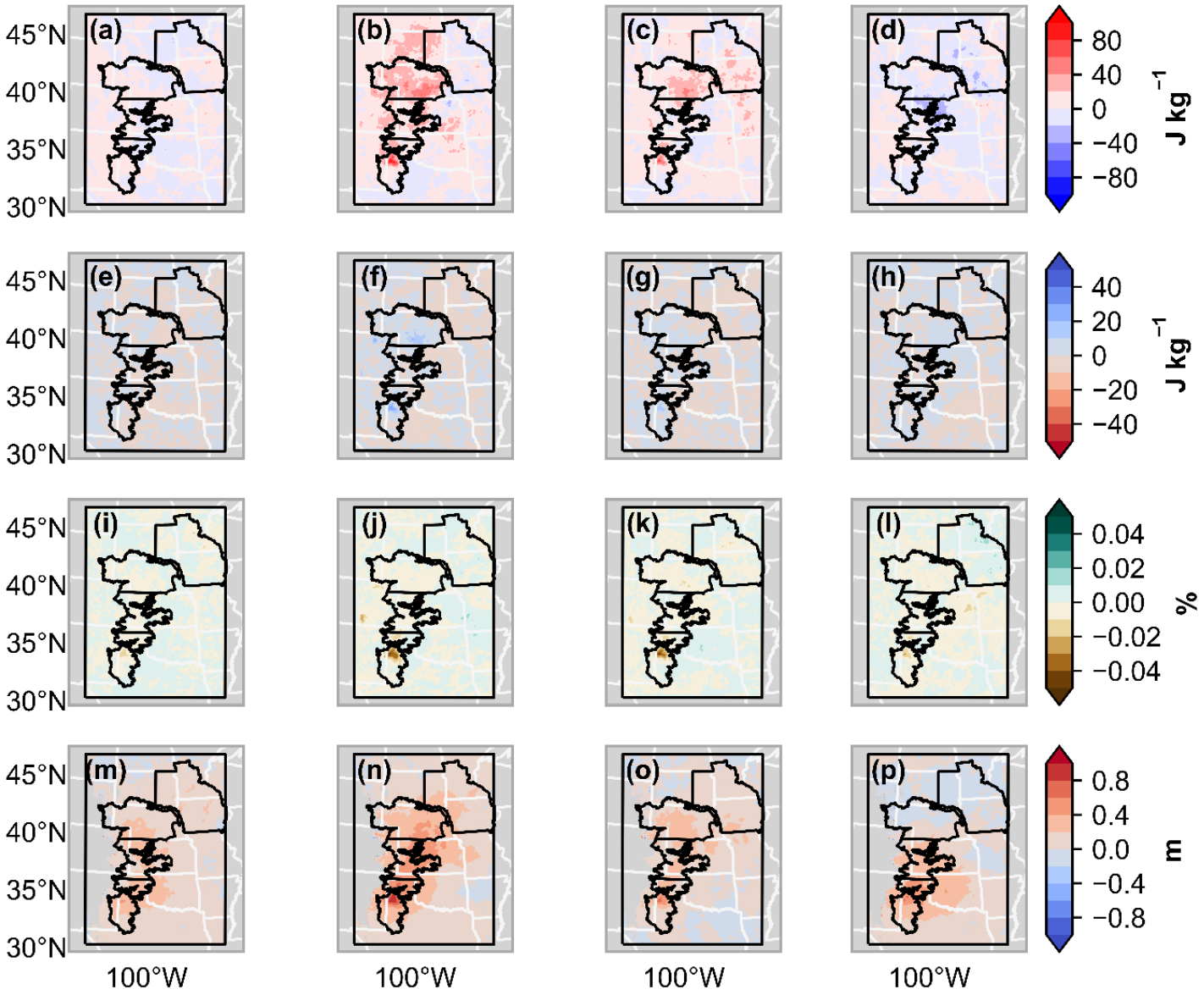
(a)
(b)
(c)
(d)
(e)
(f)
(g)
(h)
(i)
(j)
(k)
(l)
(m)
(n)
(o)
(p)
45°N
40°N
35°N
30°N
100°W
80
40
0
−40
−80
J kg−1
40
20
0
−20
−40
J kg−1
0.04
0.02
0.00
−0.02
−0.04
%
0.8
0.4
0.0
−0.4
−0.8
m

Figure A.13 Same as figure 2.6 but for the average of 1980, 1993, 2012, and 2015.

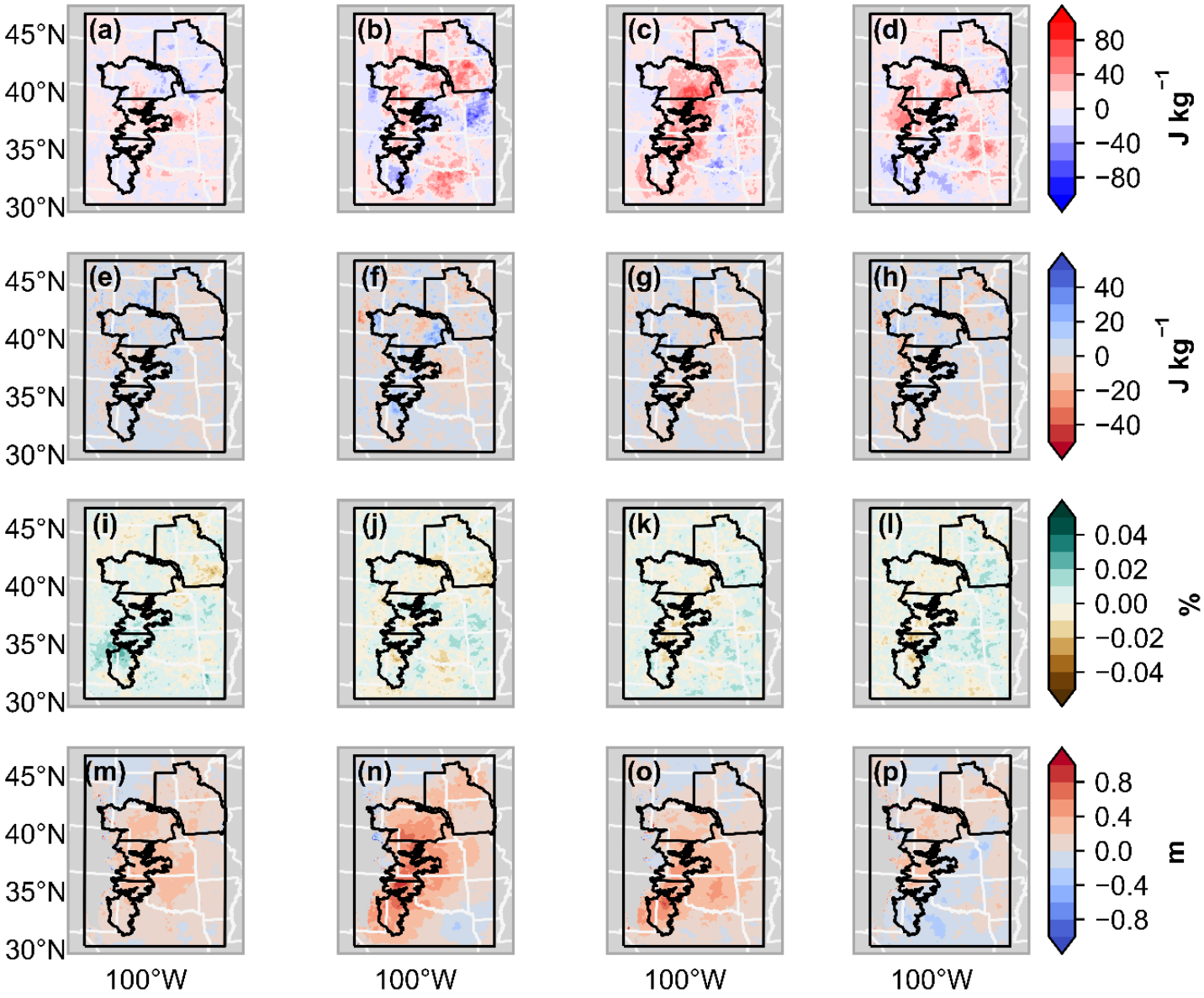
(a)
(b)
(c)
(d)
(e)
(f)
(g)
(h)
(i)
(j)
(k)
(l)
(m)
(n)
(o)
(p)
45°N
40°N
35°N
30°N
100°W
80
40
0
−40
−80
J kg−1
40
20
0
−20
−40
J kg−1
0.04
0.02
0.00
−0.02
−0.04
%
0.8
0.4
0.0
−0.4
−0.8
m

Figure A.14 Similar to figure 2.6 using climate forcing data from NARR in 2012 (drought), but differences were calculated using simulations that incorporated irrigated land use data from 2017 and 1984 (e.g. 2017 minus 1984). Both simulations were irrigated.

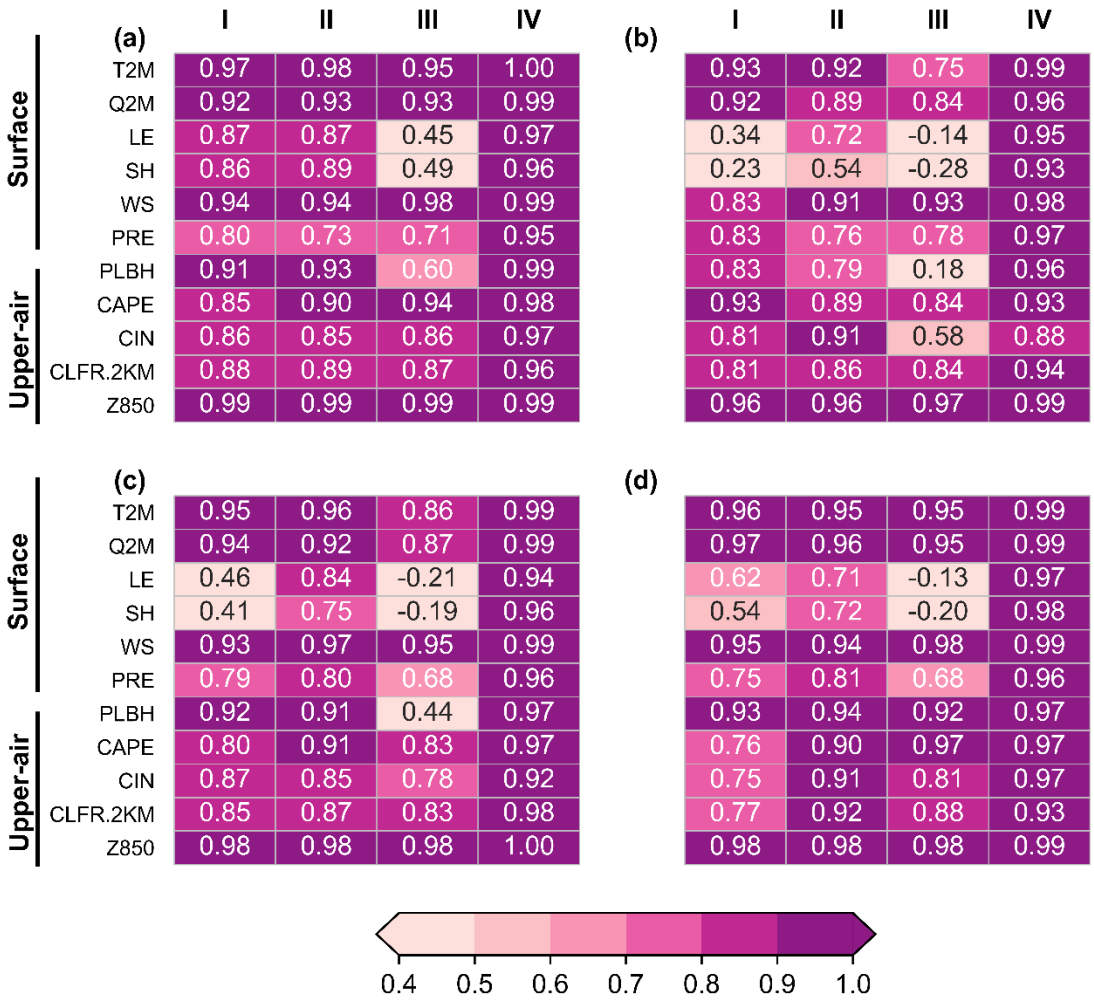

Figure A.15 Same as figure 2.5 but for 1980.

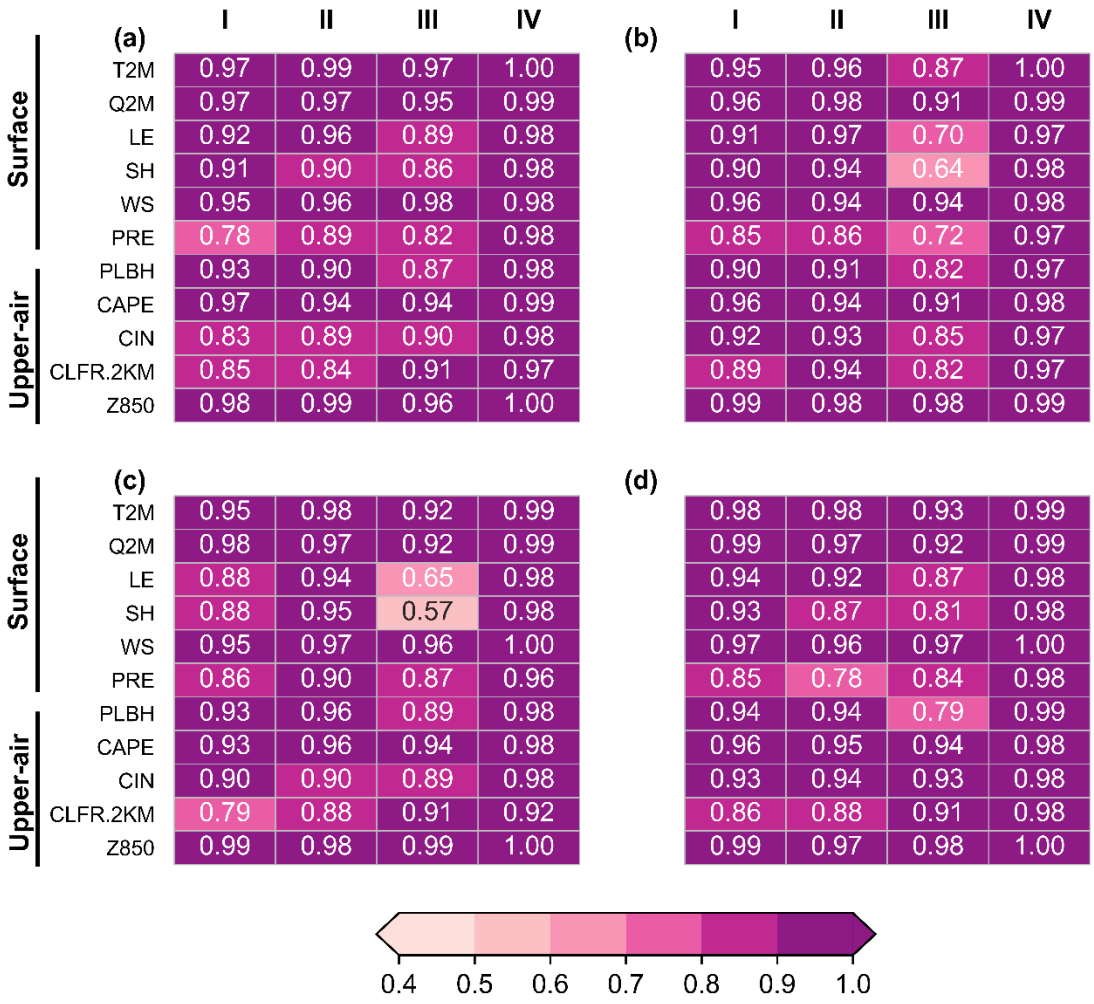

Figure A.16 Same as figure 2.5 but for 1993.

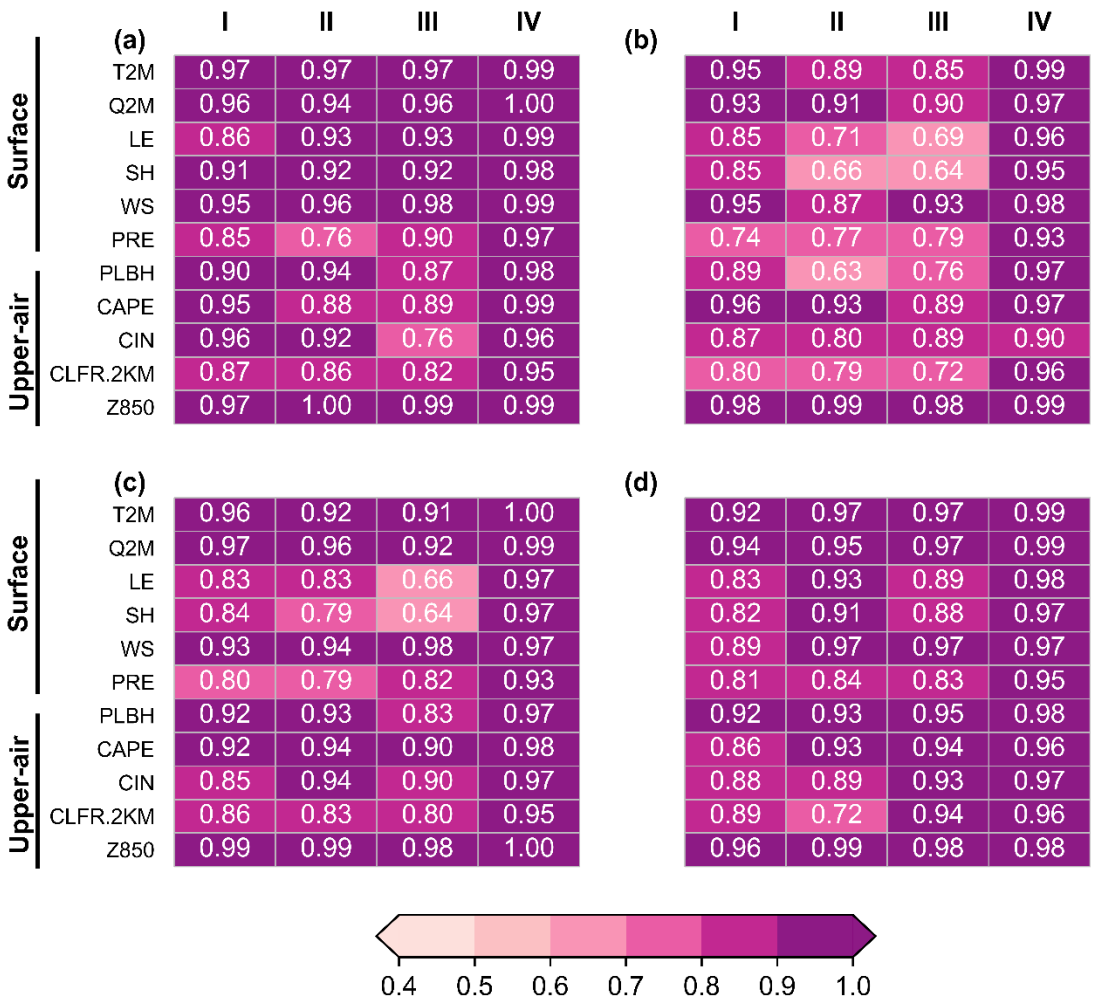

Figure A.17 Same as figure 2.5 but for 2015.

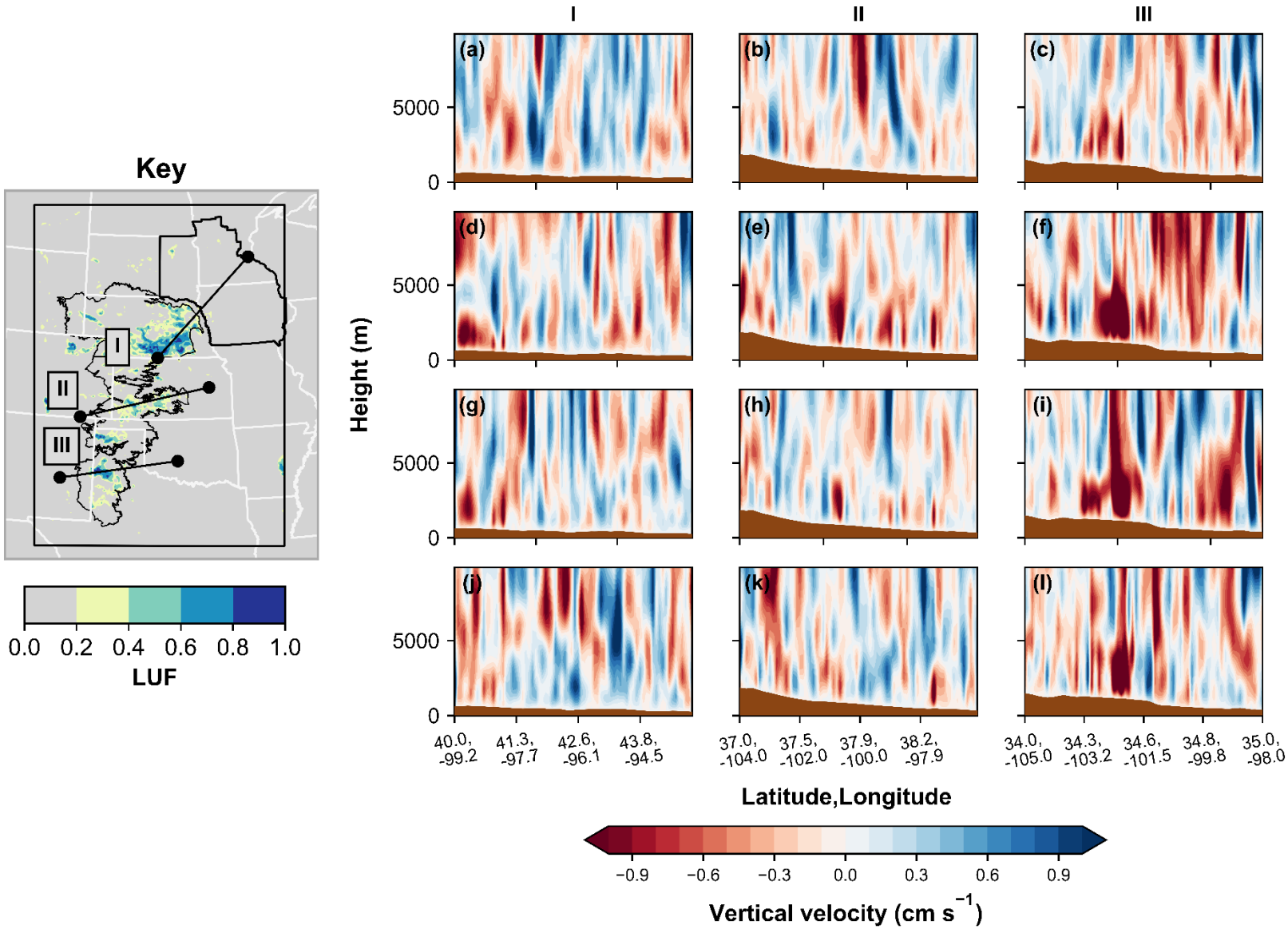

Figure A.18 Same as figure 2.7 but for vertical velocity.

Appendix B - Supplemental Information for Chapter Three

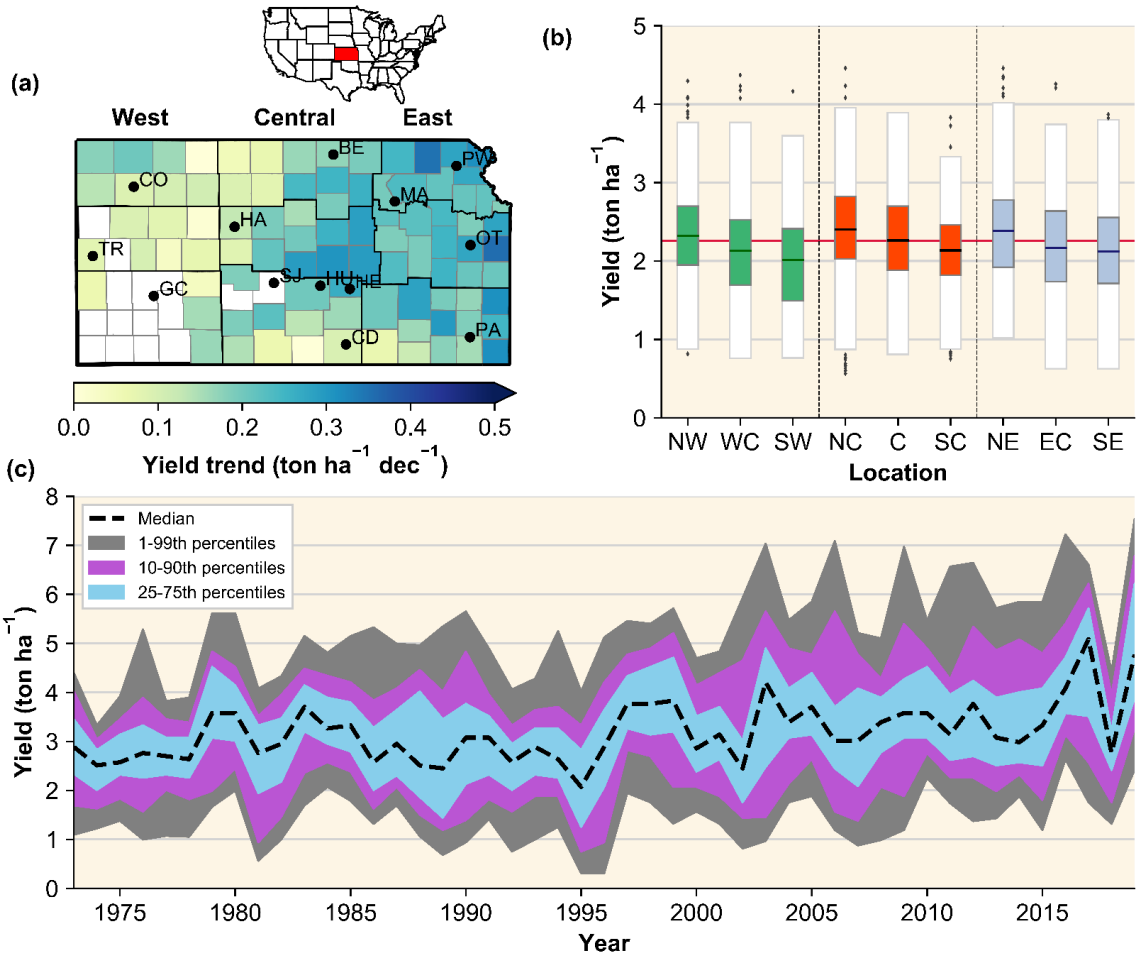

Figure B.1 (a) Same as figure 1a. (b) Same as figure 1b but for USDA-NASS county yields grouped by agricultural division. (c) Time series of combined variety trial yield statistics between 1973 and 2019.

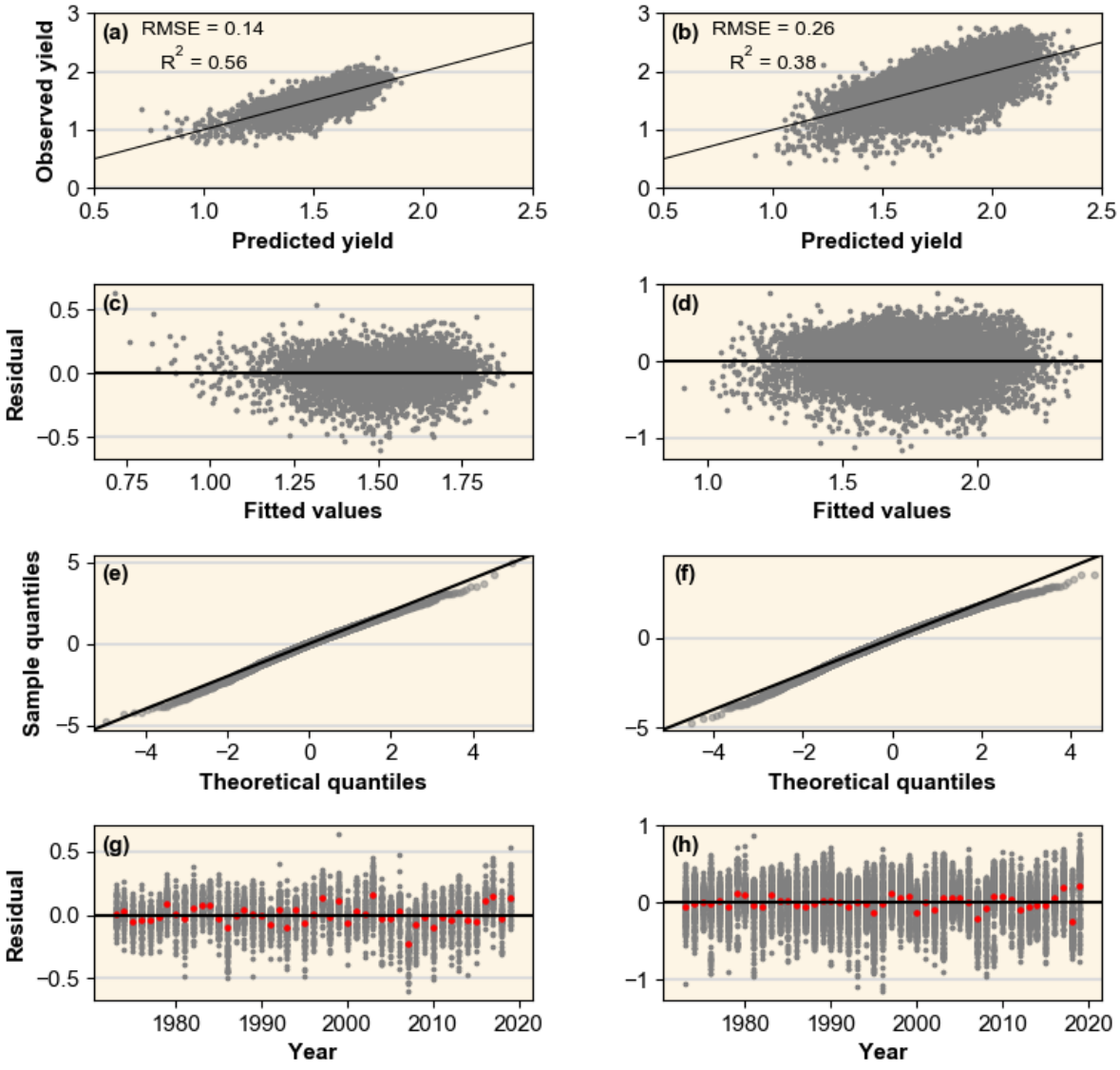

Figure B.2 Model diagnostics for the main assumptions of linear regression. (a) Scatter plot of observed yield vs. yield predictions. (b) Same as (a) but for variety trials. (c) Scatter plot of residuals vs. model fitted values. (d) Same as (c) but for variety trials. (e) Q-Q plot of the model residuals for USDA-NASS. There are small departures from normality for large residuals. (f) Same as (e) but for variety trials. (g) Residuals grouped by year for USDA-NASS. Each red dot represents the mean each year. (h) Same as (g) but for variety trials.

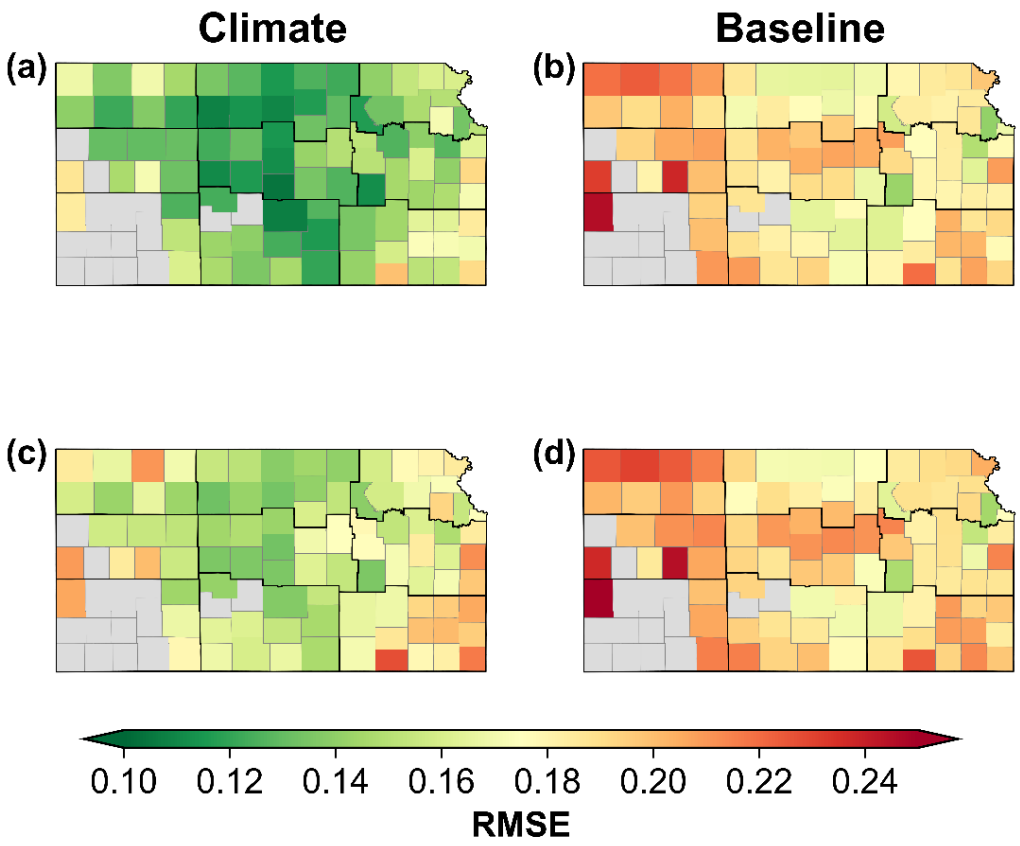

Figure B.3 (a) Root mean square error (RMSE) grouped by county for the full model with weather covariates. (b) Same as (a) but for a baseline model with only county fixed effects and time trend. (c−d) Same as (a) and (b) but for out-of-sample performance using leave-one-year-out cross validation.

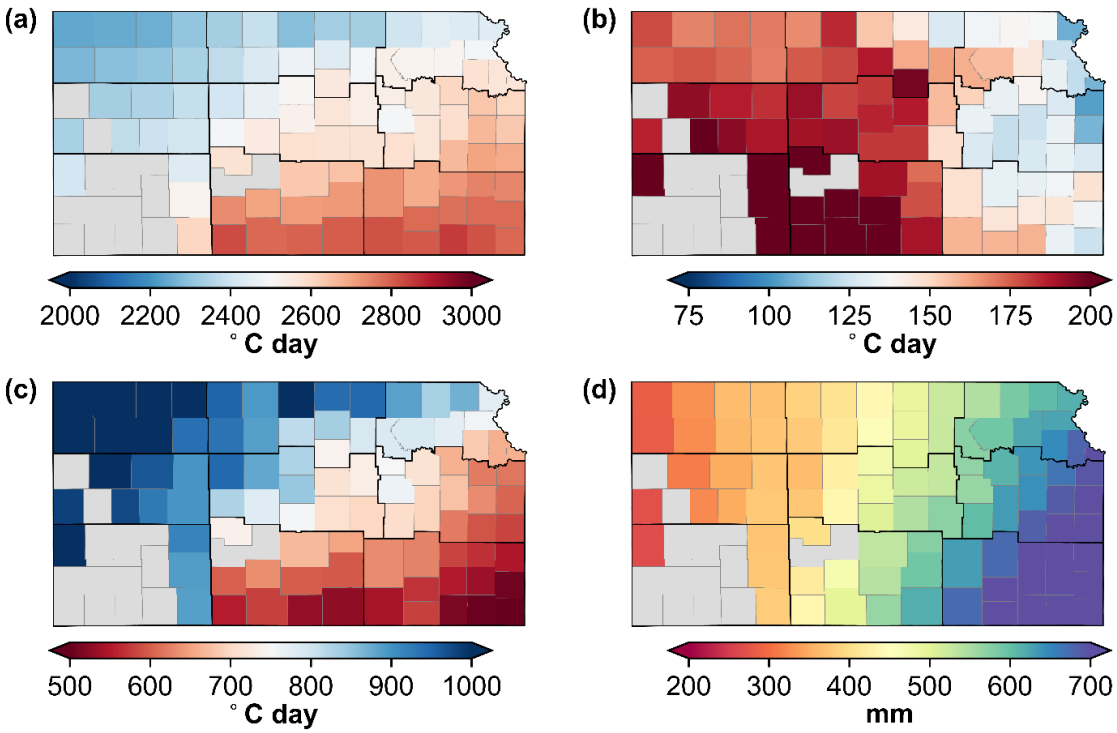

Figure B.4 Spatial distribution of average growing season accumulated (a) growing degree days, (b) killing degree days, (c) freeze degree days, and (d) precipitation. Variables are aggregated across phenological stages. The period is 1973 − 2019.

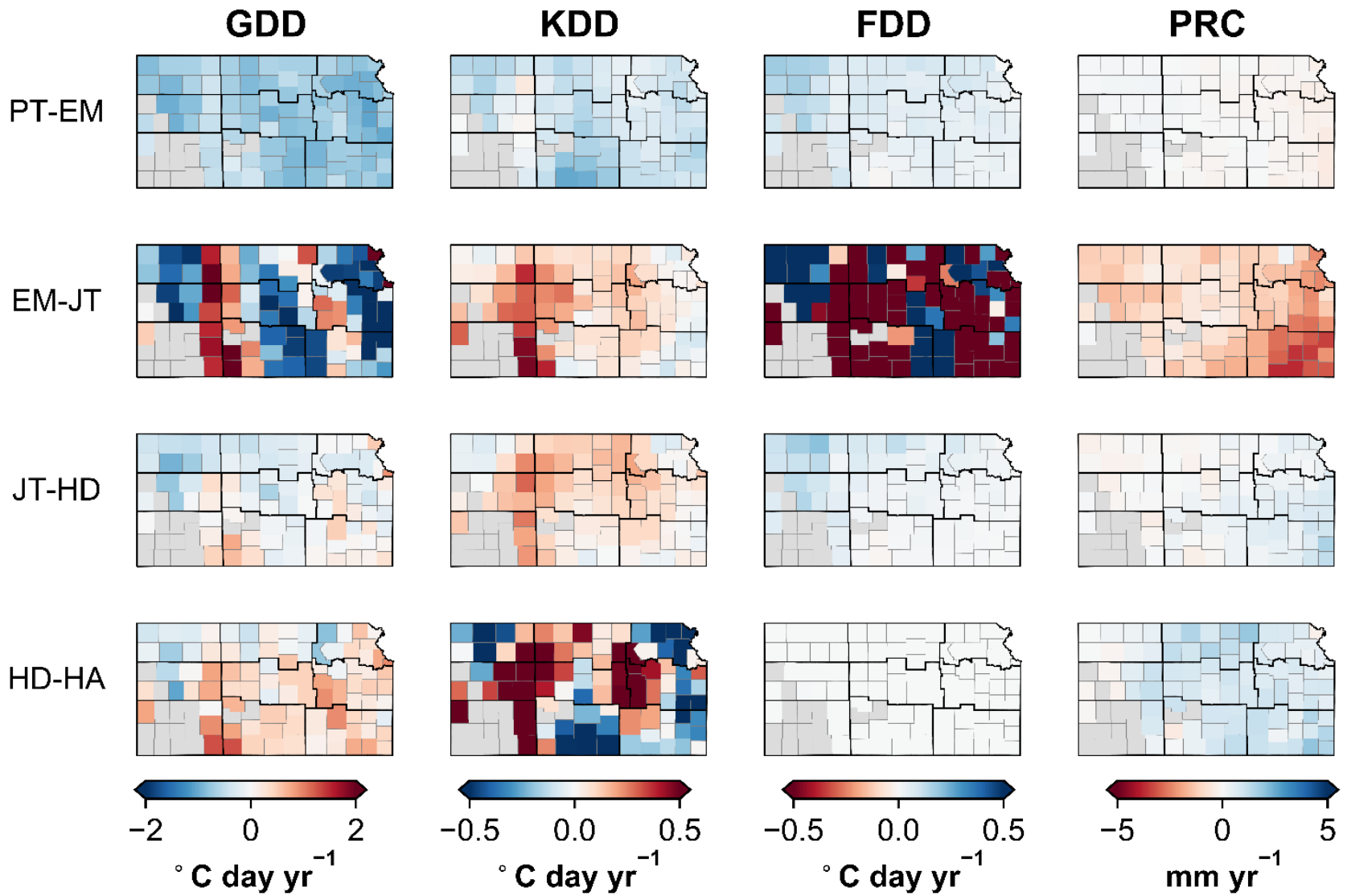

Figure B.5 Trends in environmental covariates by growth stage between 1973 and 2019. Trends were estimated using the Theil Sen slope. Weather and phenology are allowed to vary each year.

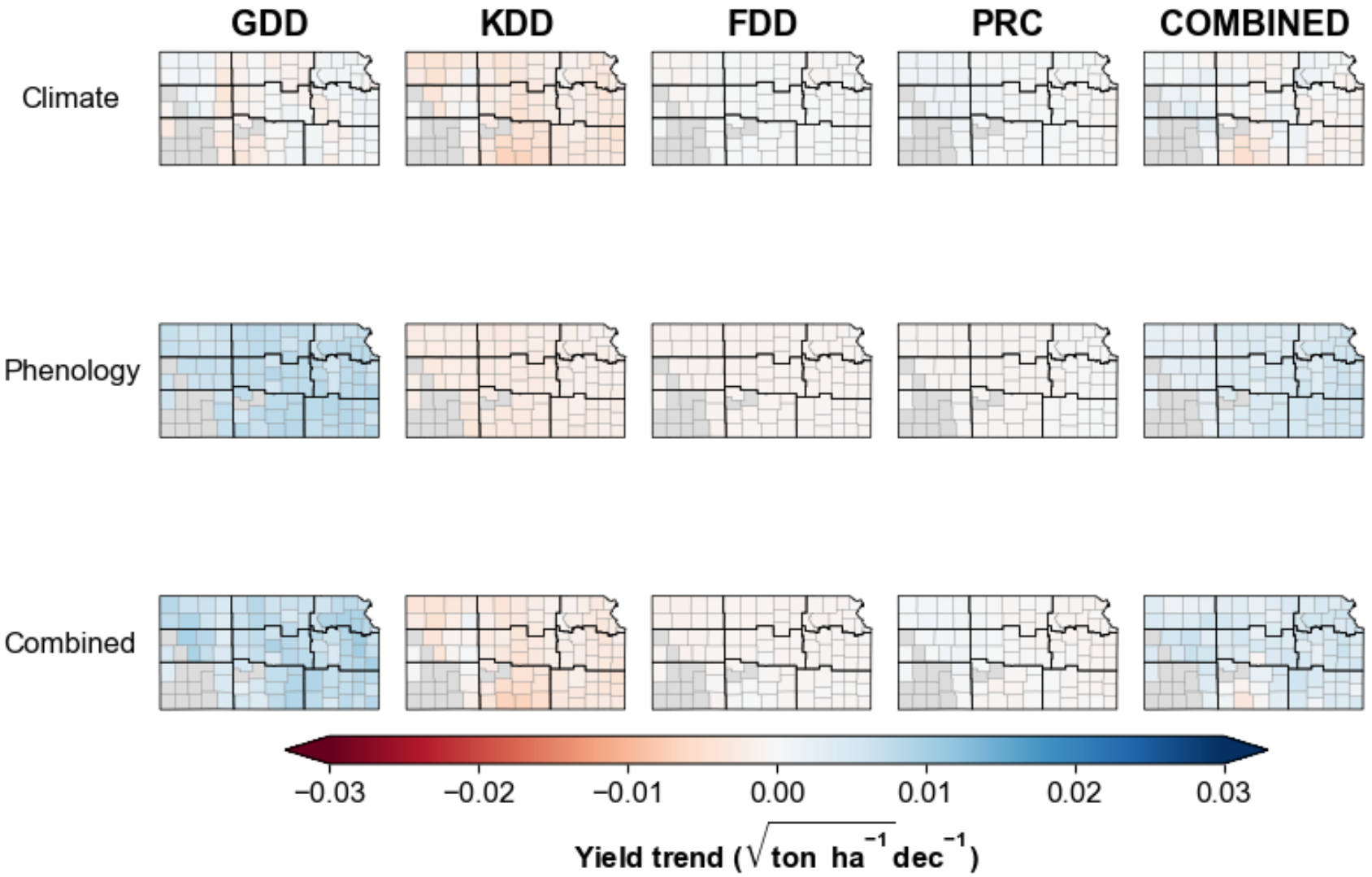

Figure B.6 Same as figure 3.4 but only for planting to emergence (PT-EM).

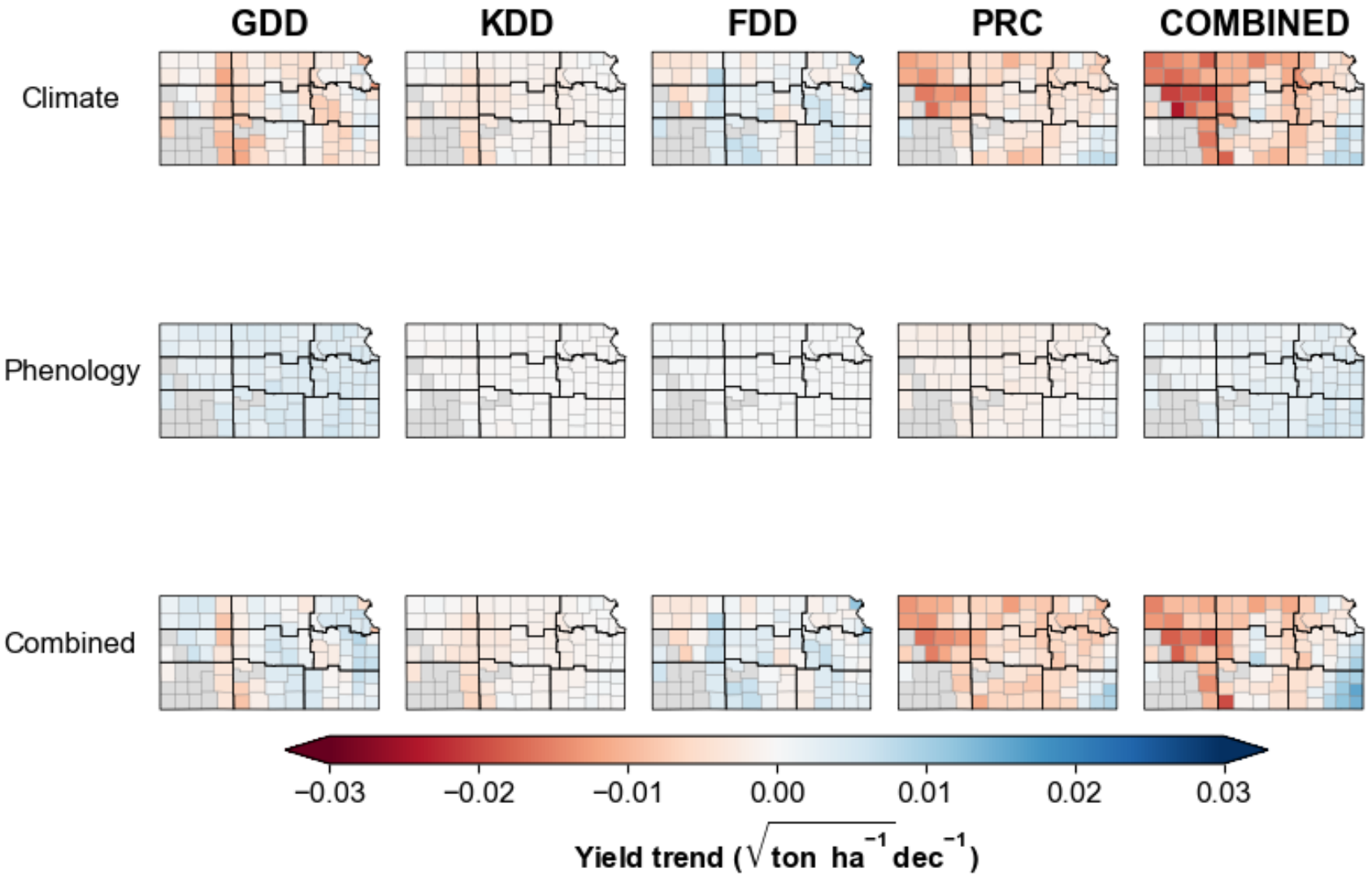

Figure B.7 Same as figure 3.4 but only for emergence to jointing (EM-JT).

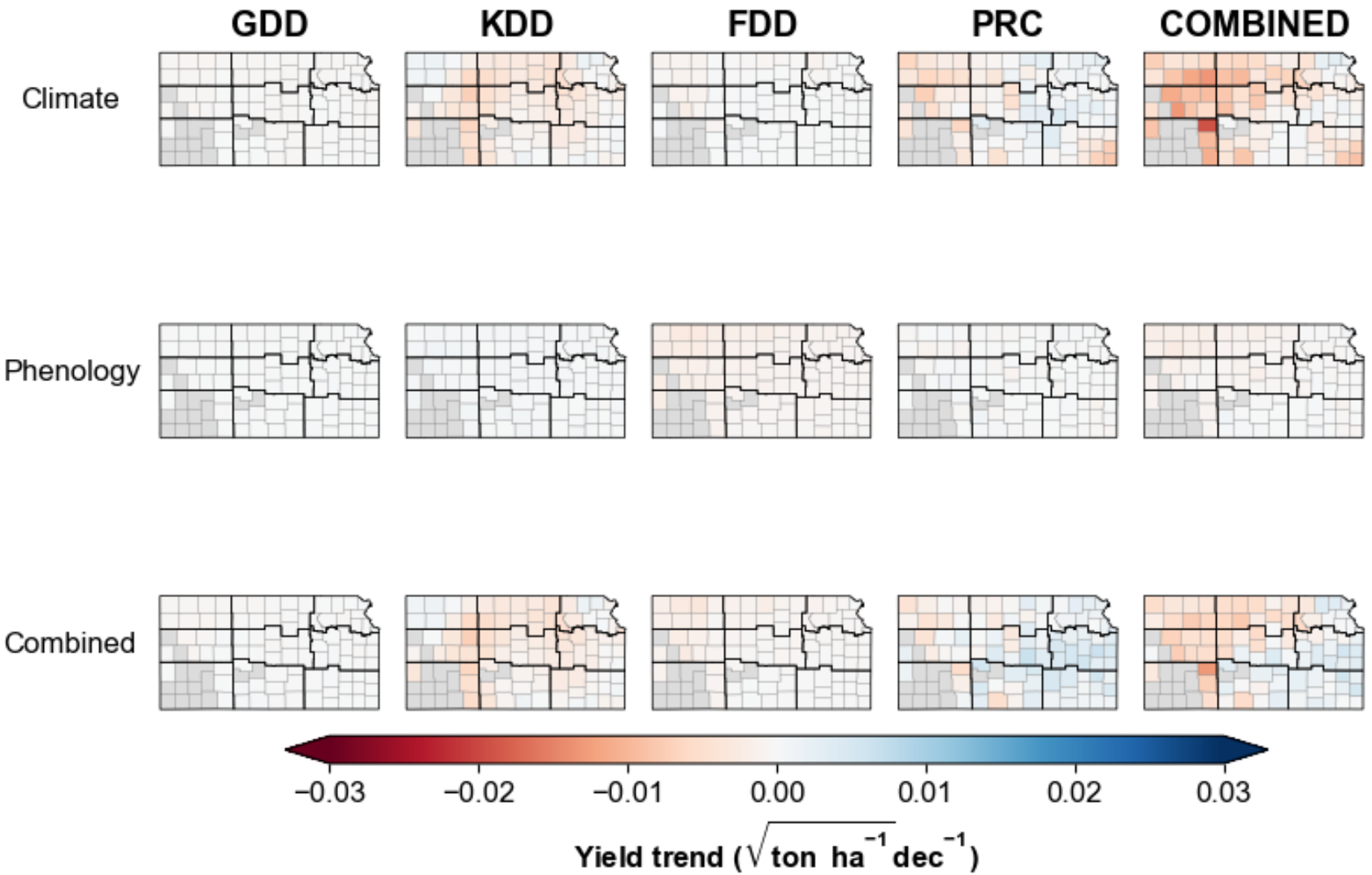

Figure B.8 Same as figure 3.4 but only for jointing to heading (JT-HD)

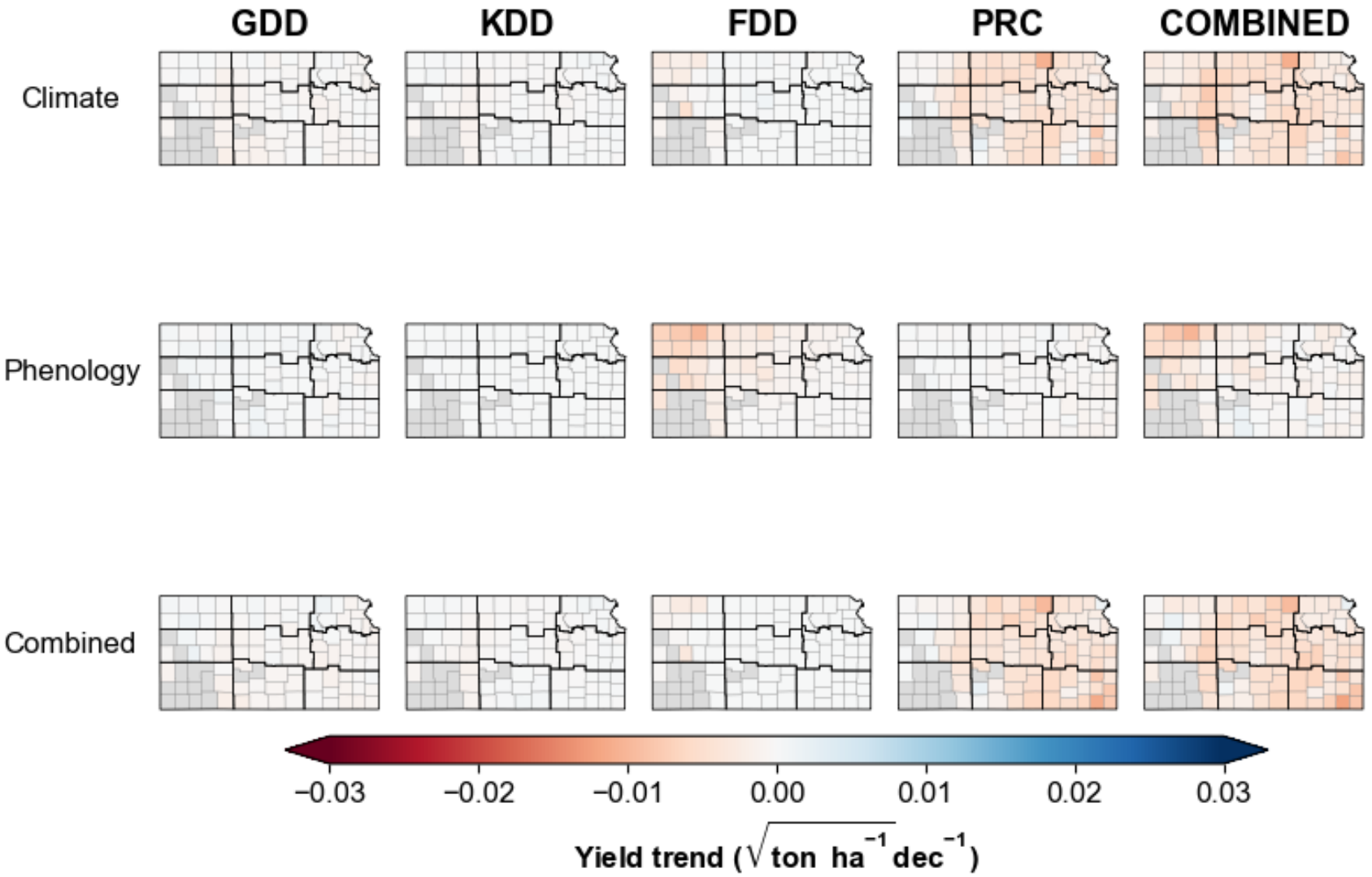

Figure B.9 Same as figure 3.4 but only for heading to harvest (HD-HA).

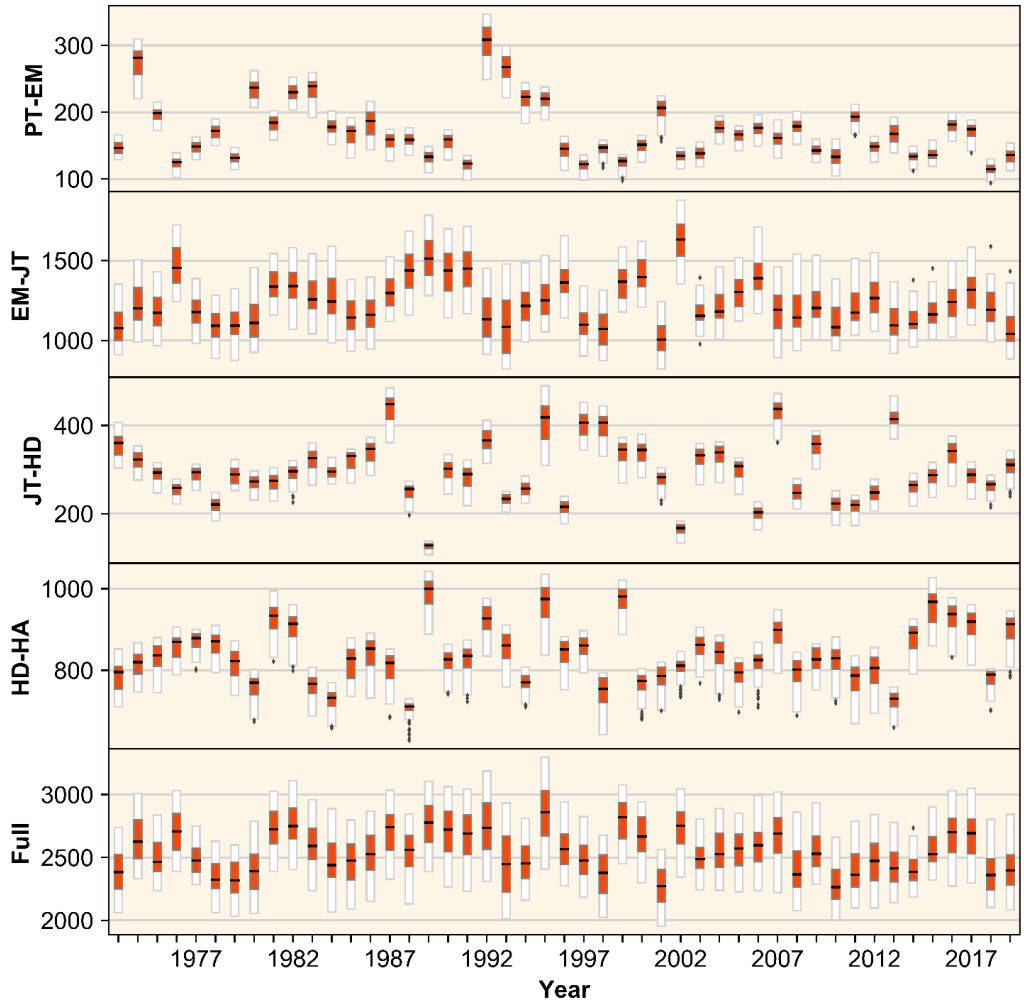

Figure B.10 Box plots of the distributions of GDDs by year and growth stage for the USDA-NASS dataset.

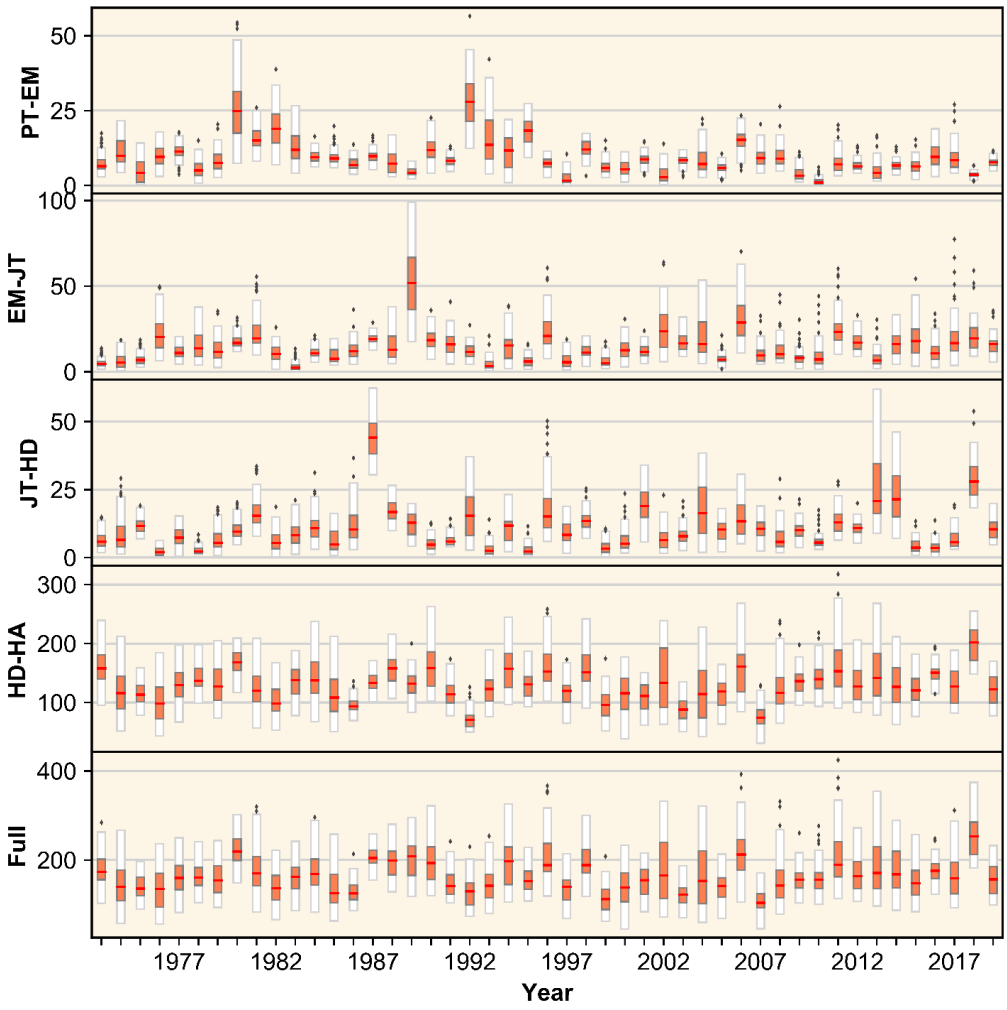

Figure B.11 Same as figure B.10 but for KDDs.

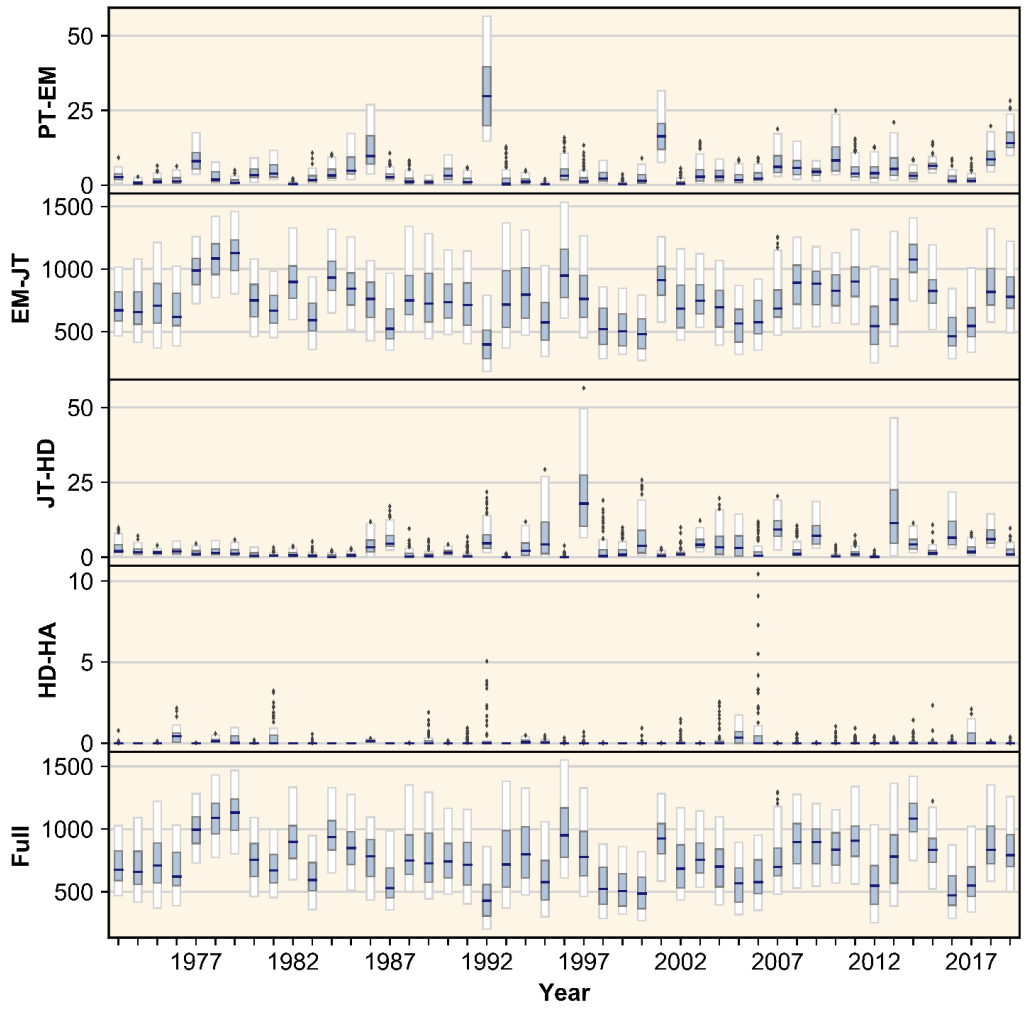

Figure B.12 Same as figure B.10 but for FDDs.

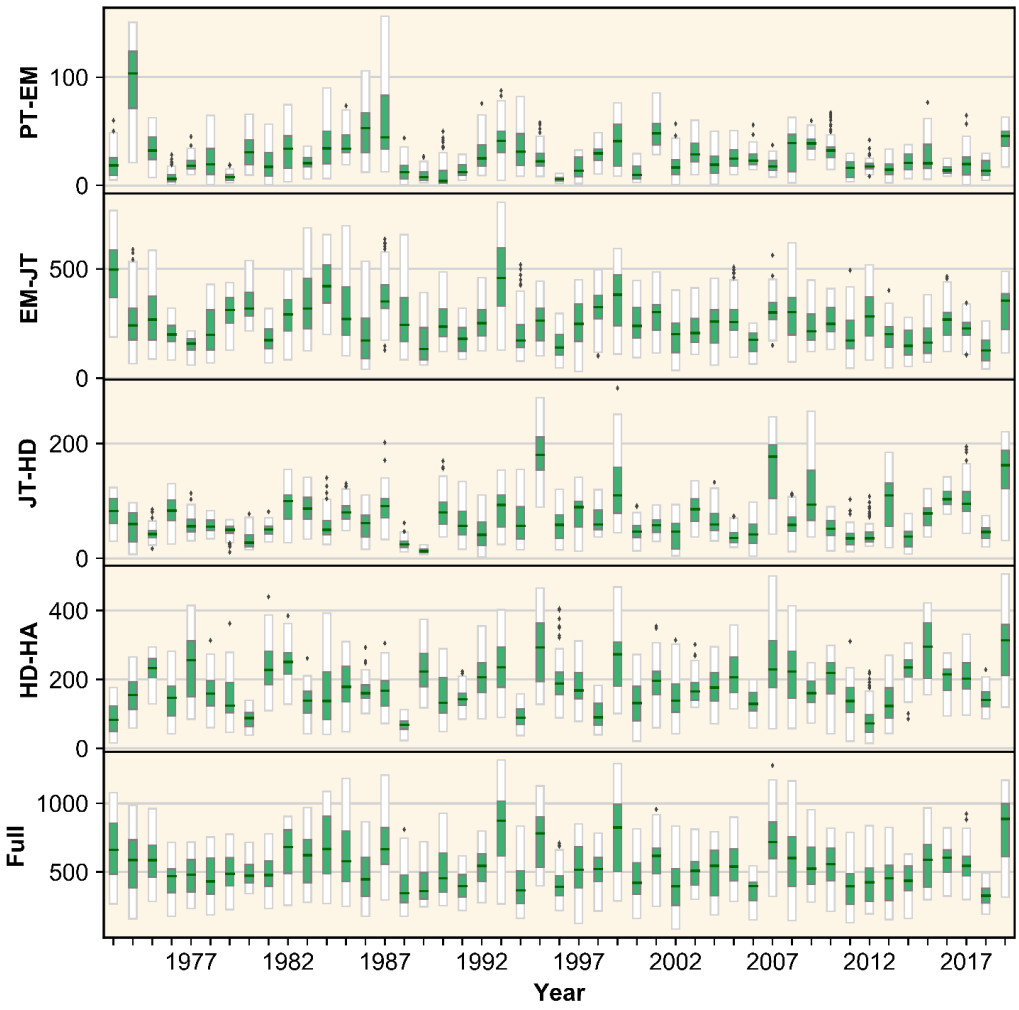

Figure B.13 Same as figure B.10 but for precipitation.

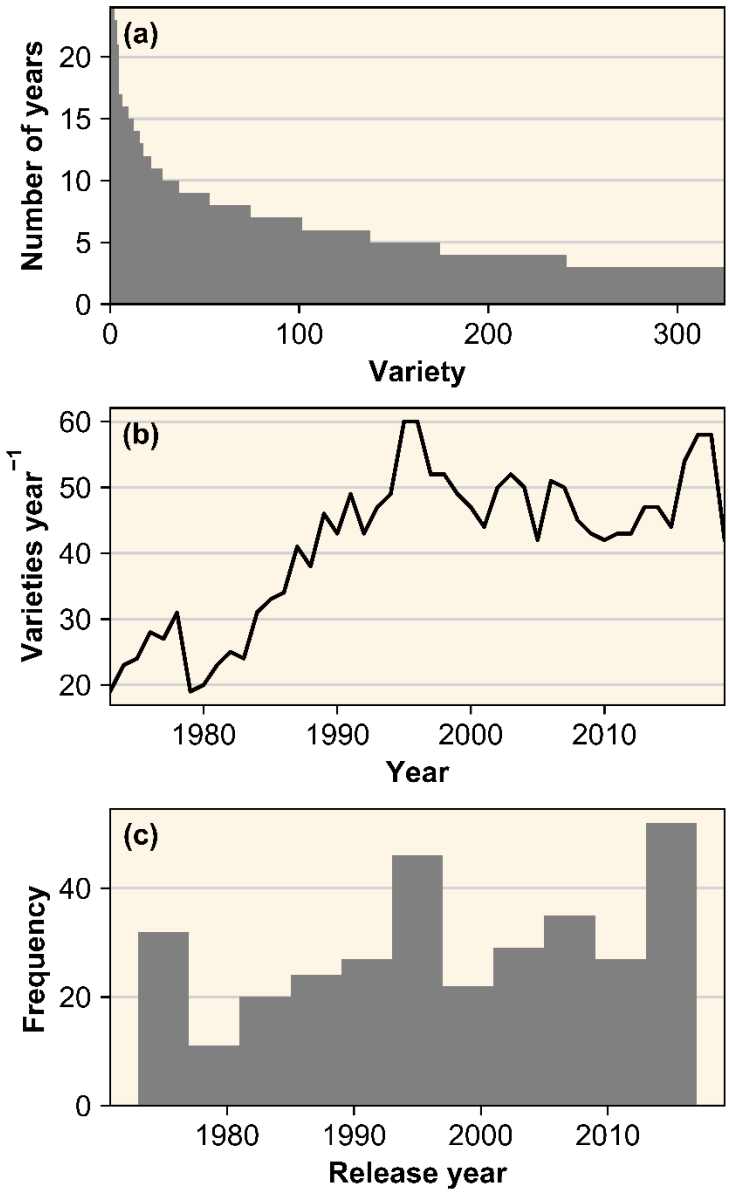

Figure B.14 (a) Number of unique years varieties appear in variety trials in descending order. The maximum and minimum were 24 and 3 years, respectively. (b) The number of unique varieties tested in each year. (c) The number of varieties newly released each year. Bin size is 4 years.

Table B.1 Site descriptions for twelve winter wheat variety trials in Kansas.

Region	Site	Abbr.	County	nYears	nObs	GHCN ID	Latitude	Longitude
East	Powhattan	PW	Brown	21	408	USC00143810	39.6679	-95.5199
	Manhattan	MA	Riley	42	859	USC00144972	39.1972	-96.5813
	Ottawa	OT	Franklin	41	818	USC00146128	38.6132	-95.2808
	Parsons	PA	Labette	49	1065	USC00146242	37.3677	-95.2881
Central	Belleville	BE	Republic	45	1053	USC00140682	39.8185	-97.6377
	Hays	HA	Ellis	44	1111	USC00143527	38.8586	-99.3358
	Hesston	HE	Harvey	38	745	USC00145744	38.0231	-97.3552
	St John	SJ	Stafford	32	697	USC00143847	38.1041	-98.6592
	Caldwell	CD	Sumner	11	217	USC00148670	37.2677	-97.4194
West	Colby	CO	Thomas	45	1141	USC00141699	39.1972	-96.5813
	Tribune	TR	Greeley	45	1126	USC00148235	38.4661	-101.773
	Garden City	GC	Finney	38	847	USW00023064	37.9272	-100.7247

Table B.2 Frequency of variety of trial abandonment by category. Years for abandonment are provided as subscripts.

Region	Site	Freeze	Wet Planting	Wet harvest	Drought	Dry Plant	Stunting	Hail	Volunteer wheat	Other
East	PW	0	0	1_{1993}	0	0	0	0	0	1_{2009}
	MA	$2_{1981,2007}$	1_{2010}	$2_{1993,2004}$	0	0	0	$2_{2002,2008}$	0	0
	OT	1_{1987}	$3_{1999,2010,2019}$	0	0	0	0	1_{2016}	0	0
	PA	$2_{1987,2007}$	1_{2019}	0	0	0	0	0	0	0
Central	BE	0	0	0	0	0	0	0	0	0
	HA	$3_{1971,2007,2016}$	0	0	0	0	0	0	0	0
	HE	0	0	0	0	0	0	0	0	0
	SJ	0	0	0	0	1_{2001}	0	0	1_{2005}	0
	CD	0	1_{2001}	0	0	0	0	0	0	$2_{1999,2006}$
West	CO	$3_{1968,1992,2006}$	0	0	0	0	0	0	0	0
	TR	$5_{1969,1976,1980,1984,2004}$	0	0	0	0	1_{1996}	1_{2004}	0	$3_{1992,1996,2000}$
	GC	$2_{1979,1996}$	0	0	$4_{2011,2012,2014,2015}$	0	0	1_{2008}	0	$3_{2016,2017,2018}$

Table B.3 Root mean square error (RMSE) and coefficient of determination (R^2) for modeling the midpoint (x_0) and growth (k) parameters of logistic growth curves by phenological stage with a large number of weather predictors using an Elastic Net using ten-fold cross validation. When there is no reported R^2, the average value was determined to be the best predictor.

Stage	Parameter	RMSE	R^2
PT	x_0	4.2	-
	k	0.03	0.11
EM	x_0	4.6	-
	k	0.04	0.16
JT	x_0	6.6	0.42
	k	0.02	0.3
HD	x_0	2.7	0.84
	k	0.03	0.56
HA	x_0	1	0.97
	k	0.06	-